Schweizerische Eidgenossenschaft
Confédération suisse
Confederazione Svizzera
Confederaziun svizra

Eidgenössisches Departement für
Umwelt, Verkehr, Energie und Kommunikation UVEK

Bundesamt für Energie BFE
Sektion Energieforschung und Cleantech

Schlussbericht vom 28. Januar 2026

Reservoir characterization of the Upper Muschelkalk aquifer in the canton of Thurgau for the optimization of geothermal utilization



Quelle: © Nagra

Thurgau

Subventionsgeberin:
Bundesamt für Energie BFE
Sektion Energieforschung und Cleantech
CH-3003 Bern
www.energieforschung.ch

Subventionsempfänger/innen:
Kanton Thurgau
Promenadenstrasse 8
CH-8510 Frauenfeld
www.tg.ch

Universität Bern
Hochschulstrasse 6
CH-3012 Bern
www.unibern.ch

Grob Gemüse AG
Bodenacker
CH-8255 Schlattingen
www.grob-gemuese.ch

Enevista Energy AG
Langfeldstrasse 80
CH-8500 Frauenfeld
www.enevista-energy.com

Autor/in:
Christoph Wanner, Universität Bern, christoph.wanner@unibe.ch
Larryn W. Diamond, Universität Bern, larryn.diamond@unibe.ch
Florian Eichinger, Hydroisotop GmbH, florian.eichinger@hydroisotop.de
Peter Alt-Epping, Universität Bern, peter.alt-epping@unibe.ch
Michael Heidinger, Hydroisotop GmbH, mh@hydroisotop.de
Michael Ballmer, TK Consult, michael.ballmer@tkconsult.ch
Rouven Künze, TK Consult, rouven.kuenze@tkconsult.ch
Christian Mair, Hydroisotop GmbH, cm@hydroisotop.de
Anne Breßler, Hydroisotop GmbH, ab@hydroisotop.de
Bernd Frieg, Enevista Energy AG, b.frieg@enevista-energy.com

BFE-Projektbegleitung:
Dr. Florence Bégué, florence.begue@bfe.admin.ch
Christian Minnig, christian.minnig@bfe.admin.ch
Stefano Benato, stefano.benato@bfe.admin.ch

BFE-Vertragsnummer: SI/502538-01

Für den Inhalt und die Schlussfolgerungen sind ausschliesslich die Autoren/Autorinnen dieses Berichts verantwortlich.

DOI: 10.5281/zenodo.18385828

Summary

As part of the geothermal project of Grob Gemüse- und Landbau in Schlattingen (TG), two boreholes (SLA-1 + SLA-2) were drilled with the financial support of the Canton of Thurgau. The boreholes encountered the Upper Muschelkalk aquifer Schinznach Formation, including the Stamberg Member Dolostone, formerly known as the Trigonodus Dolomit) at a depth of about 1150 m bgl. The thermal water temperature is approx. 60 °C with long-term production rates of up to 10 L/s in total from both boreholes. Since the Muschelkalk aquifer is one of the most important target horizon for continous hydrothermal exploitation in Northern Switzerland, this project aims to provide novel insights into the genesis, origin, age structure and flow paths of the groundwater from the this aquifer, the long-term stability of extraction and possible hydraulic and hydrochemical changes, and the regional groundwater flow paths and predictability of the development of groundwater from the Muschelkalk aquifer in the Canton of Thurgau and Northern Switzerland.

To do so, detailed geochemical, gas-physical and isotopic characterization of the Muschelkalk aquifer was undertaken during long-term pumping tests. Together with a regional compilation of hydrochemical data from the aquifer and accompanying numerical modelling, this approach allowed to demonstrate that in the region of Schlattingen, there are hydrochemically disconnected compartments of the Muschelkalk aquifer. Interestingly, the aquifer compartment towards the Randen Fault contains a significant groundwater component from the crystalline basement as evidenced by elevated concentrations of helium and lithium representing to most characteristic tracers for fluid flow through the crystalline basement. The upwelling flux of this groundwater component, however, is too slow to cause any thermal anomaly.

The two compartments drilled at Schlattingen represent two distinct geothermal plays, from which thermal water can be produced from the Muschelkalk aquifer in the Canton of Thurgau. The first play (“*regional Muschelkalk*”) is accessed by the SLA-1 well. It represents the classical aquifer-geothermal hydrodynamic properties of the Upper Muschelkalk rocks. The second play (“*faulted Muschelkalk*”) is accessed by the SLA-2 well and consists of steeply dipping fault zones that crosscut the Muschelkalk aquifer. Based on the crystalline basement component in the SLA-2 water and the high transmissivity measured in the crystalline basement at the bottom of the Schlattingen SLA-1 well, fault zones in the crystalline basement represent a third promising play in its own right (“*basement fault zone*”). The demonstrated existence of three distinct geothermal plays implies that in the Canton of Thurgau and adjacent areas future geothermal exploration activities should target all three.

For the "faulted Muschelkalk" play, mixing of upwelling saline fluids with more dilute, Ca-SO_4 type groundwater of the Muschelkalk aquifer may cause significant amounts of scales to precipitate along wells, pumps and surface installations, eventually leading to clogging and other technical issues. Likewise, the high salinity of the upwelling waters may promote corrosion of all these installations, which is also highly relevant for the “basement fault zone” play. It follows that the risk of scaling and corrosion processes must be considered in the early planning stage of geothermal exploitation of these play types. This entails understanding the causes of the processes through predictive geochemical modelling, monitoring by regular hydrochemical analyses, and designing mitigation measures such as injection of inhibitors.

Zusammenfassung

Im Rahmen des Geothermieprojekts der Grob Gemüse- und Landbau in Schlattingen (TG) wurden mit finanzieller Unterstützung des Kantons Thurgau zwei Bohrungen (SLA-1 + SLA-2) niedergebracht. Die Bohrungen stiessen auf den Oberen Muschelkalk-Grundwasserleiter (Schinznach-Formation, inkl. Stamberg Member Dolomit / Trigonodus Dolomit) in einer Tiefe von ca. 1150 m u. GOK. Die Thermalwassertemperatur liegt bei ca. 60°C mit langfristigen Förderraten von insgesamt bis zu 10 L/s aus beiden Bohrungen. Da der Muschelkalk-Aquifer einer der wichtigsten Zielhorizonte für eine kontinuierliche hydrothermale Nutzung in der Nordschweiz ist, soll dieses Projekt neue Erkenntnisse

über die Genese, Herkunft, Altersstruktur und Fließwege des Grundwassers aus diesem Aquifer, die langfristige Stabilität der Förderung und mögliche hydraulische und hydrochemische Veränderungen sowie die regionalen Grundwasserfliesswege und die Vorhersagbarkeit der Entwicklung des Grundwassers aus dem Muschelkalk-Aquifer im Kanton Thurgau und der Nordschweiz liefern.

Dazu wurden detaillierte geochemische, gasphysikalische und Isotopen Analysen zur Charakterisierung des Muschelkalk-Aquifers im Rahmen von Langzeit-Pumpversuchen durchgeführt. Zusammen mit einer regionalen Zusammenstellung hydrochemischer Daten aus dem Grundwasserleiter und numerischen Modellierungen konnte mit diesem Ansatz gezeigt werden, dass es in der Region Schlattingen hydrochemisch getrennte Kompartimente des Muschelkalk-Aquifers gibt. Interessanterweise enthält das Aquiferkompartiment in Richtung der Randenverwerfung eine bedeutende Grundwasser-komponente aus dem kristallinen Grundgebirge, was durch erhöhte Konzentrationen von Helium und Lithium belegt wird, die zu den charakteristischsten Tracern für die Fluide aus dem kristallinen Grundgebirge gehören. Die Menge an aufsteigendem Wasser aus dem Kristallin ist jedoch zu gering, um eine thermische Anomalie zu verursachen.

Die beiden hydraulischen Kompartimente stellen zwei unterschiedliche *geothermische Plays* dar, aus denen Thermalwasser aus dem Muschelkalk-Aquifer im Kanton Thurgau gewonnen werden kann. Das erste *Play* ("*regionaler Muschelkalk*") wird durch die Bohrung SLA-1 erschlossen. Sie weist die klassischen hydrodynamischen Eigenschaften der Gesteine des Oberen Muschelkalks auf. Das zweite Play ("*Faulted Muschelkalk"*) wird über die Bohrung SLA-2 erschlossen und besteht aus steil abfallenden Störungszonen, die den Muschelkalk-Grundwasserleiter durchschneiden. Aufgrund der kristallinen Grundgebirgskomponente im SLA-2-Wasser und der hohen Durchlässigkeit, die am Ende der Schlattingen-SLA-2 Bohrung gemessen wurde, stellen Störungszonen im kristallinen Grundgebirge ein drittes vielversprechendes *Play* dar ("*basement fault zone"*). Die nachgewiesene Existenz von drei unterschiedlichen geothermischen *Plays* bedeutet, dass sich künftige geothermische Explorations-aktivitäten im Kanton Thurgau und den angrenzenden Gebieten auf alle drei *Plays* konzentrieren sollten.

Beim Play "*Faulted Muschelkalk"* kann die Mischung von aufsteigenden salinen Fluids mit schwach salinem Ca-SO_4 Typ Grundwasser des Muschelkalk-Aquifers dazu führen, dass sich entlang der Bohrlochwand, Pumpen und Oberflächenanlagen erhebliche Mengen an mineralischen Ausfällungen (Scales) bilden, was schließlich zu Verstopfungen und anderen technischen Problemen führen kann. Ebenso kann die hohe Salinität des aufsteigenden Wassers die Korrosion all dieser Anlagen begünstigen, was auch für das *Play* "*basement fault zone"* von großer Bedeutung ist. Daraus folgt, dass das Risiko von Scaling- und Korrosionsprozessen in der frühen Planungsphase der geothermischen Nutzung des Muschelkalk-Aquifers berücksichtigt werden muss. Dies erfordert ein Verständnis der Ursachen dieser Prozesse durch geochemische Modellierung, Überwachung durch regelmäßige hydrochemische Analysen und die Entwicklung von Massnahmen zur Risikominderung, wie z. B. die Injektion von Inhibitoren.

Résumé

Dans le cadre du projet de géothermie de Grob Gemüse- und Landbau à Schlattingen (TG), deux forages (SLA-1 + SLA-2) ont été réalisés avec le soutien financier du canton de Thurgovie. Les forages ont rencontré l'aquifère du Muschelkalk supérieur (Formation de Schinznach, y compris le membre dolomitique de Stamberg, anciennement connu sous le nom de dolomite de Trigonodus) à environ 1150 m de profondeur. La température de l'eau thermale est d'environ 60 °C avec des débits à long terme allant jusqu'à 10 L/s au total pour les deux forages. Comme l'aquifère du Muschelkalk est l'un des principaux horizons pour une exploitation hydrothermale en cours dans le nord de la Suisse, ce projet a pour but d'apporter de nouvelles connaissances sur la genèse, l'origine, la structure d'âge et les voies d'écoulement des eaux souterraines de cet aquifère, la stabilité à long terme de la production et les éventuelles modifications hydrauliques et hydrochimiques, ainsi que sur les voies d'écoulement régionales des eaux souterraines et la prévisibilité de l'évolution des eaux souterraines de l'aquifère du Muschelkalk dans le canton de Thurgovie et le nord de la Suisse.

Pour ce faire, des analyses géochimiques, physiques des gaz et isotopiques détaillées ont été effectuées pour caractériser l'aquifère du Muschelkalk dans le cadre d'essais de pompage de longue durée. Associée à une compilation régionale de données hydrochimiques de l'aquifère et à des modélisations numériques, cette approche a permis de montrer qu'il existe des compartiments hydrochimiquement séparés de l'aquifère du Muschelkalk dans la région de Schlattingen. Il est intéressant de noter que le compartiment de l'aquifère en direction de la faille du Randen contient une importante composante d'eau souterraine provenant du socle cristallin, comme en témoignent les concentrations élevées d'hélium et de lithium, qui font partie des traceurs les plus caractéristiques des fluides provenant du socle cristallin. Le flux ascendant de cette composante des eaux souterraines est toutefois trop lent pour provoquer une anomalie thermique.

Les deux compartiments forés à Schlattingen représentent deux zones géothermiques distinctes, à partir desquelles il est possible de produire de l'eau thermale à partir de l'aquifère Muschelkalk dans le canton de Thurgovie. Le premier *play* ("*regionaler Muschelkalk*") est accessible par le puits SLA-1. Il présente les propriétés hydrodynamiques d'un aquifère géothermique classique des roches du Muschelkalk supérieur. Le deuxième *play* (*"faulted Muschelkalk"*) est accessible par le puits SLA-2 et se compose de zones de failles à forte inclinaison qui traversent l'aquifère du Muschelkalk. D'après la composante cristalline du socle dans l'eau du SLA-2 et la transmissivité élevée mesurée à l'extrémité du puits Schlattingen SLA-2, les zones de failles dans le socle cristallin représentent un troisième *play* prometteur à part entière ("*basement fault zone"*). L'existence avérée de trois *play* géothermiques distincts implique que, dans le canton de Thurgovie et les zones adjacentes, les futures activités d'exploration géothermique devraient cibler les trois.

Pour le *play* "*faulted Muschelkalk"* le mélange des fluides salins ascendants avec les eaux souterraines plus diluées de type Ca-SO_4 de l'aquifère du Muschelkalk peut entraîner la précipitation de quantités importantes de tartre le long des puits, des pompes et des installations de surface, ce qui peut finalement conduire à des obstructions et à d'autres problèmes techniques. De même, la salinité élevée des fluides ascendantes peut favoriser la corrosion de toutes ces installations, ce qui est également très pertinent pour la *play* "*basement fault zone"*. Il s'ensuit que le risque de processus d'entartrage et de corrosion doit être pris en compte dès les premières étapes de la planification de l'exploitation géothermique de l'aquifère du Muschelkalk. Cela implique de comprendre les causes de ces processus grâce à une modélisation géochimique prédictive, à une surveillance par des analyses hydrochimiques régulières et à la conception de mesures d'atténuation telles que l'injection d'inhibiteurs.

Table of Contents

1 Introduction 12

1.1 Context and motivation 12

1.2 Project aims 17

1.3 Geology and aquifer properties at Schlattingen and surroundings 18

1.3.1. Tectonic setting 18

1.3.2. Regional geology 18

1.3.3. Lithostratigraphic nomenclature 18

1.3.4. Lithologies hosting the Muschelkalk aquifer 21

1.3.5. Fracture permeability in the Muschelkalk aquifer 21

1.3.6. Confining units of the Muschelkalk aquifer 22

2 Procedure, method, results and discussion 24

2.1 Methods 24

2.1.1. Monitoring of hydraulic parameters 24

2.1.2. Thermal water sampling and analysis 27

2.1.3. Visual inspection and geophysical measurements of the SLA-2 well 33

2.1.4. Numerical modelling 33

2.2 Results 34

2.2.1. Hydraulic monitoring and evaluation of the pumping test 34

2.2.2. Detailed hydrochemical and isotopic characterization of thermal water produced from SLA-1 and SLA-1 56

2.2.3. Temporal evolution of major solutes concentrations and stable water isotopes in the two Schlattingen wells (2018-2025) 68

2.2.4. Results of the geophysical borehole inspections 76

2.2.5. Hydrogeochemistry of the Muschelkalk Aquifer in Northern Switzerland and adjacent areas in Germany 77

2.3 Discussion 86

2.3.1. Conceptual model describing the coupled thermal-hydraulic-chemical processes controlling the productivity and composition of thermal water from the two Schlattingen wells 86

2.3.2. Groundwater simulations 93

2.3.3. Reactive transport modeling: The Uni Bern THC model 99

3 Implications for harnessing geothermal energy in the Canton of Thurgau 111

4 Conclusions and Outlook 115

5 Acknowledgments 119

6 Reference List 120

Appendix 1: Extraction and analysis of gases, noble gases and isotopes including $^{85}Kr/^{81}Kr$ and $^{37}Ar/^{39}Ar$ from the thermal water extracted from the Schlattingen wells (SLA-1 and SLA-2) 123

Appendix 2: The modified TK consult numerical groundwater model 151

List of Figures

Figure 1: Drilling location in Schlattingen (© Swisstopo) 12

Figure 2: Location of the Schlattingen boreholes and schematic cross-section of Northern Switzerland (from Frieg et al., 2015) 13

Figure 3: Section of the ABF-Log (left) and drill cores of the Upper Muschelkalk (right) (from Frieg et al., 2015) 14

Figure 4: Geological profile (left) and casing scheme along horizontal well SLA-2 (from Frieg et al., 2015). 15

Figure 5: Geological block model with vertical cross section along SLA-2 (3D-view from SSE) (from Bläsi et al., 2014). 15

Figure 6: Map of depth contour of the top Trigonodus Dolomite with the positions of the geothermal boreholes SLA-1 and SLA-2 in Schlattingen and their penetration points through the top of the Trigonodus dolomite (Bläsi et al., 2014). 16

Figure 7: Geological setting of the Schlattingen geothermal site. 19

Figure 8: Key to nomenclature and ages of lithostratigraphic units relevant to the Muschelkalk aquifer at Schlattingen. 20

Figure 9: Stratigraphic sequence traversed by the vertical SLA-1 well at Schlattingen (from Albert et al., 2012). 20

Figure 10: Fractures logged in the Muschelkalk aquifer at Schlattingen. From Diamond et al. (2025) based on data from Grob AG. 23

Figure 11: Pumping test in SLA-1 starting February 2024 until June 2024. 25

Figure 12: Pumping test in SLA-2 starting February 2024 until June 2024. 26

Figure 13: Wellhead SLA-1 (left) and SLA-2 (right) 32

Figure 14: Vacuum degassing unit 32

Figure 15: Sampling under operational P- and T-conditions 33

Figure 16: Collected samples 33

Figure 17: Pressure [bar] and flow rates [l/min] at SLA-1 in 2024. 35

Figure 18. Pressure [m agl, based on a sensor depth of 255 m bgl and fluid density of 1000 kg/m^3] and flow rates [l/min] at SLA-1 in 2024. 36

Figure 19: Sequence definition for hydraulic tests performed at SLA-1 in 2024, including and approximated borehole history starting in September 2023 37

Figure 20: TNP of RWS1 and RWS2 38

Figure 21: Horner-Plot RWS1 and RWS2 39

Figure 22: TNP of RW1/RWS1 and RW2/RWS2 40

Figure 23: Simulation of RW1/RWS1 and RW2/RWS2 using hydraulic parameters estimated in Reinhard & Rösli (2013) 42

Figure 24: Single-fit simulation of RW2/RWS2 using a 2-shell radial composite model 44

Figure 25: Simulated pressures - Single-fit simulation for RW2/RWS2 using a 3-shell-composite model with flow dimensions in the inner zones. 45

Figure 26: Simulated flowrates - Single-fit simulation for RW2/RWS2 using a 3-shell-composite model with flow dimensions in the inner zones. 46

Figure 27: Simulation of RW1/RWS1 to investigate the potential change in inner-zone parameters while fixing the hydraulic parameters of the outer zone to estimates from the RW2/RWS2 analysis 48
Figure 28: SLA-2: Pressure (blue, in bar) and production rate (yellow, in l/min) in 2024 50
Figure 29: SLA-2 - Analysis setup considering a history period of 2'880 hours 51
Figure 30: SLA-2 - Analysis setup considering a history period of 11'640 hours 51
Figure 31: SLA-2 - TNP flow diagnostics 52
Figure 32: Fit results for two different history durations 54
Figure 33: SLA-2 - Analysis of SLA-2-2024 data using a 3-shell composite model with flow dimensions and different history durations 55
Figure 34: Hydrochemical composition of SLA-1 and SLA-1 in a Schoeller diagram 56
Figure 35: Sulfur and oxygen isotope ratio in SO_4 dissolved in groundwater samples collected from the Muschelkalk aquifer at Schlattingen and nearby locations. 61
Figure 36: Sr concentration and Sr isotope ratios measured in groundwater samples collected from the Muschelkalk aquifer at Schlattingen and nearby locations. 62
Figure 37: Stable carbon versus stable hydrogen isotope signatures of dissolved methane compared to endmembers and influencing processes according to Whiticar (2020) and Milkov & Ethiope (2018). 65
Figure 38: Isotope geochemical characterisation of hydrocarbons and carbon dioxide with isotope fractionation factors lines (εc) according to Whiticar (1999 & 2020). 66
Figure 39: Diagram showing the methane isotopes of the samples examined in relation to the distribution of hydrocarbons. 66
Figure 40: ^{4}He-isotope data of selected Muschelkalk groundwater samples as a function of the ^{81}Kr model age. 67
Figure 41: Production rates and sampling at SLA-1 and SLA-1 from October 2023 to July 2025; After May 2025 no production rate data was recorded for SLA-2. 69
Figure 42: Time series of main dissolved constituents of the groundwater from borehole SLA-1 (time period 2018 to 2025). 69
Figure 43: Time series of main dissolved constituents of the groundwater from borehole SLA-1 (time period 2022 to 2025). 70
Figure 44: Time series of main dissolved constituents of the groundwater from borehole SLA-1 (time period 2019 to 2025). 71
Figure 45: Time series of main dissolved constituents of the groundwater from borehole SLA-1 (time period 2022 to 2025). 72
Figure 46: Diagram presenting the results of the stable water isotopes for SLA-1 and SLA-2. ... 75
Figure 47: Excerpt from the visual camera survey of borehole SLA-1 showing the crystalline precipitations at ca. 440 m dhl. 76
Figure 48: Map showing the locations of shallow and deep Muschelkalk groundwater samples in Northern Switzerland and adjacent areas in Germany for which chemical and isotopic analyses are available (Waber et al., 2022; Nagra, 2024). 77
Figure 49: Piper plot illustrating the composition of groundwaters collected from the Muschelkalk aquifer in Northern Switzerland and adjacent areas with respect to major cations and anions Modified from Waber & Traber (2022) and supplemented with data for the two Schlattingen wells (Table 7).. 79

Figure 50: Cross plots illustrating the behavior of key hydrogeochemical parameters in groundwaters collected from the Muschelkalk aquifer in Northern Switzerland and adjacent areas. All plots are taken from Nagra (2024) and supplemented with data for the two Schlattingen wells (Table 7, Table 10, Table 11)..... 80

Figure 51: Cross plots between concentrations of Br, Cl, Li and He in groundwaters collected from the Muschelkalk aquifer in Northern Switzerland and adjacent areas. 83

Figure 52: Conceptual models illustrating the large-scale flow systems controlling the groundwater composition in the two Schlattingen wells. 87

Figure 53: Schematic, conceptual model of processes near the end of well SLA-2, explaining how the produced SLA-2 water attains a chemically hybrid signature distinct from that in SLA-1. 89

Figure 54: Saturation indices of anhydrite and calcite as a function of the mixing proportion between the modified basement water and the Ca-SO_4 type Muschelkalk groundwater at SLA-1 (Table 18) calculated by Phreeqc at a constant temperature of 57°C..... 90

Figure 55: Map of locations of deep Muschelkalk groundwater samples in the vicinity of the two Schlattingen wells..... 92

Figure 56: Linear correlations between $\delta^{18}O$ values, Li concentrations, and ^{81}Kr model ages of Muschelkalk groundwaters collected in the Nagra siting regions of ZNO and NL and in the Schlattingen 1 well (SLA-1 at bottom left). Both plots are taken from Nagra (2024) and supplemented with data for the two Schlattingen wells (Table 10, Figure 40). 92

Figure 57: Sketch of 2020 conceptual hydraulic model by TK Consult (Künze & Kuhlmann, 2020). 93

Figure 58: Updated conceptual hydrogeological model, based on the geological–geochemical concept illustrated in Figure 50. 95

Figure 59: East–west vertical cross-section of the numerical hydraulic model by TK Consult, based on the conceptual model in Figure 58. 96

Figure 60: Comparison between measured and simulated hydrostatic pressures in SLA-2 between February 2024 and May 2025..... 98

Figure 61: Comparison between measured and simulated hydrostatic pressures in SLA-2 in March/April 2015. 99

Figure 62: The Uni Bern THC model with the wells and regions R1 to R5..... 100

Figure 63: Fluxes computed by TK Consult using their regional model. 101

Figure 64: Illustration of how flux balances were obtained with the TK Consult model. 102

Figure 65: Thermal and compositional breakthrough curves for water exiting the SLA-2 well head for the lower permeability model Variant 1 (solid or long dashed) and the higher permeability Variant 2 (short dashed) using a basement flux of 1.5 $m^3/m^2/yr$ (see Table 19 for permeability values). 104

Figure 66: Thermal and compositional breakthrough curves at the SLA-2 well head for two upwelling flow rates: 1.0 $m^3/m^2/yr$ (solid or long dashed) and 0.5 $m^3/m^2/yr$ (short dashed) using the permeability structure of Variant 1. Current time (late 2025) is at approximately 550 days. 105

Figure 67: Mineral precipitation rate and volume profiles along the horizontal section of SLA-2 after 3 weeks of operation. 108

Figure 68: Mineral precipitation rate and volume profiles along the horizontal section of SLA-2 after 10 years of operation. 108

Figure 69: Time series of mineral volumes in the wall of borehole SLA-2 at three observation points, Obs 1-3. 109

Figure 70: (a) 3D view towards ENE showing the distribution of anhydrite around the horizontal section of the SLA-2 well. 109

Figure 71: Conceptual illustration of the three exploration plays identified in this study for the Canton of Thurgau. 113

List of Tables

Table 1: Overview of groundwater samples taken from borehole SLA-1 and the conducted analytical program (analytical packages according to the proposal) 28

Table 2: Overview of groundwater samples taken from borehole SLA-1 and the conducted analytical program (analytical packages according to the proposal). 29

Table 3: Overview of parameter analysed and corresponding analytical methods used in this project. 30

Table 4: Summary table of performed analyses for SLA-1 47

Table 5: Hydraulic parameter estimates for Interval TD1 and TD2 of SLA-2 (Reinhard & Rösli, 2015) 53

Table 6: Hydraulic parameter estimates for SLA-2Table 6 based on the analysis of the data 2024. 55

Table 7: Overview of physico-chemical parameters and concentrations of main anions and cations 58

Table 8: Overview of trace element concentrations 59

Table 9: Overview of organic concentrations of organic compounds 60

Table 10: Overview of stable and radiogenic isotope analyses 62

Table 11: DIC result and carbon isotopes 63

Table 12: Compilation of dissolved gas and stable gas isotopes dissolved in thermal water of the boreholes SLA-1 and SLA-2 64

Table 13: Noble gas concentrations and noble gas isotope ratios determined on samples taken from borehole SLA-1 and SLA-2 68

Table 14: Variations in major solutes concentrations in SLA-1 waters samples collected on two consecutive days on April 15 and 16, 2024 72

Table 15: Analyses of groundwater from borehole SLA-1 taken between 2022 and 2025 73

Table 16: Analyses of groundwater from borehole SLA-2 taken between 2022 and 2025 73

Table 17: Overview of $\delta^{18}O$-H_2O and $\delta^{2}H$-H2O values from SLA-1 and SLA-2 74

Table 18: Concentrations of major solutes and selected trace elements in the Muschelkalk groundwater at SLA-1, SLA-2 and the crystalline basement groundwater at Weiach, as well as the reconstructed deep saline endmember ascending and mixing with a SLA-1 type groundwater to form the SLA-2 groundwater. 85

Table 19: Two outcomes (Variant 1 and 2) of the model calibration from TK Consult based on the conceptual flow model (Figure 58) and the most recent pressure and flux measurements at SLA-2. Shown are re-calibrated formation and region permeabilities and the volumes of regions R1, R2 and R5 in the conduit. 97

Table 20: Flux contributions in the fault zone conduit water computed with the TK Consult model 102

Table 21: Flux contributions in the produced SLA-2 water computed with the TK Consult model 103

1 Introduction

1.1 Context and motivation

As part of the geothermal project of Grob Gemüse- und Landbau in Schlattingen (TG), two boreholes (SLA-1 + SLA-2) were drilled and tested with the financial support of the Canton of Thurgau. The drilling location is in the direct vicinity of the greenhouses (Figure 1). The installation site in Schlattingen is located 10 km east of Schaffhausen and 0.6 km south of the Rhine River close to the border with Germany. The hilly topography around the SLA-1 location features wide NW-striking ridges separated by wide glacially shaped valley floors. The maximum relief is 200 m.

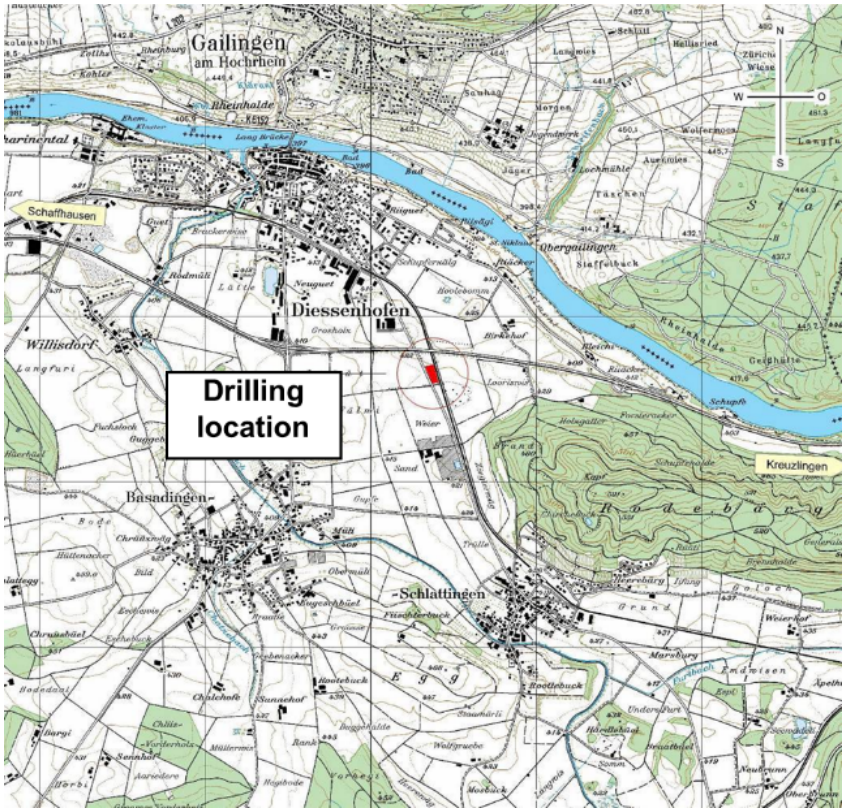


Figure 1: Drilling location in Schlattingen (© Swisstopo)

Based on a pre-study in 2007 and a feasibility study in 2010, a geothermal project for heat production was initiated and, after receiving a risk guarantee for the first borehole from Canton Thurgau, the project was initiated in November 2010. The risk guarantee was essential because the likelihood of success was estimated to be in the range of only 20% based on regional data and existing studies.

Potential geothermal reservoirs in Schlattingen are the aquifers in the sedimentary formations of the Mesozoic cover, namely the regional aquifers Malm, Upper Muschelkalk and Buntsandstein, plus the Upper Crystalline (basement) if the rock is densely fractured and/or highly altered (Figure 2). From an economic point of view, especially considering the expected drilling costs (cost / benefit ratio), the Upper Muschelkalk was defined as the first priority target formation in the case where the transmissivity is high enough to establish a minimum flow rate of about 7 L/s.

Because of the lack of detailed data in the region of Schlattingen it was decided, in cooperation with Canton Thurgau, to conduct an intensive investigation program in a first vertical borehole (SLA-1),

including drilling into the basement with partial coring (1,508 m bgl; Dec. 2010 to Jan. 2012), hydraulic packer testing combined with water sampling in all aquifers, geophysical logging, checkshot measurements and determination of the main stress orientation. Additional rock mechanical and thermal conductivity laboratory measurements were performed. For the completion of the borehole a 5" slotted liner in the Upper Muschelkalk section from 1,112 to 1,185 m bgl was installed.

Geologically, the drilling location is situated in the Swiss Molasse Basin between two regional faults. The Randen Fault some 2 km to the north strikes approximately NW and has a maximum normal fault offset of 250 m (Nagra, 2008). The Neuhausen Fault about 5 km to the south is well known from Nagra's 3D seismic survey (Birkhäuser et al., 2001). It also strikes NW and has a maximum normal fault offset of 100 m. Focal mechanisms from the basement are consistent with shortening directed NNW (Kastrup et al., 2004). However, compared with active tectonic regions the seismicity is low and GPS-derived strain rates in the Molasse Basin of north-eastern Switzerland are well below 0.5 mm/y (Sue et al., 2007).

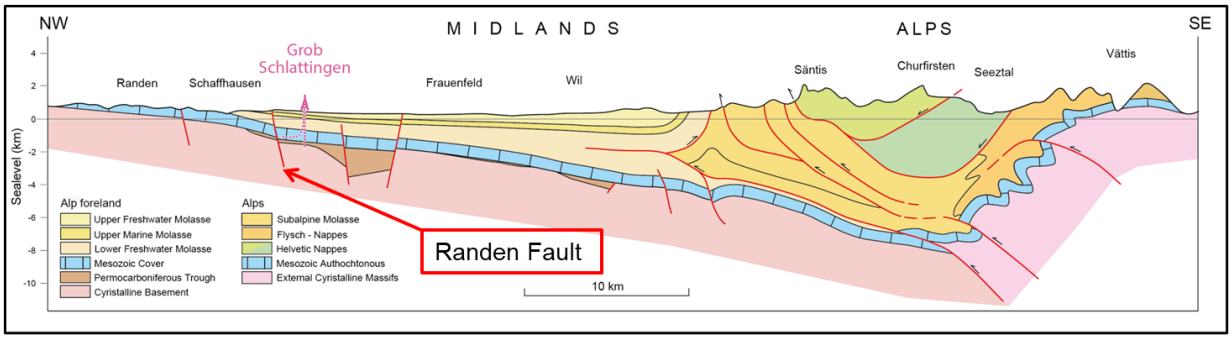


Figure 2: Location of the Schlattingen boreholes and schematic cross-section of Northern Switzerland (from Frieg et al., 2015)

The sedimentary sequence at the location of the borehole comprises marine limestones, shales and marls which are unconformably covered by Tertiary rocks of the Alpine Molasse. Further to the west the evaporitic rocks of the Triassic formations (Zeglingen Fm., *Middle Muschelkalk*) near the base of the sedimentary layer served as a regional detachments and enabled thin-skinned thrusting and the formation of the Jura fold and thrust belt in the Late Miocene. However, at the location of SLA-1 the sediments are considered to be unaffected by the Alpine thin-skinned thrusting.

It is worth noting that Permian sediments (Rotliegendes) with a thickness of about 78 m were encountered in the borehole before drilling into the crystalline basement. This means that the borehole appears to be located at the edge or at the shoulder of the so-called North Helvetic Permo-Carboniferous Trough. The main target of the project, the Upper Muschelkalk, had a thickness of 57.5 m consisting of two formations: the Stamberg Member (*Trigonodus Dolomite*) and the Hauptmuschelkalk. In fact, only the upper part of the 33 m-thick *Trigonodus Dolomite* is significantly transmissive (Figure 3). In general, the *Trigonodus Dolomite* consists of porous or clayey dolomite with marly intermediate layers, dolomitic mussel beds and oolitic dolomites.[1]

[1] For details see chapter 1.3

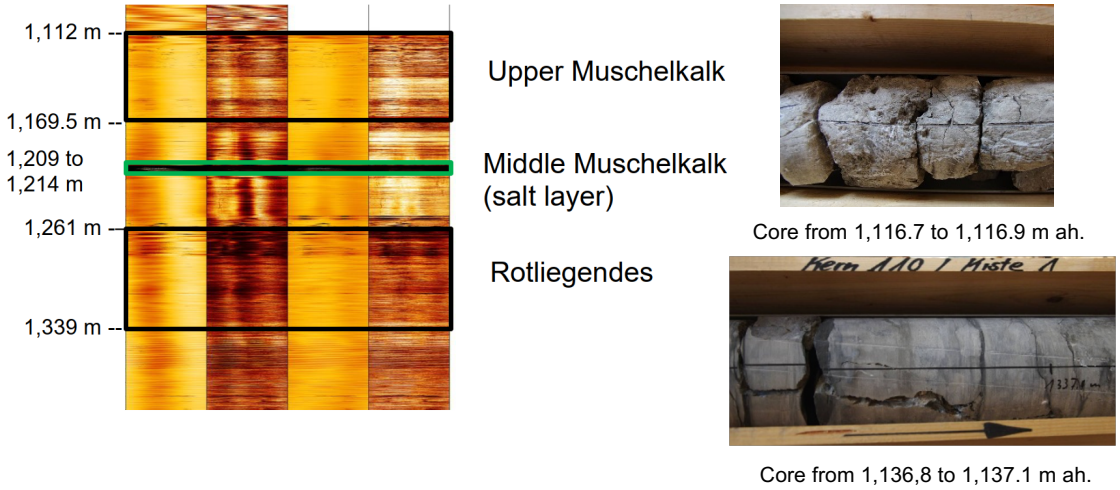


Figure 3: Section of the ABF-Log (left) and drill cores of the Upper Muschelkalk (right) (from Frieg et al., 2015)

Due to the fact that the Upper Muschelkalk was entirely cored in SLA-1, the structures in combination with the analysis of the logging data (ABF = acoustic borehole televiewer) could be studied in detail, especially to provide predictions to guide the continuation of the project with the drilling of a second borehole. It was decided by the project management to take the risk to implement a completely horizontal drill path in the target aquifer in order to intersect as many structures as possible.

On the 14th of February 2013, the drilling activities for the second geothermal borehole in Schlattingen started and after 89 days, on the 26th of April 2013, the drilling and completion activities of borehole SLA-2 were finalized. Figure 4 shows the geological profile and casing scheme of borehole SLA-2. After the analysis of the logging results, it was confirmed that the borehole left the target formation of the Upper Muschelkalk in the horizontal section for 49 m into the hanging wall by intersecting the Lettenkohle (1,818 – 1,867 m along hole; see Figure 6). This is also the reason for the installation of a blank casing in this part of the borehole.

Figure 5 shows a geological vertical cross-section along the drill path of the second borehole SLA-2 (= SLA-2b). In Figure 6 a contour map of the top of the Upper Muschelkalk with the penetration points and the borehole trajectory of the geothermal boreholes are shown. The horizontal drilling section in SLA-2b has a length of almost 800 m.

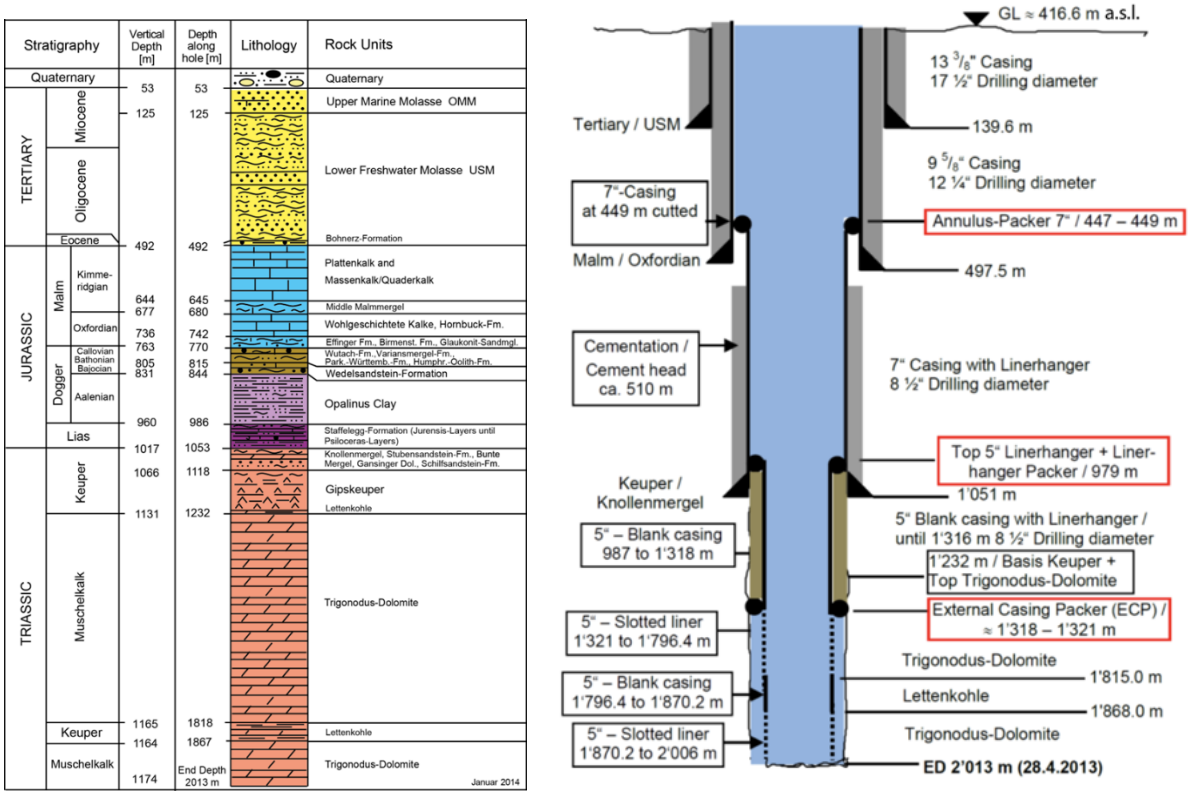


Figure 4: Geological profile (left) and casing scheme along horizontal well SLA-2 (from Frieg et al., 2015).

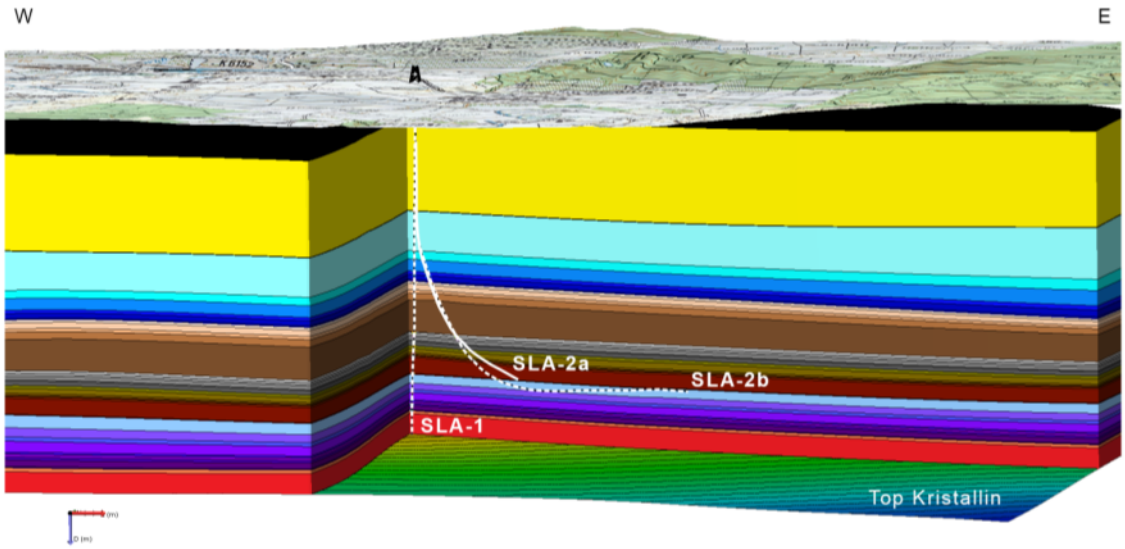


Figure 5: Geological block model with vertical cross section along SLA-2 (3D-view from SSE) (from Bläsi et al., 2014).

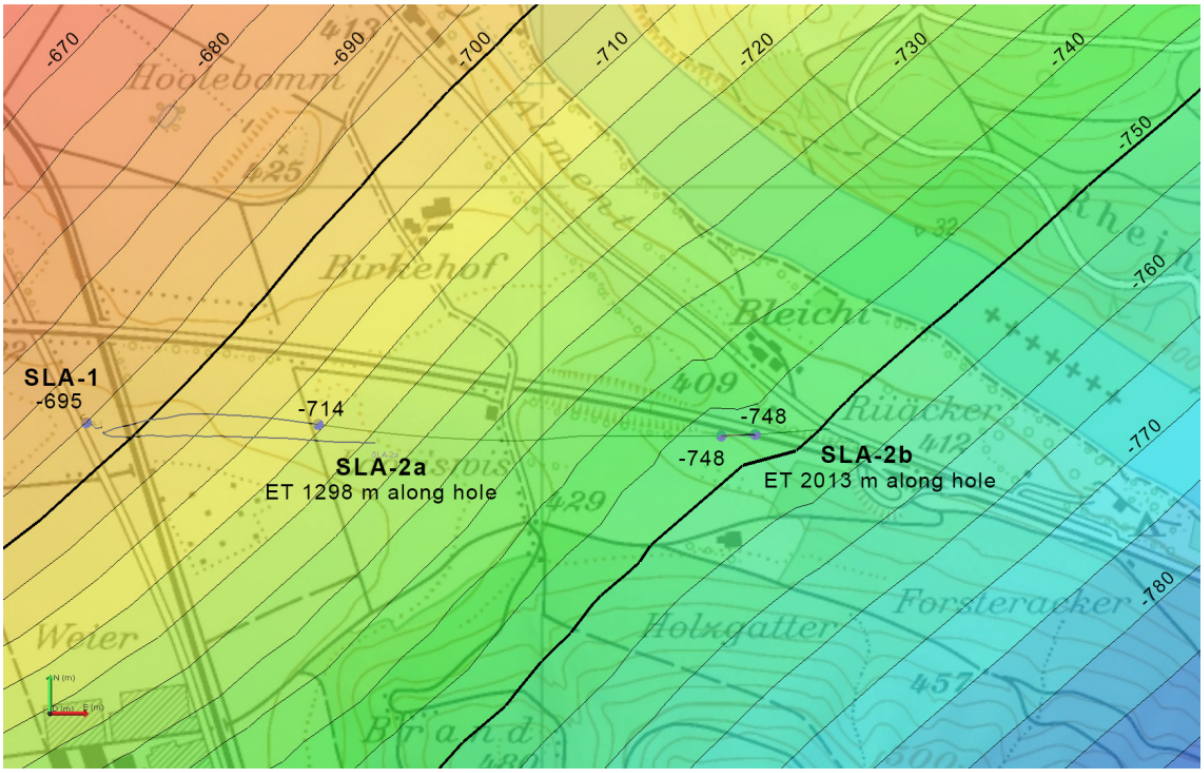


Figure 6: Map of depth contour of the top Trigonodus Dolomite with the positions of the geothermal boreholes SLA-1 and SLA-2 in Schlattingen and their penetration points through the top of the Trigonodus dolomite (Bläsi et al., 2014).

Note: Borehole branch SLA-2a must be terminated due to borehole instabilities. The map shows a contour interval of 5 m, and the depth is indicated in m above sea level.

The boreholes encountered the Upper Muschelkalk aquifer (see Chapter 1.3) at a depth of about 1,150 m bgl. The thermal water temperature is approx. 60 °C with long-term production rates of up to 10 to 13 L/s in total from both boreholes. Water samples were taken from the individual aquifers during the drilling of the boreholes and also during the subsequent test phase.

In this context, only the water samples from the Muschelkalk aquifer are of interest in the present research project. The results of the previous pumping tests in SLA-1 and SLA-2 with corresponding water sampling show that the deep groundwaters produced by the two wells are clearly different in terms of mineralization and isotope signatures. Further determination of isotopes for residence time estimation, water provenance and for the description of rock–fluid or fluid–gas interactions, the respective reservoir characteristics and the genesis and interaction of the deep waters with other aquifers, e.g., the deeper Permo-Carboniferous, have not yet been carried out. These questions are to be investigated in this research project with a particular focus on the genesis, origin, age-structure and flow paths as well as the availability of these waters to optimize their utilization.

The findings from the project should help to support the award of future drilling concessions and to improve the licensing practice and supervision of corresponding projects in the Canton of Thurgau. The Muschelkalk aquifer is the most important target horizon for ongoing hydrothermal exploitation.

In principle, the project is also relevant for other cantons (e.g. AG, BS, GE) where there are already existing or planned further uses of the Muschelkalk aquifer.

1.2 Project aims

According to the BFE project proposal the generals aims of the project are to provide information on:

- the origin, hydrochemical evolution, age structure and flow paths of the groundwater from the Muschelkalk aquifer encountered in the drillholes SLA-1 and SLA-2,
- the long-term stability of extraction and possible hydraulic and hydrochemical changes,
- the regional groundwater flow paths and predictability of the development of thermal water from the Muschelkalk aquifer in the Canton of Thurgau and Northern Switzerland for geothermal use.

The main focus of the project was to carry out a detailed geochemical, gas-physical and isotopic characterization of the Muschelkalk aquifer and thereby obtain novel insights into the following questions, which are essential to the promote exploitation of geothermal energy in the Canton of Thurgau

- Which physicochemical processes control the chemical composition of the groundwater in the Muschelkalk aquifer?
- How does the chemical composition of the Muschelkalk aquifer change at the regional scale?
- What technical challenges are expected during geothermal utilization of deep groundwater from the Muschelkalk aquifer?

1.3 Geology and aquifer properties at Schlattingen and surroundings

1.3.1. Tectonic setting

The Schlattingen geothermal site is situated in the western margin of the Hegau–Bodensee Graben (Diehl et al., 2023), within the wider tectonic realm of the South German Platform (a region formerly termed the Swiss Molasse Basin; Swisstopo, 2024). The Schlattingen geothermal wells sit between two major NW–SE trending, NE-dipping normal faults (Neuhausen in the west and Randen in the east) (Figure 7a), both of which are seismically active deep in the basement rocks (Diehl et al., 2023). The overall tectonic stress field in the region is transtensional, meaning that structures such as faults and fracture networks at and around Schlattingen are very gradually opening, and have been doing so over the past several million years. These structures thus provide potential flow paths for migration of thermal waters within and across formation boundaries.

1.3.2. Regional geology

The Schlattingen wells SLA-1 and SLA-2 draw thermal water from the Muschelkalk aquifer, one of the most extensive and productive deep saline aquifers in Northern Switzerland (Chevalier et al., 2010). The aquifer is hosted by rocks of the Triassic Upper Muschelkalk Group that occur in a layered sequence among other Mesozoic sedimentary units, with Tertiary Molasse above and pre-Mesozoic metamorphic basement rocks below (Figure 7b and Figure 7c). The bedding in the Mesozoic sequence dips very gently (3°) to the SE, parallel to the geological cross-section in Figure 7a. The cross-section in Figure 7c runs approximately parallel to the strike of the sedimentary sequence. In these cross-sections, the Muschelkalk aquifer is visible as an orange unit labelled *Oberer Muschelkalk*. Several faults are shown rising out of the basement and cutting up through the Upper Muschelkalk. Fault throws are mostly small but reach 40–80 m along the Neuhausen Fault, markedly offsetting the sedimentary sequence. It is possible that more minor faults exist in the vicinity of Schlattingen, but that they were not resolved by the Nagra 2D seismic surveys. Over wide areas between the faults, the Upper Muschelkalk is laterally extensive and consistent, and its depth is highly predictable.

1.3.3. Lithostratigraphic nomenclature

The formal lithostratigraphic nomenclature relevant to the Upper Muschelkalk and the Muschelkalk aquifer is shown in Figure 8. Note that official unit names have been changed recently. In this report we use the modern names for lithologic units accompanied by the historical names written in italics. An exception is our use of the historical name “Hauptmuschelkalk”, as this avoids quoting its three distinct members (Figure 8). The stratigraphy at the Schlattingen site is well known from the SLA-1 well (Figure 9), based on retrieved drill core (including of the Upper Muschelkalk) and drill cuttings. Historical unit names are used in Figure 8.

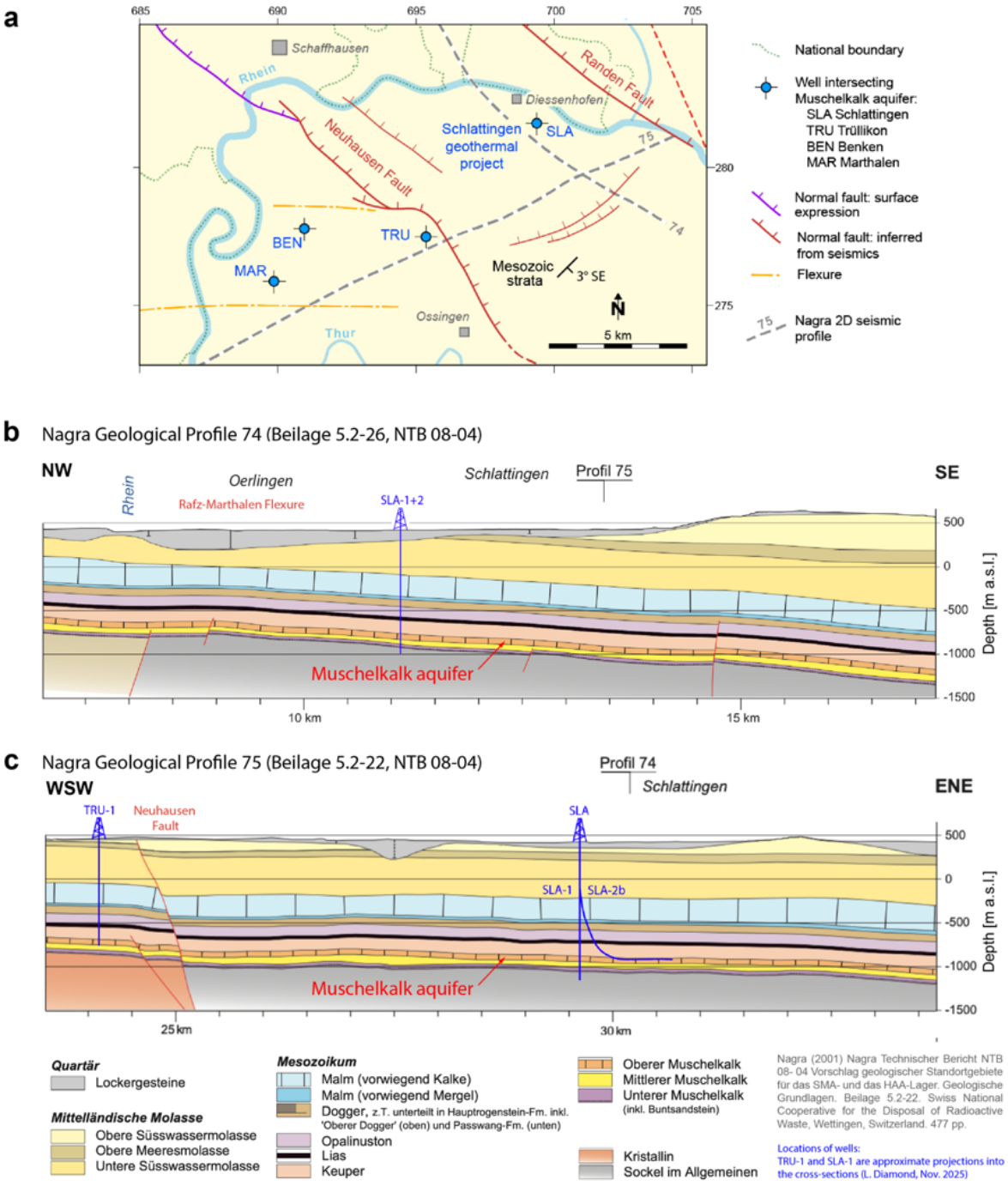


Figure 7: Geological setting of the Schlattingen geothermal site.

(**a**) Map showing local wells through the Muschelkalk aquifer, major faults and seismic lines for the geological cross-sections. (**b**) NW–SE cross-section based on seismic line 74 in panel a (Nagra, 2022: Nagra, 2008). Note exaggeration of vertical scale. (**c**) WSW–ENE cross-section based on seismic line 75 in panel a (Nagra, 2022; Nagra, 2008). Note exaggeration of vertical scale. Locations of the Schlattingen wells SLA-1 and SLA-2 are projected approximately into the cross-sections.

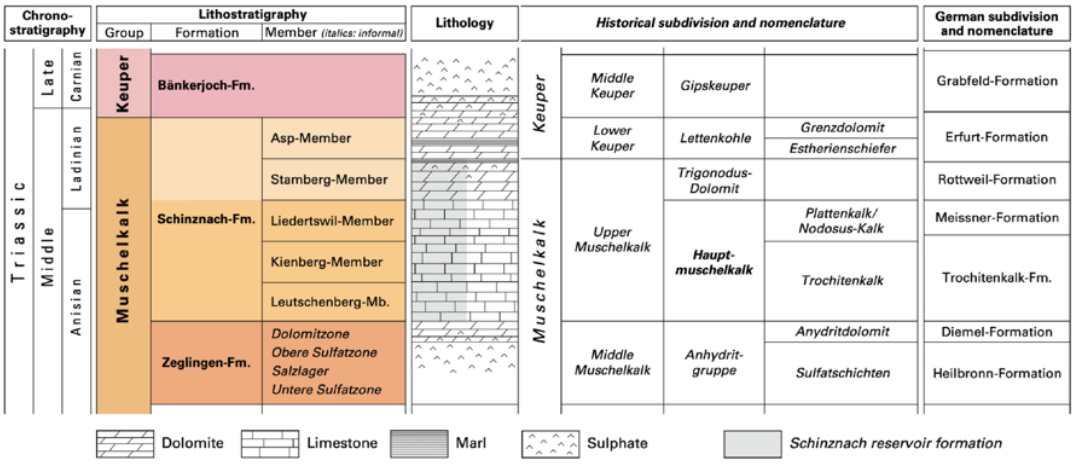


Figure 8: Key to nomenclature and ages of lithostratigraphic units relevant to the Muschelkalk aquifer at Schlattingen.

Note: The aquifer is hosted by the Schinznach Fm. and is hydraulically sealed above by the Bänkerjoch Fm. and hydraulically sealed below by the Zeglingen Fm. Figure modified from Diamond et al. (2025), based on Adams & Diamond (2019), Pietsch et al. (2016) and older references therein.

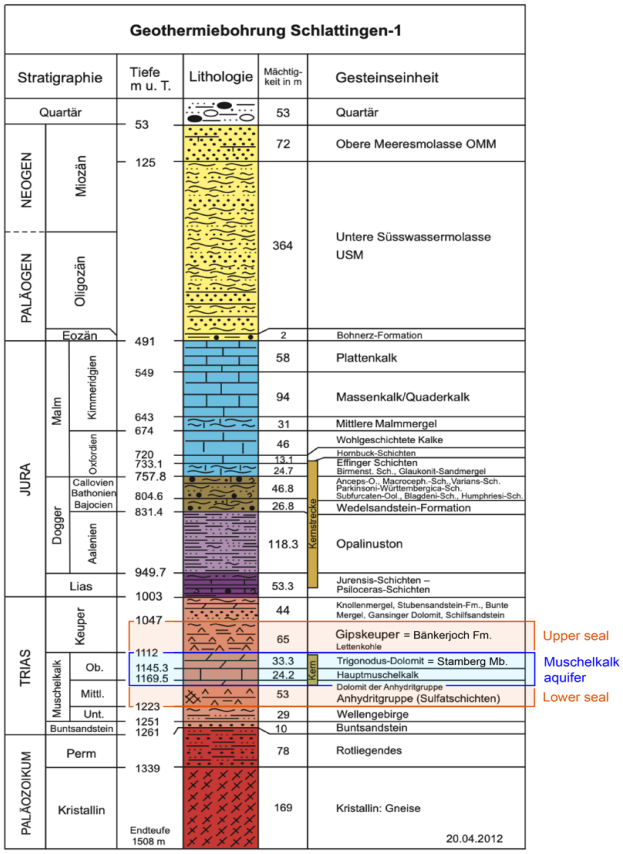


Figure 9: Stratigraphic sequence traversed by the vertical SLA-1 well at Schlattingen (from Albert et al., 2012).

1.3.4. Lithologies hosting the Muschelkalk aquifer

The Muschelkalk aquifer is hosted by three lithologic units (Figure 8 and Figure 9). The top two belong to the Schinznach Formation (57 m thick). These are the 33 m thick Stamberg Member dolostone (*Trigonodus Dolomit*) and the underlying 25 m of massive Hauptmuschelkalk limestones. The third unit is a 10 m thick layer of dolostones known as the *Dolomit der Anhydritgruppe*, which is the top layer of the Zeglingen Fm. (*Anhydritgruppe*). Mineralogically, the dolostones are almost pure dolomite with very minor contents of anhydrite, calcite, quartz, kaolinite and pyrite (Diamond et al., 2013). Despite their minor abundance, all these minerals are expected to buffer the composition of the groundwater in the aquifer, as is the presence of dolomite.

The dolostones have moderate rock-matrix porosities (mean 9%, with zones reaching 20%) and moderate rock-matrix permeabilities (≤ 4E-15 m^2 at in-situ pressure; Diamond et al., 2013). Details of the petrographic features and genesis of the rock pores are given in Diamond et al. (2013) and Aschwanden et al. (2019). The intervening Hauptmuschelkalk limestones are almost pure calcite with minor amounts of non-swelling clays. In contrast to the dolostones, they have mostly very low rock-matrix porosity (mean 0.7%; up to 7% where locally dolomitized) and negligible permeability (5E-19 m^2) (Diamond et al., 2013). Thus, the rock matrix of the Hauptmuschelkalk has no significant capacity to store or transfer groundwater.

1.3.5. Fracture permeability in the Muschelkalk aquifer

All the lithologic units making up the Muschelkalk aquifer at Schlattingen are highly fractured. The drill core retrieved from the vertical SLA-1 well contains 16 open joints, some of which have partial fillings of calcite and 7 fractures completely sealed by calcite ± kaolinite (veins) (Albert et al., 2012; Diamond et al., 2013). The attitudes of all these structures are very similar, demonstrating that one main fracture system affects the entire aquifer. The open fractures are all very steep (mean dip 84°; range 74°–90°) and their average strike is NNW–SSE (348°) (Figure 10a). The open and sealed fractures also show the same narrow range of apertures within the two units: mean 1.7 mm, range 0.05–5.00 mm (Diamond et al., 2025). None of the fractures show shear offsets (good markers to discern offsets are abundant in the core) and they are therefore classified as joints.

No core was extracted from SLA-2, but 770 m of the horizontal section was logged by Nagra using acoustic televiewer (ATV) and Formation Compact Microimager (CMI) downhole tools, revealing 2727 of fractures (intensity ~3.5 fractures per m). The log includes the dip directions and dip angles of all these fractures and a classification of the extent to which they are open and hence able to conduct water. The vast majority of the fractures show no offsets and their near vertical, NW–SE, NNW–SSE and NE–SW attitudes are the same as those of the joints in SLA-1 (Figure 10b). Their frequency distribution along the borehole shows clusters interspersed by zones of lower “background” intensity and even some significant gaps (Figure 10c). Importantly, several of the fractures show clear offsets and large apertures (> 1cm) and are therefore classified as faults. Over a horizontal distance of 1 m near the end of the SLA-2 borehole (1984 mMD), three fractures show a cumulative aperture of 28 cm. It is highly likely that these fractures are also faults. During drilling of SLA-2 and subsequent pumping tests, the highest transmissivity was recorded in the 63 m long interval 1950 – 2013 m MD, coinciding with high losses of drilling fluid (Frieg et al., 2015).

The significance of these observations for the reservoir properties of the Muschelkalk aquifer at Schlattingen is as follows:

(1) The logged water-conducting joints constitute a permeable fracture network that hydraulically links the two dolostone units and the Hauptmuschelkalk limestone unit within the Muschelkalk aquifer. The strong preferred NNW-SSE orientation of the joints confers a notable anisotropy to this permeable network. Hydraulic simulations of Discrete Fracture Networks based on the logged data suggest that the background fracture intensity has a bulk permeability approximately an order of magnitude higher than that of the rock-matrix permeability of the dolostones, and the model permeability of the weighted background + cluster networks is still higher (Diamond et al., 2025).

Thus, while the porosity of the dolostones enables the Muschelkalk aquifer to hold vast amounts of groundwater, the widely distributed permeable fracture network ensures its ability to transfer water laterally over large distances in response to regional hydraulic gradients or locally in response to pumping in wells.

(2) The 63 m long interval of high transmissivity at the end of SLA-2 borehole can be interpreted as a subvertical, NW–SE to N–S trending fault zone (marked green in Figure 10c), which may continue further east beyond the end of the SLA-2 borehole. The wide apertures of the faults suggest that they have considerable horizontal lengths (e.g. several hundred meters or more), as well as high vertical extents. Accordingly, the fault zone can be visualized in 3D as having a steep, NNW–SSE striking tabular form, which crosscuts the SLA-2 borehole. The fault zone strikes parallel to the major normal fault in the vicinity of Schlattingen, the Randen Fault, which is located about 2 km to the east (Figure 7a). Owing to this large distance it seems unlikely that the SLA-2 fault zone could belong to the damage zone of the transtensional Randen Fault, and therefore it most likely represents a distinct minor but structurally similar fault zone. The fault zone identified at the end of the SLA-2 borehole plays a key role in our conceptual and numerical models of the Schlattingen geothermal system, as described in Sections 2 and 3. Specifically, the fault zone is envisaged as a conduit that allows upflow of deep saline water from the crystalline basement into the Muschelkalk aquifer, thereby explaining the mixed chemical, isotopic and age signature of the thermal water produced from SLA-2 (see discussion in Section 2.3)

1.3.6. Confining units of the Muschelkalk aquifer

The Muschelkalk aquifer is overlain by a 65 m thick layer of clay-bearing anhydrite-rich evaporites belonging to the Bänkerjoch Fm. (*Gipskeuper*). Below the *Dolomit der Anhydritgruppe*, which marks the base of the aquifer, the remainder of the Zeglingen Fm. (*Anhydritgruppe* or *Sulfatschichten*) consists of a 42 m thick sequence of clayey, halite-bearing, anhydrite-rich evaporites (Figure 8 and Figure 9). The rock matrices of both evaporite units (Bänkerjoch above and Zeglingen below) have very low porosities (3%) and are extremely impermeable (1E-18 to 1E-20 m^2; Diamond et al., 2025).

It is notable that the joint-type fracture sets within the aquifer at Schlattingen (see preceding paragraphs) and elsewhere in Northern Switzerland do not cut across the overlying or underlying evaporite units. This is because the evaporites behaved in a ductile manner at the time in the geological past when the joints formed in the brittle dolostones and limestones (see Diamond et al., 2025 for a detailed explanation). Hence, the Muschelkalk aquifer is hydraulically confined above and below by the evaporite units throughout Northern Switzerland, wherever the sedimentary sequence is not disrupted by faulting. However, the sealing function of the evaporites may be breached by permeable faults, as is the case of the fault zone at the eastern end of the SLA-2 borehole, described above. The cross-section in Figure 7c suggests that the Neuhausen Fault may be another much larger-scale example where cross-formational flow of water may be possible, owing to its considerable throw.

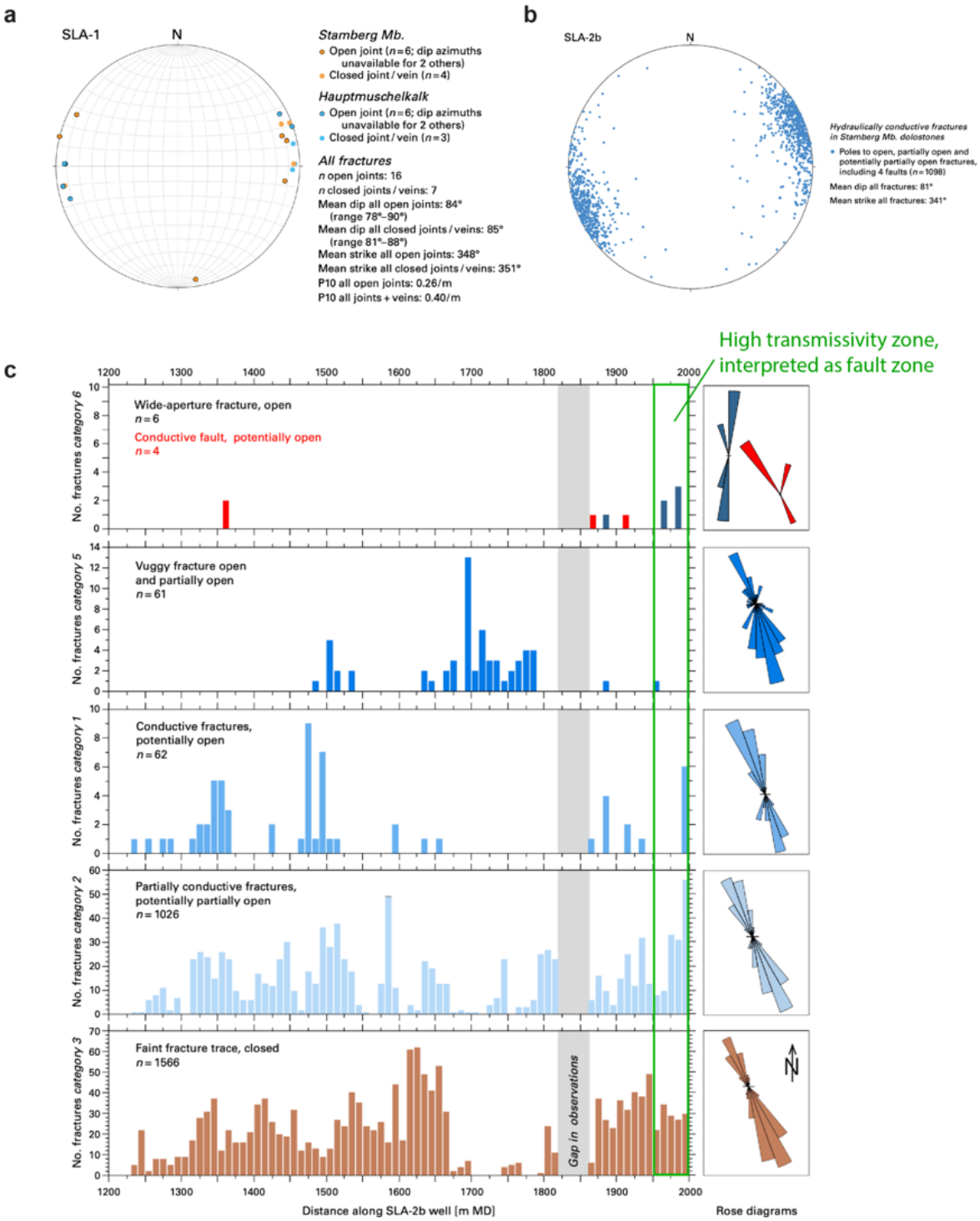


Figure 10: Fractures logged in the Muschelkalk aquifer at Schlattingen. From Diamond et al. (2025) based on data from Grob AG.

(a) Stereoplot of fractures in drill core from SLA-1. (b) Stereoplot of fractures logged by CMI tool in SLA-2. (c) Frequency distribution of fractures along SLA-2 logged by CMI. The green zone of high-aperture fractures and high proven transmissivity is interpreted here as a fault zone. This zone plays a key role in our conceptual model to explain the chemical and hydraulic properties of the SLA-2 geothermal system (Sections 2 and 3).

2 Procedure, method, results and discussion

2.1 Methods

2.1.1. Monitoring of hydraulic parameters

In order to gain insight into the long-term stability of the pumping and to predict possible hydraulic and hydrochemical changes, long-term pumping tests (Figure 11 and Figure 12) are carried out.

Due to the fact that the production of vegetables in the greenhouses needs heat more or less all around the year, the hydraulic tests could not be performed in an ideal way. This means that pumping rates had to be adjusted to the heating requirements and longer pressure build-up periods are generally missing, especially in SLA-2.

The pressure recordings of SLA-1 (Figure 11) document two redundant pressure measurements. The new gas inlet system installed at the beginning of 2024 is a measuring system (Airflow) from Lutz Energietechnik (Haag am Hausruck, Austria), which was specially adapted to the requirements of the Schlattingen geothermal wells (narrow annular space conditions) and functions perfectly in the SLA-1 well (Pegel 1). Nitrogen is used as the measuring gas in order to rule out any change in the water chemistry. The redundant pressure probe (Pegel 2) delivered consistent values and shows the same pressure curve as the gas inlet system.

In the SLA-2 borehole, there is unfortunately a leak in the inaccessible gas inlet line within the borehole, which makes it impossible to record correct measured values on surface (Figure 12, Pegel 1). The redundant pressure probe in SLA-2 gets stucked in the separate besides the tubing installed plastic hose. During a retrieval attempt, the cable of the pressure sensor is broken (Pegel 2; no pressure values could be recorded). In this case, the only correct pressure values are recorded by the second redundant pressure sensor at the bottom of the submersible pump (444 m bgl; Pegel 3).

The requirements of the scientific investigation program in particular the water sampling for the planned analyses could be achieved with the rather long pumping periods.

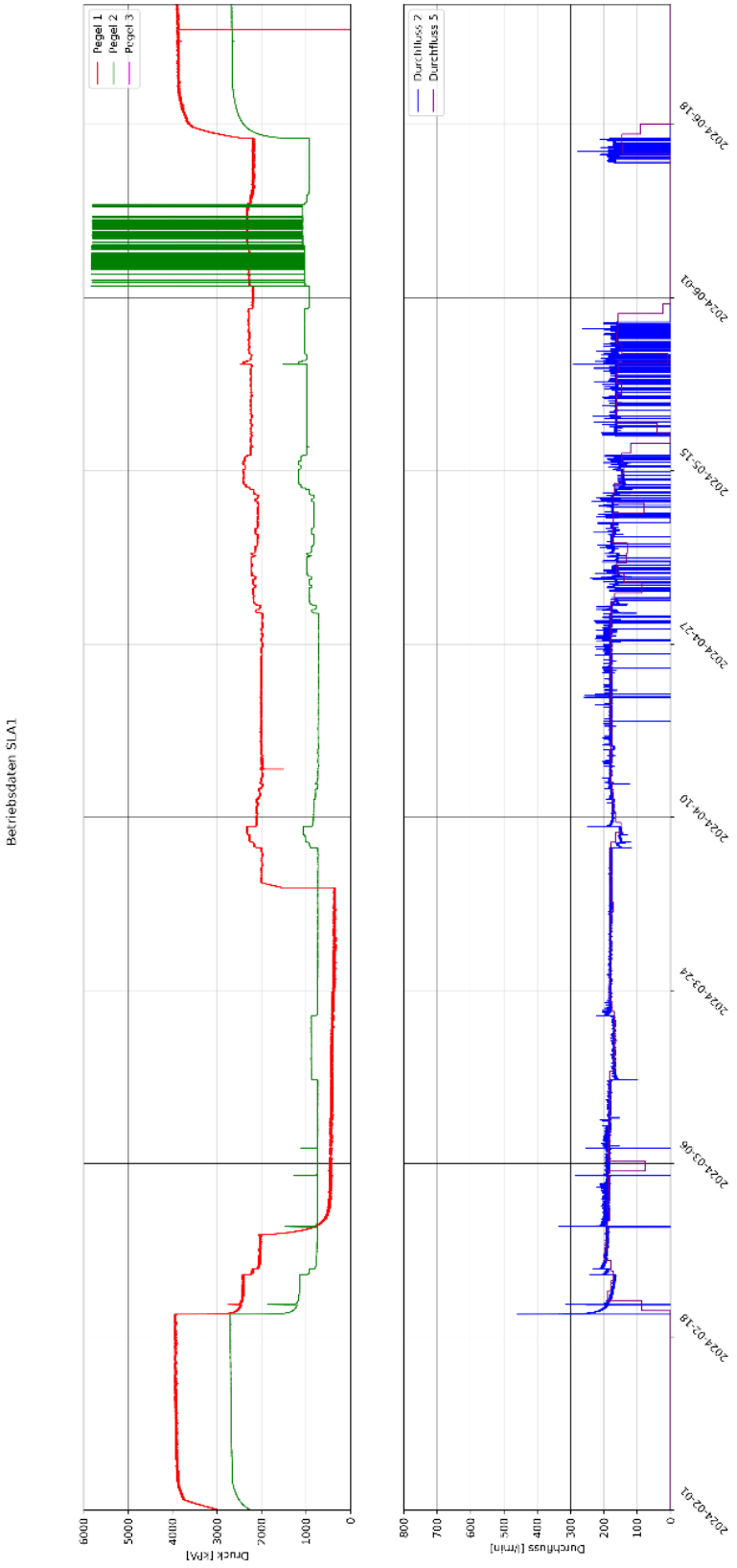


Figure 11: Pumping test in SLA-1 starting February 2024 until June 2024.

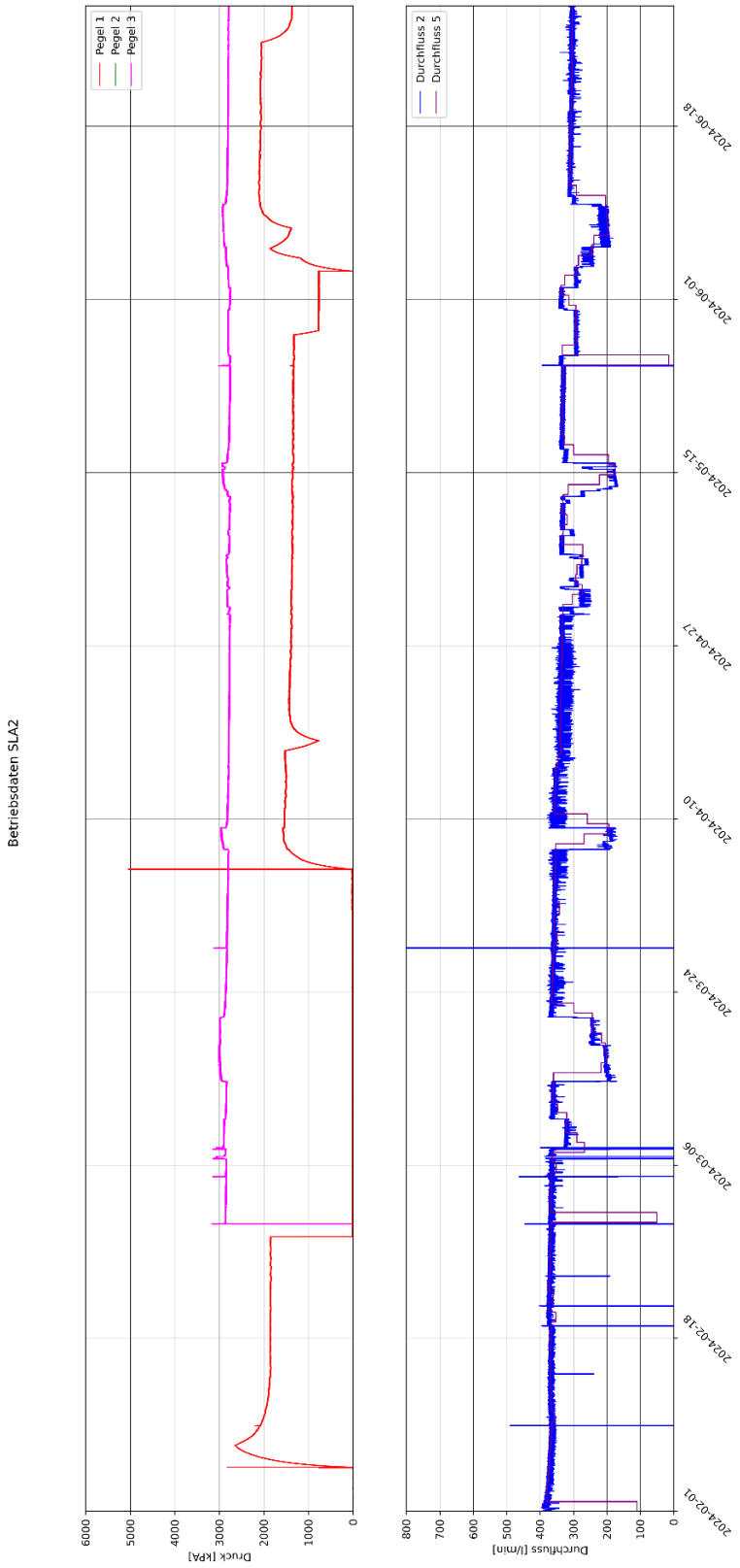


Figure 12: Pumping test in SLA-2 starting February 2024 until June 2024.

2.1.2. Thermal water sampling and analysis

During the course of the project, a total of eight water samples were collected from SLA-1, and nine samples were collected from SLA-2. Samples were taken either by Hydroisotop GmbH or the on-site staff following the instructions provided by Hydroisotop following the accreditation requirements of the DIN EN 17025. Each of the samples was analysed for a different parameter set (Table 1, Table 2). Depending on the parameter set, sampling took place directly at the wellhead or after the heat exchanger. While the former is crucial for avoiding any sampling artefacts, the latter yields reliable results for non-reactive parameters unaffected by degassing and cooling such as stable water isotopes. The most comprehensive analysis was done for the samples taken on April 15 and 16, 2024. This included the determination of major and trace element concentrations, stable isotope ratios, the analyses of dissolved ^{81,85}Kr and ^{37,39}Ar, and the isotopic characterisation of both reactive and noble gases. The taken samples and thereon analysed parameters are shown in Table 1 and 2.

To facilitate this, water samples were taken under operational temperature and pressure. Moreover, 1 m^3 of the thermal water of each borehole was degassed directly on-site by a vacuum degasser (Figure 13 − Figure 16). Details on gas sampling and analyses are provided in a standalone report by Hydroisotop GmbH including the determination of ^{81}Kr model ages characterising the residence time of the sampled groundwaters (Appendix 1). Depending on the parameter of interest, the water aliquots were stabilised in different ways following the protocol defined in the Guideline for the hydrochemical characterisation of geothermal fluids (Stopelli et al., 2024) and as listed in Table 3.

Table 1: Overview of groundwater samples taken from borehole SLA-1 and the conducted analytical program (analytical packages according to the proposal)

		Bohrung SLA 1								
Bez.	**Parameterset (gemäß Antrag)**	7.8.23	25.10.23	4.10.23	16.4.24	30.9.24	27.11.24	15.5.25	9.6.25	13.6.25
Vor Ort	pH-Wert, Temp. spez.el. LF, Redox, O2, Bk8.2, Sk4.3		x		x					
KA1	Kationen und Anionen klein									
	(Na, K, Ca, Mg, Cl, SO_4, HCO_3, NO_3, NO_2, NH_4)	x		x		x	x	x	x	x
KA2	Kationen und Anionen groß									
	(Na, K, Ca, Mg, Cl, SO_4, HCO_3, NO_3, NO_2, NH_4, Fe, Mn, F, Br, J, H_2S)		x		x					
AnOrg1	Anorganische Summenparameter				x					
	(TIC; Bestimmung mit Vorlage)									
Iso1	Basisisotope (^3H, Deuterium und Sauerstoff-18 ; entsp. D/O)	x	x	x	x	x	x	x	x	x
Iso2	Erweiterter Isotopenumfang (^3H, D/O, ^{13}C-DIC, ^{14}C-DIC-AMS)		x		x					
Iso3a	Isotope spezieller Wasserinhaltsstoffe:									
	Sr-Isotopenverhältnis Sr-86/87		x		x					
Iso3b	Isotope spezieller Wasserinhaltsstoffe:									
	Schwefelisotope; $d^{34}S/d^{18}O$-SO_4, $d^{34}S$-H_2S		x		x					
G1	Quantitative Gasanalyse				x					
GIso1	Gasisotope Basisumfang (^{13}C-CO_2, ^{13}C-CH_4, ^2H-CH_4)				x					
GIso2	Erweiterter Umfang Gasisotope				x					
	(^{13}C-CO_2, ^{13}C-CH_4, ^2H-CH_4, ^{13}C-C_2H_6, ^{13}C-C_3H_8; ^{14}C-CO_2,									
	^{14}C-CH_4, ^2H-H_2, ^{15}N-N_2)									
Edel	Edelgasanalyse inkl. Edelgasisotope und He-3/He-4				x					
pG	Bestimmung Entgasungsdruck				x					
SpCh1	anorganische Spurenstoffe (B, Sr, Ba, Si, Li, PO4)		x		x			x	x	x
SpCh2	Metalle und Nebenbestandteile (As, Al, Sb, Be, Pb, Cd, Co, Cu, Mo, Ni, Hg, Rb, Se, U, V, Zn, Sn, CN)		x		x					
Org1	Organische Summenparameter (DOC, Phenolindex, KW-H53)		x		x					
Org2	PAK, BTX, Alkyl-Phenole				x					
DTr2	Krypton-85				x					
DTr2	Argon-39				x					
DTr4	Krypton-81				x					
Rad1	Radon-222				x					
Rad2	Ra-226, Ra-228				x					
Rad3	Ra-223, Ra-224, Ra-226, Ra-228				x					
Rad4	Pb-210, Po-210				x					

Table 2: Overview of groundwater samples taken from borehole SLA-1 and the conducted analytical program (analytical packages according to the proposal).

		Bohrung SLA 2							
Bez.	**Parameterset (gemäß Antrag)**	11.11.22	25.10.23	15.4.24	10.7.24	30.9.24	27.11.24	15.5.25	9.6.25
	Probenahme	Br.kopf	nach WT	Br.kopf	nach WT	nach WT	nach WT	Br.kopf	nach WT
Vor Ort	pH-Wert, Temp. spez.el. LF, Redox, O2, Bk8.2, Sk4.3		x	x					
KA1	Kationen und Anionen klein								
	(Na, K, Ca, Mg, Cl, SO_4, HCO_3, NO_3, NO_2, NH_4)	x			x	x	x	x	x
KA2	Kationen und Anionen groß								
	(Na, K, Ca, Mg, Cl, SO_4, HCO_3, NO_3, NO_2, NH_4, Fe, Mn, F, Br, J, H_2S)		x	x					
AnOrg1	Anorganische Summenparameter								
	(TIC; Bestimmung mit Vorlage)			x					
Iso1	Basisisotope (^3H, Deuterium und Sauerstoff-18 ; entsp. D/O)		x	x	x	x	x	x	x
Iso2	Erweiterter Isotopenumfang (^3H, D/O, ^{13}C-DIC, ^{14}C-DIC-AMS)			x					
Iso3a	Isotope spezieller Wasserinhaltsstoffe:	x	x	x	x	x	x		
	Sr-Isotopenverhältnis Sr-86/87	x	x	x	x				
Iso3b	Isotope spezieller Wasserinhaltsstoffe:		x	x					
	Schwefelisotope; $d^{34}S/d^{18}O$-SO_4, $d^{34}S$-H_2S		x	x					
G1	Quantitative Gasanalyse								
GIso1	Gasisotope Basisumfang (^{13}C-CO_2, ^{13}C-CH_4, ^2H-CH_4)		x	x					
GIso2	Erweiterter Umfang Gasisotope								
	(^{13}C-CO_2, ^{13}C-CH_4, ^2H-CH_4, ^{13}C-C_2H_6, ^{13}C-C_3H_8; ^{14}C-CO_2,			x					
	^{14}C-CH_4, ^2H-H_2, ^{15}N-N_2)			x					
Edel	Edelgasanalyse inkl. Edelgasisotope und He-3/He-4			x					
pG	Bestimmung Entgasungsdruck								
SpCh1	anorganische Spurenstoffe (B, Sr, Ba, Si, Li, PO4)			x					
SpCh2	Metalle und Nebenbestandteile (As, Al, Sb, Be, Pb, Cd, Co, Cu, Mo, Ni, Hg, Rb, Se, U, V, Zn, Sn, CN)			x					
Org1	Organische Summenparameter (DOC, Phenolindex, KW-H53)			x					
Org2	PAK, BTX, Alkyl-Phenole			x					
DTr2	Krypton-85		x	x					
DTr2	Argon-39			x					
DTr4	Krypton-81		x	x					
Rad1	Radon-222			x					
Rad2	Ra-226, Ra-228			x					
Rad3	Ra-223, Ra-224, Ra-226, Ra-228			x					
Rad4	Pb-210, Po-210			x					

Table 3: Overview of parameter analysed and corresponding analytical methods used in this project.

Parameter	Container/ Stabilisation	Method	Standard	Equipment
Physico-chemical parameters	PE bottle	Conductometry, optical sensor method, pH-electrode, titration, sensor	DIN EN ISO 10523 (C5): 2012-04, DIN 38404-C6: 1984-05, DIN 38409-H7:2005-12, DIN 38404-C 4 1976-12, DIN EN 27888 (C 8), 1993-11	MultiLine 3620, Tetracon 925 / WTW, MultiLine 3620, Sentix 940 / WTW, MultiLine 3620, SenTix® ORP-T 900 / WTW
Dissolved Components				
Li^+, Na^+, K^+, Mg^{2+}, Ca^{2+}, Sr^{2+}, Ba^{2+}	PE bottle	IC	DIN EN ISO 14911 (E34): 1999-12	Ionchromatography, ICS-1500, Dionex
Rb^+, Cs^+, Ni^{2+}, Cu^{2+}, Zn^{2+}, Cd^{2+}, Pb^{2+}, Cr_{tot}, Se_{tot}, As_{tot}, Sb_{tot}, U_{tot}, B, Al, Mn_{tot}, Fe_{tot}, Si	PE bottle, filtrated and acidified with HNO_3 (if sampled)	ICP-MS and photometric	DIN EN ISO 15586 (E4): 2004-02	ICP-MS, Agilent 7500CE / Agilent 7700x, and photometric (Merck Spectroquant 1.14770: 2017-01 / 2)
NH_4^+	PE bottle, filtrated and acidified with HCl (if sampled)	Photometric	Merck Spectroquant 1.14752: 2013-12	Multiline P5, WTW
P_{tot}	PE bottle	Photometric	DIN EN ISO 17294-2 (E29), ICP-MS	Multiline P5, WTW
As^{3+}, As^{5+}	PE bottle	AAS	DIN EN ISO 15586 (E4): 2004-02	Hydrid-AAS Perkin Elmer Pin Aacle 500
F^-, Cl^-, Br^-, I^-, NO_3^-, ortho-PO_4^{3-}	PE bottle	IC	DIN EN ISO 10304-1 (D20): 2009-07	ICS-1500, Dionex
SO_4^{2-}	PE bottle or glass bottle stabilised with ZnAc	IC	DIN EN ISO 10304-1 (D20): 2009-07	ICS-1500, Dionex
NO_2^-	PE bottle, filtrated and acidified with HCl	Photometric	Merck Spectroquant 1.14776: 2017-01	Multiline P5, WTW
Other trace elements	PE bottle	ICP-MS	DIN EN ISO 17294-2 (E29), ICP-MS	ICP-MS, Agilent 7500CE / Agilent 7700x
DOC, Phenol index, Hydrocarbons	Stainless steel cell or brown glass bottle (cooled)	NDIR, GC-FID	DIN EN 1484 (H3): 2019-04, DIN EN ISO 14402 (H37), DIN EN ISO 9377-2-H53, GC-FID	TOC-V, GC-FID
BTEX	100 ml brown glass bottle	GC-MS	DIN 38407-F34 2014-10	DANI HS 86.50 Shimadzu QP 210 ultra
PAK	1 l brown glass bottle	HPLC	DIN EN ISO 17993 2004-03	Shimadzu LC 20 AD with RF-20 A xs
Isotopes				
$\delta^{18}O$ / δ^2H	50 ml PE bottle	IRMS, CRDS	QMA 504-2/3 2012-02, QMA 504-2/4 2012-02, QMA 504-2/23 2012-02	Picarro CRDS L2130-i and Finnigan MAT 251
^3H-H_2O	1l PE bottle	LSC	DIN EN ISO 9698 2015-12	Perkin Elmer Quantulus GCT 6220
$\delta^{13}C$-DIC	Stainless steel cell, PE stabilised with NAOH	IRMS	QMA 504-2/16 2012-02	DANI HS 86.50 ThermoScientific Delta V

Table 3 continued.

Parameter	Container/ Stabilisation	Method	Standard	Equipment
Isotopes				
^{14}C-DIC	Stainless steel cell, PE stabilised with NAOH	AMS		Mini radiocarbon Dating System (MICADAS), LIP 2014
^{87}Sr / ^{86}Sr	50 ml PE bottle	TIMS		TIMS, VG 54
^{3}He / ^{4}He	Copper-tube	Mass spectrometry		multi-collector Noblesse HR mass spectrometer
$\delta^{34}S\text{-}SO_4$	PE bottle, stabilised with CdAc	EA-IRMS	QMA504-2/28: 2015-03	ThermoScientific Delta V
^{85}Kr, ^{81}Kr	10 l gas bottle	Low-Level Proportional counter (LLC)		LLC
^{37}Ar, ^{39}Ar	Gas extraction by gas separator from IBCs (minican)	LLC, Atom Trap Trace Analysis (ATTA)		LLC or ATTA
Gas analysis				
Quantitative gas analysis	Stainless steel cell	Gas chromatography GC-TCD, FID after extraction	QMA 504-2/15 2007-04	Shimadzu GC17A VICI Valco Instruments (TCD)
Noble gases and isotopes	0.5 m copper tube	Mass spectrometry after cryogen separation		MM5400 sector field spectrometry, GV Instruments
$\delta^{13}C\text{-}CH_4$, $\delta^{13}C\text{-}C_2H_6$, $\delta^{13}C\text{-}C_3H_8$	Stainless steel cell	IRMS (P&T-GC-IRMS)	QMA504-2/16	ThermoScientific Delta V+
$\delta^{2}H\text{-}CH_4$	Stainless steel cell	IRMS (P&T-GC-IRMS)	QMA 504-2/4	ThermoScientific Delta V+
$\delta^{13}C\text{-}CO_2$	Stainless steel cell	IRMS (P&T-GC-IRMS)	QMA 504-2/6: 2012-02	DANI HS 86.50 ThermoScientific Delta V
Radionuclides				
^{223}Ra, ^{224}Ra, ^{226}Ra, ^{228}Ra	5 l PE bottle	α-Spectrometry, β/γ coincidence spectrometry	QMA 504-2/18 2023-03	HPGE
^{222}Rn	1 l PET	LSC	QMA 504-2/32 2023-03	LSC
^{210}Pb, ^{210}Po	5 l PE bottle	Proportional counter after radiochemical separation, α-Spectrometry		Proportional counter





Figure 13: Wellhead SLA-1 (left) and SLA-2 (right)





Figure 14: Vacuum degassing unit



Figure 15: Sampling under operational P- and T-conditions



Figure 16: Collected samples

2.1.3. Visual inspection and geophysical measurements of the SLA-2 well

In August 2025 a geophysical logging including a video inspection was conducted in borehole SLA-2. This action appeared to be necessary due to the observed corrosion of the rising pipe and the electric submersible pump (ESP). Thereby the thickness of the casing material and the inner diameter and condition of the piping was measured and valuated by electromagnetic, multifinger and visualisation. The measurements were carried from the surface down to a depth of 443 m bgl at the transition between the 9 5/8" and 7" casing.

2.1.4. Numerical modelling

Different types of numerical simulations were carried out to assess the collected data:

- Geochemical modelling using PHREEQC (Parkhurst & Appelo, 2013) in combination with the Thermodem thermodynamic database (Blanc et al., 2012) was performed to determine the saturation state of key minerals in the produced water samples, to estimate the reservoir temperature at depth and to evaluate the risk of mineral scaling.
- Large-scale hydraulic simulations constrained by the collected hydraulic data and using the code Spring (König et al., 2024) were carried out by the external contractor TK Consult to determine the permeability distribution in the Muschelkalk aquifer, including detailed fitting around the horizontal section of well SLA-2.
- Results from the groundwater simulations were subsequently used by the University of Bern to constrain small-scale coupled thermal–hydraulic–chemical simulations performed with the massively parallel, reactive transport code PFLOTRAN (Hammond et al., 2020) to assess the most likely permeability and temperature distribution in the vicinity of the two Schlattingen wells.

2.2 Results

2.2.1. Hydraulic monitoring and evaluation of the pumping test

Of particular note is the fact that it seems the drawdown at borehole SLA-1 is slightly lower than during the pumping test performed in 2012 (Reinhardt & Rösli, 2013) at the same flow rate.

In SLA-2 the following things are worth noting:

i) Compared to the measurements taken between 2013 and 2015 the average pressure head at SLA-2, at approximately 250 m asl (based on a density of 980 kg/m3), exceeds the average levels measured during the earlier pumping tests (Reinhardt & Rösli, 2015).

ii) The pressure fluctuations during the pumping period are significantly lower, with a maximum of approximately 50 m.

iii) In SLA-2, the water level reacts relatively slowly to changes in the flow rate.

The differences in formation pressure of the Upper Muschelkalk in the two boreholes, known from the beginning of the measurements, could be confirmed, i.e. SLA-1 remains artesian (about 3 bars), and SLA-2 is still clearly subartesian. It should be noted that during the entire measurement period, no crosshole responses between SLA-1 and SLA-2 could be observed as in the past. This confirms the horizontal compartmentalization of the Upper Muschelkalk aquifer in the Schlattingen area.

The subsequent hydraulic analyses should provide a confirmation of these observations.

SLA-1

Figure 17 and Figure 18 below show pressures and flow rates in SLA-1, as recorded in 2024. Two major RW (= rate withdrawal) phases are followed by RWS (= pressure recovery after rate withdrawal) phases. Both recoveries (RWS) show an abrupt change in slope related to the well becoming artesian. Based on a reported sensor depth of 255 m bgl artesian conditions are reached about 15m agl using a fluid density of 1000 kg/m^3, which suggests that the actual installation depth is somewhat lower than the 255 m bgl. However, the reported sensor depth of 255 m bgl is used in this analysis. Note that after artesian conditions were reached at the end of the RWS phases, outflow was occasionally measured manually at reported rates between 8 and 12 l/min.

Figure 19 shows the definition of the different test phases. Artesian well conditions were implemented as variable pressure events to allow for the calculation of flow rates. Note that for RW2, the data gap of flow rates in May/June 2024 was completed by using arbitrarily generated flow rates fluctuating around 170 l/min. The reason for the data gap was that the water meter at the borehole had a malfunction unnoticed.

The wellbore storage coefficients were estimated from the unit slope of the recovery periods of RWS1 and RWS2 and were used in the analyses of the corresponding RW and RWS phases. For RW1-RWS1, the estimated WBS (= wellbore storage coefficient) is 5E-7 m^3/Pa, for RW2/RWS2 1.6E-6 m^3/Pa. The estimated WBS coefficients were fixed to the above values during the analysis. Note that the estimated WBS is about 1 magnitude lower than the theoretical value (RWS1) and that drawdowns/recoveries happen in a casing with changing diameter (9 5/8” to 470 m bgl.; 7” to 1,112 m bgl.; 5” slotted liner in 6 ¼ “ borehole down to 1,185 m bgl.).

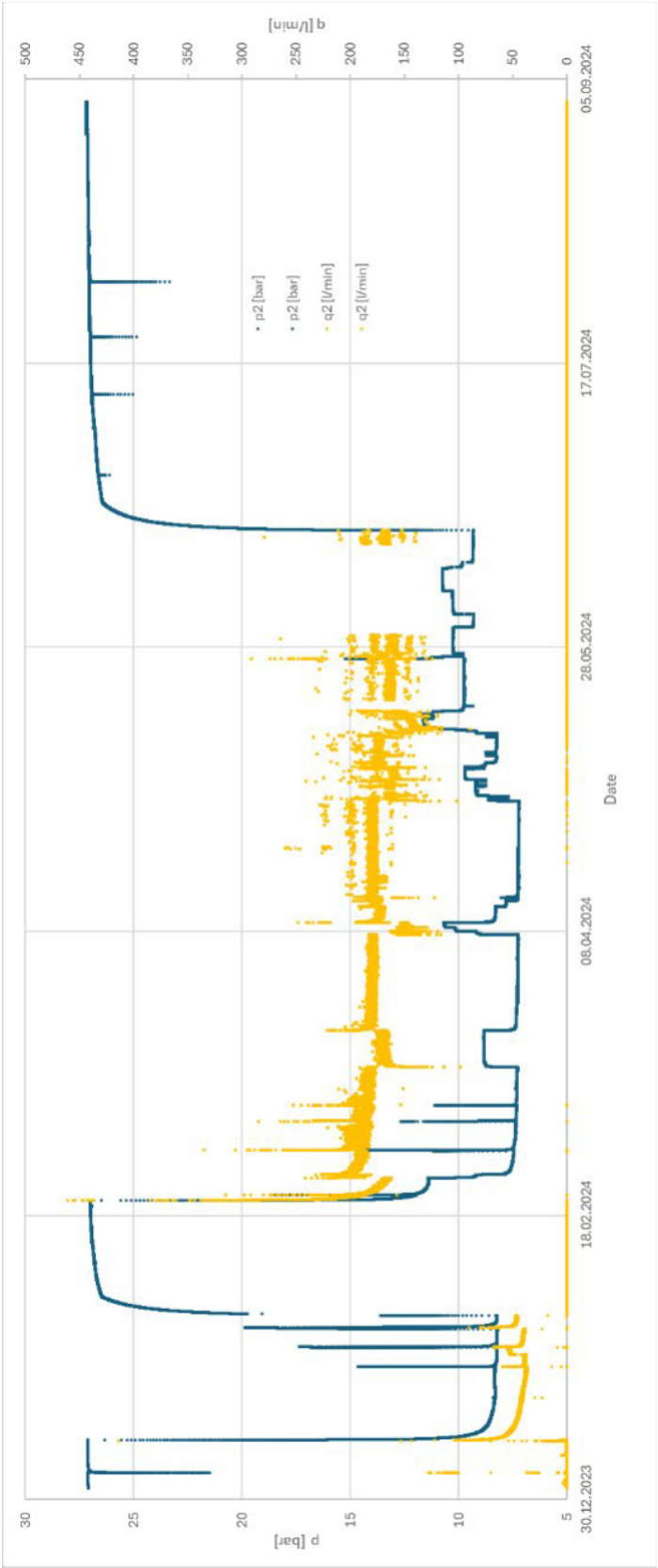


Figure 17: Pressure [bar] and flow rates [l/min] at SLA-1 in 2024.

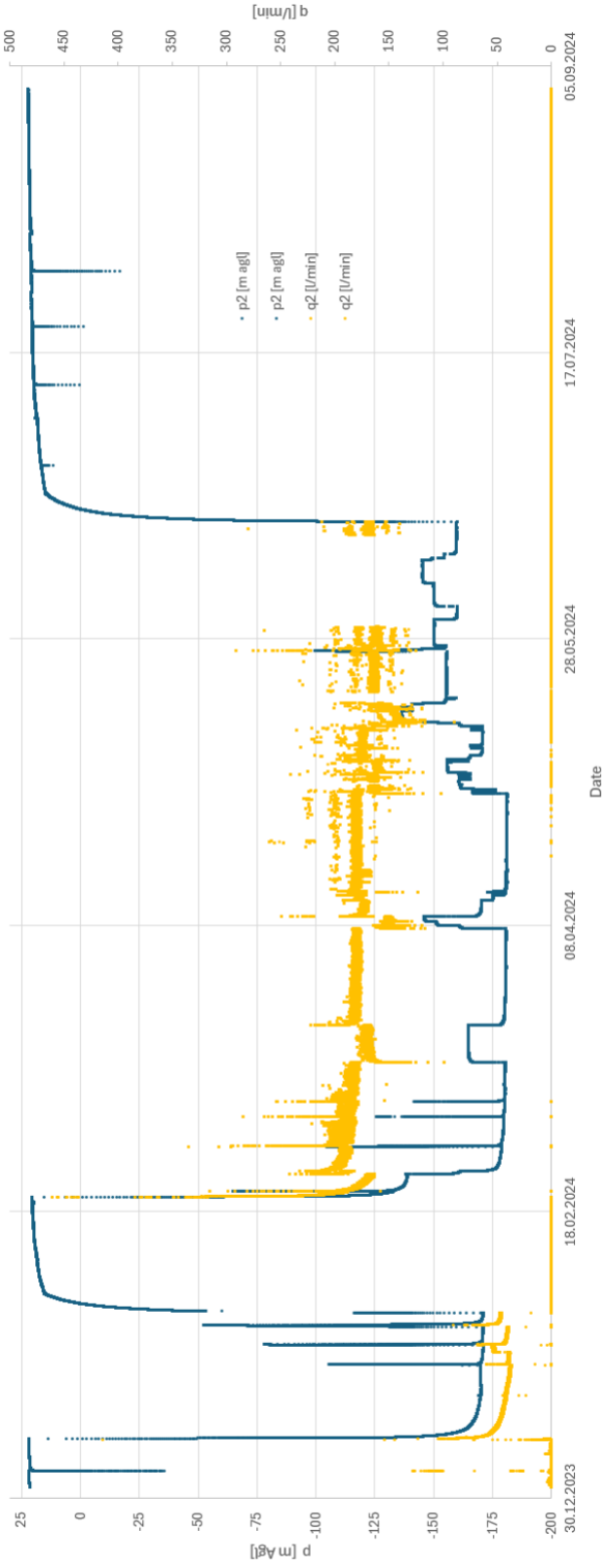


Figure 18. Pressure [m agl, based on a sensor depth of 255 m bgl and fluid density of 1000 kg/m^3] and flow rates [l/min] at SLA-1 in 2024.

For all periods with artesian well conditions (flowing), the theoretical WBS coefficient estimated from the largest casing diameter was used in the analysis. The WBS coefficient for abstraction during the history period was assumed to equal the WBS coefficient of RW1/RWS1. All WBS coefficients were fixed and no sensitivity analysis on WBS coefficient was performed as the test interval was not packed off and the water column moved freely in the borehole/casing.

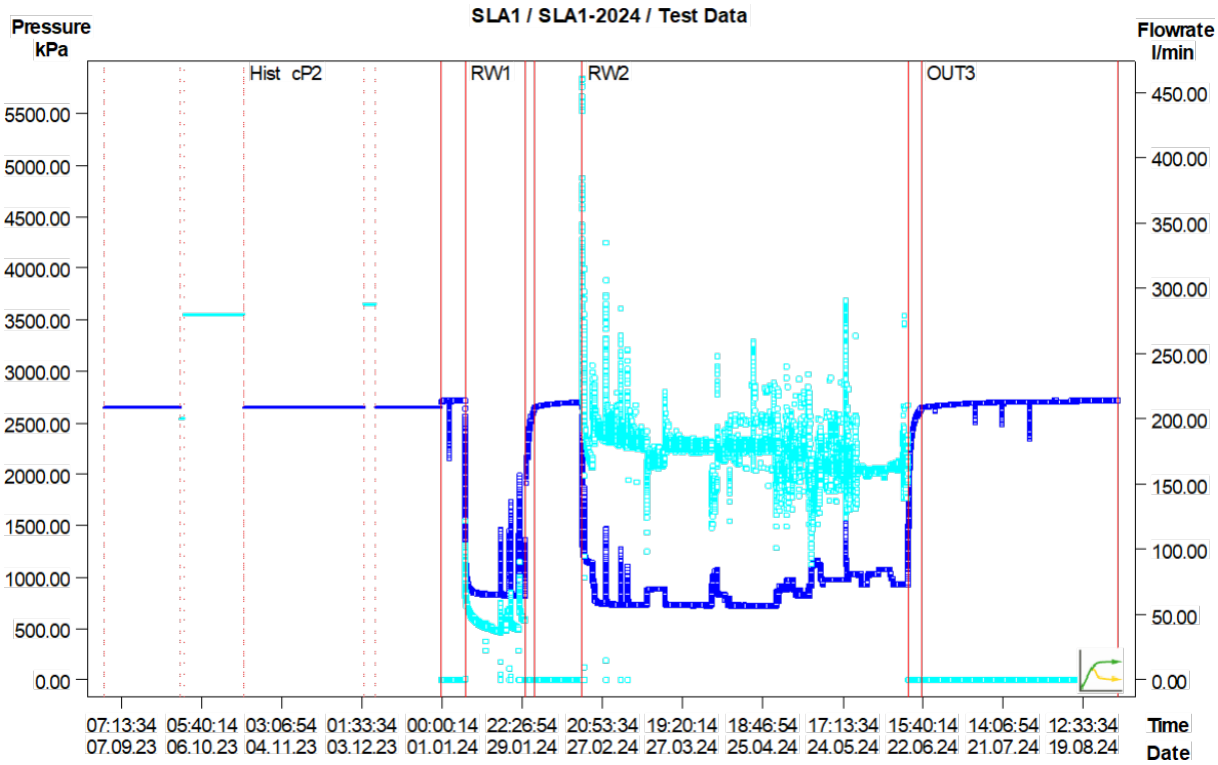


Figure 19: Sequence definition for hydraulic tests performed at SLA-1 in 2024, including and approximated borehole history starting in September 2023

Flow diagnostics - TNP analysis SLA-1

The TNPs (= Transmissivity Normalized Plots; Enachescu et al., 2004) for both recovery periods RWS1 and RWS2 are in Figure 20.

The derivatives show very similar shapes and slopes but are shifted vertically. The vertical shift indicates an increase in transmissivity from RWS1 to RWS2. Accordingly, it is expected that both tests (RW1/RWS1 and RW2/RWS2) cannot be matched using one compatible data set of hydraulic parameters. The reason for the vertical shift in the derivatives is speculative but may indicate continues development of the formation and the reservoir respectively. However, it is noted that the shape of the derivatives is almost identical, indicating that the flow regime for both test events is compatible.

From the TNPs of the RWS phases the following conclusions can be drawn.

- The early unit slope shows a wellbore storage regime.
- The early kink in the derivative is not considered to represent a formation or reservoir property but may derive from the backflow into the borehole after shut-in or the recovery in a casing with changing diameter.
- Intermediate times indicate a bilinear flow regime, fracture flow with potential matrix contribution.

- During late times, the derivate indicates a deviation of the flow dimension from radial towards spherical flow, i.e. an increase in transmissivity with increasing thickness of the aquifer affected by pumping caused by e.g. a fracture connecting to an extending fracture network or corridor.

The Horner plot in Figure 21 indicates a formation pressure of about 3240 kPa (about 492 m asl or 75 m agl).

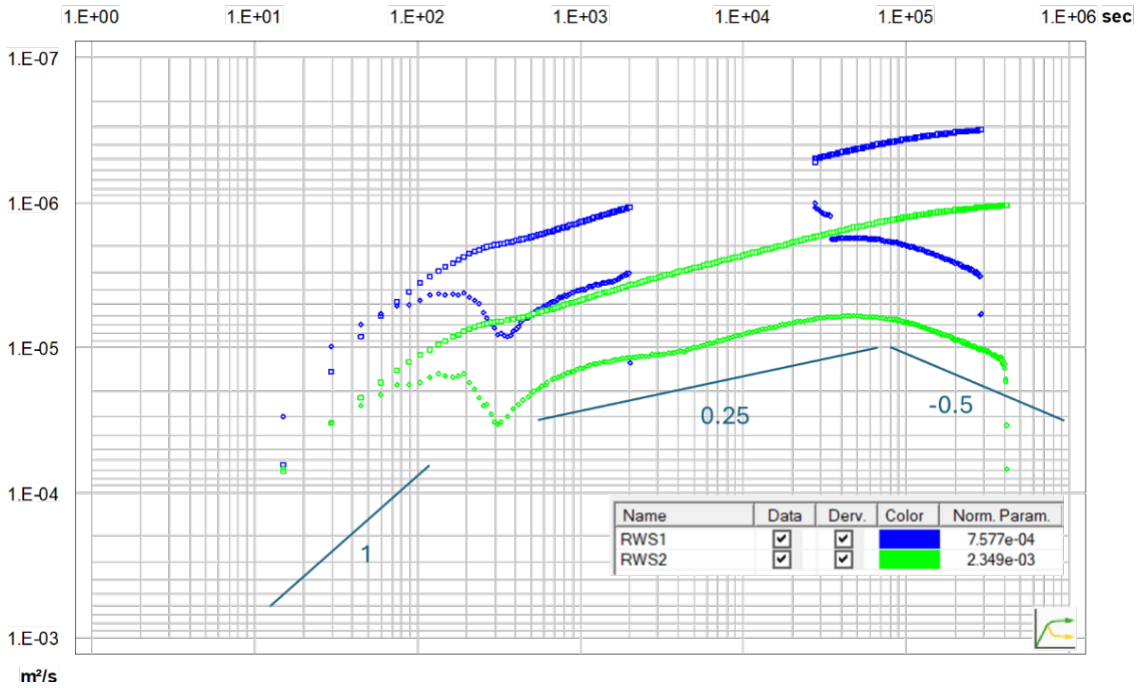


Figure 20: TNP of RWS1 and RWS2

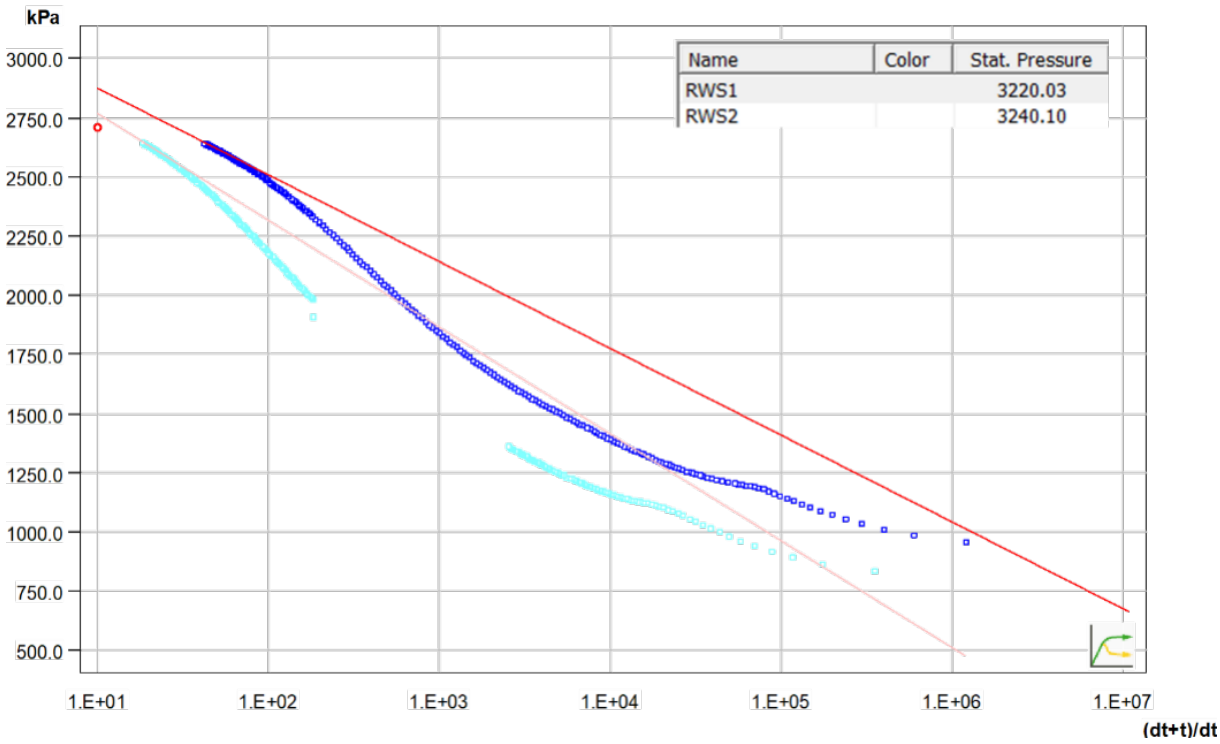


Figure 21: Horner-Plot RWS1 and RWS2

Since the duration of the RWS phases is limited by the time when the well becomes artesian, the TNP in Figure 22 also shows the derivatives of the RW drawdown phases which extend for a much longer period but contain considerable data noise due to fluctuating rates and pressures. Note that for generating a TNP the RW-phases are treated as constant rate test and normalized by constant (average) pumping rates, about 43 l/min for RW1 and 173 l/min for RW2.

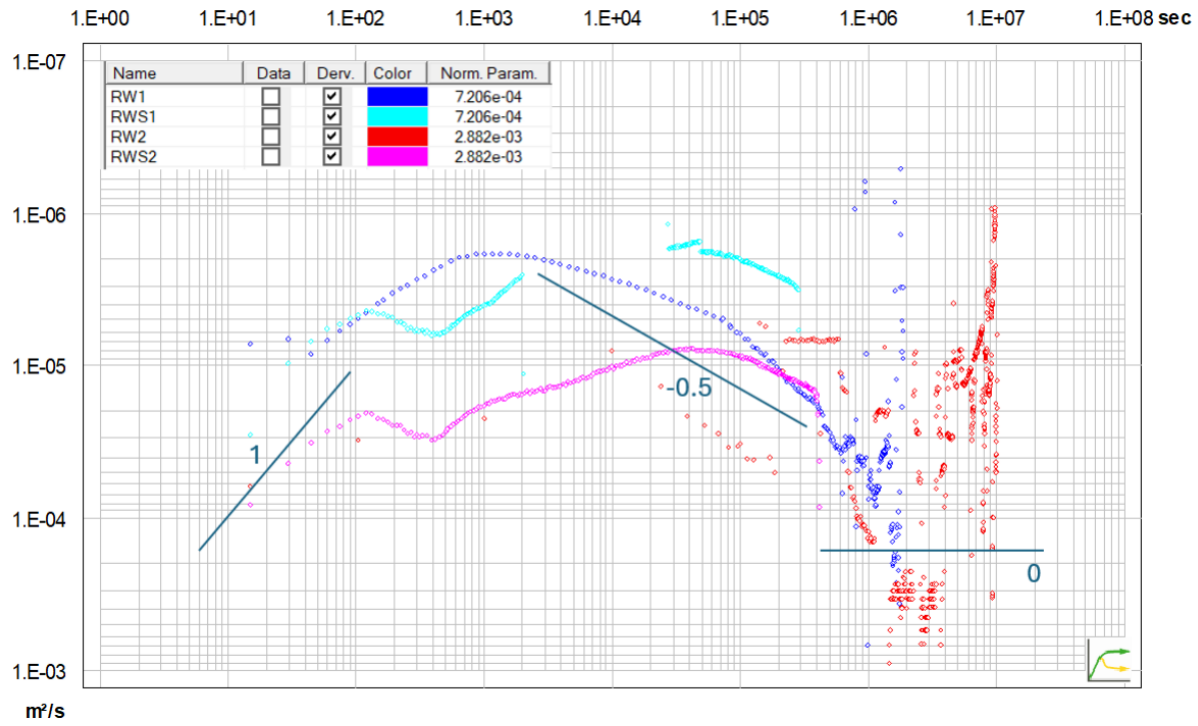


Figure 22: TNP of RW1/RWS1 and RW2/RWS2

From the TNPs of the RW phases the following conclusions can be drawn:

- After the unit slope period, both RW phases do not indicate distinct fracture flow but a quick transition to a non-radial flow regime with a flow dimension larger than 2 and an increase in transmissivity. The nearfield of the well seems to be influences by changing conditions also with regard to withdrawal vs. recovery events.
- With continued pumping the slope of the RW1 and RW2 derivatives tend to an even more negative slope which may indicate a strong contrast in the far field transmissivity or interpreted as a constant head boundary.
- For late times both derivatives become very noisy but the RW2 derivative seems to stabilize for about one log-time cycle at a transmissivity between 2 to 4E-14 m^2/s under a radial flow regime (n=2).

Note that for late pumping times, the derivatives of RW1, RW2 and even RWS2 exhibit a similar shape at similar transmissivity values, suggesting that hydraulic tests can provide compatible results of hydraulic parameters describing the far field of the tests.

Towards the end of the RWS2 phase an increase in the derivative may indicate a reservoir boundary but considering the noise in the data this interpretation is discarded.

Previous test analyses SLA-1 (Reinhardt & Rösli, 2013) vs. new results

To see how the previously estimated hydraulic parameters match the data recorded in 2024 a simple fit was performed. The estimated head (in Reinhard & Rösli, 2013; 496 m asl) was calculated to match the current setup with P2 installed at 255m bgl, resulting in a formation pressure of about 3280 kPa. The two pumping phases were considered as constant rate tests with the previously mentioned average pumping rates.

Results of the simulation are shown in Figure 23. The simulation shows that the parameter set estimated in Reinhard & Rösli (2013) reproduces the RW2/RWS2 phases at moderate quality. Though, the estimated parameters fail to reproduce the sequence RW1/RWS1. Recall that from the TNP, it was already expected that only one test sequence can be reproduced with one data set. However, the RW2/RWS2 is captured rather well with acceptable deviations between simulation and measured data during early times. For the period of artesian conditions (after RWS2) the simulated flow rates reach about 26 L/min. The estimated radius of investigation is roughly 19 km.

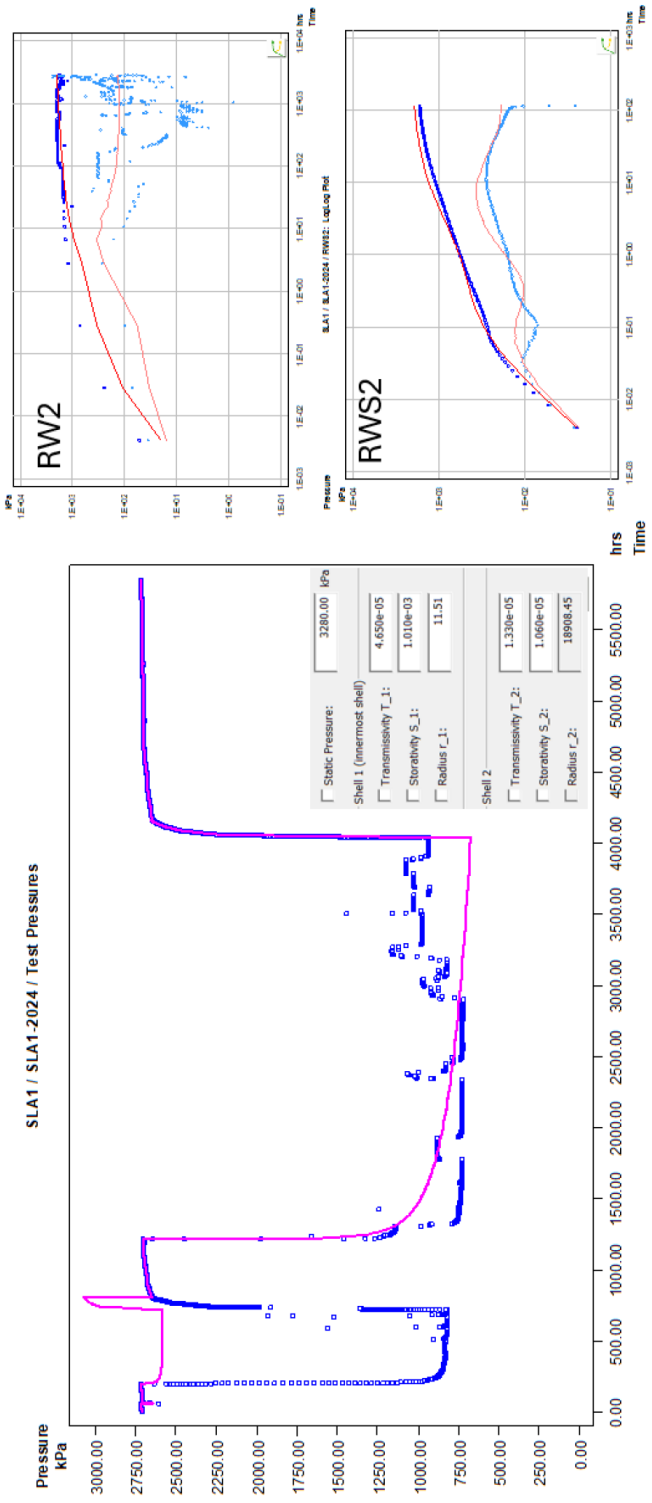


Figure 23: Simulation of RW1/RWS1 and RW2/RWS2 using hydraulic parameters estimated in Reinhard & Rösli (2013)

In a first step a 2-shell radial composite model is investigated based on the analysis of Reinhard & Rösli (2013). The results are shown in Figure 24. The cartesian fit is performed on the RW2/RWS2 sequence. Compared to the analysis in Reinhard & Rösli (2013), the estimated transmissivity did not change significantly. The difference in the parameters is limited to changes in the storativity values of the inner and outer zone and the radius of investigation, which is about 46 km. Under artesian conditions after RWS2, the well keeps producing about 25 L/min. Note that the formation pressure was not fitted but fixed at 3240 kPa, because there is very little uncertainty in the static pressure and all measurements of even longer recovery phases in the past confirm this value. On the other hand, the pressure recovery during build-up phases is very advanced. Assuming that the RW2 phase starts at near static conditions does therefore not introduce a noticeable uncertainty. Overall, at this level of permeability, pressure history has very limited effect. It follows that the fixation of the static formation pressure in such high permeability rock does also not affected the derivation of other parameters.

Since the model setup did not provide additional insight (other than in Reinhardt & Rösli, 2013) into reservoir properties, this analysis approach was not followed further. Also, it is noted that the analysis results using a 2-shell radial composite model do not agree with the findings from the TNP which suggests an increase in transmissivity with increasing distance from the well.

Therefore, a fracture model was set up to get better fits for the recorded pressure data of SLA-1. The analysis focuses on an analysis approach based on the TNP results presented above. Note that the analysis (Reinhardt & Rösli, 2013) uses a negative skin implemented in a composite model, whereas the TNP analysis suggests that the transmissivity of the reservoir increases with distance from the well. The implementation of flow dimensions in the analysis was already discussed in Reinhardt & Rösli (2013) but not considered appropriate and discarded.

The model approach develop is based on the findings from the TNP's:

- A 3-shell composite model is used for the analysis considering non-radial flow dimension in the first two shells, i.e. a flow dimension $n < 2$ in the first shell to represent fracture flow and a flow dimension $n > 2$ in the second shell to capture the transition to spherical flow. The flow dimension in the outer shell is fixed to radial flow (n=2).
- The reservoir transmissivity in the external shell is assumed higher than in the inner shells.

The analysis matches the RW2-RWS2 sequence by a cartesian fit on interval pressure. The match is performed within the following bounds

- T bounds: T1: 1E-6 – 1E-4 m^2/s, T2: 1E-6 – 1E-4 m^2/s, T3: 8E-5 – 5E-4 m^2/s
- S bounds for all shells: 1E-5 – 1E-3
- r bounds: r1: 0.079 – 100 m, r2: 0.079 – 5000 m
- Pf (= formation pressure) bounds: 2500 kPa (416.4 m asl, about GOK) to 3240 kPa (491.88 m asl, estimated from Horner plot)

Figure 25 and Figure 26 gives an overview of the analysis. Note that the formation pressure reduces to about 443.2 m asl and the flow rates under artesian conditions after RWS2 to about 2.5 l/min. Even though the flow dimension in the two inner zones changes from 1.75 to 2.8, indicating the change from fracture dominated flow to spherical flow, the estimated hydraulic conductivity of these zones changes only by a factor of 2 when compared to the simulations based on a 2-shell-radial composite model.

Though, using the 3-shell model, the (formation) hydraulic conductivity in the outermost 3_{rd} shell is estimated to 2.6E-6 m/s assuming radial flow in the outer shell (n fixed to 2), and hence about one order of magnitude higher than what was estimated in previous analyses (Reinhardt & Rösli, 2013). Note that compared to the 2-shell-radial composite model, the storativity is with 7E-4 to 1E-3 rather high, hitting almost the upper bound.

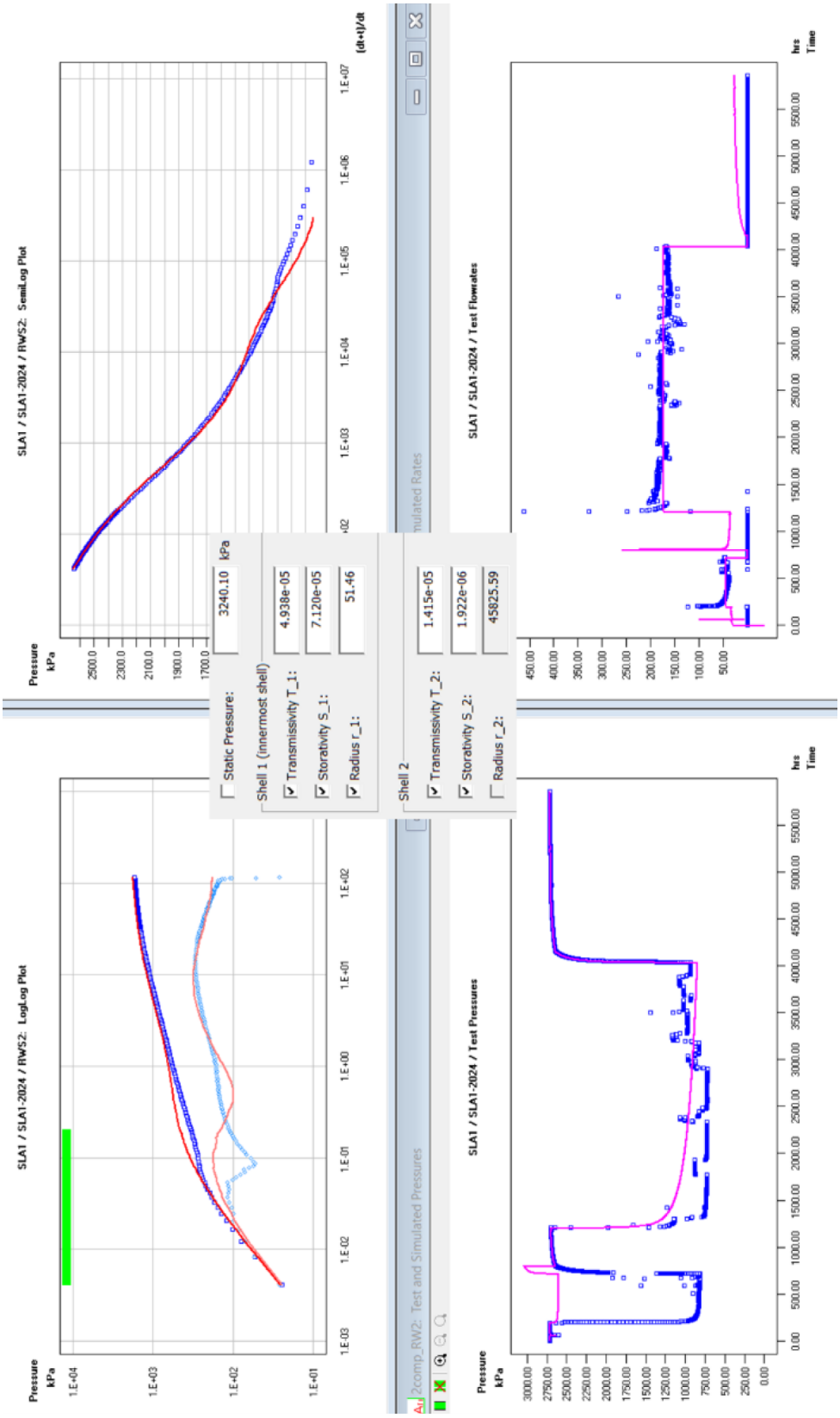


Figure 24: Single-fit simulation of RW2/RWS2 using a 2-shell radial composite model

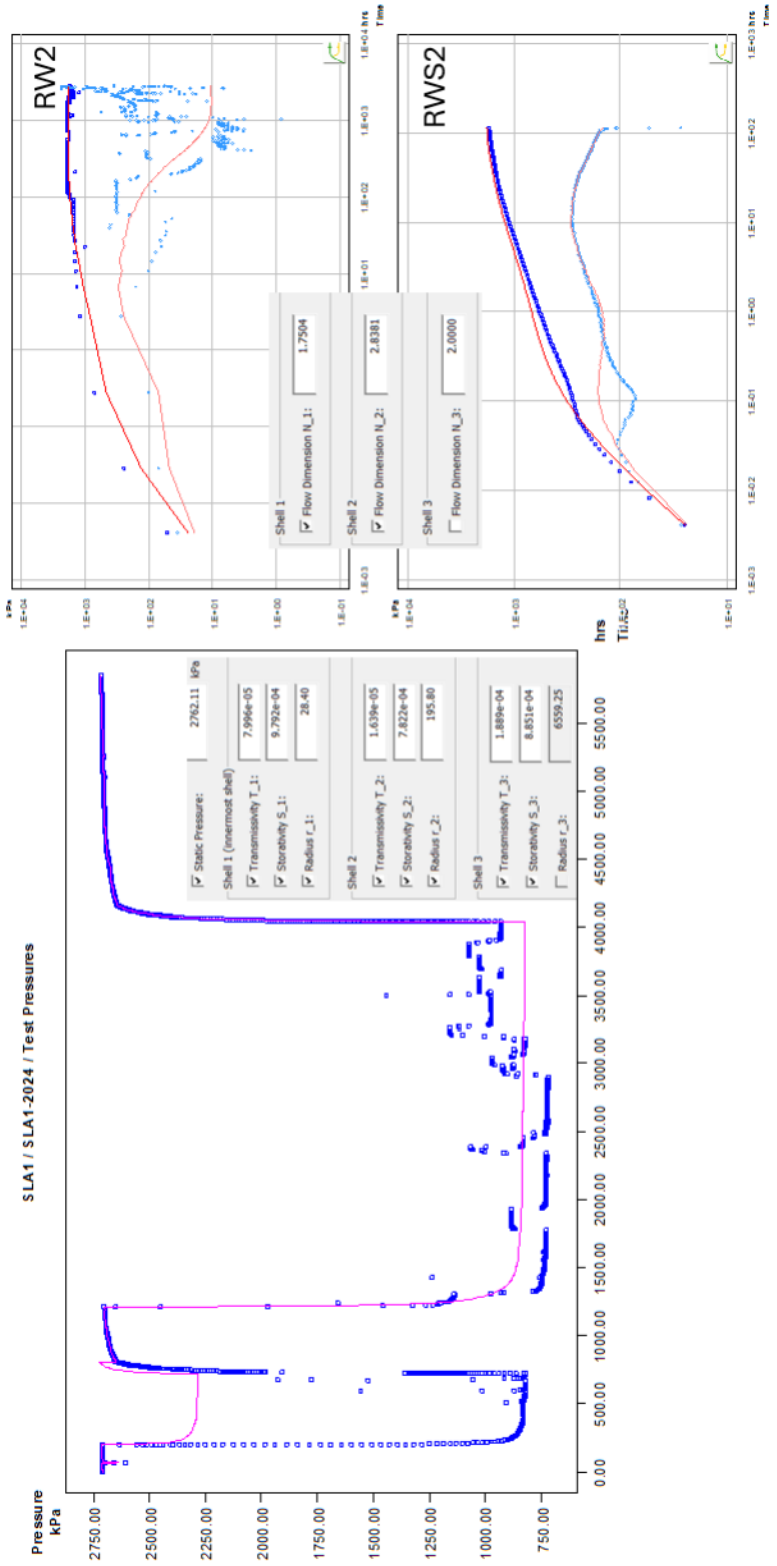


Figure 25: Simulated pressures - Single-fit simulation for RW2/RWS2 using a 3-shell-composite model with flow dimensions in the inner zones.

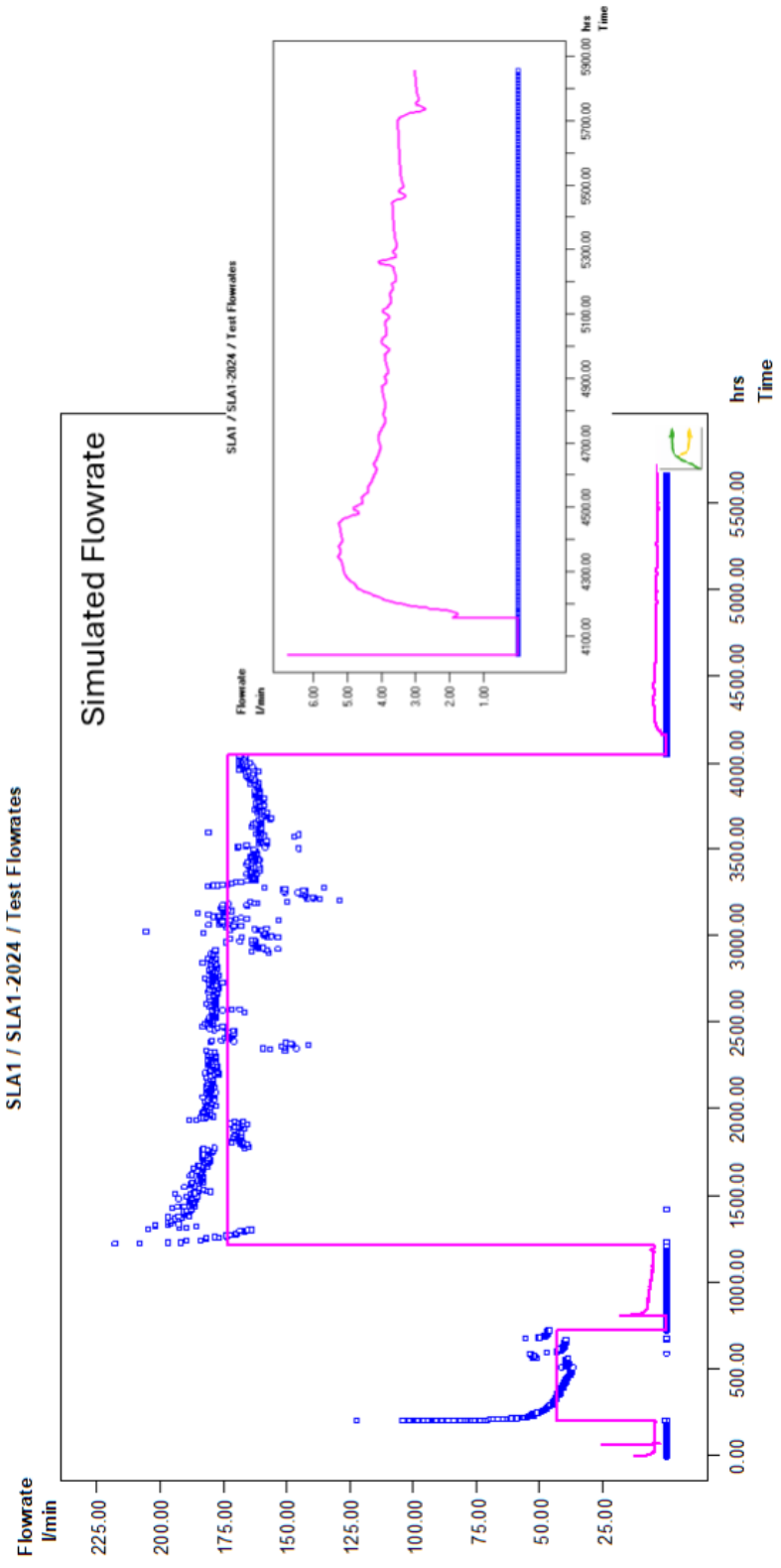


Figure 26: Simulated flowrates - Single-fit simulation for RW2/RWS2 using a 3-shell-composite model with flow dimensions in the inner zones.

Finally, an additional simulation was performed to investigate whether the RW1/RWS1 data can be matched. Note that the TNP, RW1, RW2 and RWS2 show a similar shape and behaviour.

Since the used analysis tool, namely Hydrobench, cannot handle time-dependent hydraulic parameters of the inner zones, the simulation which fitted on the RW1/RWS1 phases considers the hydraulic parameters of the two inner-shells as fitting parameters only, while keeping the hydraulic formation parameters of the outer zone (3_{rd} shell), the formation pressure, and the flow dimensions fixed to the results from the RW2/RWS2 analysis.

Figure 27 shows the results for the corresponding fit on the RW1/RWS1 phases. Keeping the flow dimension and the outer (formation) hydraulic parameters fixed, the RW1/RWS1 phase was matched to the data by changing the inner zone parameters. The estimated inner zone hydraulic conductivities for RW1/RWS1 are about one order of magnitude lower than what was estimated for RW2/RWS2, a rather strong change in the inner zone parameters and their radii.

Furthermore, the simulations show the strong dependence of the analyses on the inner-zone parameters as the RW1/RWS1 analysis fails in reproducing the drawdown and recovery of the RW2/RWS2 phases and vice versa. It also raises the question on the sensitivity of the test analysis on the outer (3_{rd} zone) hydraulic parameters. A comprehensive statistical and sensitivity analysis is recommended to provide further insight.

The table below summarizes the results of analyses performed for SLA-1. The results confirm the results of previous hydraulic tests, and the derived hydraulic parameters have remained more or less unchanged since the beginning of the pressure monitoring, which started after the acidization in the year 2011 (Frieg et al., 2015).

Table 4: Summary table of performed analyses for SLA-1

Analysis		**NPB12-14, MK5**			**RW2/RWS2**	**RW2/RWS2**	**RW1/RWS1**
Flow model		**2-rad-comp.**			**2-rad-comp.**	**3-shell-n**	**3-shell-n**
		Best	**Low. Bound**	**Up. Bound.**	**Single fit**	**Single fit**	**Single fit**
T3	m^2/s	-	-	-	-	1.90E-04	1.9E-4 (fixed)
T2	m^2/s	1.33E-05	6.08E-06	1.34E-05	1.42E-05	1.64E-05	1.53E-06
T1	m^2/s	4.65E-05	1.32E-05	1.62E-04	4.94E-05	8.00E-05	1.42E-05
K3	m/s	-	-	-	-	2.63E-06	2.63E-6 (fixed)
K2	m/s	1.84E-07	8.41E-08	1.85E-07	1.96E-07	2.27E-07	2.12E-08
K1	m/s	6.43E-07	1.82E-07	2.24E-06	6.83E-07	1.11E-06	1.96E-07
S3	[-]	-	-	-	-	8.85E-04	8.85E-4 (fixed)
S2	[-]	1.06E-05	1.74E-05	1.40E-04	1.92E-06	7.80E-04	2.68E-04
S1	[-]	1.01E-03	1.53E-04	1.00E-03	7.12E-05	9.80E-04	3.41E-04
r_i	m	(19000)	-	-	45800	6559	7872
r2	m	-	-	-	-	195.8	78.2
r1	m	11.51	0.7	14.95	51.46	28.4	69.6
n3	[-]	-	-	-	-	2 (fixed)	2 (fixed)
n2	[-]	2 (fixed)	-	-	2 (fixed)	2.84	2.84 (fixed)
n1	[-]	2 (fixed)	-	-	2 (fixed)	1.75	1.75 (fixed)
Pf	kPa	5052.5	4936.4	5054.8	3240	2763	2763 (fixed)
head	m asl	496	484.2	496.3	491.9	443.2	443.2 (fixed)

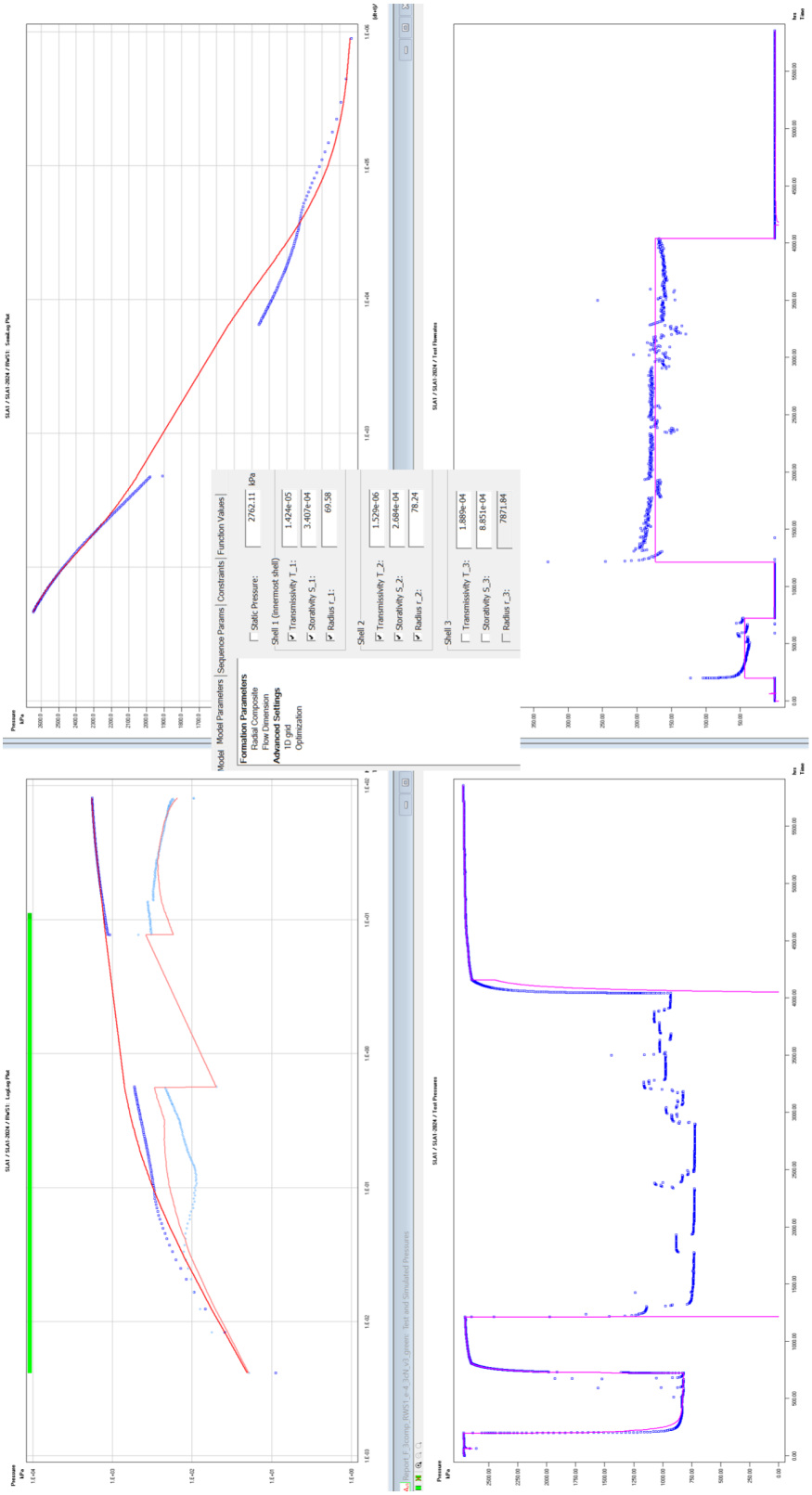


Figure 27: Simulation of RW1/RWS1 to investigate the potential change in inner-zone parameters while fixing the hydraulic parameters of the outer zone to estimates from the RW2/RWS2 analysis

SLA-2

In general, the hydraulic data for production well SLA-2 in 2024 is of low to intermediate quality as no dedicated hydraulic test was performed, because the heat production for the greenhouses was the top priority and therefore it was not possible to initiate over a longer period of time changes in flow rates or pressure build-up periods.

Figure 28 below shows the pressure and flow rates in SLA-2, as recorded in 2024. One long RW phase, which likely started already in 2023, is followed by a short recovery phase (RWS) of about 6 days in August 2024, from 11.-17.08.2024 RWS. After the RWS, production restarted. Note that the magnitude of the RWS is rather low and in the range of the hydraulic response to previous changes in (decreasing) production rates, e.g. in March or May/June 2024.

Furthermore, for February 2024 the data is limited to the flow rate and no pressure data is available, due to a failure in the programming of the data acquisition.

The simulation setup is shown in Figure 29 and Figure 30 below. Since no pressure data was available for February 2024, this period was treated as history with a constant flow rate of 320 l/min. The data used for the analysis thus starts on 29.02.204. Additional information on well operation suggest that the well was producing since (at least) 05.10.2023. Therefore, the history was extended to that date using the flow rate of 320 l/min. Eventually, the total history period sums up to 2’880 h (Figure 29).

During the analysis, it appeared that simulations are sensitive to the pumping history. Thus, a second (hypothetical) history scenario was investigated which basically extends the history for one more year of continuous pumping at 320 ml/min. This simulation is called “HIST_ex” and assumes a pumping history of 11’640 hours prior to available pressure recordings (Figure 30). Note the very short duration of the recovery period in August 2024 compared to the long abstraction periods.

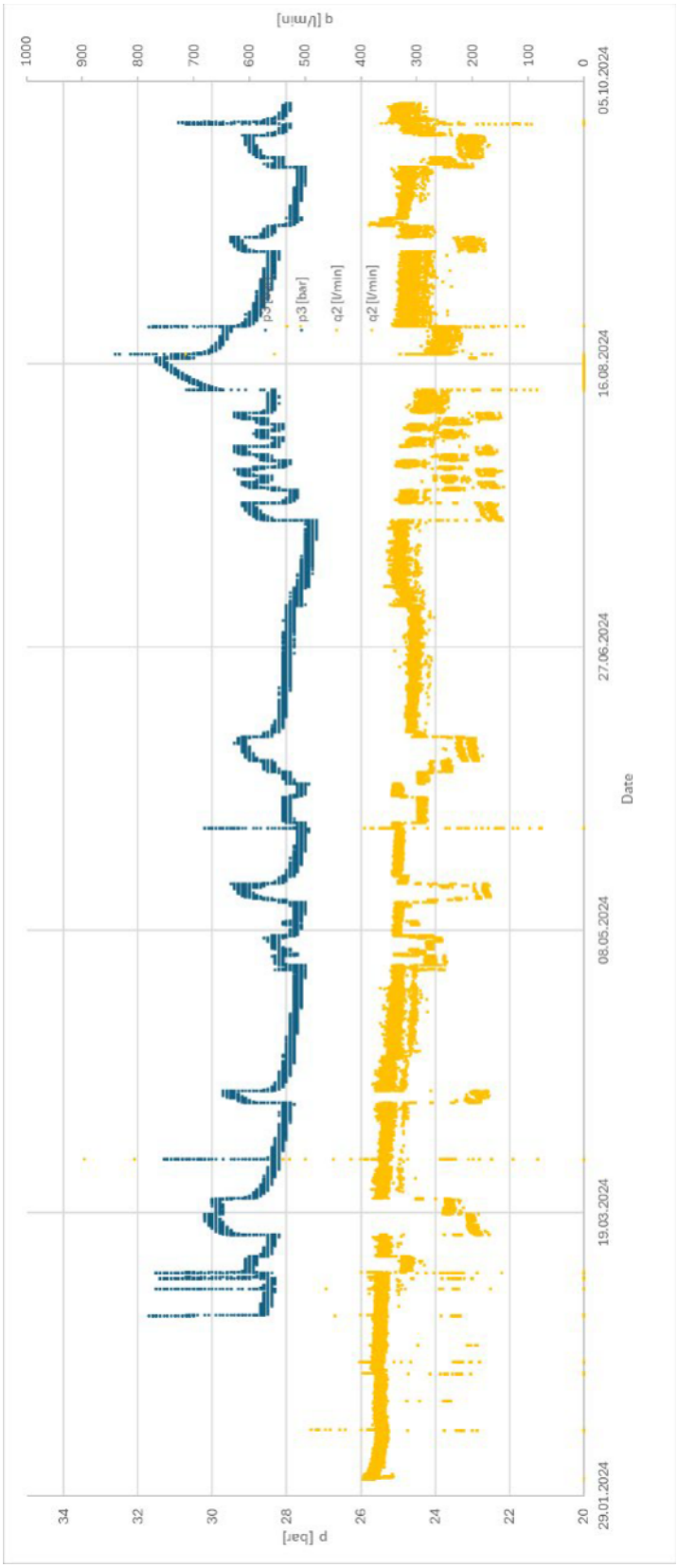


Figure 28: SLA-2: Pressure (blue, in bar) and production rate (yellow, in l/min) in 2024

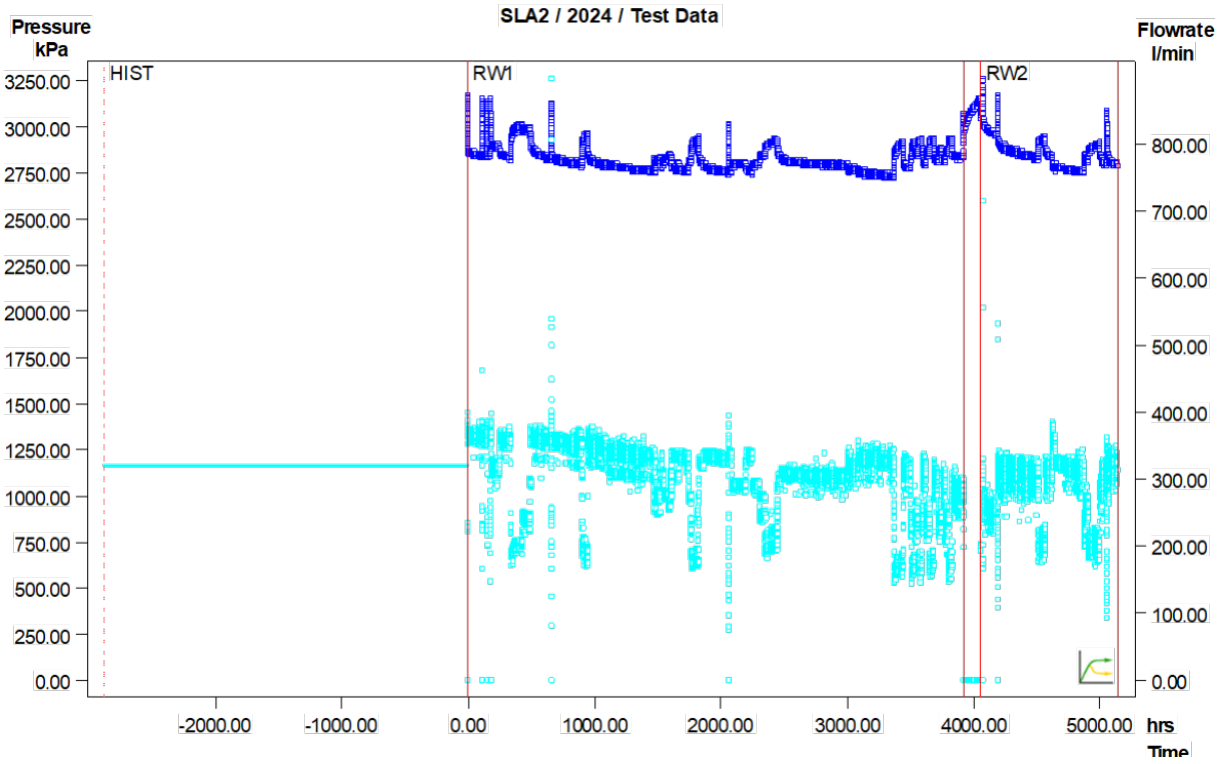


Figure 29: SLA-2 - Analysis setup considering a history period of 2’880 hours

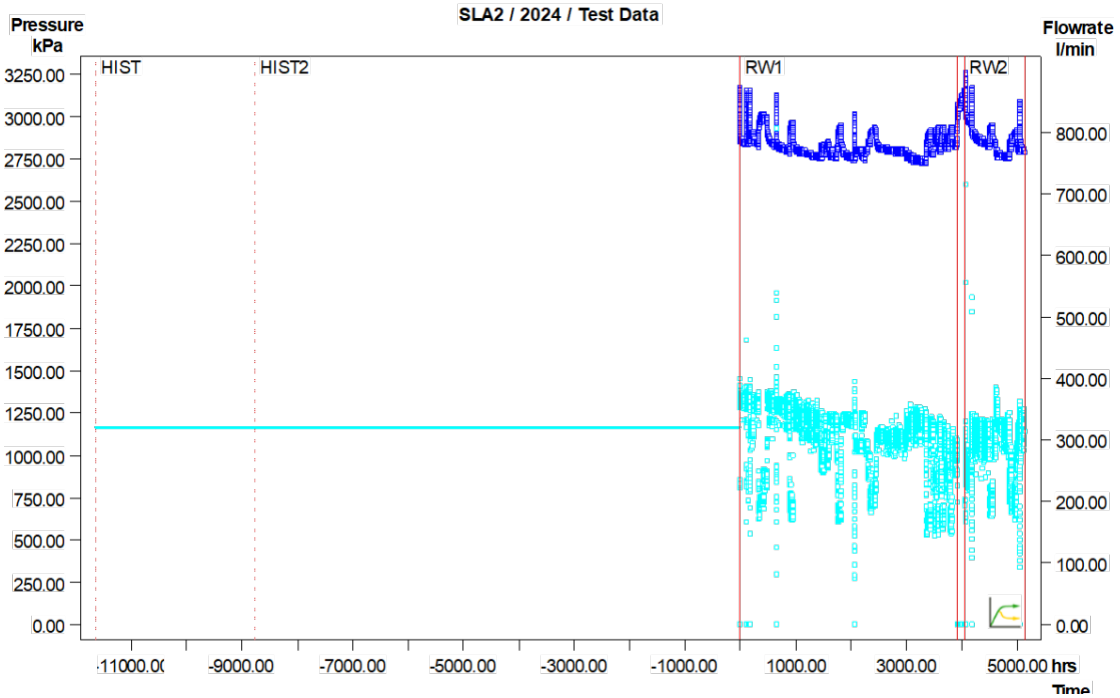


Figure 30: SLA-2 - Analysis setup considering a history period of 11’640 hours

Flow Diagnostics – TNP analysis SLA-2

The TNPs for the RWs and both RW phases is shown below in Figure 31. The data is very noisy, particularly for the PW phases which were plotted by assuming a constant rate during. Due to the short duration recovery phase, a Horner plot does not provide estimates of the formation pressure.

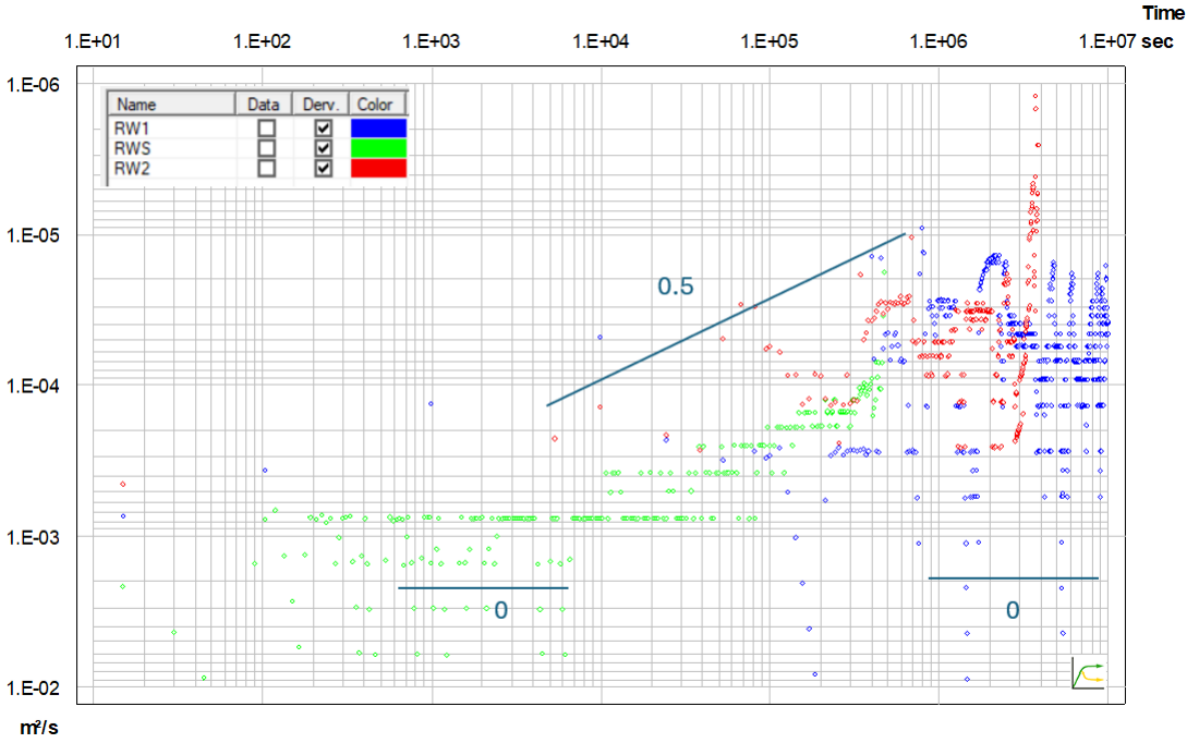


Figure 31: SLA-2 - TNP flow diagnostics

Even though the data is very noisy, the derivative of the RWS indicates the typical form for a horizontal well with an early (vertical) radial flow period followed by linear flow when the formation behaves like a infinite fracture. The second stabilisation indicating (horizontal) radial flow is not evident in the RWS derivative due to its short duration but the late time data from the RW phases suggests that a late-time radial flow regime may exist. In naturally fractured carbonate formations, such behavior can also be explained by a fracture corridor model (Enachescu et al., 2016). Such model may represent the observed steeply dipping fault zones that crosscut the Muschelkalk aquifer and provide a hydraulic connection for the upwelling of water from the crystalline basement (see Section 2.3). However, to prove such fracture corridor model, a more comprehensive dataset and additional observations including data from new test boreholes are needed.

Previous test analyses SLA-2 (Reinhard & Rösli, 2015) vs. new results

Reinhard & Rösli (2015) analysed dedicated pumping tests (TD1 and TD2; Table 5) using analytical methods and Saphir NL considering a horizontal well configuration. The analysis further mentions a slightly negative skin (-0.081) and notes hydraulic head at about hydrostatic conditions.

Table 5: Hydraulic parameter estimates for Interval TD1 and TD2 of SLA-2 (Reinhard & Rösli, 2015)

		TD2			TD1		
Parameter	Units	*Best estimate*	Lowest estimate	Highest estimate	*Best estimate*	Lowest estimate	Highest estimate
Transmissivity T	[m^2/s]	**4.7E-06**	4.4E-06	1.7E-05	**6.1E-06**	6.0E-06	1.2E-05
Hydr. Cond. K	[m/s]	**1.4E-07**	1.3E-07	5.2E-07	**1.8E-07**	1.8E-07	3.5E-07
Freshwater head h_s	[m asl]	**409.0**	409.0	446.1	**425.6**	401.6	425.6

Using the hydraulic parameters estimated in Reinhard & Rösli (2015; Table 5) in a homogeneous model using a discrete skin, did not provide a satisfying match to the 2024 data. However, extending the model conceptually to “2-shell radial composite”, provided a reasonable match. Therefore, the head was considered to equal surface level and the transmissivity of the outer shell was fixed to 4.7E-06 m^2/s. The remaining parameters (storativity of both shells, transmissivity and the radius of the inner shell) were fitted. The fit was performed for interval pressure the entire data set (RW1, RWS and RW2) in cartesian coordinates.

The results of the fit for the different history scenarios are presented below (Figure 32). Note that, it is not possible to achieve satisfying fits for the different histories with one parameter set. The main differences in the two simulations are in the inner zone storativity and radius, whereas the inner zone transmissivity shows only a minor impact. Note that the overall fit quality using the longer history (functional value 0.254) is improved over the simulation using a short history (functional value 0.437).

However, contrary to the results from Reinhard & Rösli (2015) the difference in the inner zone parameters is significant compared to the formation parameters, indicating a strong negative skin.

It is recalled that even though the fit quality of the RWS is reasonable, the RWS data does not comprise the response of horizontal radial flow as evident in the TNP (assuming a horizontal well configuration).

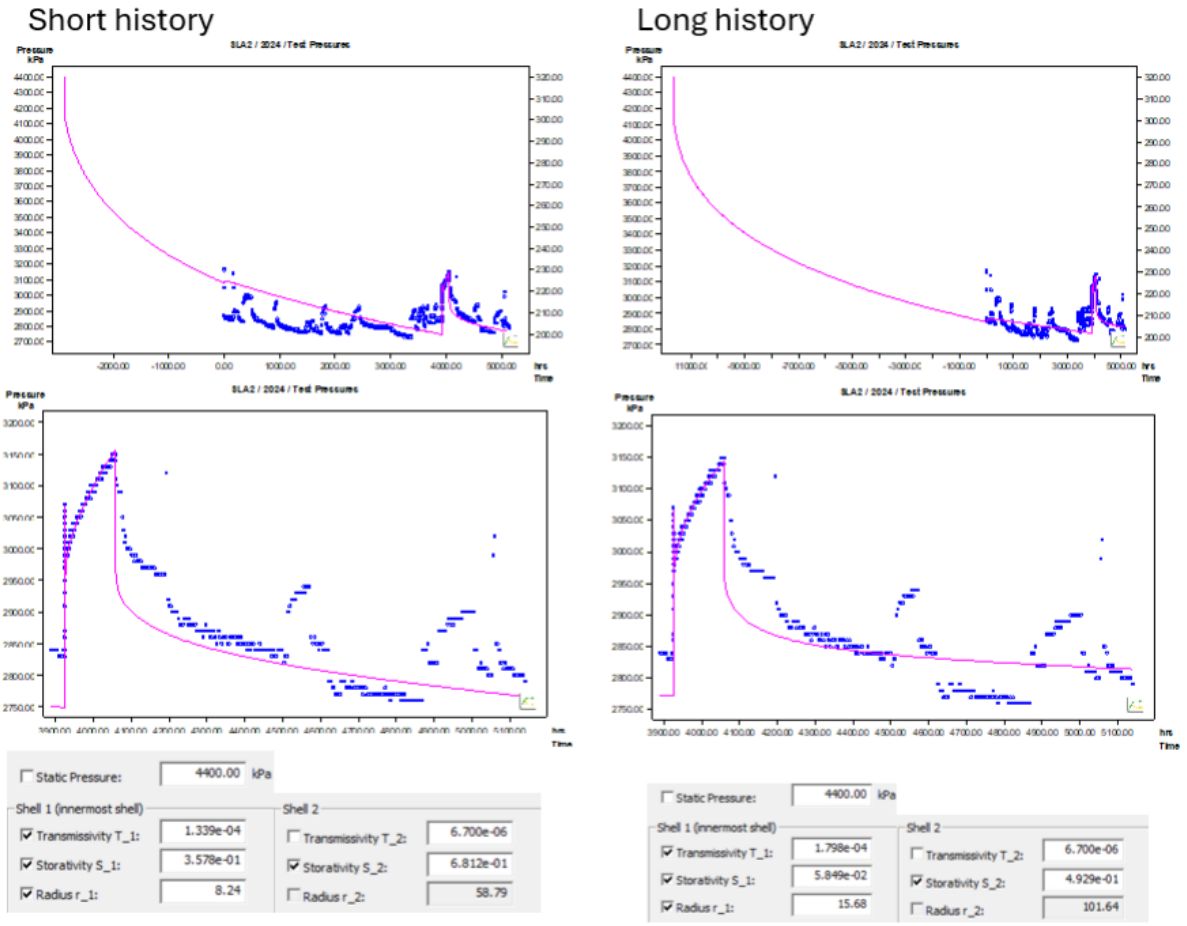


Figure 32: Fit results for two different history durations

The above analysis already shows the main challenges in analyzing the SLA-2-2024 data, namely, (1) the data of the short RWS is basically not sensitive to the formation hydraulic properties and (2) the uncertainties in the history. This was investigated by fitting the 2-shell radial composite model with keeping only the formation pressure fixed but all other hydraulic parameters free. Fits to the SLA-2-2024 data could be achieved in similar fit quality with values for the outer transmissivity between 1E-7 and 2E-5 m^2/s but with a strong variability in the fit quality to the history period and a strong variability in the estimated storativity values.

However, the transmissivity of the inner zone showed a minor variability between 1 and 3E-4 m^2/s. However, since a 2-shell radial composite mode does not satisfy the concept of a horizontal well which was found to be (at least partially) valid for SLA-2 from the TNP, the following analysis was tired. It focuses on the estimation of hydraulic parameters using a 3-shell composite model with flow dimensions (n1=2, n2=1, n3=2), i.e. it considers vertical radial flow during early-times, followed by linear flow and radial horizontal flow during intermediate to late times. It is noted that such a flow model cannot overcome the restrictions of data quality, i.e. the low sensitivity of the RWS to the formation hydraulic parameters. Furthermore, an additional skin zone (to implement an increased transmissivity near the wellbore due to acidification; Frieg et al., 2015 & Frieg, 2015) was not implemented.

The following Figure 33 shows single fit of the SLA-2-2024 data for the different history scenarios. Fits were again performed on pressure for RW1, RWS and RW2 in cartesian coordinates. Flow dimensions were not fitted but fixed at the conceptual values 2-1-2. The radii of the two inner zones were bounded by a maximum of 35 m.

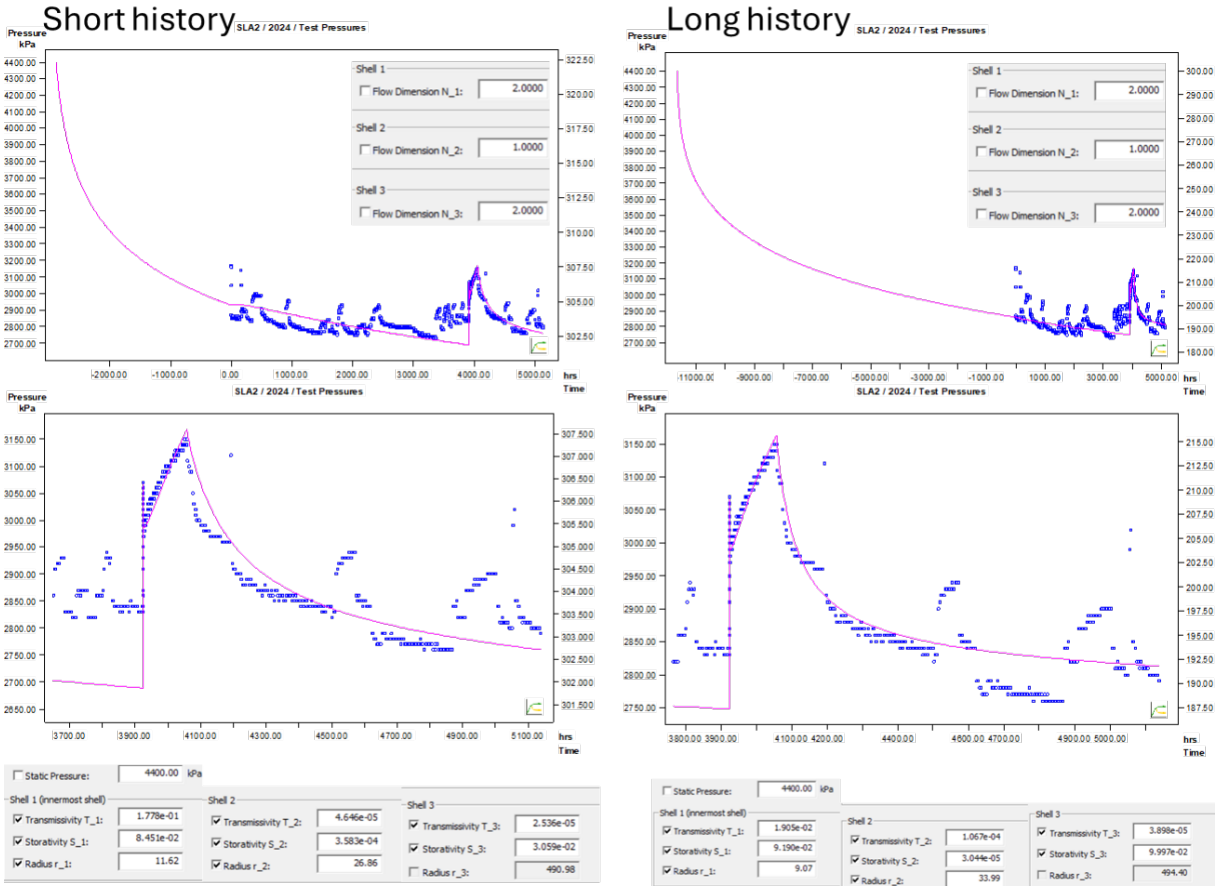


Figure 33: SLA-2 - Analysis of SLA-2-2024 data using a 3-shell composite model with flow dimensions and different history durations

The best match for a single fit is obtained with the long history. Even though the fit quality of the RWS slightly decreases in the 3-shell composite model with flow dimensions (compared to the 2-shell radial model), the fit to the RW2 phase significantly improved.

The formation transmissivity varies for the models with different history periods between 2.5E-5 and 3.9E-5 m^2/s. Considering a thickness of the formation of 33.30 m, this yields a hydraulic conductivity of about 9.4E-7 m/s, a factor 3 lower than the estimate for the formation hydraulic conductivity obtained from the SLA-1 analysis. In comparison with the test results from Reinhard & Rösli (2015), the transmissivity of the formation increases by a maximum of nearly one order of magnitude (Table 5, Table 6). These results demonstrate the need for an update of the hydraulic model presented in Künze & Kuhlmann (2020) in the area of borehole SLA-2.

Table 6: Hydraulic parameter estimates for SLA-2 based on the analysis of the 2024 data.

Transmissivity (m^2/s)	**Hydraulic conductivity (m/s)**
2.5E-5 to 3.9E-5	7.5E-7 to 1.1E-6

2.2.2. Detailed hydrochemical and isotopic characterization of thermal water produced from SLA-1 and SLA-1

The water samples for the most extended analyses were taken on April 15 and 16, 2024 after having produced for more than two months at quasi constant rates of 200 and 400 L/min from SLA-1 and SLA-2, respectively (Figure 18 and Figure 28). These samples are thus not affected by artefacts caused by stagnant conditions in the well such as cooling or exchange with the atmosphere. Hence, they represent the natural state in the geothermal reservoirs tapped by the two wells. The extended chemical and isotopic characterization is provided below. In the follow-up chapter (Section 2.2.3), hydrochemical data collected between 2018 and 2025 are used to describe the variation of the hydrochemical signature over time.

Major solutes

The analysis of the major ions revealed distinct hydrochemical characteristics for the two wells (Figure 22, Table 7). The water from SLA-1 is characterized as a neutral (pH= 6.8), saline (EC = 2730 µS/cm), reducing (Eh = -20 mV), Ca-Mg-SO_4 type water. It is dominated by calcium (550 mg/l), magnesium (120 mg/l), and sulphate (1,700 mg/l), with a total dissolved solid concentration of approximately 2.6 g/L. Sodium and potassium concentrations are comparatively low, at 27 mg/l and 15 mg/l respectively, while ammonium shows only a minor presence (0.11 mg/lL). The water exhibits low alkalinity (180 mg/l as HCO_3^-) and a chloride concentration of 12 mg/L.

In contrast, the thermal water of SLA-2 is characterized as neutral (pH = 6.7), saline (EC = 12,700 µS/cm), oxidizing (Eh = 154 mV), Na-SO_4-type water. It is dominated by sodium (2,900 mg/l) and sulphate (6,000 mg/l), with a very high salinity of about 10.5 g/L. Calcium was determined at 360 mg/L, while magnesium and potassium were measured at 78 mg/L and 55 mg/L, respectively. The ammonium concentration is slightly higher than in SLA-1, reaching 2.4 mg/L. On the anion side, bicarbonate and chloride concentrations were 422 and 730 mg/L, respectively.

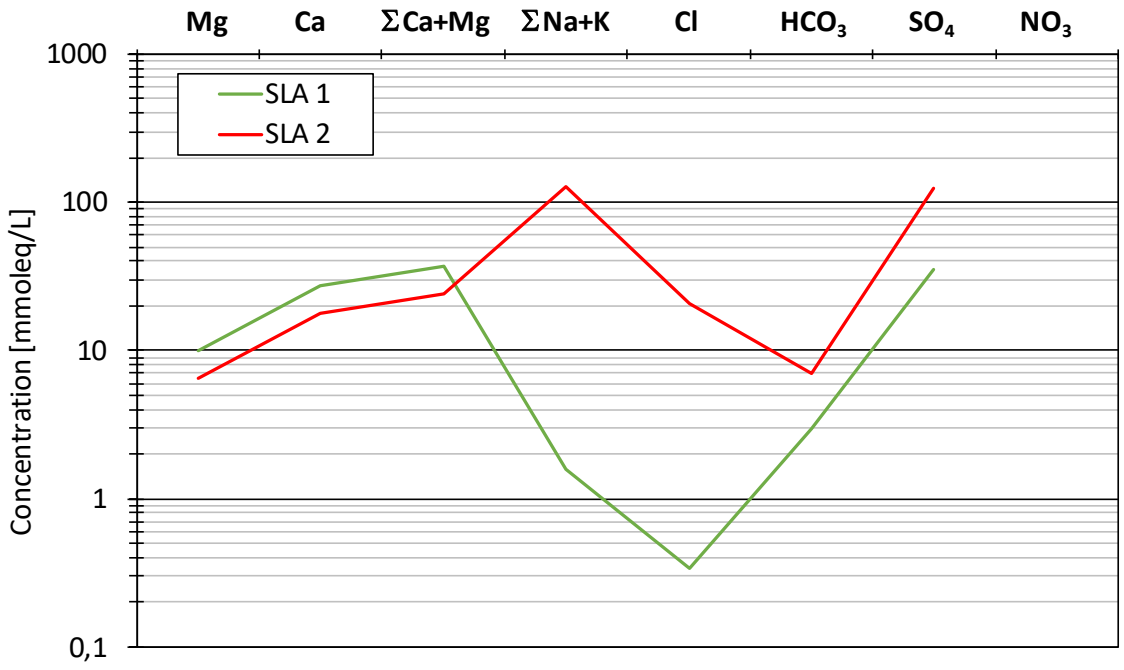


Figure 34: Hydrochemical composition of SLA-1 and SLA-1 in a Schoeller diagram

Trace elements

The trace element analyses covered a wide range of major and minor constituents. In both samples, most trace element concentrations were within the lower mg/L range, indicating generally low levels of dissolved trace elements (Table 8). Overall, concentrations were lower in SLA-1 than in SLA-2, consistent with the previously observed higher salinity in SLA-2.

Among the alkaline and alkaline earth metals, strontium showed the highest concentrations, reaching 4.4 mg/L in SLA-1 and 16 mg/L in SLA-2. Lithium occurred at lower levels, with 0.17 mg/L in SLA-1 and 2.3 mg/l in SLA-2. Barium, beryllium, cesium, and rubidium were detected only in minor amounts.

For the transition metals, slightly higher concentrations were observed in SLA-1. Only iron (1.24 mg/L in SLA-1; 0.48 mg/L in SLA-2) and manganese (0.62 mg/L in SLA-1; 0.61 mg/L in SLA-2) reached noticeable levels, while titanium, vanadium, chromium, cobalt, nickel, copper, zinc, molybdenum, aluminum, and niobium were detected only at trace levels or below detection limits.

Among the metalloids, boron and silica showed higher concentrations in SLA-2 (B: 8.4 mg/L; Si: 18 mg/L) than in SLA-1 (B: 0.29 mg/L; Si: 15 mg/L). Arsenic was measured at 2.0 mg/L in SLA-1 and 0.19 mg/L in SLA-2, while antimony remained below the detection limit.

For the halogens, iodine was below detection limits in both wells. Bromine was detected at low concentration in SLA-2 (1.5 mg/L) but was not detectable in SLA-1. Fluoride concentrations were similar in both samples, with 2.7 mg/L in SLA-1 and 2.3 mg/L in SLA-2.

All heavy metals were below detection limits except cadmium, which was present at very low concentrations in both wells.

Other detectable trace constituents include total phosphorus, which was slightly higher in SLA-2 (0.13 mg/L) than in SLA-1 (0.08 mg/L). Ortho-phosphate was only detected in SLA-1 at 0.13 mg/L. Total sulphide concentrations (H_2S, HS^-, S^{2-}) were higher in SLA-2 (0.39 mg/L) than in SLA-1 (0.12 mg/L). Based on the measured pH values, the distribution of sulphide species was calculated. At a pH of 6.8 in SLA-1, the calculated concentrations are 0.09 mg/L for H_2S and 0.03 mg/L for HS^-. In SLA-2, with a pH of 6.7, the concentration of HS^- is 0.11 mg/L, while H_2S is 0.28 mg/L. All remaining trace elements occurred in very low concentrations or were not detectable.

Organic parameters

The analysis of organic parameters shows generally very low concentrations in both samples (Table 8). Dissolved organic carbon (DOC) was 0.16 mg/L in SLA-1 and 0.19 mg/L in SLA-2. The phenol index was below the detection limit (< 0.006 mg/L). Total hydrocarbons were below detection (<0.05 mg/L) in SLA-1 and slightly higher in SLA-2 (0.11 mg/L).

Among the aromatic hydrocarbons, benzene, toluene, ethylbenzene and xylenes (BTEX) were detected in low concentrations, with slightly higher values in SLA-1. The sum of aromatic hydrocarbons (Σ arom. HC) was 7.6 µg/L in SLA-1 and 6 µg/L in SLA-2. Polycyclic aromatic hydrocarbons (Σ PAH) were very low, amounting to 0.32 µg/L in SLA-1 and 0.26 µg/L in SLA-2.

Overall, the concentrations of all detected organic compounds were in the low µg/L to sub-µg/L range, indicating only minor organic content in both thermal waters.

Table 7: Overview of physico-chemical parameters and concentrations of main anions and cations

Lab.-No.		**415039**	**415040**
		SLA 1	**SLA 2**
		16.04.2024	**15.04.2024**
		16:00	**16:00**
Physico-chemical parameters			
Colour		colourless	colourless
Visual turbidity		clear	clear
Odour		H_2S	H_2S
Temperature at sampling	°C	29.6	39.2
Specific electrical conductivity (25°C) on site	µS/cm	2730	12700
Specific electrical conductivity (25°C) laboratory	µS/cm	2650	13010
pH-value on site		6.8	6.7
pH-value laboratory		6.9	6,9
Temperature laboratory	°C	21.7	21.3
Redox potential (relative to NHE)	mV	-20	154
Acid capacity (pH 4.3) on site	mmol/l	3	6.45
Acid capacity (pH 4.3) laboratory	mmol/l	2.95	6.92
Main anions and -cations			
Sodium (Na^+)	mg/l	27	2900
Potassium (K^+)	mg/l	15	55
Calcium (Ca^{2+})	mg/l	550	360
Magnesium (Mg^{2+})	mg/l	120	78
Ammonium (NH^{4+})	mg/l	0.11	2.35
Hydrogen carbonate (HCO_3^-)	mg/l	180	422
Chloride (Cl^-)	mg/l	12	730
Sulphate (SO_4^{2-})	mg/l	1700	6000
Nitrate (NO_3^-)	mg/l	< 0.2	< 1
Nitrite (NO_2^-)	mg/l	0.01	< 0.01
Ion balance error	%	0.41	1.58

Table 8: Overview of trace element concentrations

Lab.-No.		**415039**	**415040**
		SLA 1	**SLA 2**
		16.04.2024	**15.04.2024**
		16:00	**16:00**
Trace elements			
Antimony	mg/l	< 0.000002	0.00
Barium (Ba^{2+})	mg/l	0.03	0.03
Beryllium	mg/l	0.00	0.00
Boron	mg/l	0.29	8.40
Bromide (Br^-)	mg/l	< 0.1	1.50
Total Cyanide	mg/l	< 0.005	< 0.005
Fluoride (F^-)	mg/l	2.70	2.30
Gold	mg/l	0.00	0.00
Iodide (I^-)	mg/l	< 0.1	< 1
Lithium (Li^+)	mg/l	0.17	2.30
Molybdenum	mg/l	< 0.00001	0.00
Ortho-phosphate (PO_4^{3-})	mg/l	0.13	-
Total phospherus	mg/l	0.08	0.13
Selenium	mg/l	0.00	0.00
Silver	mg/l	< 0.000002	< 0.000002
Silica	mg/l	15.00	18.00
Strontium (Sr^{2+})	mg/l	4.40	16.00
Total sulfide (H_2S. HS^-. S^{2-})	mg/l	0.12	0.39
Vanadium	mg/l	< 0.00001	0.00
Aluminium	mg/l	< 0.01	0.02
Arsenic	mg/l	2.00	0.19
Lead	mg/l	< 0.00002	< 0.00002
Cadmium	mg/l	0.00	0.00
Cesium	mg/l	0.01	0.02
Total chromium	mg/l	0.00	0.00
Cobalt	mg/l	< 0.00002	0.00
Total iron	mg/l	1.24	0.48
Gallium	mg/l	0.00	0.00
Indium	mg/l	< 0.00001	< 0.00001
copper	mg/l	< 0.00005	0.00
Total manganese	mg/l	0.62	0.61
Nickel	mg/l	0.00	0.04
Mercury	mg/l	< 0.0001	< 0.0001
Rubidium	mg/l	0.04	0.08
Thallium	mg/l	< 0.000005	< 0.000005
Thorium	mg/l	0.00	0.00
Titanium	mg/l	< 0.0001	0.00
Uranium	mg/l	0.00	0.00
Bismut	mg/l	< 0.000002	< 0.000002
Zinc	mg/l	0.00	0.01
Tin	mg/l	< 0.00002	< 0.00002
Cerium	mg/l	0.00005	0.00002
Zirconium	mg/l	0.00072	0.00054
Lanthanum	mg/l	0.00003	0.00001
Europium	mg/l	0.00001	< 0.000002
Gadolinium	mg/l	0.00001	0.00001
Niobium	mg/l	< 0.000002	< 0.000002
Neodymium	mg/l	0.00	0.00

Table 9: Overview of organic concentrations of organic compounds

Lab.-No.		415039	415040
		SLA 1	SLA 2
		16.04.2024	15.04.2024
		16:00	16:00
Organic Parameters			
DOC	mg/l	0.16	0.19
Phenol index	mg/l	< 0.006	< 0.006
Hydrocarbons	mg/l	< 0.05	0.11
Benzene	µg/l	0.4	0.2
Toluene	µg/l	1.3	1.3
Ethylbenzene	µg/l	0.6	0.6
m,p-Xylene	µg/l	2.3	1.7
o- Xylene	µg/l	0.8	0.6
Mesitylene	µg/l	0.4	0.2
1,2,3-Trimethylbenzene	µg/l	0.4	0.2
1,2,4-Trimethylbenzene	µg/l	1.4	1.2
Σ* Aromatic Hydrocarbons	µg/l	7.6	6
Naphthalene	µg/l	0.15	0.06
1-Methylnaphthalene	µg/l	0.09	0.08
2-Methylnaphthalene	µg/l	0.08	0.08
Acenaphthylene	µg/l	< 0.005	< 0.005
Acenaphthene	µg/l	< 0.005	0.04
Fluorene	µg/l	< 0.005	< 0.005
Phenanthrene	µg/l	< 0.005	< 0.005
Anthracene	µg/l	< 0.005	< 0.005
Fluoranthene	µg/l	< 0.005	< 0.005
Pyrene	µg/l	< 0.005	< 0.005
Benzo(a)anthracene	µg/l	< 0.005	< 0.005
Chrysene	µg/l	< 0.005	< 0.005
Benzo(b)fluoranthene	µg/l	< 0.005	< 0.005
Benzo(k)fluoranthene	µg/l	< 0.005	< 0.005
Benzo(a)pyrene	µg/l	< 0.0025	< 0.0025
Dibenz(ah)anthracene	µg/l	< 0.005	< 0.005
Benzo(ghi)perylene	µg/l	< 0.005	< 0.005
Indeno(1,2,3 cd)pyrene	µg/l	< 0.005	< 0.005
Σ* PAH (Polycyclic Aromatic Hydrocarbons)	µg/l	0.32	0.26

Stable isotopes of water, strontium and sulfate, and radionuclide activities

As part of the sampling of SLA-1 and SLA-1 in April 2024, separate sample bottles were filled in accordance with the order for the determination of the isotope signature of water, as well as of the dissolved sulphate and strontium content. Moreover, the natural radionuclides radium-226, radium-228, radon-222, Lead-210 and Polonium-210 were analysed as well (Table 10).

The stable water isotope signatures, $\delta^{18}O\text{-}H_2O$ and $\delta^{2}H\text{-}H_2O$, showed distinct differences between SLA-1 and SLA-2. In the SLA-1 sample, the $\delta^{18}O\text{-}H_2O$ and $\delta^{2}H\text{-}H_2O$ values were at -12.68 $‰_{VSMOW}$ and -91.2 $‰_{VSMOW}$, respectively. In contrast much higher values of -9.79 $‰_{VSMOW}$ and -63.7 $‰_{VSMOW}$ were observed at SLA-2. Since both samples plot on or close to the Global Meteoric Water Line (GMWL), this indicates meteoric water as only water source but that recharge occurred under different climatic conditions. More details on stable water isotopes are provided in the section below, presenting historical data collected from the two Schlattingen wells (Section 2.2.3).

In the SLA-1 and SLA-2 samples, the signature of the stable isotopes of sulphate ($\delta^{34}S/\delta^{18}O$) was analysed with δ-values of 18.1 or 18.9 ‰$_{VCDT}$ for sulphur-34 and 14 to 14.4 ‰$_{VSMOW}$ for oxygen-18, while the $^{87}Sr/^{86}Sr$ signatures were determined to 0.708437 and 0.708996. These signatures show good agreement with other Muschelkalk groundwater in Northern Switzerland and are likely derived from evaporites and marine limestones of Triassic units (Figure 35, Figure 36; Waber & Traber, Ufrecht & Hölzl 2006).

The Radium-226 activity in SLA-2 was 0.325 ± 0.013 Bq/kg while a notably higher value of 0.880 ± 0.024 Bq/kg was observed in SLA-1. The Radium-228 activity in SLA-1 was comparable (0.047 ± 0.009 Bq/kg), whereas SLA-1 showed a nearly twofold higher activity of 0.080 ± 0.011 Bq/kg. Radon-222 activities in SLA-2 were at 16.4 ± 1.3 Bq/kg 2. In SLA-1 the measured activity was higher with 22.3 ± 5.3 Bq/kg. For lead-210, two identical measurements of 0.01 Bq/kg were reported. Polonium-210 was below the detection limit (< 0.005 Bq/kg) in both samples.

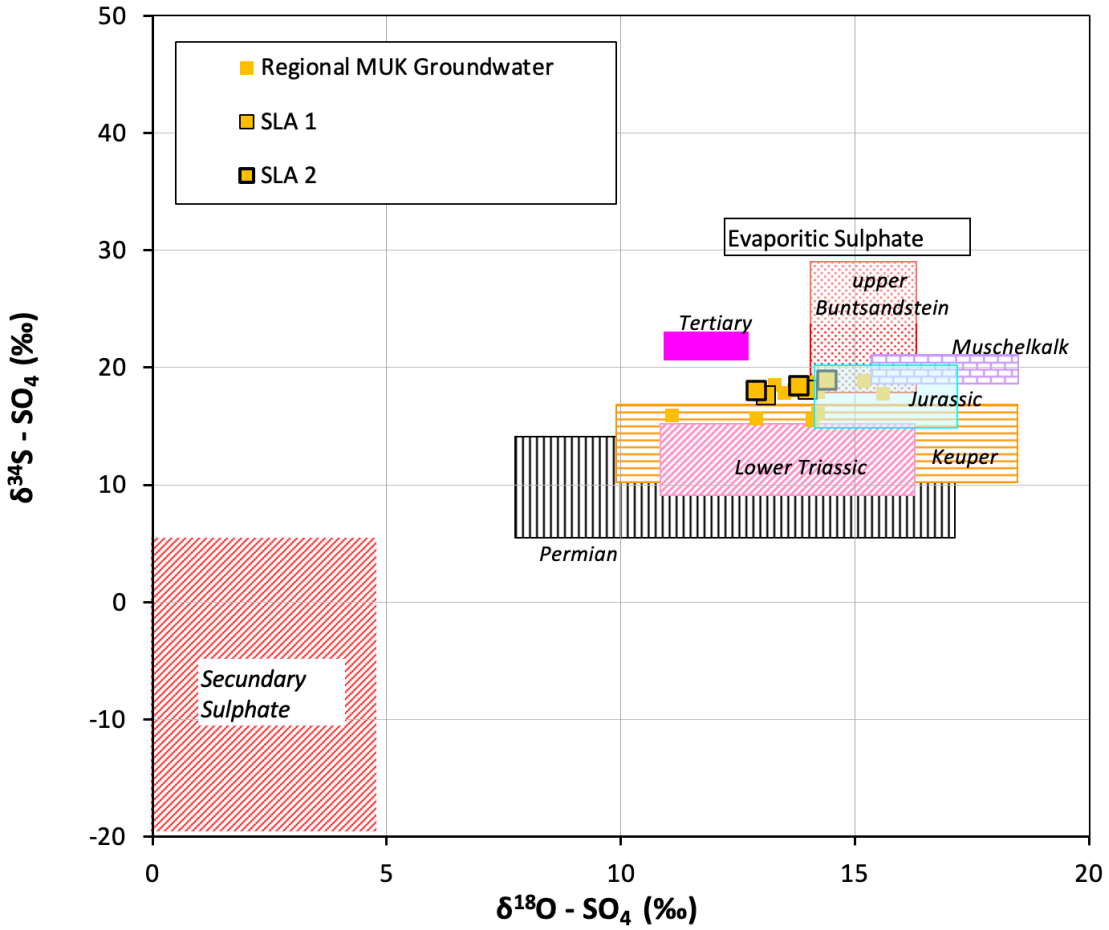


Figure 35: Sulfur and oxygen isotope ratio in SO_4 dissolved in groundwater samples collected from the Muschelkalk aquifer at Schlattingen and nearby locations.

The sulfate isotope signatures of the SLA samples compare well with those of evaporitic sulphates of Triassic units.

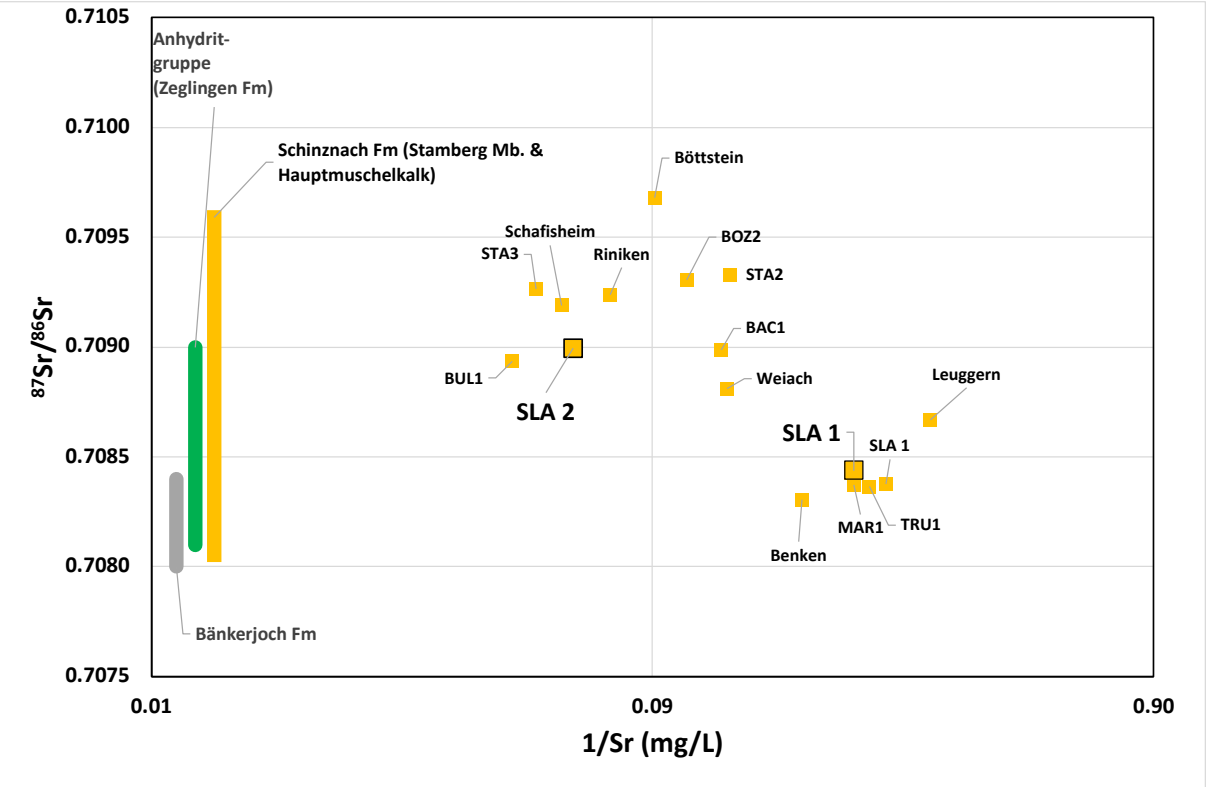


Figure 36: Sr concentration and Sr isotope ratios measured in groundwater samples collected from the Muschelkalk aquifer at Schlattingen and nearby locations.

The $^{87}Sr/^{86}Sr$ ratio are all within the range observed for evaporites and marine limestones of Triassic units (Waber & Traber, 2022; Ufrecht & Hölzl, 2006.)

Table 10: Overview of stable and radiogenic isotope analyses

Lab. No.		415039	415040
		SLA-1	SLA-2
		16.04.2025	15.04.2025
		16:00	16:00
Isotopes			
Radium-226 (^{226}Ra)	Bq/kg	0.88 ± 0.024	0.325 ± 0.013
Radium-228 (^{228}Ra)	Bq/kg	0.08 ± 0.011	0.047 ± 0.009
Radon-222 (^{222}Rn)	Bq/kg	22.3 ± 5.3	16.4 ± 1.3
Lead-210 (^{210}Pb)	Bq/kg	0.01	0.01
Polonium-210 (^{210}Po)	Bq/kg	< 0.005	< 0.005
Oxygen-18 (^{18}O-H_2O)	‰ VSMOW	-12.68	-9.79
Deuterium (^{2}H-H_2O)	‰ VSMOW	-91.2	-63.7
Deuterium-Excess	‰	10.24	14.62
Sulphur-34 (^{34}S-SO_4^{2-})	‰	18.1	18.9
Oxygen-18 (^{18}O-SO_4^{2-})	‰	14.0	14.4
Strontium isotope ratio (^{87}Sr / ^{86}Sr)		0.708437 ± 0.00003	0.708996 ±0.00003

Dissolved inorganic carbon and carbon isotope

The total content of dissolved inorganic carbon (DIC) amounted to 95 (SLA-1) and 200 (SLA-2) ccSTP/kg in the stainless steel cells (Table 11).

The DIC and carbon isotope results for SLA-1 are well within the known range of regional groundwater, showing only moderate isotope exchange with the Muschelkalk aquifer and still a detectable ^{14}C-DIC activity of 2.9 pmC.

In contrast, the DIC level in SLA-2 is significantly elevated. At the same time, the results of the isotope analyses show a depleted stable isotope signature (δ^{13}C) parallel to a^{14}C-DIC activity below detection (< 2 pmC).

Table 11: DIC result and carbon isotopes

Lab. Nr.		415039	415040
Sample		SLA 1	SLA 2
Date		16.04.2024	15.04.2024
Total DIC (steel cylinder)	ccSTP/kg	94.9	200
	mmol/l	4.24	8.92
Isotopes of DIC (steel cylinder)			
δ^{13}C-DIC		-7.5	-9.3
^{14}C-DIC		2.9±0.2	< 2

Dissolved gases and gas isotopes

Dissolved gas composition and gas isotope signatures were determined in the groundwater sample taken in stainless steel cells in flow-through directly at the well heads.

The total dissolved gas concentrations are 62 Nml/L_{H2O} for SLA-1 and 86 Nmol/L_{H2O} for SLA-2 respectively (Table 12). The gases dissolved in the thermal water consist mainly (96 Vol.%) of N_2 and CO_2 in both wells. N_2 is the dominating gas phase (82 Vol.%) in SLA-1 and CO_2 dominates in SLA-2 (50 Vol.%).

Argon was detected in relatively low proportions of 0.85 (SLA-1) and 0.51 (SLA-2) Nml/L. The N_2/Ar volume ratios of 45 (SLA-1) and 62 (SLA-2) are higher than in air saturated water (40) but below air (78), indicating low portions of additional nitrogen source, e.g. from biogenic material. The detected He content of 0.255 Nml/L in the steel container SLA-2 indicates significant He-production by U- and Th-bearing minerals attributed to a prolonged residence time in the underground. In SLA-1 the He-concentration was below detection in the steel container (<0.02 Nml/L).

The dissolved concentration of methane is 0.05 Nml/L (SLA-1) and 0.79 Nml/L (SLA-2) with higher hydrocarbons up to butane present in very low concentrations, ranging between 0.00035 and 0.0046 Nml/L (Table 12). The low $C_1/(C_2+C_3)$ ratios of 35 and 153 indicate a thermogenic provenance of the dissolved methane.

Hydrogen could also be detected in low concentrations of 0.03 Nml/L in SLA-1 and 0.04 Nml/L in SLA-2. Hydrogensulfide could not be detected in both wells.The analyzed isotope signatures of CH_4 in SLA-1 are -41 ‰$_{VPDB}$ for δ^{13}C-CH_4 and -197 ‰$_{VPDB}$ for δ^{2}H-CH_4. In SLA-2, the methane isotopes are enriched in ^{13}C and ^{2}H and show signatures of -21.8 ‰$_{VPDB}$ for δ^{13}C-CH_4 and -116 ‰$_{VPDB}$ for δ^{2}H-CH_4. The carbon isotope signatures of CO_2 (δ^{13}C) are -13.5 ‰VPDB for SLA-1 and --16.3 ‰$_{VPDB}$ for SLA-2 (Table 12). They are depleted in ^{13}C compared to atmospheric CO_2, which indicates an organic provenance or an oxidation of methane.

For comparison, the $\delta^{13}C$ values of dissolved inorganic carbon (DIC) are −7.6 ‰$_{VPDB}$ for SLA-1 and −9.6 ‰$_{VPDB}$ for SLA-2. These values are consistent with a predominantly biogenic carbon source and support the interpretation derived from the CH_4 and CO_2 isotopic compositions. The slightly more negative δ^{13}CDIC in SLA-2 suggests a stronger influence of organic carbon oxidation or methane oxidation processes compared to SLA-1.

For higher hydrocarbons, the $\delta^{13}C$ - values of ethane and propane were also analysed. The carbon isotope signature of ethane ($\delta^{13}C$-C_2H_6) was -33.5 ‰$_{VPDB}$ in SLA-1 and -29.4 ‰$_{VPDB}$ in SLA-2. The carbon isotope signature of propane ($\delta^{13}C$-C_3H_8) is -31.2 ‰$_{VPDB}$ for SLA-1.

As displayed in Figure 37 and Figure 38, the isotope signatures of methane show a thermogenic origin for SLA-1, which is in agreement with other groundwater samples of the region. The isotope signatures of methane dissolved in thermal water of SLA-2 plot along the trend towards more pronounced methane oxidation in the $\delta^{13}C$- vs $\delta^{2}H$-CH_4 diagram according to Whiticar (2020). Nevertheless, the dissolved methane of both waters appears to be influenced by methane oxidation, probably via sulphate reduction, which is more evolved in SLA-2 (Figure 38) This is in agreement with the $\delta^{13}C$-CO_2 values, which are more depleted for CO_2 dissolved in water from SLA-2 (Figure 39).

The correlation of the methane carbon isotope signatures with the $C_1/(C_2+C_3)$ ratios shows that both thermal waters fall within the thermogenic value range. SLA-2 more specifically plots within the range of kerogen type 3 which mostly consists of condensed polyaromatics and stems from terrestrial plants. The values of SLA-2 suggest a higher maturity than SLA-1 and other surrounding groundwater samples.

Table 12: Compilation of dissolved gas and stable gas isotopes dissolved in thermal water of the boreholes SLA-1 and SLA-2

Lab-No.		**415039**	**415040**
		SLA-1	**SLA-2**
		16.04.2024	**15.04.2024**
Physico-chemical onsite parameter			
Temperature at sampling	°C	29.6	39.2
Spec. electr. conductivity (25 °C) at sampling	µS/cm	2730	12700
pH-value at sampling		6.8	6.7
Dissolved oxygen content	mg/l	0.13	0.13
Redox potential (related to NHE)	mV	-20	154
Alkalinity (pH 4.3) onsite	mmol/l	3.0	6.45
Dissolved gas contents			
Hydrogensulfide	Nml/L	< 0.09	< 0.12
Hydrogen	Nml/L	0.029	0.048
Oxygen	Nml/L	< 0.1	< 0.1
Nitrogen	Nml/L	38.6	31.5
Carbon dioxide	Nml/L	22.3	52.9
Helium	Nml/L	< 0.02	0.255
Argon	Nml/L	0.852	0.508
Methane	Nml/L	0.0498	0.7927
Ethane	Nml/L	0.00106	0.00461
Propane	Nml/L	0.00035	0.00056
Butane	Nml/L	0.00035	< 0.00001
Pentane	Nml/L	< 0.00012	< 0.00016
Sum Gases	Nml/L	62	86

Lab-No.		415039	415040
Gas ratios			
$C_1/(C_2+C_3)$		35	153
N_2/Ar		45	62
Stable Isotopes of dissolved gases			
Carbon-13 ($\delta^{13}C$-CO_2)	‰-VPDB	-13.5	-16.3
Carbon-13 ($\delta^{13}C$-CH_4)	‰-VPDB	-41	-21.8
Deuterium ($\delta^{2}H$-CH_4)	‰-VSMOW	-197	-116
Carbon-13 ($\delta^{13}C$-C_2H_6)	‰-VPDB	-33.5	-29.4
Carbon-13 ($\delta^{13}C$-C_3H_8)	‰-VPDB	-31.2	-

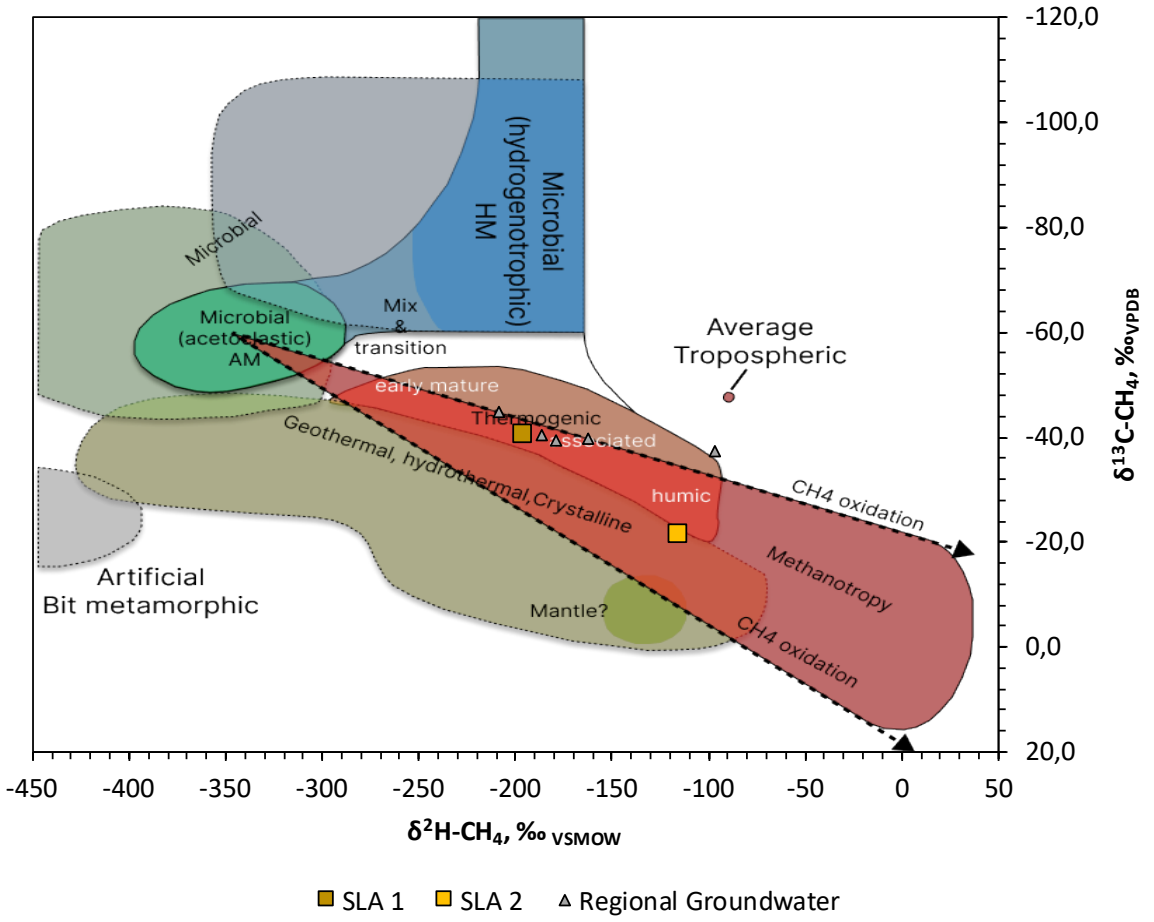


Figure 37: Stable carbon versus stable hydrogen isotope signatures of dissolved methane compared to endmembers and influencing processes according to Whiticar (2020) and Milkov & Ethiope (2018).

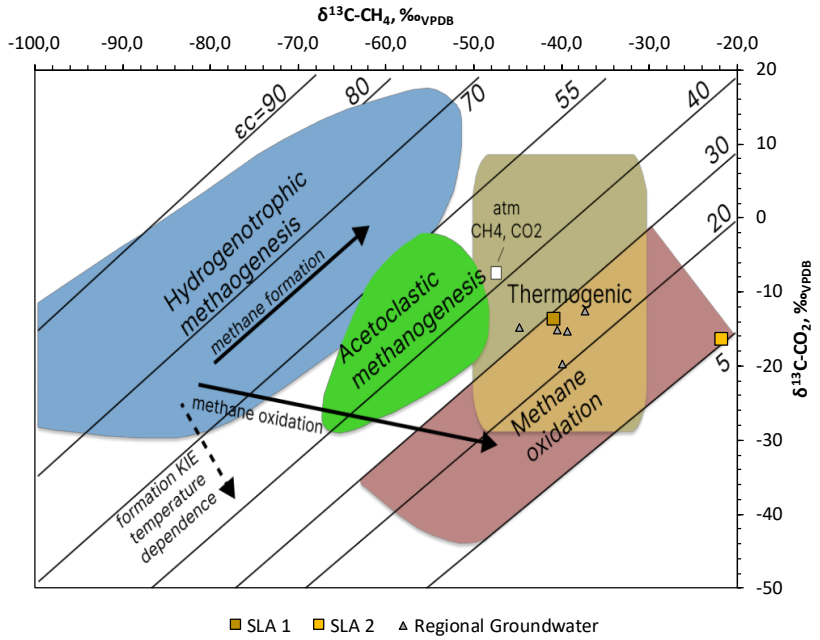


Figure 38: Isotope geochemical characterisation of hydrocarbons and carbon dioxide with isotope fractionation factors lines (εc) according to Whiticar (1999 & 2020).

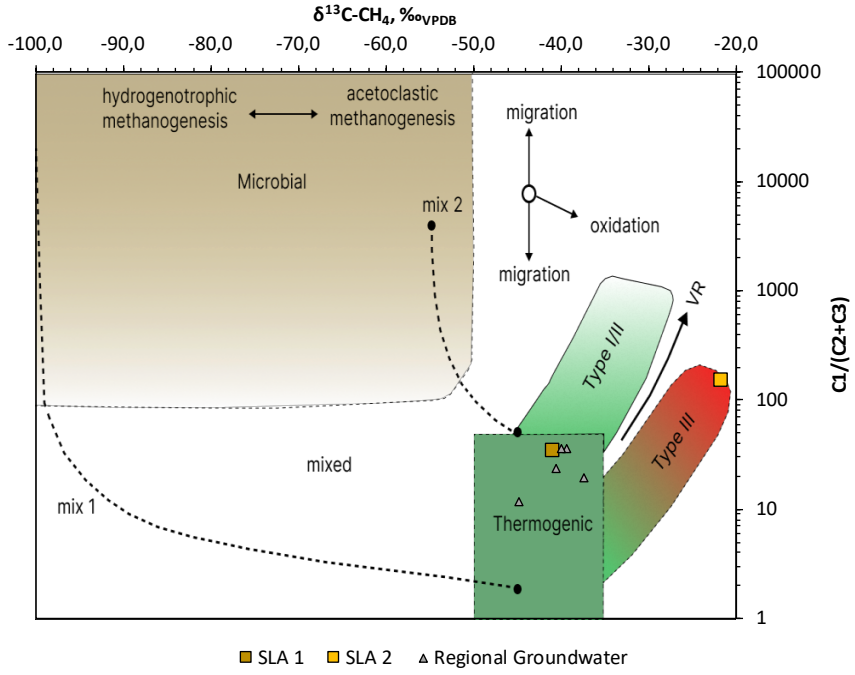


Figure 39: Diagram showing the methane isotopes of the samples examined in relation to the distribution of hydrocarbons.

Ranges for different methane origins wer taken from Bernard (1978), Faber (1987), Whiticar (1994); and Kietäväinen et al. (2017; and references therein). MOR: mid ocean ridge, artificial sources of methane: landfills, agriculture, cattle pastures, industry, etc.

Noble gases concentrations (He, Ne, Ar, Kr, Xe) and noble gas isotope ratios

Noble gas concentrations and noble gas isotope ratios determined on samples taken from borehole SLA-1 and SLA-2 are listed in Table 13. Noble gas concentrations (Ne, Ar, Kr, Xe) measured for SLA-1 suggest a very low recharge temperature of about 2.5 °C inconsistent with climatic conditions in the current Holocene. This fits very well to the low $\delta^{18}O$ value (-12.7‰, Table 10) and suggests that recharge occurred during glacial climatic conditions. In contrast, for SLA-2 the noble gas spectra suggest an elevated recharge temperature of about 21 °C, which is fully consistent with the comparatively high $\delta^{18}O$ value of -9.8 ‰.

For both samples, the noble gas spectra did not provide any indication of a possible gain or loss of Kr during sampling. Hence, the reconstructed ^{81}Kr activities and the subsequently derived ^{81}Kr model ages are unaffected by sampling artefacts and of high quality. Eventually, a mean ^{81}Kr model age of 19'326 years was obtained for SLA-1 (17900 – 20'748 a). For SLA-2, the mean ^{81}Kr model age is 491'000 years (467'000 – 515'000), and hence about 25 times higher.

The large difference in ^{81}Kr model age compares well with the varations in ^{4}He concentrations. For SLA-2, the ^{4}He concentrations is about two orders of magnitude higher than in the SLA-1 sample (Table 13). This difference can be nicely explained by a ^{4}He production rate of ca. 2.5E-7 ccSTP/g in 1'000 years (Figure 40). More details about noble gas concentrations, their isotope ratios, as well as the derived infiltration temperatures and ^{81}Kr model ages are provided in a standalone report by Hydroisotop GmbH (Appendix 1).

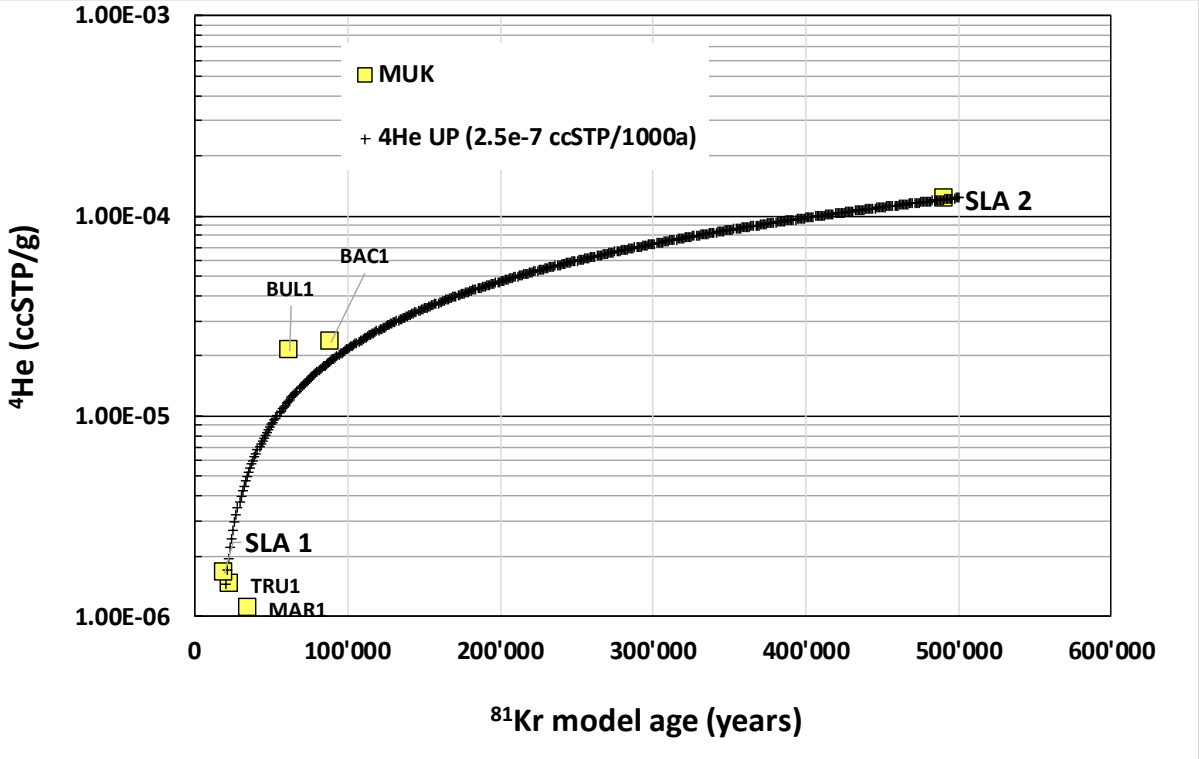


Figure 40: ^{4}He-isotope data of selected Muschelkalk groundwater samples as a function of the ^{81}Kr model age.

An underground production rate of 2.5E-7 ccSTP/1000 years matches both the ^{81}Kr model age and the ^{4}He concentration measured in the two Schlattingen wells.

Table 13: Noble gas concentrations and noble gas isotope ratios determined on samples taken from borehole SLA-1 and SLA-2

Labor-Nr.		**415039**	**415040**
		SLA 1	**SLA 2**
		16.04.2024	**15.04.2024**
		16:00	**16:00**
Argon-37	dpm	0.096	0.045
Argon-39	dpm	37	35
Krypton-81	dpm	94.3	22.6
Krypton-85	dpm	2.36	0.28
Noble gases			
He	NmL/g	1,63E-06	1,20E-04
Ne	NmL/g	4,75E-07	1,28E-08
Ar	NmL/g	6,12E-04	3,48E-04
Kr	NmL/g	1,39E-07	7,50E-08
Xe	NmL/g	2,08E-08	9,35E-09
Nobel gas isotope ratios			
3He	NmL/g	6,31E-13	3,57E-11
4He	NmL/g	1,63E-06	1,20E-04
3He/4He		3,88E-07	2,97E-07
20Ne	NmL/g	4,30E-07	1,16E-08
21Ne	NmL/g	4,40E-08	1,16E-09
22Ne	NmL/g	1,53E-07	4,14E-09
21Ne/22Ne		0,29	0,28
36Ar	NmL/g	1,99E-06	1,08E-06
40Ar	NmL/g	6,12E-04	3,48E-04
40Ar/36Ar		307	322
129Xe	NmL/g	5,48E-09	2,46E-09
130Xe	NmL/g	8,45E-10	3,79E-10
132Xe	NmL/g	5,59E-09	2,51E-09

2.2.3. Temporal evolution of major solutes concentrations and stable water isotopes in the two Schlattingen wells (2018-2025)

A large number of water samples have been analyzed since 2018 (Table 14, Table 15). During this project, water levels and production rates were continuously monitored from the end of October 2023 until July 2025 (Figure 41). Figure 42 and Figure 44 show the temporal evolution of the main ion concentrations in the two wells since 2018. In contrast, Figure 43 and Figure 45 focus on the monitoring period covered by this project and only present main ion concentrations between October 2023 and July 2025.

For the water produced from SLA-1, with a few exceptions, very little variations occurred over the entire monitoring period (Figure 42, Figure 43). A notable exception is the increase in the concentrations of Na and Cl of around 25 and 40 mg/L recorded in March 2022 and a single increase in Na of around 17 mg/L and HCO_3 of 66 mg/L in October 2023 (25.10.2023). For this event, Cl only showed a very slight increase. The electrical conductivity showed increases of around 180 µS/cm and 80 µS/cm for the Na excursions in March 2022 and October 2023, respectively. This indicates that there has been a real increase in salinity. During the October 2023 event, the pumping rates from the two wells were similar (SLA-1: ca. 215 L/min; SLA-1: ca. 260 L/min). No production data is available for the March 2022 event.

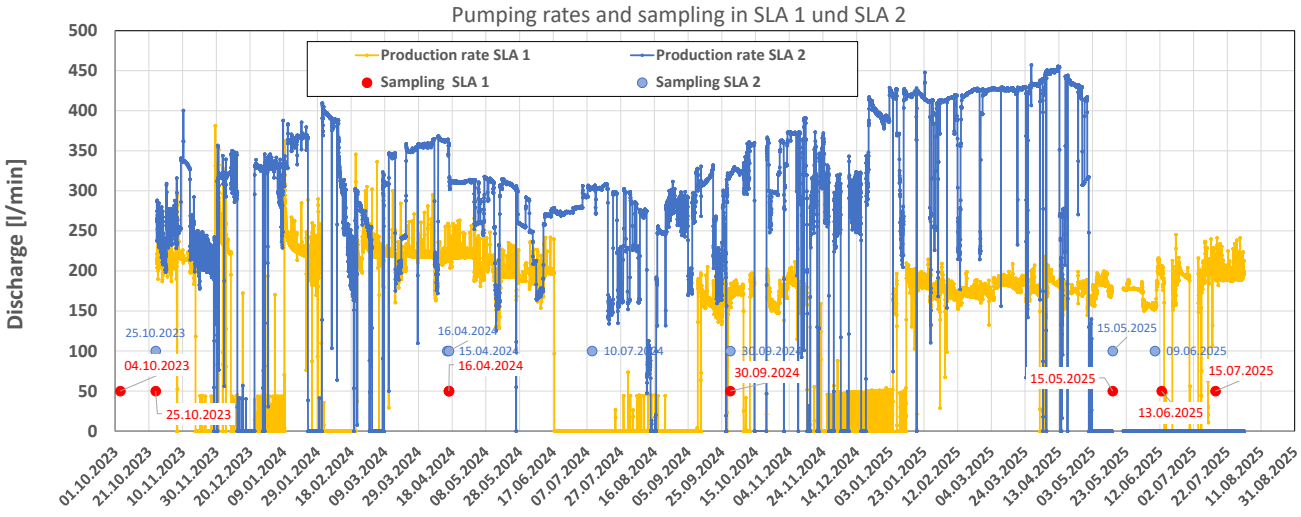


Figure 41: Production rates and sampling at SLA-1 and SLA-1 from October 2023 to July 2025; After May 2025 no production rate data was recorded for SLA-2.

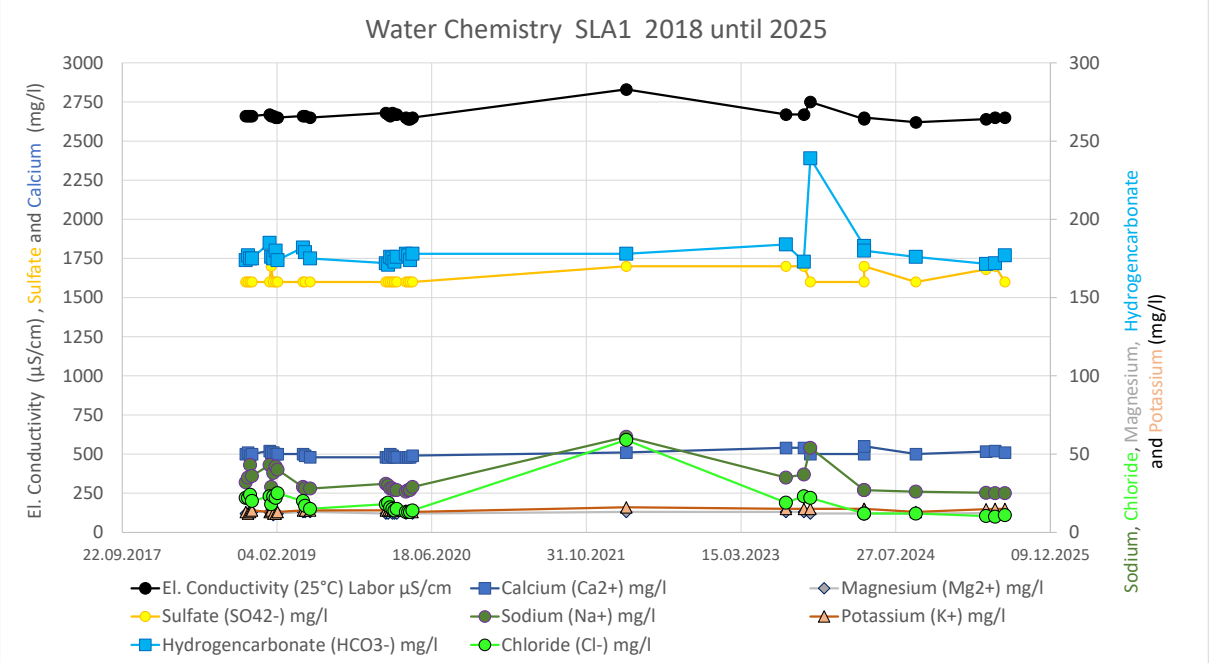


Figure 42: Time series of main dissolved constituents of the groundwater from borehole SLA-1 (time period 2018 to 2025).

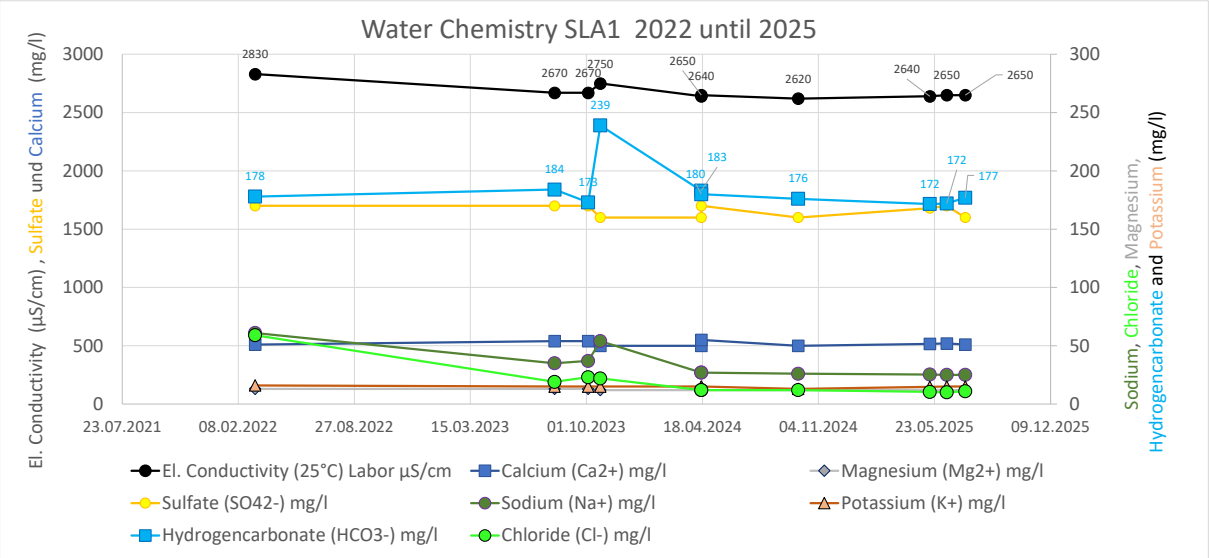


Figure 43: Time series of main dissolved constituents of the groundwater from borehole SLA-1 (time period 2022 to 2025).

The groundwater produced from SLA-2 showed greater variations in main ion concentrations than in SLA-1 (Figure 44, Figure 45, Table 15, Table 16). At the beginning of the monitoring period in 2019, Cl levels decreased to approx. 700 mg/L in 2020 and then increased again to the previous level of around 850 mg/L by mid 2021. In July 2022, the Cl concentration temporally increased to around 900 mg/L accompanied by a simultaneous but unclear variation in the HCO_3 content. During this event, the SO_4 content increased from 6700 to 6900 mg/L. An additional HCO_3 excursion was observed on 25.10.2023, although an associated salinity increase was not apparent because the other water constituents and the electrical conductivity remained at the same levels. Based on the pumping tests carried out in 2024 and 2025, the variations observed in July 2022 can be related to the chemical variations during the starting phase of pumping after a shut-off. In contrast, the causes for the variations in HCO_3 observed in Oct 2023 remain unclear.

Relatively strong concentrations variations were observed in the samples collected from SLA-2 on two consecutive days on April 15 and April 16, 2024, which is likely associated with the decrease of the production rate from 350 to 310 L/min. For Na, Ca and SO_4 such relatively minor change of the production rate caused a concentration increase of 200, 140 and 800 mg/L, respectively (Table 14). On the other hand, the Cl concentration increased only slightly (30 mg/L).

During the current project and hence between fall 2022 and summer 2025, the concentration of most major ions and hence the salinity showed an overall decreasing trend in SLA-2 (Figure 45). This coincides with the almost continuous production from this well at rates of at least 300 L/min (Figure 41). All temporary rebounds (16.4.2024; 30.9.2024; 13.6.2026) coincide with a reduction of the production rate (Figure 41). For June 13, 2025, however, this represents a qualitative statement because the production rate was not recorded due to failure of the discharge sensor. The manual report sheets showed ongoing production in SLA-1 until the 9th June, but it was reported that the discharge decreased due to a leakage in the riser pipe. Despite the overall decreasing trend observed in SLA-2 during this project, the concentration remained nearly constant between January and April 2025, even with continuous production at high rates of 400–450 L/min.

In summary, no clear permanent change in the chemical composition of the groundwaters produced from the two wells were observed since 2018. For SLA-1, the composition was almost invariant. In contrast, the concentrations of major solutes in the SLA-2 groundwater significantly decreased with ongoing production until new steady state concentration levels were reached. These changes most likely represent a change of the mixing proportions of different groundwater components caused by the production from the well. Once the production rate was reduced or even ceased, however, the concentrations returned to higher levels reflecting a hydraulically less disturbed state of the reservoir.

Until now there are no clear indications that the production of water from one well affects the concentrations of major solutes in the other well.

It should be noted that observed variations in the chemical inventory may reflect the chemical stimulation of the borehole carried out right after drilling the two wells (Frieg et al., 2015; Frieg, 2015). Since these stimulation measures were implemented more than 10 years ago, and given that both wells have been extensively used for thermal water production (Figure 41), this scenario is considered unlikely.

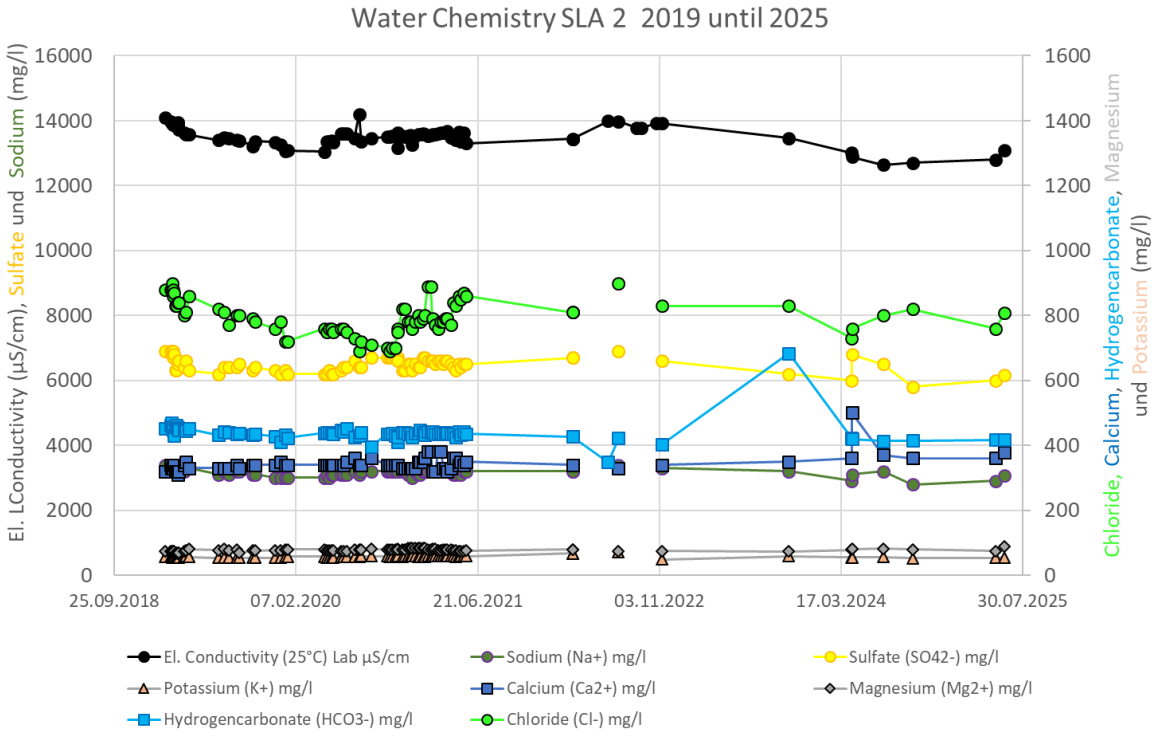


Figure 44: Time series of main dissolved constituents of the groundwater from borehole SLA-1 (time period 2019 to 2025).

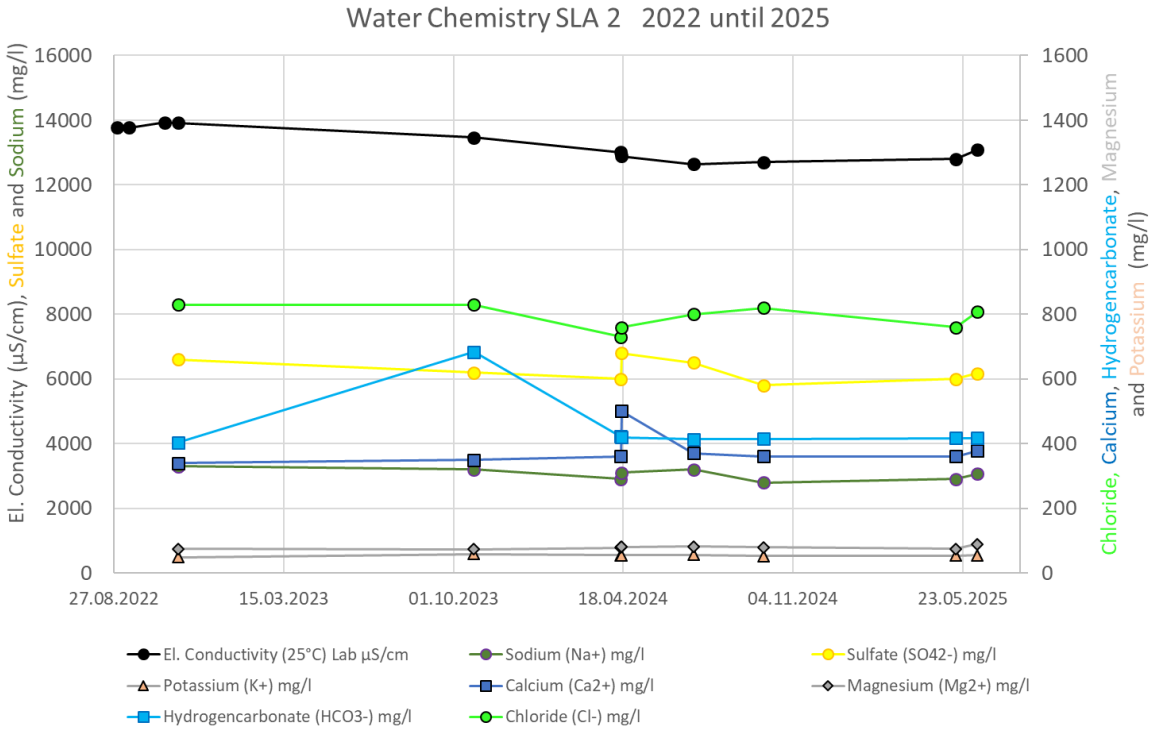


Figure 45: Time series of main dissolved constituents of the groundwater from borehole SLA-1 (time period 2022 to 2025).

Table 14: Variations in major solutes concentrations in SLA-1 waters samples collected on two consecutive days on April 15 and 16, 2024.

Lab. #.		415029	415039		415040	415030
		SLA-1	SLA-1		SLA-1	SLA-1
		15.04.2024	16.04.2024		15.04.2024	16.04.2024
		15:00	16:00		16:00	16:30
Color		colorless	colorless		colorless	colorless
Visual turbidity		clear	clear		clear	clear
Temperature at sampling	°C	26,1	29,6		39,2	25,4
Specific electrical conductivity (25°C) on site	µS/cm	2660	2730		12700	12920
Specific electrical conductivity (25°C) lab	µS/cm	2640	2650		13010	12890
pH value (tgem) on site		6,8	6,8		6,7	6,9
pH value laboratory		6,9	6,9		6,9	6,9
Dissolved oxygen content	mg/l	< 0,1	n.b.		n.b.	< 0,1
Redox potential (relative to NHE)	mV	n.b.	-20		154	n.b.
Acid capacity (pH 4.3) lab	mmol/l	3	2,95		n.b.	n.b.
Sodium (Na^+)	mg/l	27	27		2900	3100
Potassium (K^+)	mg/l	15	15		55	55
Calcium (Ca^{2+})	mg/l	500	550		360	500
Magnesium (Mg^{2+})	mg/l	120	120		78	80
Hydrogen carbonate (HCO_3^-)	mg/l	183	180		422	420
Chloride (Cl^-)	mg/l	12	12		730	760
Sulfate (SO_4^{2-})	mg/l	1600	1700		6000	6800

Table 15: Analyses of groundwater from borehole SLA-1 taken between 2022 and 2025

Lab.#		381052	403849	407328	407330	415029	415039	422936	434187	436950	436951
		SLA 1	SLA 1	SLA 1	SLA 1	SLA 1	SLA 1	SLA 1n. WT	SLA 1	SLA 1 n. WT	SLA 1 n. WT
		09.03.22	07.08.23	25.10.23	04.10.23	16.04.24	16.04.24	30.09.24	15.05.25	13.06.25	15.07.25
		16:20	11:30	14:30	8:30	n.b.	16:00	14:00	8:30	n.b.	n.b.
Color		colorless	n.b.	n.b.	n.b.	colorless	colorless	n.b.	n.b.	n.b.	n.b.
Visual turbidity		clear	n.b.	n.b.	n.b.	clear	clear	n.b.	n.b.	n.b.	n.b.
Temperature at sampling	°C	32,3	n.b.	n.b.	n.b.	26,1	29,6	n.b.	n.b.	n.b.	n.b.
Specific electrical conductivity (25°C) on site	µS/cm	2830	n.b.	n.b.	n.b.	2660	2730	n.b.	n.b.	n.b.	n.b.
Specific electrical conductivity (25°C) lab	µS/cm	2830	2670	2750	2670	2640	2650	2620	2640	2650	2650
pH value (tgem) on site		6,7	n.b.	n.b.	n.b.	6,8	6,8	n.b.	n.b.	n.b.	n.b.
pH value laboratory		6,9	7,0	6,9	7,0	6,9	6,9	7,0	6,9	6,9	6,9
Dissolved oxygen content	mg/l	0,1	n.b.	n.b.	n.b.	< 0,1	n.b.	n.b.	n.b.	n.b.	n.b.
Redox potential (relative to NHE)	mV	n.b.	n.b.	n.b.	n.b.	n.b.	-20	n.b.	n.b.	n.b.	n.b.
Acid capacity (pH 4.3) lab	mmol/l	2,92	3,01	3,92	2,83	3	2,95	2,88	2,89	2,81	2,91
Sodium (Na^+)	mg/l	61	35	54	37	27	27	26	25	25	25
Potassium (K^+)	mg/l	16	15	15	15	15	15	13	14	15	15
Calcium (Ca^{2+})	mg/l	510	540	500	540	500	550	500	510	520	510
Magnesium (Mg^{2+})	mg/l	130	130	120	130	120	120	120	110	120	120
Hydrogen carbonate (HCO_3^-)	mg/l	178	184	239	173	183	180	176	176	172	177
Chloride (Cl^-)	mg/l	59	19	22	23	12	12	12	11	10	11
Sulfate (SO_4^{2-})	mg/l	1700	1700	1600	1700	1600	1700	1600	1600	1700	1600
Nitrate (NO_3^-)	mg/l	<0,5	<0,5	<0,5	<0,02	<0,2	< 0,2	< 0,2	< 0,2	< 0,2	< 0,2
Ion balance error	%	1,75	0,64	0,55	0,97	1,28	n.b.	0,43	0,39	2,37	1,81
Bromide (Br^-)	mg/l	n.b.	n.b.	< 0,5	n.b.	< 0,1	n.b.	< 0,1	n.b.	n.b.	n.b.
Fluoride (F^-)	mg/l	n.b.	n.b.	3,6	3,1	2,6	n.b.	5,2	n.b.	3,2	3,1
Lithium (Li)	mg/l	n.b.	n.b.	0,19	n.b.	n.b.	n.b.	0,15	0,16	0,18	0,18
Strontium (Sr)	mg/l	n.b.	n.b.	n.b.	n.b.	n.b.	n.b.	3	6,5	n.b.	n.b.
Total sulfide (H_2S, HS^-, S_2^-)	mg/l	n.b.	n.b.	n.b.	n.b.	n.b.	n.b.	2,1	n.b.	n.b.	2,4
Arsenic	mg/l	2,56	2,89	2,8	n.b.	3,2	n.b.	1,29	n.b.	n.b.	4,91
Total iron	mg/l	5,7	10,6	3,8	n.b.	3,9	n.b.	0,2	n.b.	n.b.	0,38
Manganese total	mg/l	n.b.	0,16	0,3	n.b.	0,37	n.b.	n.b.	n.b.	n.b.	n.b.
Oxygen-18 ($\delta^{18}O$-H_2O)	‰	n.b.	-12,47	-12,44	-12,53	n.b.	-12,68	-12,57	-12,53	-12,43	-12,64
Deuterium (δ^2H-H_2O)	‰	n.b.	-90,5	-90,2	-90,3	n.b.	-91,2	-91,4	-90,7	-90	-91
Deuterium excess	‰	n.b.	9,26	9,32	9,94	n.b.	10,24	9,16	9,54	9,44	10,12

Table 16: Analyses of groundwater from borehole SLA-2 taken between 2022 and 2025

Lab. No.		381053	386362	386275	388072	389299	391203	392005	407329	415040	415030	419451	422937	434188	436949
		SLA2 nWT	SLA2	SLA 2	SLA2	SLA2	SLA2	SLA 2	SLA2	SLA 2	SLA 2	SLA2 nWT	SLA2 nWT	SLA 2	SLA 2 nWT
		09.03. 2022	15.06. 2022	13.07. 2022	31.08. 2022	14.09. 2022	26.10. 2022	11.11. 2022	25.10. 2023	15.04. 2024	16.04. 2024	10.07. 2024	30.09. 2024	15.05. 2025	09.06. 2025
time		17:35							15:00	16:00		15:00	14:00	9:10	23:00
Color		n.b.	n.b.	n.b.	n.b.	n.b.	n.b.	n.b.	n.b.	farblos	farblos	n.b.	n.b.		n.b.
Visual turbidity		n.b.	n.b.	n.b.	n.b.	n.b.	n.b.	n.b.	n.b.	klar	klar	n.b.	n.b.		n.b.
Temperature at sampling	°C	n.b.	n.b.	n.b.	n.b.	n.b.	n.b.	n.b.	n.b.	39.2	25.4	n.b.	n.b.		n.b.
Specific electrical conductivity (25°C) on site	µS/cm	13540	n.b.	n.b.	n.b.	n.b.	n.b.	n.b.	n.b.	12700	12920	n.b.	n.b.		n.b.
Specific electrical conductivity (25°C) lab	µS/cm	13440	13990	13980	13780	13770	13930	13920	13460	13010	12890	12640	12700	12800	13080
pH value (tgem) on site		6.9	n.b.	n.b.	n.b.	n.b.	n.b.	n.b.	n.b.	6.7	6.9	n.b.	n.b.		n.b.
pH value laboratory		7.1	7.7	7.3	7.1	7.5	7.7	8.1	6.7	6.9	6.9	7	7.2	7	7.2
Dissolved oxygen content	mg/l	0.1	n.b.	n.b.	n.b.	n.b.	n.b.	n.b.	n.b.	n.b.	< 0.1	n.b.	n.b.	n.b.	n.b.
Redox potential (relative to NHE)	mV	62	n.b.	n.b.	n.b.	n.b.	n.b.	n.b.	n.b.	154	n.b.	n.b.	n.b.	n.b.	n.b.
Acid capacity (pH 4.3) lab	mmol/l	7	5.7	6.92	n.b.	n.b.	n.b.	6.6	11.2	n.b.	n.b.	6.77	6.78	6.84	6.84
Sodium (Na^+)	mg/l	3200	n.b.	3400	n.b.	n.b.	n.b.	3300	3200	2900	3100	3200	2800	2900	3100
Potassium (K^+)	mg/l	67	n.b.	72	n.b.	n.b.	n.b.	49	58	55	55	56	52	53	55
Calcium (Ca^{2+})	mg/l	340	n.b.	330	n.b.	n.b.	n.b.	340	350	360	500	370	360	360	380
Magnesium (Mg^{2+})	mg/l	79	n.b.	73	n.b.	n.b.	n.b.	74	73	78	80	82	79	75	90
Hydrogen carbonate (HCO_3^-)	mg/l	n.b.	n.b.	n.b.	n.b.	n.b.	n.b.	n.b.	n.b.	n.b.	n.b.	3.94	4.3		n.b.
Chloride (Cl^-)	mg/l	427	348	422	n.b.	n.b.	n.b.	403	683	422	420	413	414	417	417
Sulfate (SO_4^{2-})	mg/l	810	n.b.	900	n.b.	n.b.	n.b.	830	830	730	760	800	820	760	810
Nitrate (NO_3^-)	mg/l	6700	n.b.	6900	n.b.	n.b.	n.b.	6600	6200	6000	6800	6500	5800	6000	6200
Ion balance error	mg/l	< 0.5	n.b.	1.5	n.b.	n.b.	n.b.	15	< 0.5	n.b.	< 1	< 0.5	< 0.5	< 0.2	< 0.2
Bromide (Br^-)	‰	1.74	n.b.	2.14	n.b.	n.b.	n.b.	0.34	1.71	n.b.	0.97	0.03	0.99	1.44	1.85
Fluoride (F^-)	mg/l	n.b.	n.b.	n.b.	n.b.	n.b.	n.b.	n.b.	1.2	n.b.	1.3	1.3	1.1	n.b.	n.b.
Lithium (Li)	mg/l	n.b.	n.b.	2.1	n.b.	n.b.	n.b.	n.b.	1.9	n.b.	1.8	1.4	3.2	n.b.	1.7
Strontium (Sr)	mg/l	n.b.	n.b.	n.b.	n.b.	n.b.	n.b.	n.b.	3.5	n.b.	n.b.	3.4	2.3	2.23	2.56
Total sulfide (H_2S, HS^-, S^{2-})	mg/l	n.b.	n.b.	n.b.	n.b.	n.b.	n.b.	n.b.	n.b.	n.b.	n.b.	0.013	0.19	0.5	n.b.
Arsenic	mg/l	0.157	< 0.05	< 0.075	< 0.05	< 0.025	< 0.025	0.009	0.083	n.b.	0.25	4.82	0.72	n.b.	n.b.
Total iron	mg/l	7.86	n.b.	2.01	n.b.	n.b.	n.b.	0.01	11.6	n.b.	4.12	0.4	0.14	n.b.	n.b.
Manganese total	mg/l	n.b.	n.b.	0.05	n.b.	n.b.	n.b.	< 0.01	0.78	n.b.	0.27	n.b.	n.b.	n.b.	n.b.
Oxygen-18 ($\delta^{18}O$-H_2O)	‰	n.b.	n.b.	n.b.	n.b.	n.b.	n.b.	n.b.	-9.53	-9.79	n.b.	-9.63	-9.76	-9.78	-9.63
Deuterium (δ^2H-H_2O)	‰	n.b.	n.b.	n.b.	n.b.	n.b.	n.b.	n.b.	-61.4	-63.7	n.b.	-63.2	-64.3	-63.8	-62.4
Deuterium excess	‰	n.b.	n.b.	n.b.	n.b.	n.b.	n.b.	n.b.	14.84	14.62	n.b.	13.84	13.78	14.44	14.64

Temporal evolution of stable isotopes of water

Between August 2023 and July 2025, $\delta^{18}O\text{-}H_2O$ values of water produced from SLA-1 remained almost constant, ranging from -12.43 and -12.68 $‰_{VSMOW}$ only (Table 17). Corresponding $\delta^{2}H\text{-}H_2O$ values showed the same trend and varied slightly between -90.0 and -91.0 $‰_{VSMOW}$. In contrast, since 2019, $\delta^{18}O\text{-}H_2O$ values of water produced from SLA-2 became gradually more depleted in heavy isotopes over time (Table 17). $\delta^{18}O$ values ranged from -9.07 to -9.79 $‰_{VSMOW}$, while $\delta^{2}H$ values were between -58.4 and -64.5 $‰_{VSMOW}$. These temporal changes in isotopic composition likely reflect the mixed origin of SLA-2, consistent with the hydrochemical evidence for varying contributions from different groundwater components (see section above).

The stable isotope data from SLA-1 plot directly on the Global Meteoric Water Line (GMWL), indicating a meteoric origin that was likely recharged under cooler climatic conditions. In contrast, SLA-2 signatures are heavier consistent with recharge under warmer, moderate climate conditions. They plot slightly above the GMWL (Figure 46).This can be caused by long-term interaction with dissolved gases like CH_4 and/or H_2S.

Table 17: Overview of $\delta^{18}O\text{-}H_2O$ and $\delta^{2}H\text{-}H2O$ values from SLA-1 and SLA-2

	Date	**Lab-No.**	**$\delta^{18}O - H_2O$ [$‰_{VSMOW}$]**	**$\delta^{2}H - H_2O$ [$‰_{VSMOW}$]**
SLA-1	07.08.2023	403849	-12.47	-90.5
	25.10.2023	407328	-12.44	-90.2
	04.10.2023	407330	-12.53	-90.3
	16.04.2024	415039	-12.68	-91.2
	30.09.2024	422936	-12.57	-91.4
	27.11.2024	426323	-12.58	-90.6
	15.05.2025	434187	-12.53	-90.7
	13.06.2025	436950	-12.43	-90.0
	15.07.2025	436951	-12.64	-91.0
SLA-1	13.02.2019	323579	-9.07	-58.4
	04.03.2019	324286	-9.19	-59.1
	08.03.2019	324338	-9.24	-59.2
	03.04.2019	325367	-9.42	-60.0
	25.10.2023	407329	-9.53	-61.4
	15.04.2024	415040	-9.79	-63.7
	10.07.2024	419451	-9.63	-63.2
	30.09.2024	422937	-9.76	-64.3
	27.11.2024	426324	-9.79	-64.5
	15.05.2025	434188	-9.78	-63.8
	09.06.2025	436949	-9.63	-62.4

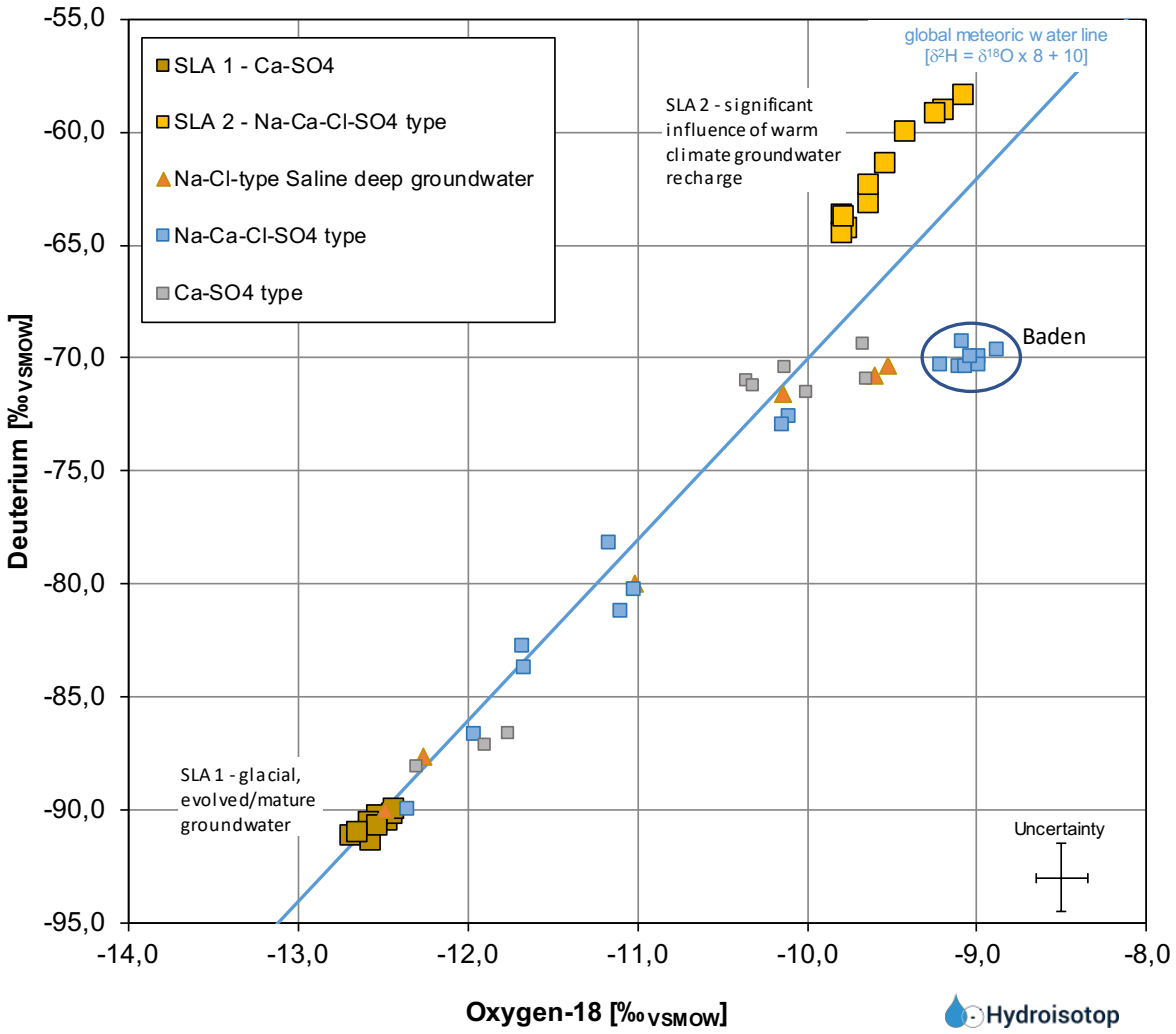


Figure 46: Diagram presenting the results of the stable water isotopes for SLA-1 and SLA-2.

The global meteoric water line is presented as well as isotope data from other groundwater samples of the region categorized according to their main water-type.

2.2.4. Results of the geophysical borehole inspections

The geophysical and visual inspection of the borehole SLA-2 provided a good opportunity to evaluate and assess potential processes like corrosion and the formation of mineral precipitates. The borehole SLA-2 has been in operation since 2014 with variable production rates. Hence, the conducted inspection provides long-term information, which is valuable for the material design of future projects.

The results are presented in an internal report and can be summarised as follows:

- Corrosion is only minor, leading to a residual pipe thickness of 80 – 90% of the initial thickness.
- Along the pipe light to dark grey, thin, planar, non-crystalline precipitations could be observed.
- At the transition between the 9 5/8'' and 7'' pipe at 443 m dhl massive, light grey, crystalline mineral precipitations were observed, which minimize the inner diameter of the 7'' pipe to about 50% of its original volume (Figure 47).

The formation of such massive mineral precipitations is a severe thread for the operation of the borehole. A prerequisite for the evaluation and assessment of the processes is a mineralogical identification of the precipitations and a hydrochemical modelling to understand the formation processes. Because the solids in the borehole cannot be sampled, it was attempted to find hints about their consistency by investigating residues caught in the surface filters, installed before heat exchanger at the SLA-2 geothermal system. The investigated filter residues mainly consisted of thin, platey, amorphous, Fe-sulphides with minor Ca-phases.

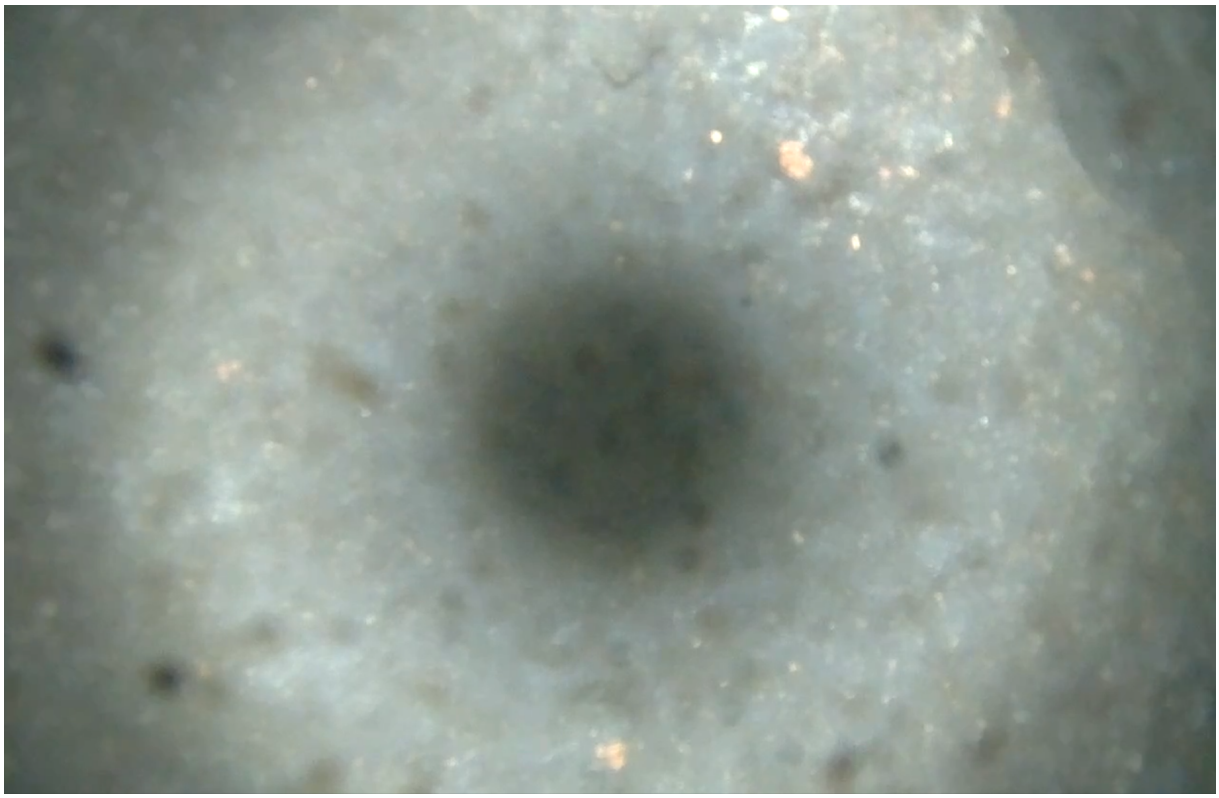


Figure 47: Excerpt from the visual camera survey of borehole SLA-2 showing the crystalline precipitations at ca. 440 m dhl.

2.2.5. Hydrogeochemistry of the Muschelkalk Aquifer in Northern Switzerland and adjacent areas in Germany

Data source

To put the hydrogeochemical composition of the groundwaters collected from the Schlattingen wells (Section 2.2.2 and 2.2.3) in the regional context of Northern Switzerland and adjacent areas in Germany, we have synthesized the chemical and isotopic composition of shallow and deep Muschelkalk groundwaters in this region. For our assessment, we used data collected since the 1960's and reported in Waber & Traber (2022) as well as analyses performed during the most recent Nagra deep drilling campaign (Nagra, 2024). The locations with chemical analyses span a rather large region from Pfaffnau in the SW, Riehen in the NW, to Fronhofen in the NE (Figure 48).

To streamline the discussion, we have grouped the different groundwater samples according to the so called *general water types* defined by Waber & Traber (2022). Their definition considers all cations and anions with relative abundances exceeding 30 meq-%. If among a group of water samples two cations or anions show abundances above 30 meq-% with variable order, rectangular brackets are used between the corresponding ions. For the compiled Muschelkalk groundwater samples, this approach results in the five following general water types: (i) Ca-HCO_3, (ii) Ca-[Mg]-[HCO_3/SO_4], (iii) Ca-SO_4 , (iv) [Na/Ca]-[SO_4/Cl], and (v) Na-Cl.

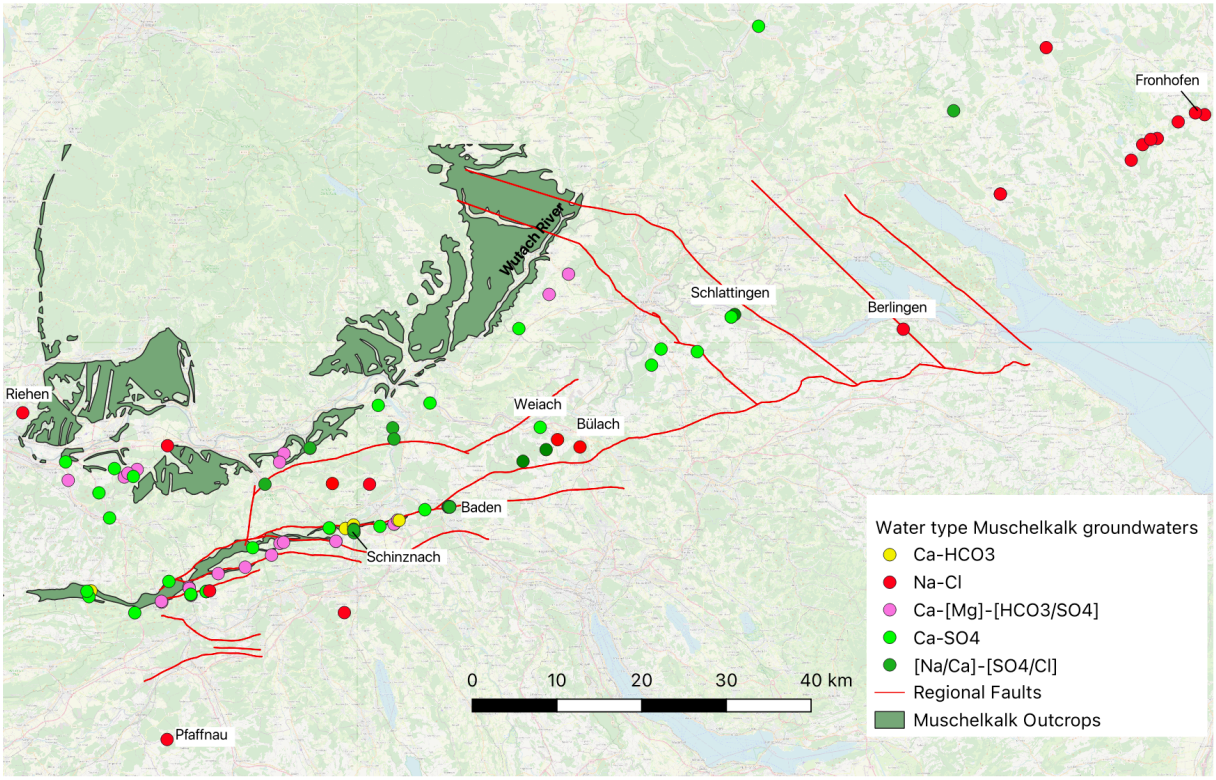


Figure 48: Map showing the locations of shallow and deep Muschelkalk groundwater samples in Northern Switzerland and adjacent areas in Germany for which chemical and isotopic analyses are available (Waber et al., 2022; Nagra, 2024).

Note: The color code refers to the general water type. Besides Schlattingen, sampling locations are only provided for a few reference sites showing distinct compositions as discussed below.

Hydrogeochemical characterization and groundwater origin

The compiled groundwater samples display large variations in their composition as manifested by the Piper plot in Figure 49, illustrating the relative abundance of major cations and anions. Likewise, they show very large variations in their salinity, with concentrations of total dissolved solid concentrations (TDS) ranging from 0.5 to 156 g/L (Figure 50a). Groundwaters with TDS concentrations above 8 g/L are of the Na-Cl type. If the TDS concentration is between 2 and 8 g/L, groundwaters are of the Ca-SO_4 or [Na/Ca]-[SO_4/Cl] type. The latter for instance refer to the groundwaters sampled from the thermal baths at Baden and Schinznach, both containing a component from the crystalline basement (Vuataz, 1982). Groundwaters with TDS concentrations below 2 g/L are of the Ca-HCO_3 or Ca-[Mg]-[HCO_3/SO_4] type.

With a few exceptions (e.g. highly saline Na-Cl waters from North of Lake Constance, SLA-2), all Muschelkalk groundwaters plot on or close to the 1:1 correlation between the concentrations of alkaline earth metal cations (Ca^{2+} + Mg^{2+}) and SO_4^{2-} (Figure 50b). This indicates that Ca and SO_4 are mainly inherited from the dissolution of gypsum in the recharge areas and anhydrite at greater depth in the aquifer, resulting in a typical dedolomitisation scenario where gypsum/anhydrite and dolomite ($CaMg(CO_3)_2$) dissolve while calcite precipitates. Consequently, the Muschelkalk groundwaters are at, or close to, saturation with respect to calcite, dolomite and gypsum/anhydrite.

In terms of stable water isotopes, with the exception of highly saline Na-Cl waters collected north of Lake Constance, all Muschelkalk groundwaters plot on, or very close to the GMWL, confirming their meteoric origin (Figure 50c). However, the actual $\delta^{18}O$ and $\delta^{2}H$ values show rather strong variations. This demonstrates that recharge occurred during different climatic conditions. Groundwater with $\delta^{18}O$ values below -11‰ formed under colder climatic conditions than today, whereas values between -11 and -8.5 ‰ are indicative for recharge under similar climatic conditions than today. The variable recharge conditions suggest a large range in subsurface residence time, which is well reflected by ^{3}H and ^{14}C activities of Muschelkalk groundwaters. The Ca-HCO_3 and Ca-[Mg]-[HCO_3/SO_4] type groundwaters are ^{3}H-bearing and show ^{14}C activities generally above 15 pmC (Figure 50c), suggesting that meteoric water recharge occurred in the recent past. In contrast, most of the Ca-SO_4, [Na/Ca]-[SO_4/Cl] and Na-Cl type groundwaters show ^{14}C activities below 15 pmC. This indicates that for groundwater of these types showing $\delta^{18}O$ values below -11‰, meteoric water recharge occurred during a cold glacial period, most likely during the last glacial cycle (i.e. 11.5 – 115 ka ago; Schlüchter et al. 2021). In contrast, for Ca-SO_4, [Na/Ca]-[SO_4/Cl] and Na-Cl type groundwaters with $\delta^{18}O$ values above -11‰, meteoric water recharge occurred in an interglacial period such as the current Holocene (<11.5 ka ago).

The groundwater composition in the Muschelkalk aquifer in the two Schlattingen wells shows very large variations despite that the horizontal distance between the two sampling locations is only about 1200 m. The groundwater in the SLA-1 well is of moderate salinity (TDS: 2.6 g/L), Ca-SO_4 type and displays a cold climatic recharge signature (Figure 50). It compares very well with other Ca-SO_4 type Muschelkalk groundwaters in Northern Switzerland. In contrast, the groundwater in the SLA-2 borehole is of much higher salinity (TDS: 10.5 g/L), [Na/Ca]-[SO_4/Cl] type and stable isotopes indicate recharge conditions similar than today. Moreover, the SLA-2 groundwater is shifted to the right of the 1:1 correlation between alkaline earth metal cations (Ca^{2+} + Mg^{2+}) and SO_4^{2-} (Figure 50b), indicating an excess of SO_4 or depletion of Ca with respect to the anhydrite-dolomite-calcite equilibrium. The piper plot (Figure 49) as well as the various cross plots (Figure 50) suggest that the groundwater at SLA-2 is related to other [Na/Ca]-[SO_4/Cl] type as well as Na-Cl Muschelkalk groundwaters in Northern Switzerland such as the thermal baths at Baden and Schinznach, and the groundwater produced at the geothermal heat plant at Riehen. Based on these plots, there is also a similarity with [Na/Ca]-[SO_4/Cl] and Na-Cl type groundwaters from deeper units such as the Crystalline Basement (CB), Permokarboniferous (PK) and Buntsandstein (Bsst) aquifers. Besides the strong contrast in their chemical and stable isotope composition, the two samples from Schlattingen also show very different ^{81}Kr model ages (19 ka vs. 490 ky, Figure 40), demonstrating that the two wells produce from completely separated hydrological compartments of the Muschelkalk aquifer.

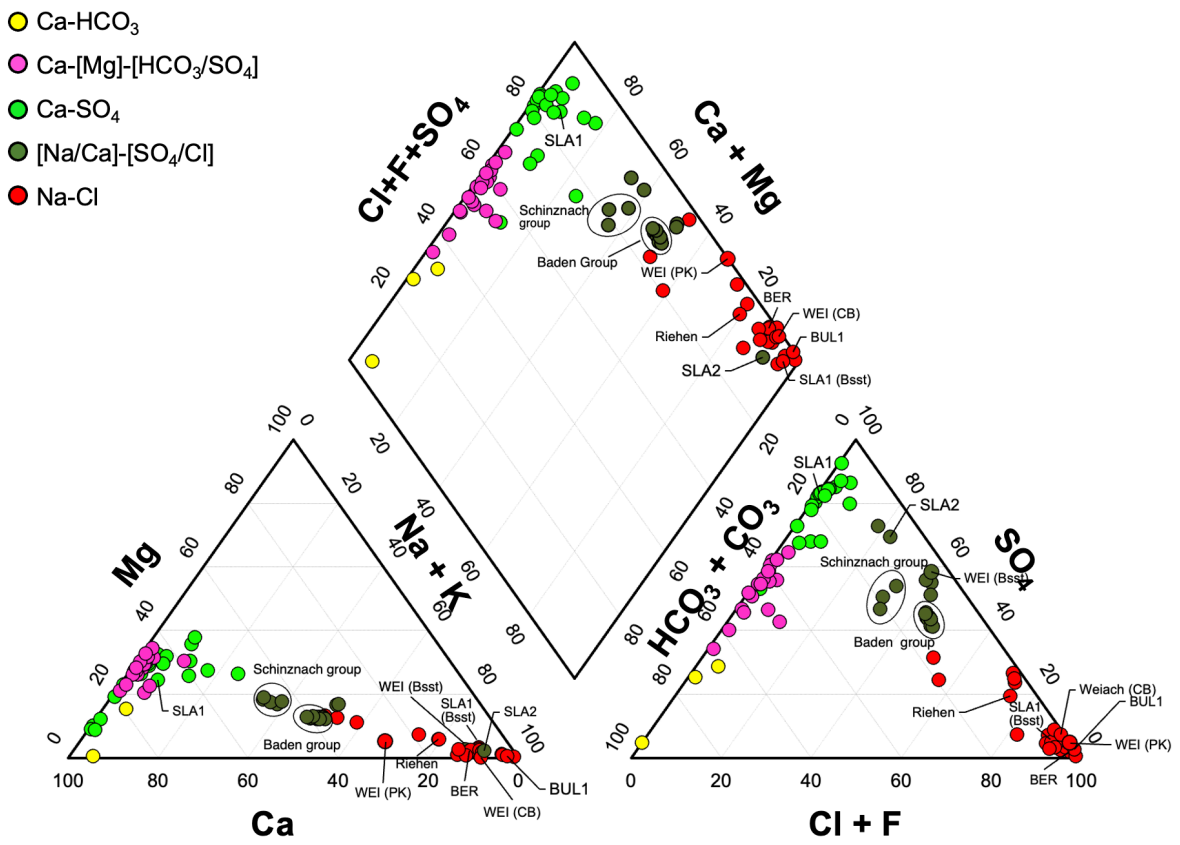


Figure 49: Piper plot illustrating the composition of groundwaters collected from the Muschelkalk aquifer in Northern Switzerland and adjacent areas with respect to major cations and anions. Modified from Waber & Traber (2022) and supplemented with data for the two Schlattingen wells (Table 7).

Note: The color code refers to the general water type. Besides the samples from Schlattingen (SLA-1, SLA-2), sampling locations are only provided for a few reference sites. These include the geothermal heat plant at Riehen and the thermal baths at Schinznach and Baden showing similarities with the Schlattingen 2 sample, Bülach (BUL1) where an extreme salinity of 156 g/L was observed, and Berlingen known for its high Li concentration of 144 mg/L. To illustrate the similarity of [Na/Ca]-[SO_4/Cl] and Na-Cl type groundwaters with those collected from deeper units such as the Crystalline Basement (CR), Permokarboniferous (PK), and Buntsandstein (Bsst), samples collected from these three aquifers in the nearby Weiach well (WEI) are shown in a)-c) as well. Also plotted is the groundwater collected from the Buntsandstein aquifer at SLA-1.

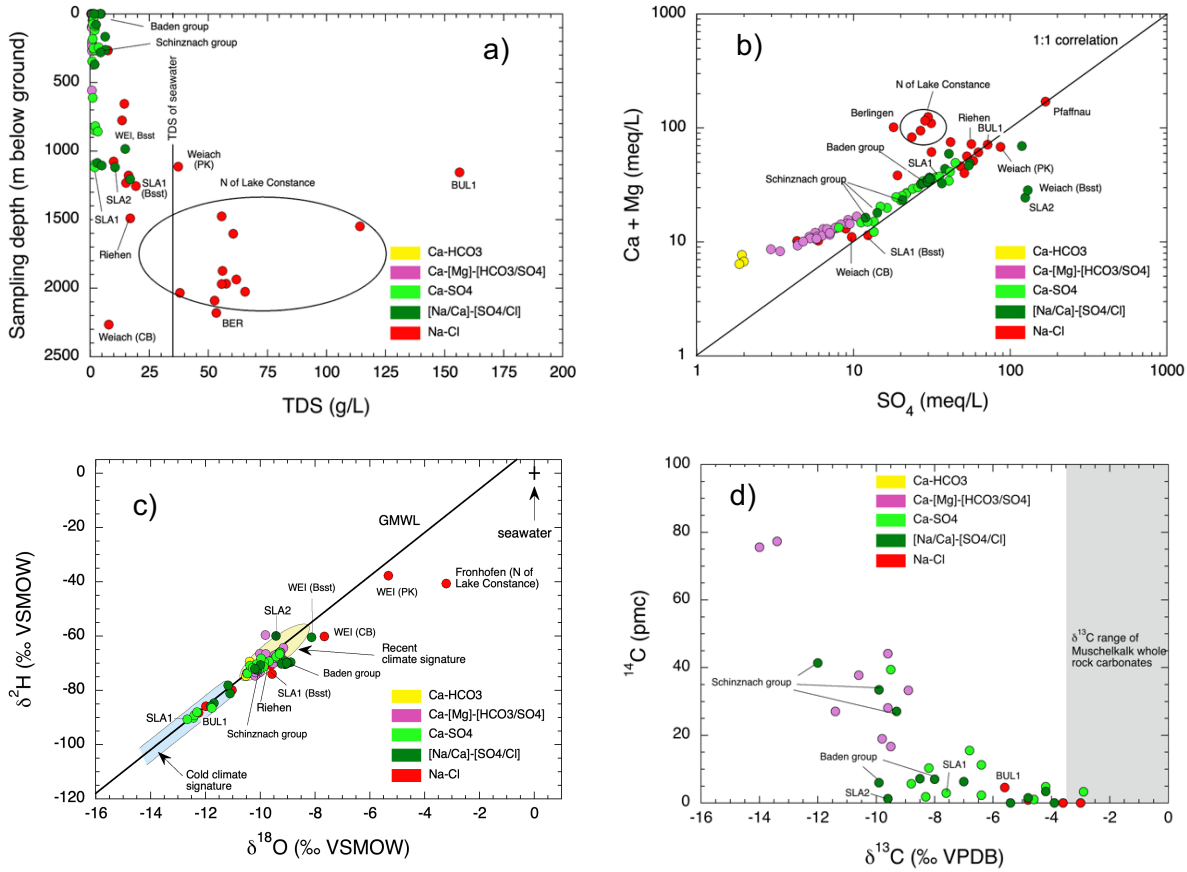


Figure 50: Cross plots illustrating the behavior of key hydrogeochemical parameters in groundwaters collected from the Muschelkalk aquifer in Northern Switzerland and adjacent areas. All plots are taken from Nagra (2024) and supplemented with data for the two Schlattingen wells (Table 7, Table 10, Table 11).

Note: The color code refers to the general water type. Besides the samples from Schlattingen (SLA-1, SLA-2), sampling locations are only provided for a few reference sites. These include the geothermal heat plant at Riehen and the thermal baths at Schinznach and Baden showing similarities with the groundwater at Schlattingen 2, Bülach (BUL1) where an extreme salinity of 156 g/L was observed, and Berlingen known for its high Li concentration of 144 mg/L. In addition, for a) and b) the samples from the hydrocarbon wells north of Lake Constance in Germany are highlighted. Additional locations are provided for a few outliers (e.g. Pfaffnau in b) and Fronhofen in c)). To illustrate the similarity of [Na/Ca]-[SO_4/Cl] and Na-Cl type groundwaters with those collected from deeper units such as the Crystalline Basement (CR), Permokarboniferous (PK), and Buntsandstein (Bsst), samples collected from these three aquifers in the nearby Weiach well (WEI) are shown in a)-c) as well. Also plotted is the groundwater collected from the Buntsandstein aquifer at SLA-1.

Regional groundwater evolution

The different hydrogeochemical signatures of the Muschelkalk groundwaters in Northern Switzerland and adjacent areas in Germany reflect different stages in their hydrogeochemical evolution. This is discussed below for the five general water types illustrated in Figure 48 and Figure 49.

Ca-HCO_3 and Ca-[Mg]-[HCO_3/SO_4] type groundwaters: Shallow groundwaters close to outcrops

In the study area, Ca-HCO_3 and Ca-[Mg]-[HCO_3/SO_4] type groundwaters occur at relatively shallow depths where the Muschelkalk units outcrop at the surface or where they are in contact with Quaternary gravel aquifers such as at the southern margin of the Black Forest or north of the Aare River in the Jura Mountains (Figure 48). They represent the first stage of the hydrogeochemical evolution when meteoric water infiltrates into the Muschelkalk aquifer. This is consistent with their short residence times inferred from ^{3}H and ^{14}C activities as well as their $\delta^{18}O$ signatures, which fall within the range of meteoric water infiltrating under similar climatic conditions than today (Figure 50). High recharge rates through the Muschelkalk outcrops and the high solubility of gypsum probably lead to a depletion of gypsum with time. Accordingly, these groundwaters slightly deviate from the 1:1 correlation between alkaline earth metal cations (Ca^{2+} + Mg^{2+}) and SO_4^{2-} (Figure 50b), and their chemical composition is mainly controlled by the dissolution of calcite and dolomite with a variable contribution from the dissolution of gypsum or anhydrite.

Ca-SO_4 type groundwaters: Groundwaters at considerable depth controlled by dedolomitization

Compared to the Ca-HCO_3 and Ca-[Mg]-[HCO_3/SO_4] type groundwaters, the chemical composition of Ca-SO_4 groundwaters is more strongly controlled by the dissolution of anhydrite/gypsum and dolomite as well as the precipitation of calcite as manifested by the 1:1 correlation of alkaline earth metal cations (Ca^{2+} + Mg^{2+}) and SO_4^{2-} (Figure 29). They represent a more evolved state, which is consistent with low ^{14}C activities and higher ^{13}C values, which are with a few exception below 10 pmc and above -9‰, respectively, whereas Ca-HCO_3 and Ca-[Mg]-[HCO_3/SO_4] type groundwaters show values above 10 pmc and below -9 ‰ (Figure 50c). This indicates that the Ca-SO_4 type groundwaters experienced more carbon isotope exchange with Muschelkalk carbonates than the more shallow Ca-HCO_3 and Ca-[Mg]-[HCO_3/SO_4] types (Figure 50a). Accordingly, these groundwaters occur at significant depth (> 100 m, Figure 50a) and the residence time is sufficiently high to interact with the small amounts of gypsum/anhydrite occurring in the Muschelkalk aquifer to cause the typical dedolomitization scenario causing the 1:1 correlation in Figure 50b. The groundwater in the Schlattingen 1 well is a typical example for such Ca-SO_4 type groundwater.

Na-Cl type groundwaters: Deep groundwaters affected by different Na-Cl sources

In the study area, Na-Cl type groundwaters occur at the largest depth (>500 m, Figure 50a) and hence represent the most evolved state of all Muschelkalk groundwaters. Compared to seawater, all Na-Cl type groundwaters display an excess of Cl over Br and hence strongly deviate from the seawater dilution line (Figure 51a). Moreover, the Na-Cl groundwaters collected from the region north of Lake Constance as well as those from Berlingen and Bülach display TDS concentrations strongly exceeding that of modern seawater (Figure 50). Hence, the Na-Cl signature originates from non-marine sources. Based on cross plots where the concentrations of Br and L are plotted against the Cl concentrations (Figure 51a,b) there are at least two distinct Na-Cl sources:

1) Dissolution of rock salt (i.e. halite) occurring in the Zeglingen Formation. With a TDS concentration of 156 g/L ([Na]: 59 g/L; [Cl]: 93 g/L), the Muschelkalk groundwater at Bülach displays by far the highest salinity. Since this sample is also showing the lowest Br/Cl ratio in the study area (0.01, Figure 51a), the dissolution of rock salt occurring in the Zegglingen Formation, some 100 m below the Muschelkalk aquifer, is the most likely source of Na and Cl in this particular sample.
2) Remnants of metamorphic/hydrothermal brines showing elevated concentrations of Cl and Na. The Na-Cl groundwater from Berlingen known for its high Li concentration (144 mg/L), other Na-Cl type

groundwaters from the study area, as well as all Ca-HCO_3, Ca-[Mg]-[HCO_3/SO_4], Ca-SO_4 and [Ca/Na]-[SO_4/Cl] type groundwaters show a liner correlation between the concentrations of Li and Cl with a molar [Li]/[Cl] ratio x 1000 of about 13 (Figure 51b). The observation that the groundwater from Bülach affected by the dissolution of rock salt is essentially Li free ([Li]/[Cl] x 1000 = 0.01, Figure 51) demonstrates that the correlation is caused by a Cl source other than the dissolution of rock salt. This is fully consistent with Li-free aqueous extracts obtained using halite samples from the Salzlager of the Zeglingen formation at the Nagra wells STA2 and STA3. The most likely candidate for such additional chloride source is the upwelling of Cl- and Li-rich brines from the underlying crystalline basement along regional fault zones. This is consistent with a rather long list of previous findings. Most importantly, Stober et al. (2023) suggested that the high Li and Cl concentrations observed in Muschelkalk groundwaters north of Lake Constance originate from the upwelling of brines from the crystalline basement because these groundwaters also display a temperature anomaly. Moreover, high Li concentrations in saline crystalline basement aquifers have been demonstrated elsewhere such as in the Rheingraben (Sanjuan et al., 2016) or in the Aar Massif (Wanner et al., 2017). An input of Li and Cl from the crystalline basement into the Muschelkalk aquifer is further supported by the observation that the sample collected from the crystalline basement aquifer at Weiach close to Schlattingen (Figure 48) displays essentially the same Li/Cl ratio than the Muschelkalk groundwaters collected at Berlingen as well as all Ca-HCO_3, Ca-[Mg]-[HCO_3/SO_4], Ca-SO_4 and [Ca/Na]-[SO_4/Cl] type groundwaters from the study area (Figure 51b). Moreover, such crystalline basement contribution is nicely manifested by the linear correlation between the concentrations of Li and He (Figure 51c). Like Li, He exclusively originates in the crystalline basement because it is produced by the radioactive decay of U and Th enriched in crystalline rocks. Finally, Aschwanden et al. (2019) demonstrated that upwelling of groundwater from the crystalline basement into the Muschelkalk aquifer has already occurred some 8-13 Ma ago and thereby caused the dissolution of anhydrite nodules.

The Na-Cl type groundwaters from the study area (Figure 48) showing Li/Cl ratios in between 0.01 and 13 likely contain a contribution from both Cl sources. This agrees well with the Br/Cl ratio also varying by two orders of magnitude (Figure 51a). It follows that the lower the Li/Br and Br/Cl ratios, the higher the contribution from rock salt dissolution on the concentrations of Cl and Na in the Na-Cl type groundwater samples.

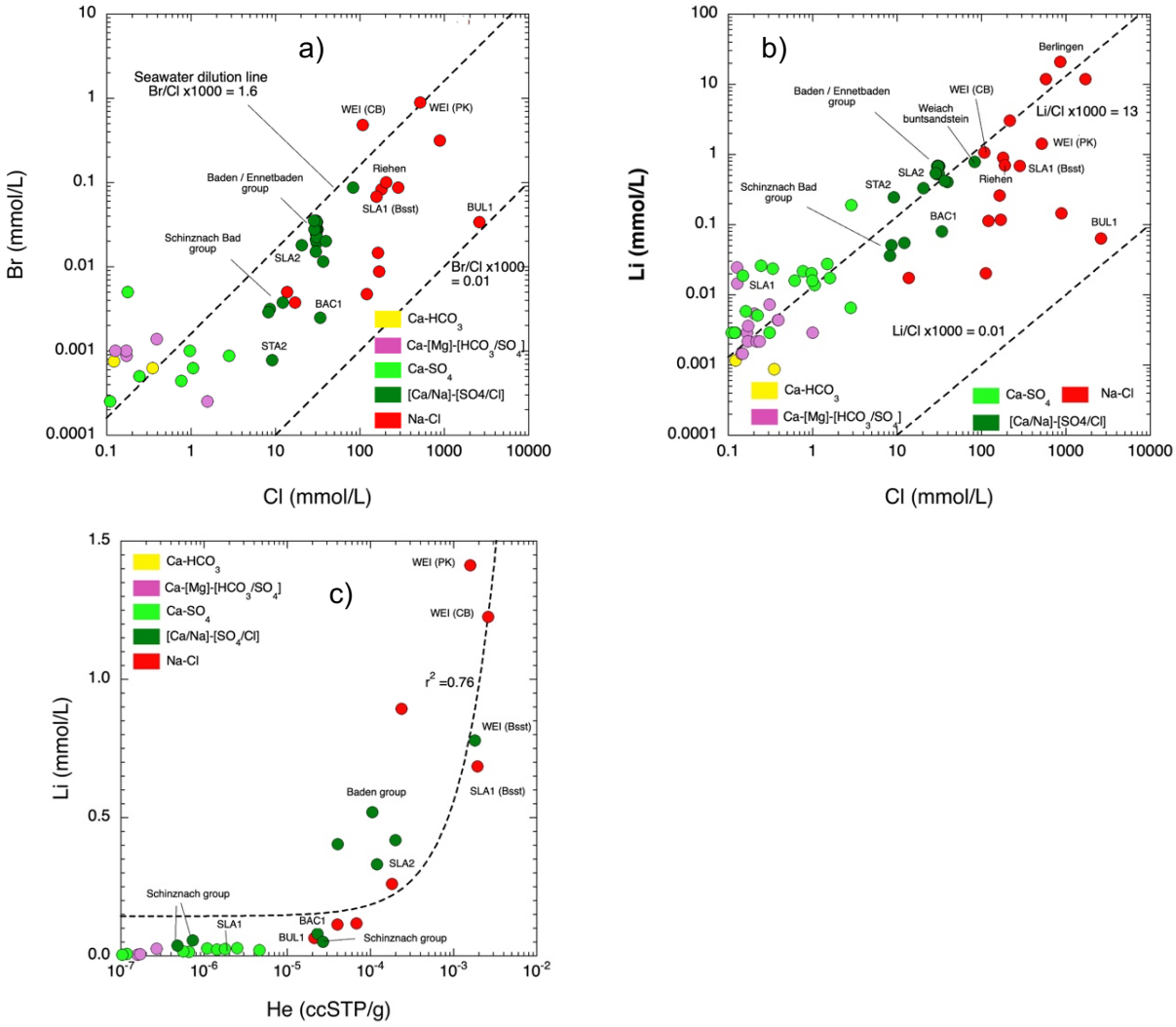


Figure 51: Cross plots between concentrations of Br, Cl, Li and He in groundwaters collected from the Muschelkalk aquifer in Northern Switzerland and adjacent areas.

To illustrate that the Na-Cl signature of Muschelkalk groundwaters in the study area may origin from the dissolution of halite and/or the contribution from saline brines upwelling from the crystalline basement groundwater samples collected at Weiach (WEI) from the Crystalline Basement (CR), Permokarboniferous (PK), and Buntsandstein (Bsst) aquifers are plotted as well. Also plotted is the groundwater collected from the Buntsandstein aquifer at SLA-1. Note: **a)** Br vs. Cl cross plot: The higher the Br/Cl ratio (labelled as molar ratio x 1000) the higher the Na-Cl input from the crystalline basement. The sample from Bülach (BUL1) with a ratio of 0.01 reflects the halite dissolution endmember. The molar Br/Cl ratio x 1000 in modern seawater is 1.6. Modified from Nagra (2024) and supplemented with data for the two Schlattingen wells. **b)** Li vs. Cl cross plot: For samples with a molar Li/Cl ratio close to 13 (labelled as molar ratio x 1000), Cl almost exclusively originates from the crystalline basement. For these samples, the crystalline basement contribution increases with increasing concentrations of Li and Cl. If Cl is also derived from the dissolution of halite, the samples are shifted towards lower Li/Cl ratios because halite can be considered as Li-free based on the very low Li concentrations of the BUL1 sample showing the maximum TDS concentration in the study area (156 g/L). **c)** Li vs. He cross plot. Both parameters exclusively originate from the crystalline basement. The linear correlation thus confirms that in the study area, upwelling from the crystalline basement into the Muschelkalk aquifer is relevant. The higher the concentrations of Li and He, the higher the contribution from the basement. The color code and the provided sampling locations follow the same criteria as in Figure 48 to Figure 50.

[Ca/Na]-[SO_4/Cl] type groundwaters: Deep groundwaters reflecting mixtures between Ca-SO_4 and Na-Cl type groundwaters

In the Piper plot (Figure 49) as well as in most of the cross plots shown in Figure 50 and Figure 51 (e.g. Ca+Mg vs. SO_4, Li vs. Cl, Li vs. He), the [Ca/Na]-[SO_4/Cl] type groundwaters plot in between those of the Ca-SO_4 and Na-Cl types, respectively. Accordingly, they represent a mixture between endmembers of these types. In other words, Ca and SO_4 originate from dedolomitization exclusively occurring in the Muschelkalk aquifer, whereas Na and Cl are inherited from the upwelling of saline groundwaters from the crystalline basement or other deep aquifers (i.e. Permokarboniferous or Buntsandstein), and/or the dissolution of halite in the Zeglingen formation. Based on the elevated Br/Cl and Li/Cl ratios of most of the [Ca/Na]-[SO_4/Cl] type groundwaters, the upwelling of saline water from the deep aquifers appears as a more relevant source for Na and Cl than the dissolution of halite. The thermal water sampled at Baden and Schinznach, displaying anomalously high temperatures of up to 47 °C in the shallow subsurface and hence partly originate from greater depths, are typical examples for such [Ca/Na]-[SO_4/Cl] type groundwater. Regarding the groundwater collected at SLA-2, the situation is more complex. Based on the Br/Cl and Li/Cl ratios, Cl and Na mainly originate from the upwelling of saline groundwaters from the crystalline basement (Figure 51). In contrast, the shift to the right of the 1:1 correlation between alkaline earth metal cations (Ca^{2+} + Mg^{2+}) and SO_4^{2-} (Figure 50b) suggest a sulfate source and Ca sink in addition to the dedolomitization reaction taking place in the Muschelkalk aquifer and the subsequent admixture of Ca-SO_4 type groundwaters.

To reconstruct the composition of the saline endmember mixing with SLA-1 type groundwater to form the SLA-2 groundwater, we took the concentration of Cl and Li in the groundwater collected from the crystalline basement in the nearby Weiach well ([Cl]: 4 g/L; [Li]: 7.8 mg/L; Waber & Traber, 2022) and applied a binary mixing model. This yields contributions from the saline endmember of 18 and 29%, respectively. Interestingly, similar contributions of 21 and 35% are obtained, when using the fluoride and magnesium concentration form the Weiach sample instead ([F]: 8.5 g/L; [Mg]: 0.4 mg/L). Accordingly, the mean of the four calculations (25%) is considered a reasonable estimate for the contribution of this saline endmember on the SLA-2 groundwater. Subsequently, this proportion can be used to calculate the concentration of other, more reactive solutes in the saline endmember such as sulfate, strontium, and CO_2 (Table 18). It follows that the SLA-2 groundwater represents approximately a 1:3 mixture between a Na-Cl type groundwater originating from a deeper aquifer such as the crystalline basement and a Ca-SO_4 type groundwater originating from the Muschelkalk aquifer. Before or after mixing, sulfate, strontium, and CO_2 was added to the groundwater (see conceptual model below). Therefore this saline endmember is subsequently referred to as modified basement water. The reconstructed Si concentration of 27 mg/L (Table 18) suggest an equilibration temperature of around 100 °C with respect to quartz. It follows that the reservoir temperature of the modified basement water ascending at SLA-2 is at least 100 °C. Taking into account the local geothermal gradient of around 45°C/km, this yields upflow from a depth of at least 1 km below the Schinznach Formation (ca. 2 km below surface). Based on the geological profile recorded for the SLA-1 well (Figure 9), such fluid reservoir must be located in the crystalline basement.

Table 18: Concentrations of major solutes and selected trace elements in the Muschelkalk groundwater at SLA-1, SLA-2 and the crystalline basement groundwater at Weiach, as well as the reconstructed deep saline endmember ascending and mixing with a SLA-1 type groundwater to form the SLA-2 groundwater.

		[1]SLA-1	[1]SLA-2	[2]Reconstructed composition of deep saline endmember (modified basement water)	[3]Crystalline basement groundwater at Weiach
pH value		6.41	6.62	6.49	7.7 to 8.2
Na	mg/L	27	2900	11534	2725
K	mg/L	15	55	175	93
Mg	mg/L	120	78	0.4[4]	0.4
Ca	mg/L	550	360	221[4]	221
Cl	mg/L	12	730	2888	4000
SO_4	mg/L	1700	6000	18923	468
DIC as HCO_3^-	mg/L	241	566	1544	97.97
F	mg/L	0	1.8	7.2	8.5
Li	mg/L	0.17	2.3	8.7	8.5
Sr	mg/L	4.4	16	50.9	6.9
Si	mg/L	15	18	27.0	20.4
[5]Saturation index quartz at T=57°C	-	0.08	0.17	0.36	n.a.
[5]Saturation index calcite at T=57°C	-	0.00	0.00	0.00	0.00
[5]Saturation index anhydrite at T=57°C	-	0.14	0.00	0.00	-0.93
[5]Saturation index dolomite at T=57°C		-0.03	-0.06	-2.18	-0.60
[5]Quartz equilibration temperature	°C	65	75	99	n.a.

[1]Samples collected on 15./16. April 2024
[2]Assuming a contribution of 75% SLA-1 groundwater on SLA-2 based on the concentration of Li, Cl, F, Mg in the crystalline basement groundwater at Weiach, SLA-1 and SLA-2
[3]Waber & Traber (2022)
[4]Set to the concentration of the crystalline basement groundwater at Weiach
[5]Calculated by geochemical modelling using PHREEQC (Parkhurst & Appelo, 2013) in combination with the Thermodem thermodynamic database (Blanc et al., 2012).

2.3 Discussion

The data collected during this project have provided novel insights into the thermal, hydraulic and chemical behavior of the Muschelkalk aquifer, allowing a more informed assessment of its suitability for harnessing geothermal energy in the Canton of Thurgau and adjacent areas in Northern Switzerland (see Section 3 below). As demonstrated by the strongly differing hydrochemical signatures of the two Schlattingen wells (stable isotopes, concentrations of solutes, ^{81}Kr model ages, recharge temperatures), the water produced from the Muschelkalk aquifer must derive from at least two geological sources. This evidence aligns well with the observation of Künze & Kuhlmann (2020), that the SLA-1 and SLA-2 wells are not hydraulically connected via the aquifer, even though they are separated at their closest points by a distance of only 575 m and that no crosshole responses were detected between SLA-1 and SLA-2 during the pumping test carried out in this project (Section 2.2.1). Together, these points imply that the aquifer is divided into hydraulically disconnected compartments, as illustrated schematically in Figure 52a. Moreover, hydraulic data from SLA-2 (Section 2.2.1.; Table 5 and Table 6) suggest that the production of thermal water may increase the permeability of the aquifer and hence the productivity of the well over time. The visual inspection of the SLA-2 casing, however, showed that extensive mineral scaling may occur when producing thermal water from steeply dipping fracture zones such as at SLA-2.

In the following sections we propose a conceptual model explaining the governing coupled thermal-hydraulic-chemical processes that control the productivity and chemical compositions of the thermal waters from the two Schlattingen wells. In addition, we present and discuss results from numerical modelling including groundwater and coupled thermal-hydraulic-chemical simulations to verify the conceptual model and to estimate the permeability distribution and quantify groundwater flow within the Muschelkalk aquifer and adjacent units.

2.3.1. Conceptual model describing the coupled thermal-hydraulic-chemical processes controlling the productivity and composition of thermal water from the two Schlattingen wells

Groundwater sources

The recharge conditions for the two distinct groundwater types produced today at Schlattingen can be deduced by combining evidence from the geological setting of the area (Figure 52), the stable isotope signatures of the well waters (Figure 50), the noble gas infiltration temperatures (Appendix 1) and tracers of subsurface residence times (Figure 40) as follows:

<u>SLA-1</u>

The groundwater at SLA-1 is clearly inherited from the infiltration of meteoric water into the Muschelkalk aquifer. The low $\delta^{18}O$ value (-12.7‰) and infiltration temperature (ca. 2.5 °C) imply that recharge occurred during the last glacial cycle (i.e., between 11.5 and 115 ka ago), which is consistent with the 19 ka ^{81}Kr model age of the produced SLA-1 water (Figure 40). The most recent regional groundwater models (Gmünder et al., 2014, Nagra, 2024) suggest that infiltration occurred through the Muschelkalk outcrops that lie at high elevations some 22–25 km NW of Schlattingen along the Wutach Valley on the southern flank of the Black Forest Highlands (Figure 48). Given this flow system, the chemical composition of the groundwater is almost exclusively controlled by the mineralogy of the aquifer, namely via buffering by dolomite, anhydrite and calcite, which has resulted in the characteristic Ca-SO_4 signature of the produced water at SLA-1.

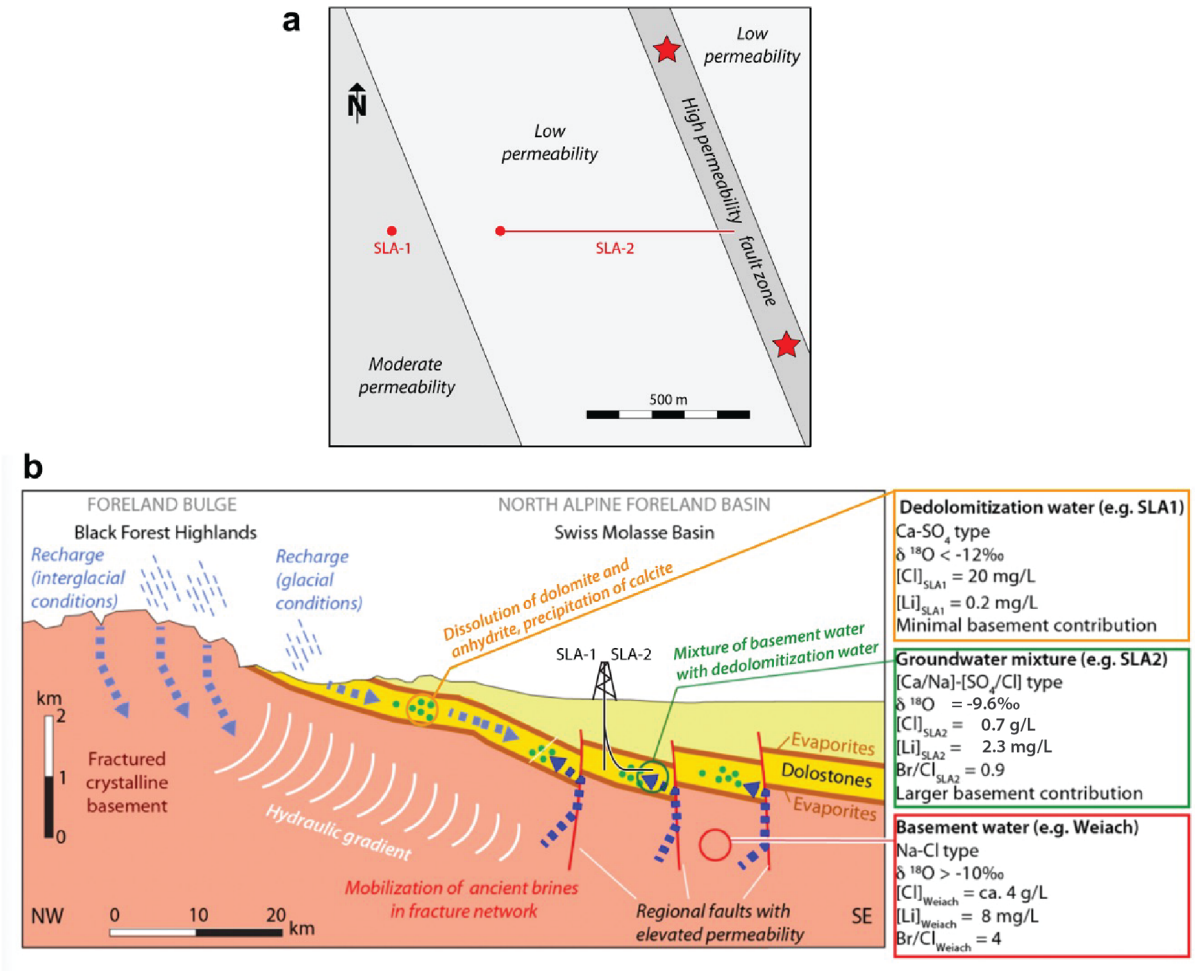


Figure 52: Conceptual models illustrating the large-scale flow systems controlling the groundwater composition in the two Schlattingen wells.

(**a**) Schematic map at local scale showing inferred compartmentalization of permeability zones in the Muschelkalk aquifer at Schlattingen (see text). Upwelling of the basement water component (red stars) through the high-permeability fault zone into the Muschelkalk aquifer is either too far away or too slow to raise the temperature of the water produced from SLA-2. (**b**) Schematic NW–SE cross-section between the Black Forest Highlands and the Molasse Basin showing location of wells SLA-1 and SLA-2. The groundwater at SLA-1 (orange box) derives from infiltration of meteoric water into the Muschelkalk aquifer, which has been modified by dedolomitization reactions along its flowpath (dissolution of dolomite and anhydrite, precipitation of calcite). In contrast, SLA-2 water (green box) is a mixture of SLA-1 type water and Na-Cl type water upwelling from the crystalline basement along permeable fault zones. Modified from Aschwanden et al., (2019).

SLA-2

Based on its chemical composition, the groundwater produced at SLA-2 consists of 75% SLA-1 type groundwater component (Table 18). The remaining 25% is a saline, chemically modified Na-Cl type water enriched in He, Li, and Si, which has ascended from the crystalline basement or other deep aquifers. Based on the stable isotope signature of the produced SLA-2 water, both of its components are originally of meteoric origin (Figure 50c), suggesting that they have both infiltrated on the southern flanks of the Black Forest highlands (Figure 52). The basement water infiltrated at slightly higher altitude where fractured crystalline rocks are present in outcrop (Figure 52b). Thus, rather than infiltrating the Muschelkalk aquifer, this water migrated through the fracture network in the deep basement as far as Schlattingen, in response to the hydraulic head gradient induced by the elevation difference with respect

to the recharge location. The high ^{81}Kr model age (490 ka, Figure 40) and $\delta^{18}O$ values (> -10‰; Figure 46) suggest that recharge of both water components occurred during similar or even warmer climatic conditions to those of today (Figure 50c), but during a previous interglacial period (> 115 ka ago). This agrees nicely with the noble gas infiltration temperatures of around 21 °C (Appendix 1).

Transmissive fault zone in SLA-2

In Section 1.3.5 it is shown that a subvertical, highly transmissive fault zone is present within the easternmost 60 m of the horizontal SLA-2 borehole, and that this fault zone may extend further to the east beyond the end of the borehole. We propose that this fault zone is the high-permeability upflow pathway required to transport the chemically modified basement water into the Muschelkalk aquifer, where it mixes with SLA-1 type water before being produced from SLA-2.

Based on the evidence discussed in Section 1.3.5, the fault zone at the end of SLA-2 can be visualized in 3D as a vertical, NNW–SSE striking tabular body that extends over several hundred meters in the horizontal plane on either side of the borehole, and that reaches down to the fractured aquifer in the crystalline basement (Figure 53a). How far the fault zone rises into the overlying Bänkerjoch (*Gipskeuper)* unit is unknown.

Upwelling of saline Na-Cl type groundwaters at SLA-2

Although the upwelling basement fluid rises from a reservoir in which temperatures are above 100 °C (Table 18), its mixing with 60 °C SLA-1 type water in the Muschelkalk aquifer does not raise the temperature of the water produced from SLA-2. So far, the production temperature at SLA-2 is very similar to that of the thermal water produced at SLA-1, in which there is no evidence for a fluid component upwelling from deeper units. This lack of a thermal impact on the produced SLA-2 water indicates that the rate of upwelling of the basement water is either very slow, or that the point at which the basement water enters the fault zone is distant from SLA-2 (e.g., red stars in Figure 52a), such that any temperature increase it causes dissipates before it reaches SLA-2.

To hydraulically connect the Muschelkalk aquifer with the crystalline basement, the open fracture at the downhole end of SLA-2 must cut through several intervening formations (Figure 53): the Zeglingen (*Anhydritgruppe*), Kaiseraugst, (*Wellengebirge*), Dinkelberg (*Buntsandstein*) and Weitenau (*Rotliegend*). The Zeglingen is dominantly composed of anhydrite (with a 5 m layer of halite), but the other units are marly (Kaiseraugst) or quartzofeldspathic. Since the upwelling Na-Cl type groundwater is undersaturated with respect to anhydrite and saturated with respect to calcite (Table 18; Aschwanden et al., 2019), anhydrite is expected to dissolve as the basement water traverses the Zeglingen Fm. via the fault zone. The Ca^{2+} released by anhydrite dissolution is in turn expected to re-precipitate as calcite from the saturated basement water or exchanged with Na from the clay-rich part of the Zeglingen Fm., leaving the chemically modified water enriched in SO_4^{2-} but not Ca^{2+}.

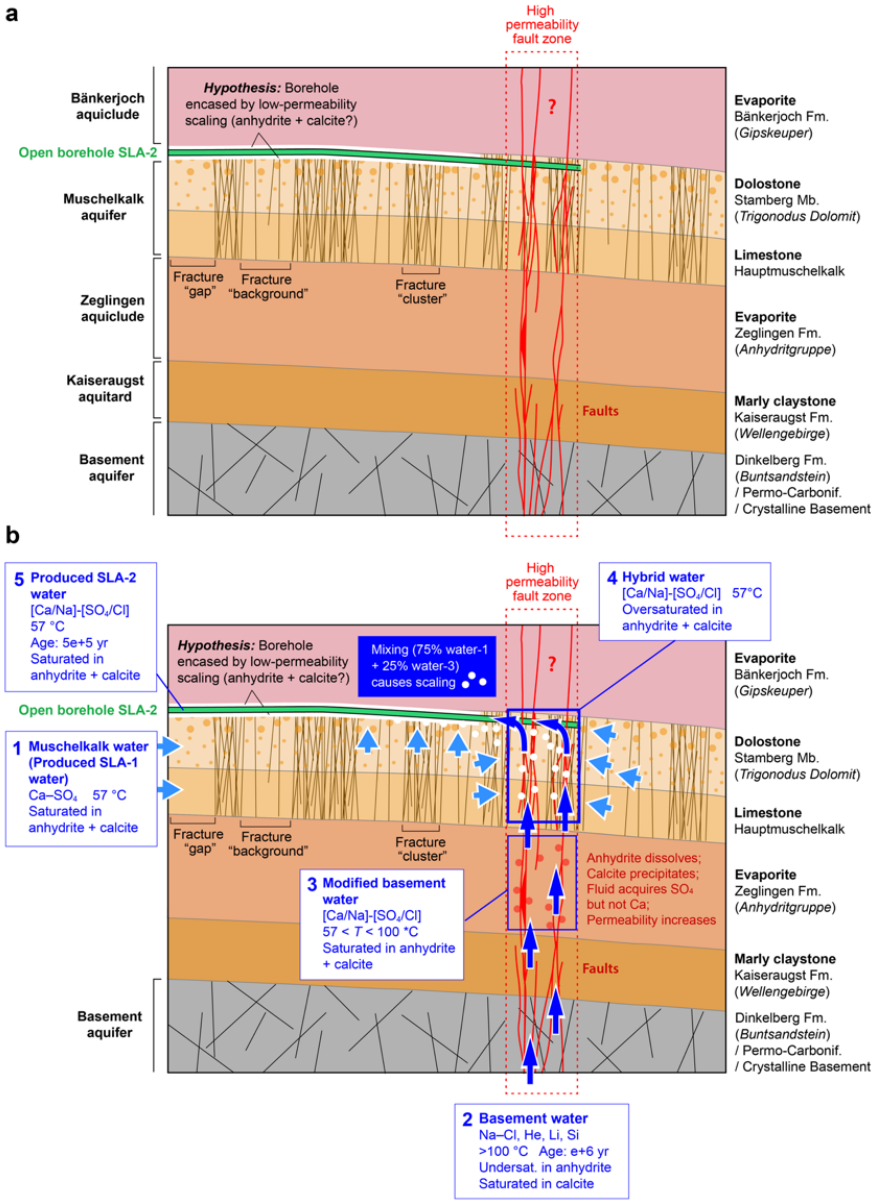


Figure 53: Schematic, conceptual model of processes near the end of well SLA-2, explaining how the produced SLA-2 water attains a chemically hybrid signature distinct from that in SLA-1.

Compare with larger scale models in Figure 52. a) Geological setting of the Muschelkalk aquifer within the Stamberg Mb. dolostone and Hauptmuschelkalk limestone, which are hydraulically linked by joint fractures. A high permeability fault zone connects the Muschelkalk aquifer with the basement aquifer. It is hypothesized that anhydrite + calcite scaling is present along the borehole (scales have been observed only as deep as 443 m in the well; deeper observations have yet to be made). b) Five distinct waters are identified (blue boxes). Saline, He-, Li- and Si- enriched Na-Cl type groundwater (water-2) ascends from the basement (see Figure 52 for driving force for ascent). Where this water crosses the Zeglingen (Anhydritgruppe) evaporites, anhydrite dissolves and calcite precipitates, increasing the content of SO42- in the resulting chemically modified basement water (water-3). Before entering the well, water-3 mixes with the native SLA-1 type groundwater in the Muschelkalk aquifer (water-1), generating the hybrid water-4 composition (75% water-1 + 25% water-3) that enters the borehole. The mixing induces supersaturation of calcite and anhydrite and likely triggers precipitation of these minerals as scales, possibly coating the borehole.

The above postulated water–rock interaction provides a sulfate source outside of the Muschelkalk aquifer, which is needed to explain the observed shift of the SLA-2 groundwater to the right of the 1:1 correlation between alkaline earth metal cations (Ca^{2+} + Mg^{2+}) and SO_4^{2-} in Figure 50b. The same applies with respect to sulfur isotopes (Figure 35), suggesting that the Triassic Zeglingen evaporites are likely the main source for sulfate in the SLA-2 groundwater. Furthermore, the interaction with the Zeglingen Fm. likely also represents the Sr source required to explain the elevated Sr concentration observed in the SLA-2 groundwater (Table 18). This is also compatible with the $^{87}Sr/^{86}Sr$ ratio of around 0.7090 in the SLA-2 water, which falls within the range of ratios in the Muschelkalk aquifer and in the Triassic units (Figure 36). The basement water is expected to have much higher $^{87}Sr/^{86}Sr$ ratios (above 0.714) but lower total Sr contents (Table 18). It is therefore likely that the basement isotope signal is swamped by the addition of Sr from the Zeglingen evaporites

Scale formation due to mixing of different groundwaters

After interacting with the Zeglingen (*Anhydritgruppe*) evaporites, the upwelling water from the basement has transitioned from a Na-Cl type to a [Ca/Na]-[SO_4/Cl] type groundwater. Before entering the SLA-2 well, this chemically modified basement water mixes with the Ca-SO_4, SLA-1 type groundwater of the Muschelkalk aquifer where the fault zone cuts through the Hauptmuschelkalk and Stamberg dolostone (Figure 53). Taking into account the composition of these two groundwater types (Table 18), geochemical model simulations demonstrate that anhydrite and calcite both become supersaturated during mixing (Figure 54). Other thermodynamically stable minerals are either not over-saturated or they are likely to be present in only trivial quantities. It follows that the scales observed along the SLA-2 well (Figure 47) are likely caused by such fluid mixing. It remains unclear though, whether they consist of anhydrite or calcite, as no sample from the scales has been retrieved from the SLA-2 well and analyzed so far. Other processes to induce scale formation, such as an inadvertent pressure drop that induces CO_2 degassing, are considered unlikely. This is because the downhole pump has been observed to be free of scales, despite its intake being a site of lowered pressure during pumping (Wanner et al., 2017). Nevertheless, it is emphasized that the mixing hypothesis has yet to be proven. For instance, the mixing hypothesis predicts that there should be no scales in SLA-1. Therefore, observations deep within SLA-1 could be used to verify or refute the hypothesis.

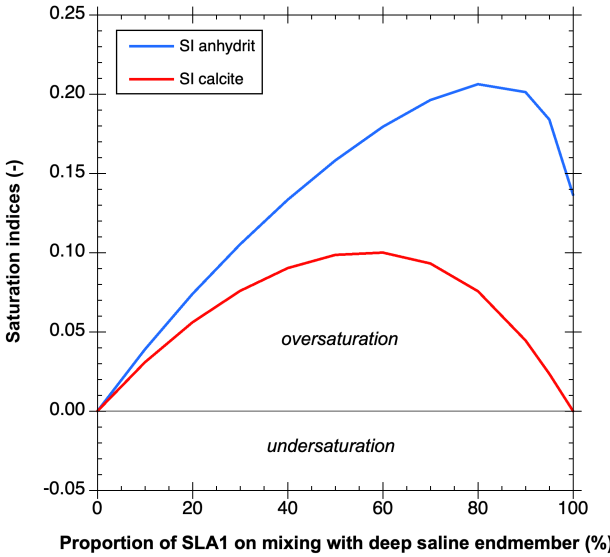


Figure 54: Saturation indices of anhydrite and calcite as a function of the mixing proportion between the modified basement water and the Ca-SO_4 type Muschelkalk groundwater at SLA-1 (Table 18) calculated by Phreeqc at a constant temperature of 57°C.

Note that the minor supersaturation of the SLA-1 groundwater with respect to anhydrite is likely caused by uncertainties regarding the thermodynamic data. It is assumed this groundwater is saturated with respect to anhydrite (saturation index = 0, Figure 53).

Lack of hydraulic connection between SLA-1 and SLA-2

The processes described above (Figure 52 – Figure 54) explain how the Schlattingen wells tap into hydrochemically distinct compartments of the Muschelkalk aquifer. However, they are not sufficient to explain the lack of hydraulic connection between the two wells as inferred from hydraulic tests carried out in 2015 and earlier hydraulic simulations (Künze & Kuhlmann, 2020). There is no evidence for an abrupt sedimentary facies change in the Schinznach Fm. or for a local absence of dolomitization in its upper portion, which could be responsible for the lack of connectivity. In fact, the lithostratigraphic properties of the Schinznach Fm. have been demonstrated to be monotonous and highly predictable over the entire region of northern Switzerland (Pietsch et al., 2016). The hydraulic compartmentalization at Schlattingen therefore likely results from one of the following hypotheses or a combination thereof:

1) The regional groundwater model for the greater Schlattingen area (Gmünder et al., 2014) shows that the two Schlattingen wells are located close to a groundwater flow divide in the Muschelkalk aquifer (dashed line in Figure 55). Although it would be a great coincidence if the groundwater divide was exactly located between the two wells, it is fully consistent with the observation that the groundwater at SLA-1 shows a very similar hydrochemical signature to the Muschelkalk groundwaters collected from the Nagra siting region in Zürich Nordost and Nördlich Lägern (NL), located up to 30 km to the west. For instance, $\delta^{18}O$ values, ^{81}Kr model ages, as well as Li concentrations increase to the west, along the flow path inferred from the groundwater model (Figure 55, Figure 56).

2) A local but hidden, NNW–SSE-trending fault may be present between the two Schlattingen wells. If this fault is sealed by clay gouge, then it might hydraulically separate the two wells. Logging of the SLA-2 well high above the Muschelkalk aquifer revealed slightly but anomalously dipping bedding where the well trajectory intersected the Opalinus Clay Fm. If this represents a small ductile fold, it may hint at the presence of a discrete brittle fault at greater depth, e.g., within the Muschelkalk aquifer (pers. comm. H. Madritsch). The known points of intersection of the SLA-1 and SLA-2 wells with the top of the Muschelkalk aquifer leave little room for a normal fault offset of more than a few meters. Nevertheless, if such a fault exists and is sealed by clay gouge, then it could conceivably block hydraulic connection between the wells. However, none of the logged faults in the horizontal section of the SLA-2 well showed any gouge, and all in fact show notably wide apertures. Whether a fault exists between the two wells could be perhaps be tested if the well site is surveyed in the future by high-resolution 3D reflection seismics and if the fault displays a throw of ~ 20 m or more.

3) As shown in Figure 10c and Figure 53a, the fracture log along the horizontal section of well SLA-2 shows occasional gaps. As the fractures are responsible for raising the permeability of the aquifer above that of the rock-matrix permeability (4E-15 m^2), the presence of such a gap or series of gaps between SLA-1 and SLA-2 could conceivably inhibit the hydraulic connection between the two wells. However, the logged gaps may simply be due to the borehole having missed intersecting nearby fractures owing to the low intensity of the “background” fracture domains. Indeed, the Discrete Fracture Network simulations in Diamond et al. (2025) show good lateral connectivity throughout the “background” domains, despite numerous gaps appearing where a borehole may pass without intersecting fractures. At present it is difficult to evaluate the feasibility of this “gap” hypothesis.

4) Mineral scaling has been observed by wireline televiewer down to 450 m in the cased section of the SLA-2 well (Figure 47). Lowering the televiewer to deeper levels was not possible because the scaling has reduced the diameter of the well. Evidently, the scaling is increasing its thickness with depth. This fact aligns with our conceptual model (Figure 53), which predicts the existence of scaling at least near the end of the SLA-2 well (Section 2.3.1). These points lead us to hypothesize that the wellbore of SLA-2 is completely coated by scales down to its termination, including along its entire open-hole (horizontal) section. The coating of scales would hinder hydraulic connectivity with the enclosing Muschelkalk aquifer, and hence hinder connectivity between SLA-2 and SLA-1. An argument against this hypothesis is that the wells

appeared to be disconnected as soon as drilling of SLA-2 was completed, whereas the buildup of a hydraulically significant coating of scales should take considerable time.

The four hypotheses above are assessed below when discussing the results of the different numerical simulations.

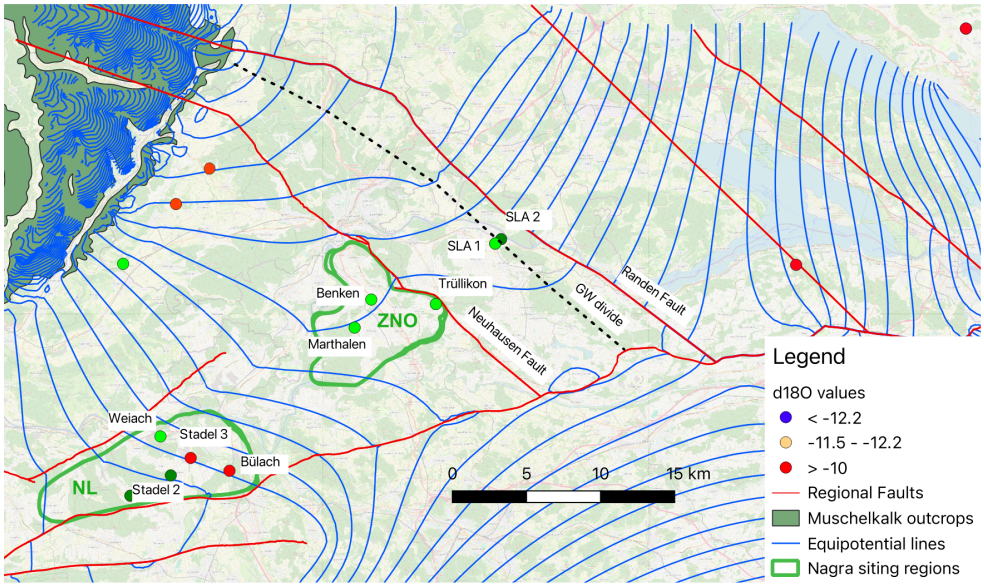


Figure 55: Map of locations of deep Muschelkalk groundwater samples in the vicinity of the two Schlattingen wells.

Also shown are the piezometric contour lines obtained from the regional groundwater model (Gmünder et al., 2014), the Nagra siting regions Zürich Nordost (ZNO) as well as Nördlich Lägern (NL), and Regional Faults. Note: The color code of the sampling locations reflects their $\delta^{18}O$ values. Together with the piezometric contour lines, the distribution of $\delta^{18}O$ values suggests the occurrence of groundwater divide (GW divide) that may cross in between the two Schlattingen wells, separating the two wells hydraulically and causing the strong difference of the $\delta^{18}O$ values in these wells.

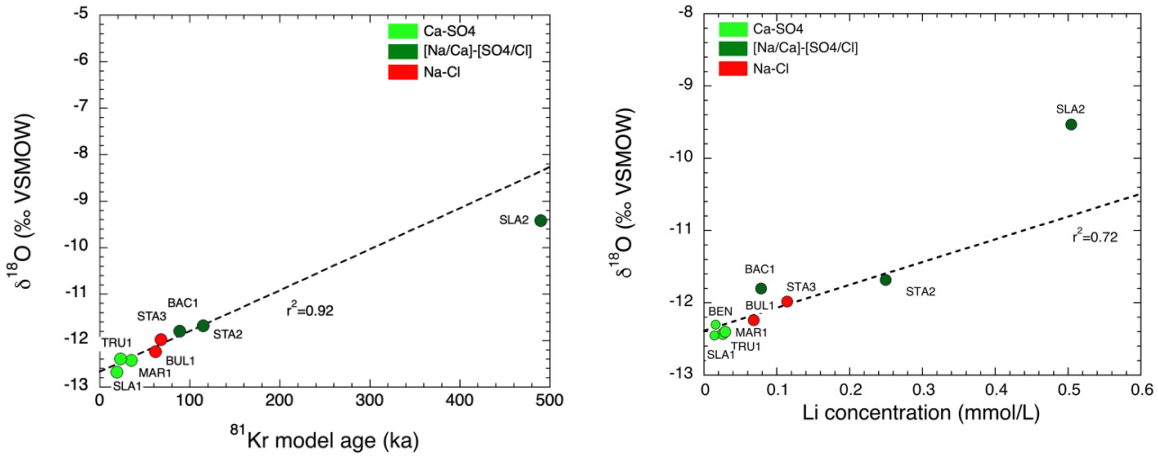


Figure 56: Linear correlations between $\delta^{18}O$ values, Li concentrations, and ^{81}Kr model ages of Muschelkalk groundwaters collected in the Nagra siting regions of ZNO and NL and in the Schlattingen 1 well (SLA-1 at bottom left). Both plots are taken from Nagra (2024) and supplemented with data for the two Schlattingen wells (Table 10, Figure 40).

Note: The correlations indicate that west of the apparent groundwater divide (Figure 55), all these parameters increase along the groundwater flow path inferred from the piezometric contour lines, confirming that the corresponding sampling sites including SLA-1 belong to the same, well-connected groundwater flow system. In contrast, the groundwater from SLA-2 falls off the correlations, indicating that it belongs to a different, hydraulically disconnected flow system.

2.3.2. Groundwater simulations

The subcontractor TK Consult has been involved in the analysis and interpretation of hydraulic tests carried out at SLA-1 and SLA-2 since the beginning of the Schlattingen geothermal operation. In 2020 they published a conceptual model of the permeability distribution around SLA-2 based on pumping tests performed in 2013-2015 (Künze & Kuhlmann, 2020). In this model (Figure 57) the horizontal section of SLA-2 is embedded in a region made up of permeable rock of finite extent (in the report referred to as regions R1 and R2, surrounded by a rock of lesser permeability R3). The existence of a low-permeability region R3 was inferred from the slow pressure recovery observed during the 2015 pumping test. This complex local permeability distribution around SLA-2 was part of a large regional-scale hydraulic model that extends from the recharge areas of the Muschelkalk in the Wutachtal (D) to a distance of about 35 km towards the SE. These early hydraulic studies were very valuable in terms of understanding the pattern of regional groundwater flow as well as unravelling the complexity of the permeability structure near SLA-2.

Künze & Kuhlmann (2020) emphasized that their proposed permeability distribution around SLA-2 (Figure 57) represents a concept rather than a realistic hydrogeological model. In other words, alternative geometries and arrangements of the three permeability zones could be adopted as long as they honor the central concept of their analysis, that is the withdrawal of water from a permeable reservoir of finite extent during the early stage of pumping, followed by later exhaustion of the reservoir whereupon the flux is controlled by a more distal, lower permeability unit.

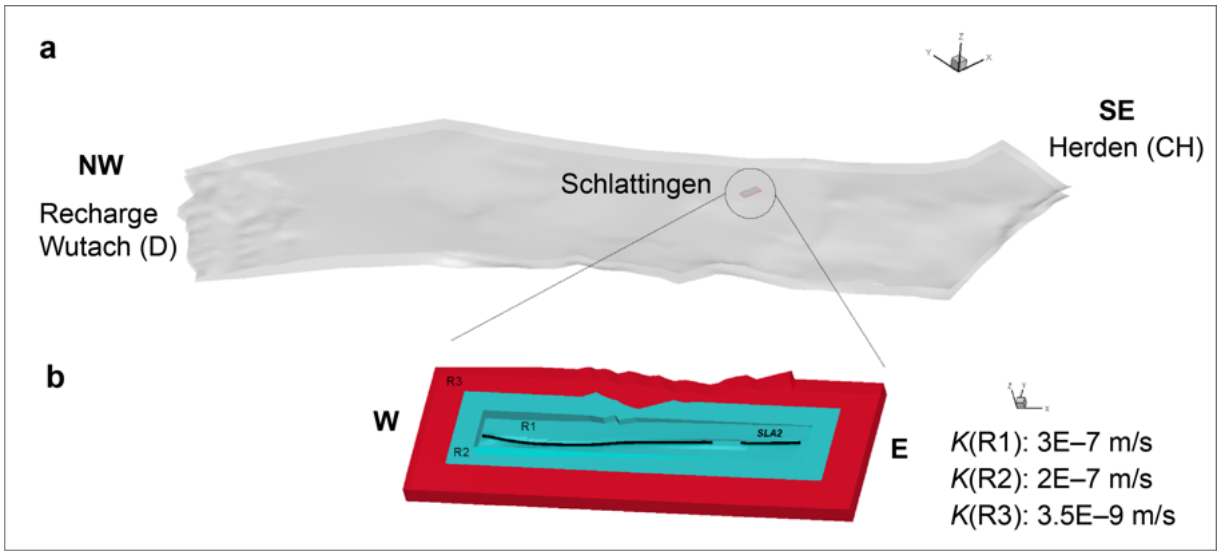


Figure 57: Sketch of 2020 conceptual hydraulic model by TK Consult (Künze & Kuhlmann, 2020).

(a) Regional-scale domain covering 35 km between the high elevation recharge area in the NW and the low elevation outflow boundary in the SE. (b) Detail of model around the 660 m long horizontal section of the SLA-2 well within the Stamberg Member dolostone (formerly known as the Trigonodus Dolomit). Rectangles show nested hydraulic conductivity (K) regions R1, R2 and R3, which collectively are consistent with the SLA-2 pump tests up to 2020.

Modification of TK Consult 2020 conceptual model

In Section 2.3.1 we have presented a new geological–geochemical conceptual model (Figure 53), which is consistent with many of the structural and chemical compositional features of the SLA-2 system. This model includes a vertical conduit that allows upwelling basement water to mix with water in the Stamberg dolostone and Hauptmuschelkalk, thereby explaining the difference in chemical compositions between the produced SLA-1 and SLA-2 waters. Here, we take advantage of the flexibility allowed by the Künze & Kuhlmann (2020) hydrogeological model by rearranging their permeability zones around SLA-2, such that the result is compatible with all but one feature of the new geological–geochemical model and its supporting evidence. The rearrangements have been integrated by TK Consult into their numerical

hydrogeological model and then calibrated, yielding an “updated 2025 model”. This calibrated model has served as the basis for Uni Bern to construct a thermal–hydraulic–chemical (THC) model to quantitatively test the feasibility of the processes envisaged in the new geological–geochemical conceptual model (Figure 53).

The one feature that is not included in the modified conceptual hydrogeological model presented below, is the assumed presence of scaling around most of the horizontal section of well SLA-2. This is not included because (1) scaling in a shallow level of SLA-2 was first discovered very late in our project (3 months before project termination); (2) the modified conceptual model presented below was conceived and passed on to TK Consult for implementation two months prior to the discovery of scaling; (3) the presence of scaling in the horizontal section is purely *hypothetical* at this time, as no observations are available deeper than 443 m in the vertical section of SLA-2 (Section 2.2.4); (4) the mineralogy of the scaling is still unknown, and hence the relation of the scaling to the demonstrated mixing of basement and Muschelkalk waters is also unverified. Nevertheless, the hypothetical presence of scaling is included in the subsequent thermal–hydraulic–chemical (THC) modelling presented in Section 2.3.3.

Our updated conceptual hydrogeological model is shown in Figure 58. The high areal extent of region R3, its low permeability and its abrupt contact with region R4 surrounding well SLA-1 are all features that have been retained unmodified from the Künze & Kuhlmann (2020) model of TK Consult (see Section 2.3.5 for a second update of these features). The low permeability of region R3 compared to R4 ensures poor hydraulic connectivity between wells SLA-1 and SLA-2, consistent with the discussion in Section 2.3.1. In contrast, regions R1 and R2 have been rearranged compared to the 2020 TK Consult model. They have been moved from the surroundings of well SLA-2 (Figure 57) to new positions at the end of the horizontal section of SLA-2. These new positions represent the top of the steep fault zone that conducts basement fluid up into the Muschelkalk aquifer. Despite their new positions, regions R1 and R1 and R2 still honor the central concept of the 2020 TK Consult model (Figure 57), namely that they permit withdrawal of water from a permeable reservoir of finite extent during the early stage of pumping, followed by later exhaustion of the reservoir whereupon the flux is controlled by the lower permeability region R3.

To enable the vertical conduit to reach the basement, an additional region R5 has been added to the conceptual model in Figure 58. Thus, R5 traverses the Zeglingen (*Anhydritgruppe*) and Kaiseraugst (*Wellengebirge*) formations. Note that, whereas in the new geological–geochemical model just a few very narrow but very high permeability faults channel upflow from the basement (Figure 53), for computational expediency these zones are lumped together to form one wide zone of lowered permeability (regions R1+R2+R3) in the updated conceptual hydrogeological model. Unlike in Künze & Kuhlmann (2020), where the entire horizontal SLA-2 borehole is surrounded by nested R1 and R2 regions (Figure 57), in the first updated model only the easternmost 37 m of SLA-2 tap into the conduit via region R1 (Figure 58b). The SLA-1 well is unaffected by the permeability structure related to the conduit and is hosted by the Stamberg dolostone with “background” permeabilities referred to as zone R4 (Figure 58).

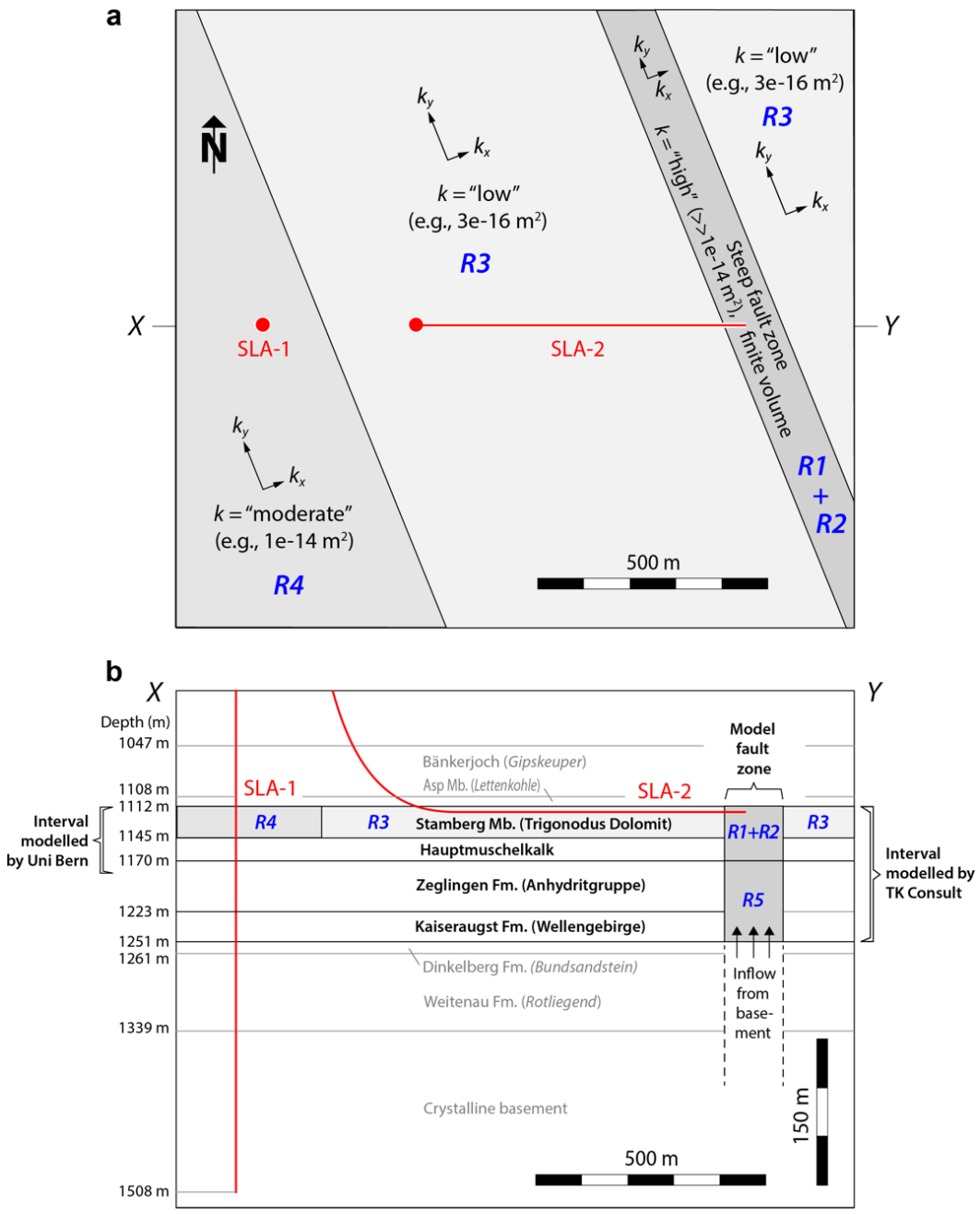


Figure 58: Updated conceptual hydrogeological model, based on the geological–geochemical concept illustrated in Figure 50.

(**a**) Map view of the distribution of regions R1 to R4 with preliminary (pre-calibration) estimated permeabilities and the locations of wells. The high areal extent of region R3, its low permeability and its abrupt contact with zone R4 surrounding well SLA-1 are all features that have been retained unmodified from the Künze & Kuhlmann (2020) model of TK Consult. While regions R1 and R2 correspond conceptually to those in the TK Consult model from 2020, their positions have been changed. The drainable reservoirs R1 + R2 in the 2020 TK Consult model (Figure 57) are now combined to represent a steep, permeable fault zone, which acts as a conduit for water rising from the crystalline basement. (**b**) East–west vertical cross-section of the model domain at the two SLA wells (vertical scale is highly exaggerated). A new region R5 is defined, extending the hydraulically conductive fault zone below the permeable regions R1 and R2, allowing inflow from the basement.

Modification of TK Consult 2020 numerical model

TK Consult first revised the permeability structure around SLA-2 in their numerical model to accommodate the updated conceptual hydrogeological model shown in Figure 58. As well as incorporating all regions R1 to R5, this required refining the stratigraphy into the sequence Stamberg dolostone (*Trigonodus Dolomite*) - Hauptmuschelkalk – Zeglingen (*Anhydritgruppe*) – Kaiseraugst (*Wellengebirge*) (Figure 59). TK consult then (re-)calibrated the permeabilities of all formations and regions R1 to R5, estimated the volume of the confined reservoir (i.e. the conduit) made up of R1+R2+R5, and calculated fluxes across model and formation boundaries to be used in the Uni Bern thermal–hydraulic–chemical (THC) model as boundary conditions. The recalibration of permeabilities and reservoir volumes was constrained by the pumping rates and pressure potentials measured in 2024-2025. In addition, in the new TK model the permeability of the basement was adjusted to match the 25% flux contribution from the basement to the produced SLA-2 water (Section 2.3.1). The calibrated permeabilities for the different regions and formations are summarized in Table 19, while the comparison between the pressure potentials measured in 2024-2025 and those predicted by the calibrated model is shown in Figure 60. More details about the groundwater simulations can be found in the TK consult report provided as Appendix 2.

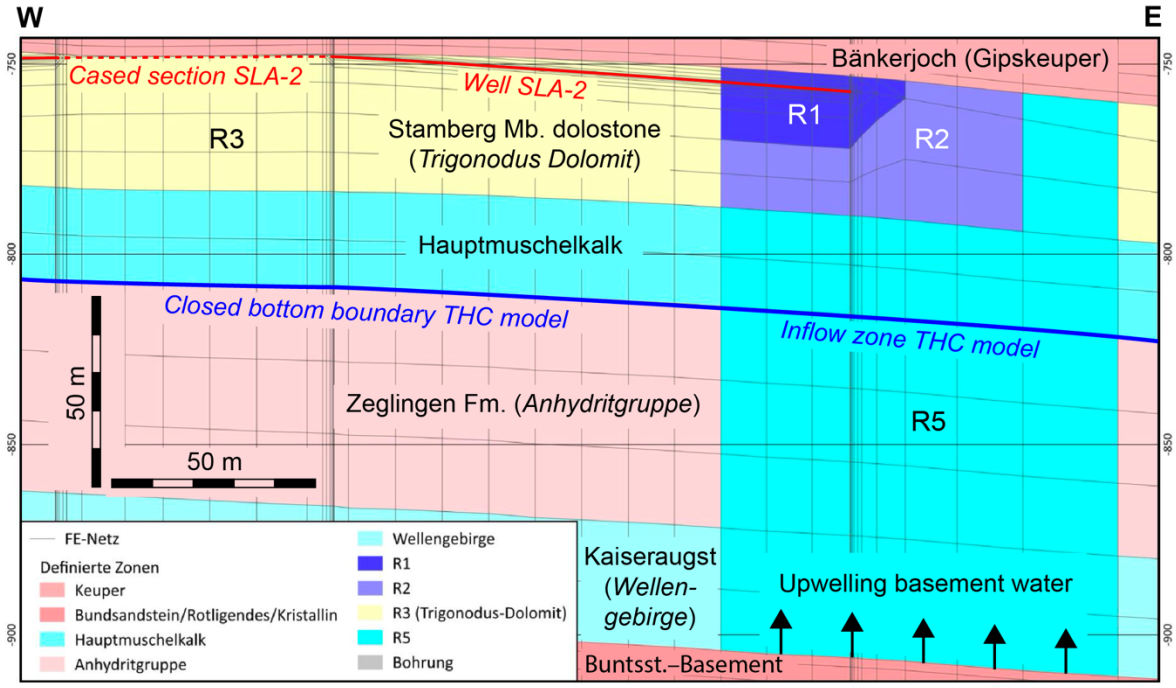


Figure 59: East–west vertical cross-section of the numerical hydraulic model by TK Consult, based on the conceptual model in Figure 58.

The full numerical model is of regional scale (Figure 57) and only a small part of the model at the end of the SLA-2 well (red line) is shown here. This model was used to recalibrate the permeabilities of the rock formations and the numbered regions, determine the volumes of regions R1, R2 and R5, and constrain boundary fluxes for the Uni Bern thermal–hydraulic–chemical (THC) model. The lower boundary of the Uni Bern model is shown in blue.

The calibration effort by TK Consult concluded that, due to the large number of degrees of freedom, there is no unique solution as to the permeabilities of regions R1, R2 and R5. Regardless of the non-uniqueness of specific region permeabilities, regions R1 and R2 have retained their high permeability and have a finite reservoir volume as in Künze & Kuhlmann (2020). Below these highly permeable regions R1 and R2 follows region R5, which completes the permeable fault zone conduit for upwelling basement waters. The permeability of this conduit is higher than the surrounding formation permeabilities but equal to or lower than the permeability of R1 and R2. Two possible permeability combinations obtained from the model calibration are shown in Table 19 as Variants 1 and 2. Note that in Variant 2, the conduit (regions R1+R2+R5) has a uniform permeability of 2E-13 m^2.

One interesting result of this calibration is the low permeability of region R3 (Table 19). Although the estimated permeability (2E-16 m^2) is in agreement with region R3 from 2020 (Künze & Kuhlmann, 2020), the existence of such a low-permeability zone and its sharp contact to the much higher "background" Muschelkalk permeability of region R4 (9E-15 m^2) (Figure 58) is challenging to explain. One could explain the strong permeability contrast between R3 and R4 as being exerted by the distribution of discrete permeable fracture zones or clusters and tight rock with lower matrix permeability in between. However, the background fracture network is essentially the same along the Muschelkalk segments drilled by the two Schlattingen wells, and east of SLA-2 the Muschelkalk represents a regionally very well-connected aquifer (Figure 55, Figure 56). This makes such a strong permeability contrast highly unlikely from a geological point of view (Diamond et al., 2025). Moreover, even the matrix permeability of the Muschelkalk is probably higher than 2E-16 m^2. It follows that the presence of an isolated low permeability domain and/or hidden fault zone between SLA-1 and SLA-2 (Hypotheses 2 and 3 proposed in Section 2.3.1) is not satisfactory to explain the low permeability of the region R3. The same applies to a possible groundwater divide located between SLA-1 and SLA-2 (Hypothesis 1). A more plausible explanation and hence the only remaining hypothesis for the low permeability of region R3 is the recent discovery of mineral scales within the horizontal borehole SLA-2 (Hypothesis 4, Section 2.3.1). Scales precipitating along the margin of the SLA-2 borehole during the early operation stage, forming a barrier between the rocks of R3 and the well early on, offers an explanation for the observations from the pumping tests at SLA-2. This issue will be discussed further in Section 2.3.3 below. Despite Hypotheses 1 (groundwater divide) and 2 (hidden fault zone) failing to explain the low permeability of region R3 and hence the hydraulic data from SLA-2, they may contribute to the hydraulic compartmentalization observed at Schlattingen.

Table 19: Two outcomes (Variant 1 and 2) of the model calibration from TK Consult based on the conceptual flow model (Figure 58) and the most recent pressure and flux measurements at SLA-2. Shown are re-calibrated formation and region permeabilities and the volumes of regions R1, R2 and R5 in the conduit.

		Variant 1			Variant 2	
Zones / Formations	**V [m^3]**	**K [m^2]**	**kf [m/s]**	**V [m^3]**	**K [m^2]**	**kf [m/s]**
Hauptmuschelkalk		5E-15	1.0E-07		5E-15	1.0E-07
Wellengebirge		5E-18	1.0E-10		5E-18	1.0E-10
Bundsandstein/Rotligendes/Kristallin		3E-16	7.0E-09		3E-16	7.0E-09
R1	2E+04	9E-12	2.0E-04	2E+04	2E-13	5.0E-06
R2	2E+05	5E-12	1.0E-04	2E+05	2E-13	5.0E-06
R3 (Trigonodus-Dolomit)		2E-16	5.0E-09		2E-16	5.0E-09
R4 (Trigonodus-Dolomit)		9E-15	2.0E-07		9E-15	2.0E-07
R5	6E+06	5E-14	1.0E-06	6E+06	2E-13	5.0E-06

The most recent pumping activity (2024-2025) revealed important differences compared to those from 10 years ago. The pressure potential has since dropped by some 230 m (about 50%) using the same pumping rate, and there is much less temporal variability in the potential measurements. Accordingly, the calibrated permeability for R1, R2 and R5 (Table 19) are by a factor of 25 higher than those determined for the production test carried out in 2015 (Figure 61). These observations point to a permeability increase in zones R1, R2, and/or R5 or perhaps even in the basement. It is reasonable to assume that this permeability increase is associated with the pumping activity at SLA-2. One plausible process leading to a permeability increase is the dissolution of anhydrite from the rocks in the Zeglingen Fm. (*Anhydritgruppe*) in R5 following the ascent of water from the crystalline basement which is undersaturated with respect to anhydrite (Figure 53). Basement water is therefore capable of dissolving anhydrite while passing through the Zeglingen (see Section 2.3.1 for a more detailed discussion). Since the current THC model only extends to the bottom of the Hauptmuschelkalk, the quantitative efficiency of this dissolution remains to be tested.

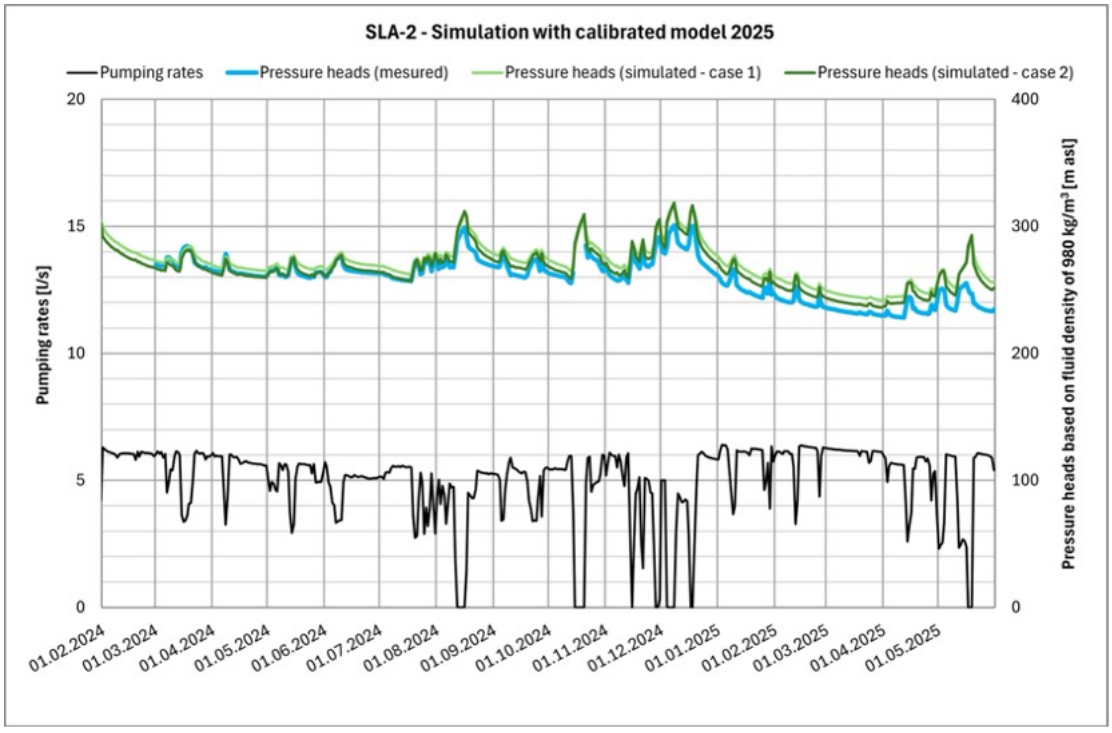


Figure 60: Comparison between measured and simulated hydrostatic pressures in SLA-2 between February 2024 and May 2025.

Note: Feb. 2024 to May 2025 is the time window used for calibration of the groundwater simulations. The permeability distribution for Variants 1 and 2 are provided in Table 19.

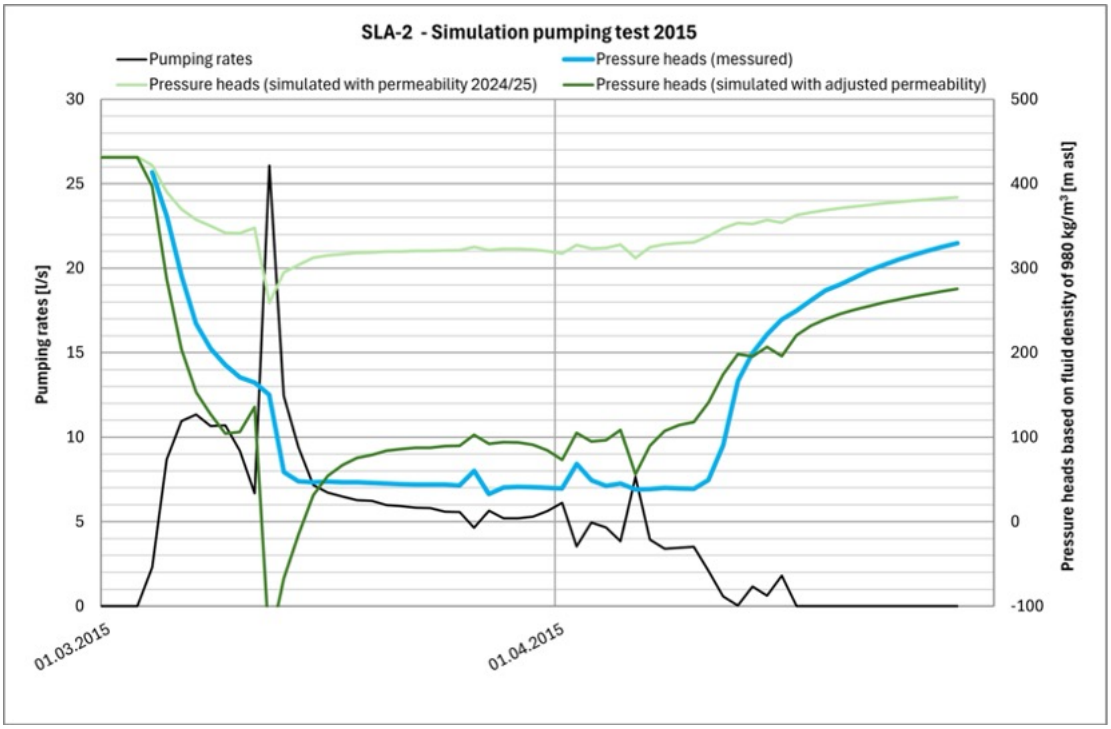


Figure 61: Comparison between measured and simulated hydrostatic pressures in SLA-2 in March/April 2015.

Note that the 2015 production vs. pressure data can only be matched by reducing the permeability of Region R1, R2 and R5 compered to Variant 1 of the updated TK Consult 2020 numerical model allowing to match the hydrostatic pressure data recorded in 2024/2025 (Figure 60).

2.3.3. Reactive transport modeling: The Uni Bern THC model

A local, smaller scale but high-resolution 3D coupled thermal-hydraulic-chemical (THC) model of the geothermal operation at Schlattingen was constructed at Uni Bern using the reactive transport code PFLOTRAN (Hammond et al., 2020). The lateral extent of the THC model is 2.5 km x 2.5 km and it includes both wells SLA-1 and SLA-2 (Figure 62). The model comprises the Muschelkalk aquifer within the Schinznach Formation, consisting of 35 m of the Stamberg Member dolostone overlying 24.2 m of the Hauptmuschelkalk and 11.2 m of dolostone at the top of the Zeglingen Fm. (*Dolomit der Anhydritgruppe*). To simplify the following discussion, the latter two units are referred to collectively as the Hauptmuschelkalk.

The vertical SLA-1 well is situated in the center of the domain and taps into the Stamberg dolostone (*Trigonodus Dolomit*). The deviated SLA-2 well enters the Stamberg some 575 m to the east of SLA-1, then runs horizontally within the Stamberg formation for a distance of 784 m. At 747 m the horizontal well reaches the upflow conduit (fault zone) and taps into region R1 (Figure 62). The well extends for another 37 m into the conduit itself.

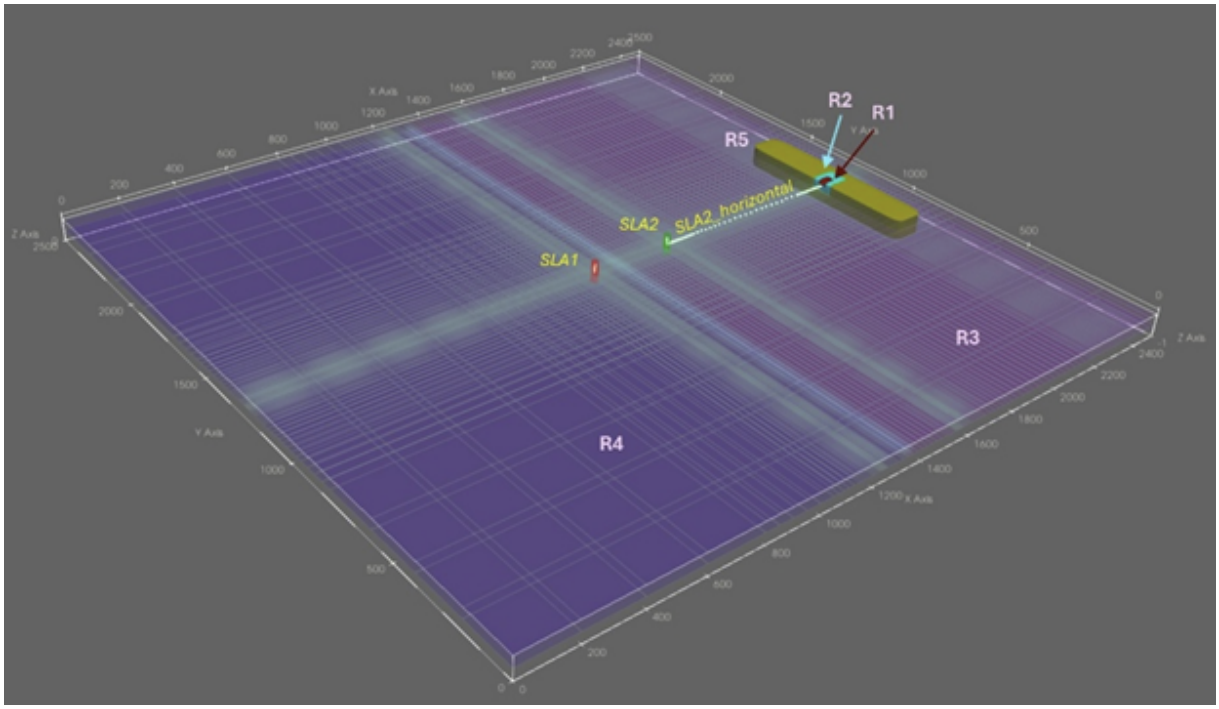


Figure 62: The Uni Bern THC model with the wells and regions R1 to R5.

The model is truncated at the bottom of the Hauptmuschelkalk. Upwelling from the basement through region R5 is implemented as a boundary flux into R5 at the bottom of the Hauptmuschelkalk Figure 59.

The calibrated permeabilities from the TK Consult model (Section 2.3.2) were used as input to the Uni Bern THC model. Similarly, internal fluxes were extracted from the calibrated TK Consult model to be implemented as boundary fluxes for the smaller scale THC model. Of particular importance is the flux of the upwelling basement water. Because the current THC model is truncated below the Hauptmuschelkalk (Figure 62), the flux of the upwelling water was extracted from the TK Consult model and input as boundary flux at the base of the fault zone conduit (Figure 62). Both models, the revised TK Consult model and the Uni Bern THC model, are thus consistent in terms of the underlying geological model, distribution of permeability zones, hydraulic parametrization, and flux conditions. Small discrepancies may arise from the use of different numerical grids, resulting in different spatial resolutions in certain parts of the domain. More significant, however, are differences arising from the fact that in the THC model, groundwater flow and heat transport are fully coupled, meaning that heat is transported conductively through the bulk rock and advectively by the moving water. The water properties density and viscosity are then computed based on the local temperature at each point in the system and at each time step (i.e. after the heat transport step) during the simulation. In contrast, the TK Consult simulations are purely hydraulic and assume constant water properties.

The TK Consult model and the Uni Bern model cover different spatial scales. The former is a regional scale model that considers natural recharge into the Muschelkalk aquifer where it outcrops some 22–25 km to the NW. The Uni Bern model is a local model that only encompasses the wells SLA-1 and SLA-2 and the zone of influence around them. The boundaries of the local model do not represent natural boundaries (such as infiltration zones or groundwater divides). Instead, the boundary conditions were extracted from the large-scale TK Consult model. This is not an easy task because the groundwater flow direction is not aligned with the principal coordinate directions of the THC model such that there are flux gradients along the boundary faces. Given that the “background” groundwater flow rates computed with the TK model are low (generally < 10 L/min, Figure 63), we assume in the first instance that there is zero background groundwater flow and all water movement across the boundaries are caused by pumping at SLA-1 and SLA-2. In other words, we assume fixed hydrostatic pressure conditions on all boundary faces with pressure gradients induced only by pumping. While TK Consult

used the recorded pumping history in SLA-1 and SLA-2 in 2024-2025, we use constant pumping rates of 2.5 L/s and 6 L/s at SLA-1 and SLA-2, respectively. These are the same pumping rates that were used by TK Consult to compute the fluxes shown in Figure 63.

Comparing the fluxes induced by pumping with natural background fluxes in Figure 63 shows that the former are at least a factor of five higher – and, in the south, opposite in direction to the natural fluxes. Hence, pumping clearly dominates the flow regime within the bounds of the THC model. Thus, our assumption of using hydrostatic conditions along the boundary and ignoring natural groundwater flow through the domain seems reasonable. However, fixing hydrostatic conditions introduces some artifacts during pumping in that if boundaries are too close to the drawdown cone around the well, pressure gradients are over-steepened and too much water is drawn across this boundary. This bias is avoided by increasing the size of the model beyond the zone of influence of pumping. Here we consider the size of the domain to be sufficiently large such that these kinds of boundary-related artifacts are negligible.

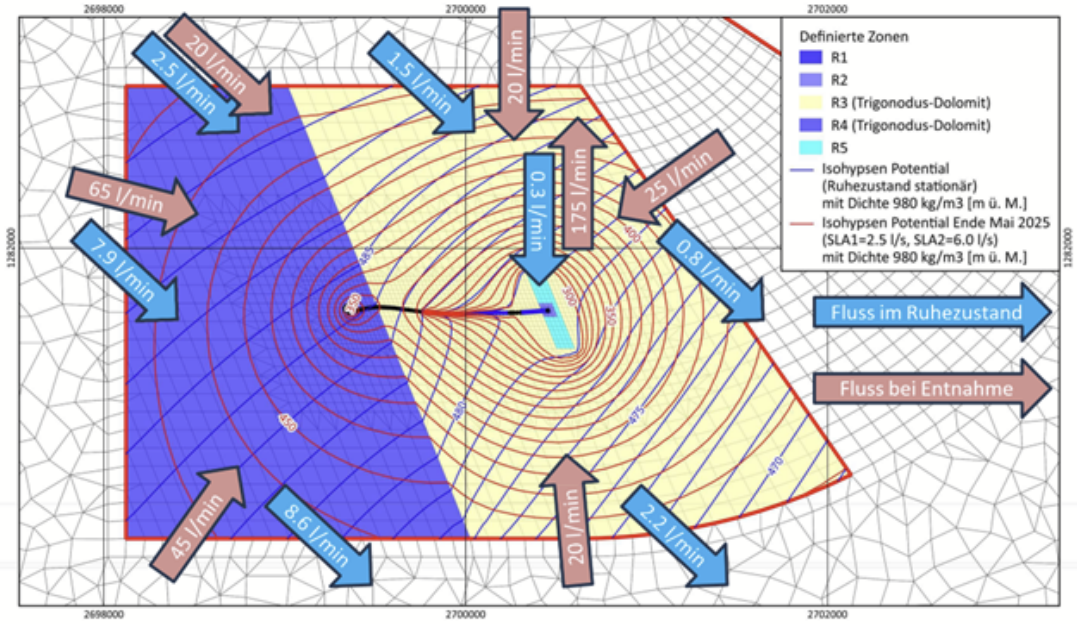


Figure 63: Fluxes computed by TK Consult using their regional model.

These provided the boundary fluxes for the smaller scale Uni Bern THC model. Note that the pumping activity at SLA-1 and SLA-2 dominates fluxes into the model domain.

The low-permeability units Asp Mb. (*Lettenkohle*) and Bänkerjoch Fm. (*Gipskeuper*), which overlie the Muschelkalk aquifer, and the underlying Zeglingen Fm. (*Anhydritegruppe*) are represented as impermeable boundaries. Only where region R5 (the permeable fault zone conduit) intersects the bottom boundary of the model, i.e., the bottom of the Hauptmuschelkalk, is water allowed to enter the domain according to specified flux, water composition and inflow temperature (Figure 59). This inflow zone represents the upwelling of basement water that has been chemically modified by reaction with the lower units of the Muschelkalk and undergone some degree of cooling. This water has been referred to as modified basement water in Table 18.

While the flux across the inflow zone into the Hauptmuschelkalk can be extracted from the TK Consult model, there is some uncertainty regarding the exact composition and temperature of the water. Given that the fluxes of the upwelling water are on the order of 1.5 m^3/m^2/sec, as suggested by the TK Consult model and based on the knowledge that the basement water was at a temperature over 100 °C at some point at depth (Table 18.), it is reasonable to assume that the upwelling water carries excess heat compared to the local geotherm. We assume that the upwelling water has an elevated temperature of 75 °C at the bottom of the Hauptmuschelkalk. This assumption is somewhat arbitrary because without extending the model to the basement we do not know how much the upwelling water has cooled during its ascent from the reservoir to the inflow boundary of our model at the base of the Hauptmuschelkalk.

This vertical flux of 1.5 $m^3/m^2/yr$ was derived by adjusting the basement permeability to match the roughly 25% content of basement water in the produced SLA-2 water. A total flux balance over the fault zone conduit (R1 + R2 + R5 regions outlined in red in Figure 64), reveals the flux contributions summarized in Table 20. Taking into account the contribution from region R3 along the horizontal section of SLA-2 results in the flux balance shown in Table 21. The basement fraction is 27.3%, slightly higher than the target 25% but still within the acceptable range given the overall uncertainty of the simulations. The fraction of R3 water increases from only 4.3% in the conduit to 13% in the SLA-2 water, owing to flow into the open-hole sections of the well to the west of the fault zone conduit (green arrows in Figure 64).

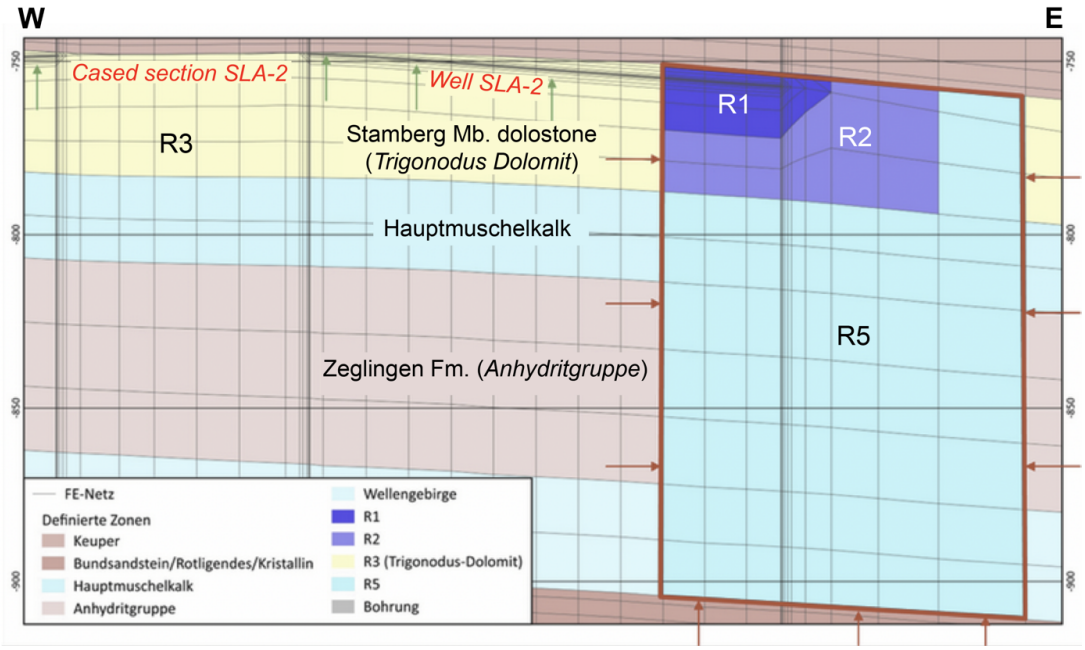


Figure 64: Illustration of how flux balances were obtained with the TK Consult model.

The region outlined in red is the fault zone conduit, which shows flux contributions from the surrounding formations. These flux contributions were introduced upon the onset of pumping and subsequently over time, when the initial pre-pumping water has been replaced, thereby controlling the composition of the water in the conduit (Table 20). The SLA-2 water containing the estimated 25% basement fraction is the water from the conduit plus the contribution from R3 along the horizontal segment of SLA-2 (green arrows) (Table 21).

Table 20: Flux contributions in the fault zone conduit water computed with the TK Consult model

Keuper	0.0%
R3 (Trigonodus-Dolomit)	4.3%
Hauptmuschelkalk	64.8%
Anhydritgruppe	0.3%
Wellengebirge	0.6%
Bundsandstein/Rotliegendes/Kristallin	30.0%

Table 21: Flux contributions in the produced SLA-2 water computed with the TK Consult model

Keuper	0.0%
R3 (Trigonodus-Dolomit)	13.0%
Hauptmuschelkalk	58.9%
Anhydritgruppe	0.3%
Wellengebirge	0.5%
Bundsandstein/Rotligendes/Kristallin	27.3%

Note that Table 20 and Table 21 show the flux contribution during pumping and not the natural pre-pumping water composition in the conduit. When pumping started at SLA-2, the first water produced from the well was dominated by the natural, pre-pumping porewater extracted from the conduit with some admixture of R3 water via the open-hole horizontal section of SLA-2. Over time, as pumping activities proceeded, the flow conditions and flux contributions from different units, controlled by their individual hydraulic properties, started to overprint the composition of the initial water and successively became the determining factor of the water composition in the conduit (i.e. the hybrid water shown in Figure 53). Given the estimated volume of the regions R1, R2 and R5 (Table 19) and a pumping rate of 5-6 L/s, this overprinting would be a slow process and probably take several years. However, there is no evidence in the geochemical data for a major change in the water composition during the pumping activities over the past 10 years which means that the flux-dominated water composition is probably similar to the natural water from the pre-pumping stage.

In the first set of simulations we represent the system in its current (late 2025) state, consistent with the TK Consult model. The initial water composition in the conduit is fixed according to the flux contributions from the surrounding formations (Table 20). The SLA-2 water is then expected to have mixing ratios as in Table 21. Note that pumping at SLA-2 was intermittent and pumping rates varied in time. A pumping rate of 6 L/s, as assumed in our model, would represent above-average pumping activity. The integrated effect of I pumping at SLA-2 during this project (2023 - 2025, Figure 41) would be equivalent to a continuous production at 6 L/s over a time span of 1.5 - 2 years (500-700 days). This is important context for the interpretation of the modelling results. In particular, given that continuous production at SLA-2 only started in 2023 (Appendix 2, Figure 11), it means that the current (late 2025) state of the system is defined after about 550 days of simulated time, and results for times after 550 days are predictions of the future evolution of the system, which are obviously not verifiable at present.

Using the permeability distribution of model Variant 1 (Table 19) and a flow rate along the conduit of 1.5 $m^3/m^2/yr$ results in a breakthrough of water components and temperature at the SLA-2 well head as shown in Figure 65. The breakthrough curves indicate that in the first 1.5 years (550 days) a slight dilution of the produced SLA-2 water occurs as the Hauptmuschelkalk (HMK) component increases at the expense of the saline modified (reconstructed) basement water that constitutes roughly 30% of the initial water in the reservoir. This is consistent with the observed decrease in the Cl- concentration in thermal water produced from SLA-2 in the years 2019-2020 and 2023-2025 (Figure 44, Figure 45) as well as with the decrease of the corresponding $\delta^{18}O$ values between 2019 and 2025 (Table 17, Figure 46). The R3 component in the SLA-2 water amounts to about 10%, which is somewhat lower than the value of 13% in Table 21 but still in good agreement.

After 550 days in Variant 1 the first aliquots of modified basement water (i.e. the water drawn into the reservoir from below the Hauptmuschelkalk) are predicted to appear in the produced SLA-2 water, and the fraction of HMK water steadily decreases thereafter. This change is expected to correlate with an increase in salinity and production temperature, such that upon 2500 days of simulated time the production temperature exceeds 63 °C. If in the near future no temperature increase is observed in reality, then we can infer that the assumed flux contribution from the basement (1.5 $m^3/m^2/yr$) is too high.

Running the same simulation with the high-permeability Variant 2 (Table 19) leads to an earlier breakthrough (0.5 years) and an even higher basement fraction (and higher salinity) and to temperatures

that are 1-2 °C higher than Variant 1 during the first 2000 days. After that, the thermal and solute breakthrough curves of the two variant cases tend to merge. This is an interesting observation that suggests that the permeability distribution in the conduit only has a temporary effect on the composition and temperature of the SLA-2 water. In the long-run, conditions at the well head of SLA-2 seem to converge to the same steady state. This is principally consistent with the conclusion of TK Consult that the calibration of the permeability structure around SLA-2 is non-unique (both variants reproduce the hydraulic data collected during pumping), but before converging to the same or similar stead state, there are significant transient differences in the thermal and compositional evolution of the SLA-2 water that are indeed dependent on the permeability structure. Based on current knowledge, the early breakthrough of the basement component in Variant 2 is inconsistent with current observations and it appears that the low-permeability Variant 1 better matches the available hydrochemical observations (Figure 44). Nevertheless, even though geochemical constraints help narrow down the range of plausible formation permeabilities, uncertainties regarding the permeability structure around SLA-2 remain. This concerns not only the hydraulic properties of the formations and regions, but also the distribution, size and geometry of those regions. Additional observational data would help reduce these uncertainties.

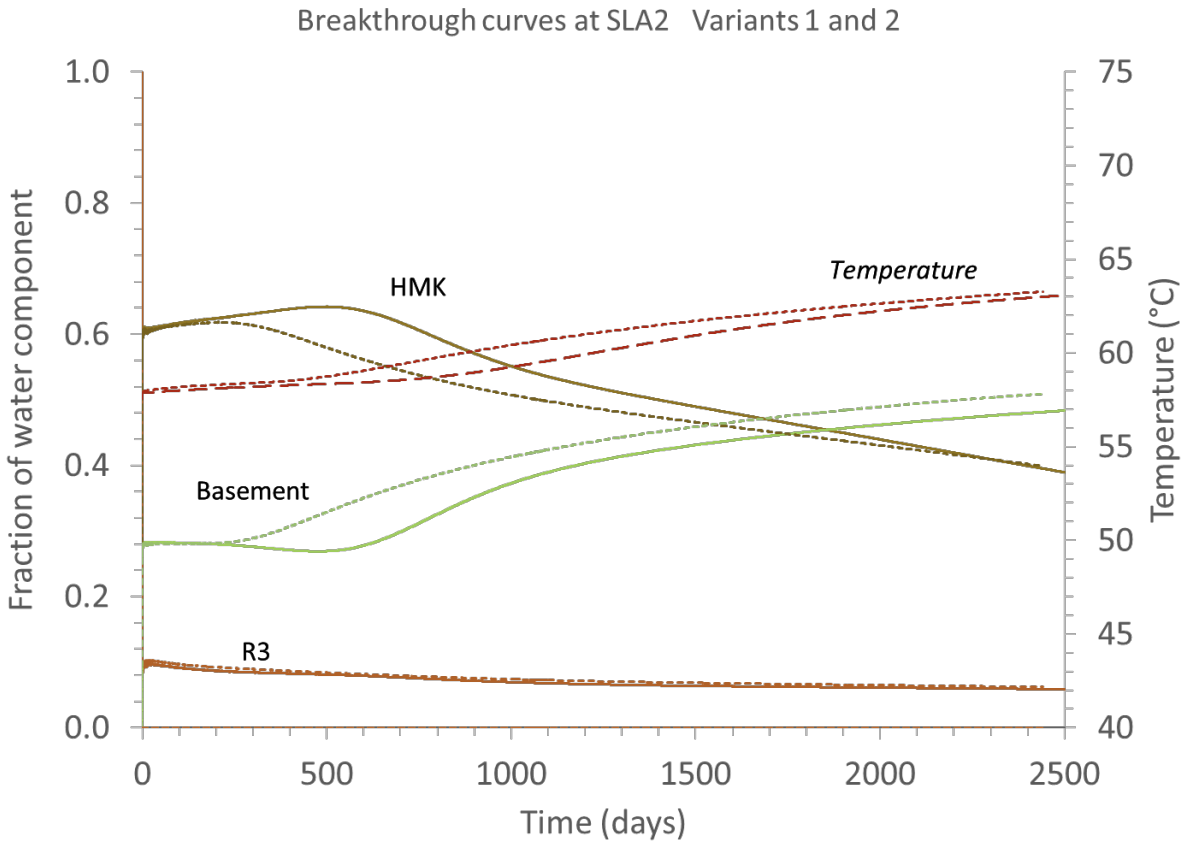


Figure 65: Thermal and compositional breakthrough curves for water exiting the SLA-2 well head for the lower permeability model Variant 1 (solid or long dashed) and the higher permeability Variant 2 (short dashed) using a basement flux of 1.5 $m^3/m^2/yr$ (see Table 19 for permeability values).

Present time (late 2025) corresponds to approximately 550 days on the *x*-axis. Abbreviation HMK denotes the Hauptmuschelkalk. See Figure 59 for definition of region R3. Both HMK and R3 waters have low salinity, whereas the basement water has relatively high salinity. Both variants show initially increasing HMK fractions (dilution of salinity) followed by a rebound in the fraction of basement water (HMK component decreases, salinity increases). The temperature increases steadily and is predicted to reach about 63-64 °C after 2500 days (6.9 yr). Both variants show a very similar evolution in the first year, then deviate strongly before merging again in the long-run.

The primary process controlling composition and temperature of the SLA-2 water seems to be the influx of the chemically modified basement water in relation to the volume of the upflow zone. Looking at the long-term evolution in Figure 65 (basement flux 1.5 $m^3/m^2/yr$), we would expect to see a relatively strong temperature and salinity increase within the next 2 years. To test the implication of the basement flux on temperature and the fraction of the basement component, we run two additional scenarios using basement fluxes of 1.0 $m^3/m^2/yr$ and 0.5 $m^3/m^2/yr$.

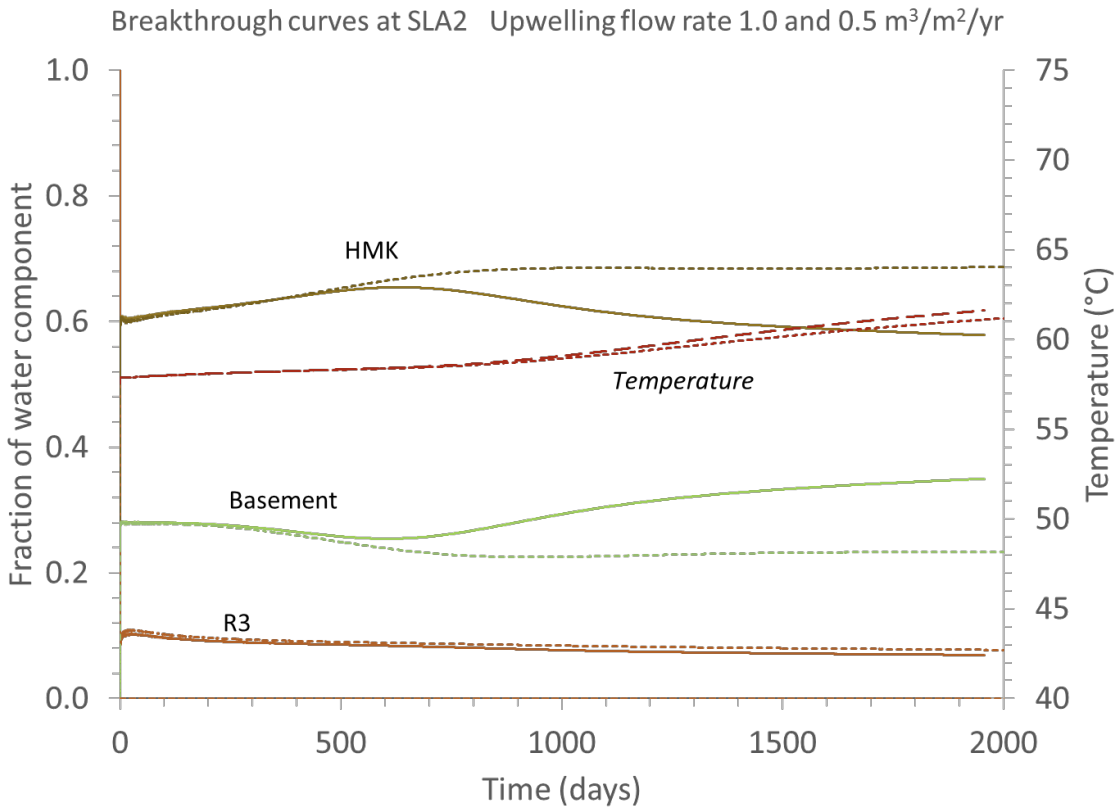


Figure 66: Thermal and compositional breakthrough curves at the SLA-2 well head for two upwelling flow rates: 1.0 $m^3/m^2/yr$ (solid or long dashed) and 0.5 $m^3/m^2/yr$ (short dashed) using the permeability structure of Variant 1. Current time (late 2025) is at approximately 550 days.

Both scenarios show the same initial dilution as in Figure 65. The fraction of modified basement water serves as a proxy for salinity. While the salinity at higher fluxes rebounds – albeit less than in Figure 65– the salinity at lower fluxes remains constant with a modified basement component of around 25%. The water temperature is slightly lower than in Figure 65 at the same snapshots in time. Thus, the magnitude of the upwelling basement flux controls the salinity and temperature of the water at the SLA-2 well head. Future observations of salinity evolution in the produced SLA-2 water will afford better evaluation of the basement upwelling flow rates.

Figure 66 shows that with an upwelling flux of 1.0 $m^3/m^2/yr$, after an early-stage dilution (Hauptmuschelkalk component increases, basement component decreases) up to the present (550 days; late 2025), the trend is reversed and the modified basement component and salinity exceed their respective initial values. Although lower than in Figure 65, this increase in salinity implies that there is still sufficient modified basement water upwelling, relative to the influx of dilute water from the Muschelkalk aquifer, such that SLA-2 draws more modified basement water than the observed 25% (roughly 32%). By reducing the basement flux to 0.5 $m^3/m^2/yr$, we achieve a near perfect 25% modified basement component in the SLA-2 water after a period of dilution during the first 2 years. This early dilution seems to be a persistent feature in all simulation cases (Figure 65 and Figure 66). Unlike at higher basement influx rates, the basement component remains constant at 25% even in the long run (Figure 66). This indicates that after 2 years a steady state mixing ratio has been attained between upwelling saline modified basement water and dilute Muschelkalk aquifer water. This ratio is in perfect

agreement with geochemical data. We conclude that with a basement flux on the order of 0.5 $m^3/m^2/yr$ we can achieve a very good agreement with the evolution of salinity as seen in Figure 44 and Figure 45, but, again, it remains to be seen how the salinity evolves in the next 1-2 years. Although we have achieved agreement with the fraction of modified basement water at these relatively low fluxes, the model still predicts a noticeable temperature increase in the produced SLA-2 water (~63 °C after 2000 days, Figure 66).

Our conclusions do not contradict the TK Consult model. We have used the same permeability structure around SLA-2. The difference is that we used additional constraints (explicit mixing and temperature) to assess the upwelling flux from the basement. If within the next two years or so there is no significant increase in salinity and temperature at the SLA-2 well, the flux (and probably the basement permeability as well) can be deduced to be lower than that assumed in the TK Consult model, i.e. on the order of 0.5 $m^3/m^2/yr$. If this turns out to be true, the basement fluxes in the TK Consult model could be adapted and the permeabilities of regions R1 to R5 may have to be re-adjusted accordingly. In any case, with the current models we have developed a good understanding of how the system works. But in terms of the predicted evolution of the system (Figure 65 and Figure 66), we are still in the early stage (< 500-700 days) where we see a dilution of the mixed water due to an increase in the Hauptmuschelkalk component in all model scenarios. This increase in the Hauptmuschelkalk component is entirely consistent with geochemical observations. However, it remains to be seen if and how the SLA-2 water composition and temperature will change in the next 1-2 years (assuming that pumping continues at the current rate) and which of the scenarios presented above most closely approximates reality.

Assessing scale formation as potential cause for the permeability anomaly in R3

As detailed in Section 2.3.1 above, scales of unknown mineralogy have been observed coating the inner casing wall of well SLA-2 at a depth of 443 m, but no observational information is available for greater depths. The possibility of the scaling being present along the deep horizontal section of the well within the Muschelkalk aquifer is important to evaluate, as it may explain the low permeability of R3 inferred from the calibration of pumping tests and the strong permeability contrast of several orders of magnitude between regions R3 and R4. Mineral scaling may lead to clogging of the connected porosity at the end of the borehole, thereby inhibiting flow between R3 and the borehole. Such a local permeability reduction along the horizontal section of the borehole could have caused the slow pressure recovery observed after pumping in 2015 and the apparent low permeability of zone R3 (Table 19). The triggering mechanism for scale formation is the admixture of Muschelkalk aquifer water (Water 1, Figure 53) to the modified basement water pumped from the conduit (Water 3, Figure 53). Both waters are in equilibrium with the highly reactive minerals calcite and anhydrite, hence a slight change in chemical conditions could already trigger their precipitation. Batch-type calculations have shown that mixing the two endmembers, modified ("reconstructed") basement water and SLA-1 type Muschelkalk water, leads to the oversaturation of anhydrite and calcite (Figure 54), hence their precipitation is expected.

To assess these possibilities, we integrated the fundamental chemical processes leading to scale formation into the THC model. A first aim was to test whether immediately upon onset of pumping, mineral scaling indeed takes place along the whole length of the horizontal section of SLA-2, thereby limiting water inflow from the surrounding rocks and hence mimicking the effect of the low formation permeability assigned to region R3. Note that because the observation of scale formation within SLA-2 is recent, these simulations only provide first-order insights at this stage. For instance, for lack of time we have not yet included the full feedback loop between scale formation, porosity and permeability reduction and the update of flow and transport conditions, i.e. the feedback of scaling on mixing itself. Inclusion of these features in future modelling work would allow a more stringent test of the efficacy of the conceptual chemical processes proposed in Section 2.3.1, and would allow more reliable predictions of the likely evolution of scaling in SLA-2 and its implications for the hydraulic conditions around SLA-2. The feedback between scale formation and permeability reduction is essential for making a reliable long-term assessment of reservoir performance. Without it, there is no self-limitation of the scaling process and it will continue unless other mechanisms inhibit the mixing process. The current model is still very useful in terms of confirming the physical and chemical plausibility of our conceptual model and providing

valuable insights into the scaling process (e.g. the mineral composition of scales), but long-term predictions about its impact on reservoir performance should be made with caution. The hydrogeological model is identical to that of the mixing model described in the previous section. A new feature is that flow and heat transport are coupled to a reaction network that consists of three reacting minerals, dolomite, calcite and anhydrite, and a suite of aqueous species that are part of the composition space defined by these minerals. The rock of the Stamberg formation is composed of dolomite with accessory calcite, that of the Hauptmuschelkalk of calcite. There is no primary anhydrite in the rock, but the initial pore water and the inflowing modified basement water are in anhydrite equilibrium. The simulations are conceptually different compared to the mixing simulations above in that we start with an assumed initial natural state of the system in which R3 and R4 have the same hydraulic properties (permeability 9E-15 m^2). These ensure effective hydraulic connection between the open-hole section of SLA-2 and the surrounding formation. We assume that the initial porewater in the fault zone conduit is the modified (reconstructed) basement water (Table 18), without any admixture of water from the Muschelkalk aquifer. Hence, the underlying assumptions regarding the endmember water compositions are the same as in the batch mixing model in Figure 54. Finally, we assume that anhydrite and calcite will precipitate instantly wherever they reach supersaturation.

The simulation results confirm that, immediately upon onset of pumping, anhydrite and calcite precipitate along the open borehole. The profiles in Figure 67 show the distribution of active mineral precipitation and the amount of precipitated minerals in R3 at the end of the open well. This region constitutes a mixing zone between water from the fault zone conduit and R3. Mixing and mineral precipitation occur within the pore network of the rock, such that a small volume of scales may be sufficient to significantly lower permeability.

Anhydrite is the predominant scaling mineral predicted to occur along the entire length of the well, except along the 37 m long interval protruding into the fault zone conduit (zone R1). There, calcite dominates the mineral scales. The amount of anhydrite increases towards the vertical section of the well (distance = 0 m) (Figure 67).

Over time, both anhydrite and calcite accumulate (Figure 68 and Figure 69). Anhydrite remains the predominant mineral in scales, and calcite precipitates in lesser quantities. The interval of calcite predominance in region R1 shifts slightly downstream with time (i.e., upwards along the well) and anhydrite becomes the predominant mineral in region R1 (Figure 68). This indicates that after 10 years, the system has not yet attained steady state. One possible reason for this could be the slow replacement of the initial water in the fault zone conduit by water from the surrounding formations. Once the initial water in the conduit has been replaced, the system should attain steady state.

Footage from remote cameras inserted into the well reveal that the volume of the well has been reduced by about 50% at the transition to the 7'' casing at 443 m depth due to clogging by scales (Section 2.2.4). If we integrate the volume of anhydrite that the model predicts to precipitate around the horizontal section of SLA-2, this integrated amount would fill only around 2–3% of the volume of the borehole. This may imply a significant discrepancy between observations and model results. Figure 70 shows that large quantities of anhydrite precipitate in the conduit (regions R1, R2 and R5). As a consequence, the potential for clogging the borehole is significantly reduced. Two zones of enhanced anhydrite precipitation can be identified: one above the upflow zone (R5), the other in region R1 (Figure 70). Owing to the relatively high permeability of the fault zone conduit, mixing between upwelling modified basement water and Muschelkalk water is very effective, especially in region R1. If we include the amount of anhydrite precipitating within the conduit, the total amount would easily fill 50% of the borehole.

Thus, it seems that mixing between the two endmember waters and the ensuing precipitation of anhydrite in the conduit, outside the borehole, has been overestimated. There are several ways to reduce mixing within the conduit. The most obvious would be kinetic retardation of precipitation. At low degrees of supersaturation, scales can form at some distance downstream from the site of physical mixing, owing to slow precipitation kinetics (the water is only at 57 °C, and reaction rates are not likely to be high). Evidence for kinetic retardation of precipitation is the occurrence of scales within the borehole more than 300 m above the aquifer, that is downstream from the active mixing zone. Alternatively, hydraulic conditions such as a strong anisotropy within the conduit, with preferential flow

in the vertical direction, preventing lateral inflow from the Hauptmuschelkalk, could reduce mixing within the upper conduit. In fact, such an anisotropy has been inferred from fracture measurements along the Schlattingen borehole (Diamond et al., 2025). An anisotropic permeability distribution could be easily implemented in the model, but would require another recalibration of the overall permeability structure.

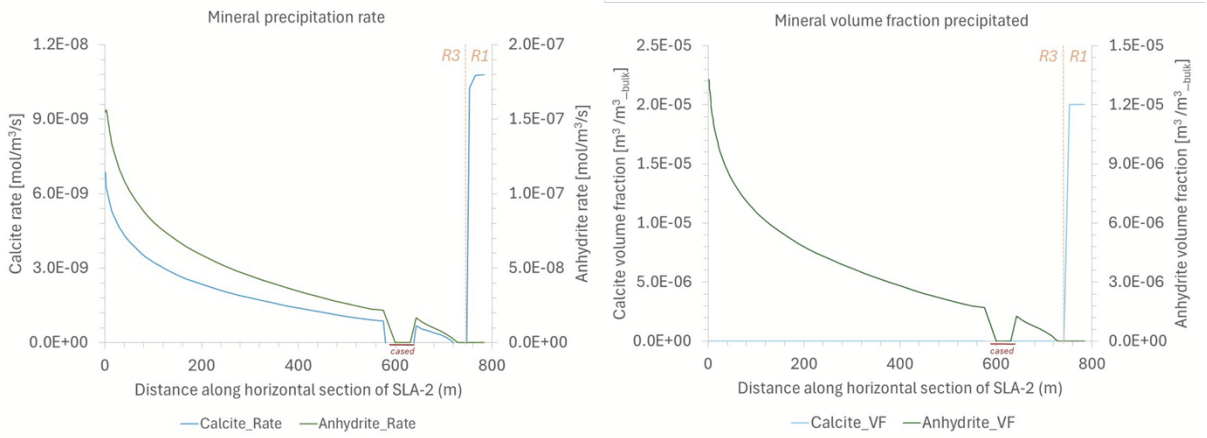


Figure 67: Mineral precipitation rate and volume profiles along the horizontal section of SLA-2 after 3 weeks of operation.

Distances are relative to the western end of the horizontal section. Added to the profiles are the position of the boundary between R1 and R3 as well as the location of the cased interval where scales are absent. The profiles show that scaling along the entire length of the borehole (except for the cased interval) is initiated as soon as pumping starts. Anhydrite and calcite are the predominant minerals in the scales in regions R3 and R1, respectively.

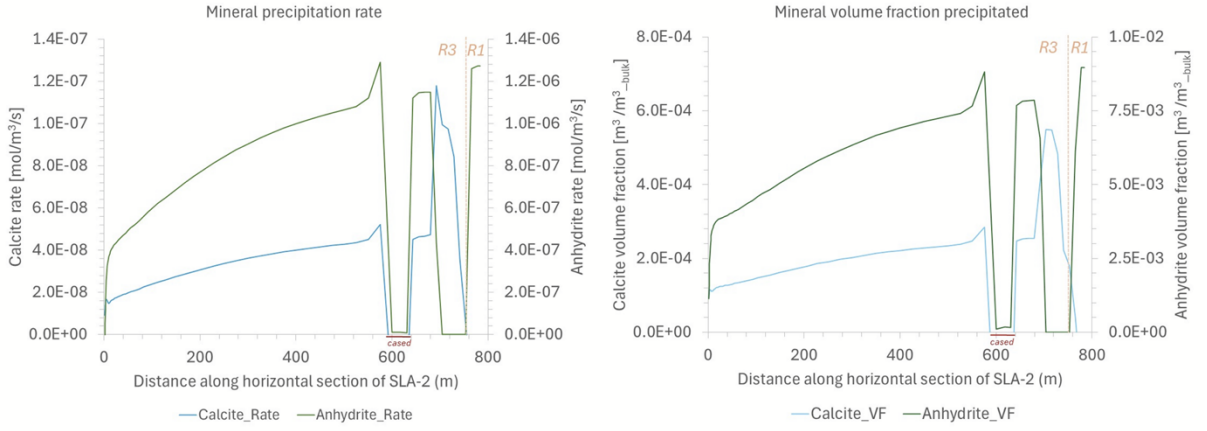


Figure 68: Mineral precipitation rate and volume profiles along the horizontal section of SLA-2 after 10 years of operation.

Distances are relative to the western end of the horizontal section. Added to the profiles are the position of the boundary between R1 and R3 as well as the location of the cased interval. The predominant mineral in the scales is anhydrite, and calcite occurs in lesser amounts. Both minerals continue to precipitate along the entire length of the borehole (except for the cased interval), although the distribution is more heterogeneous than during the early times (Figure 67). Anhydrite is now the most important mineral precipitating in R1, while calcite is predominant slightly downstream of region R1.

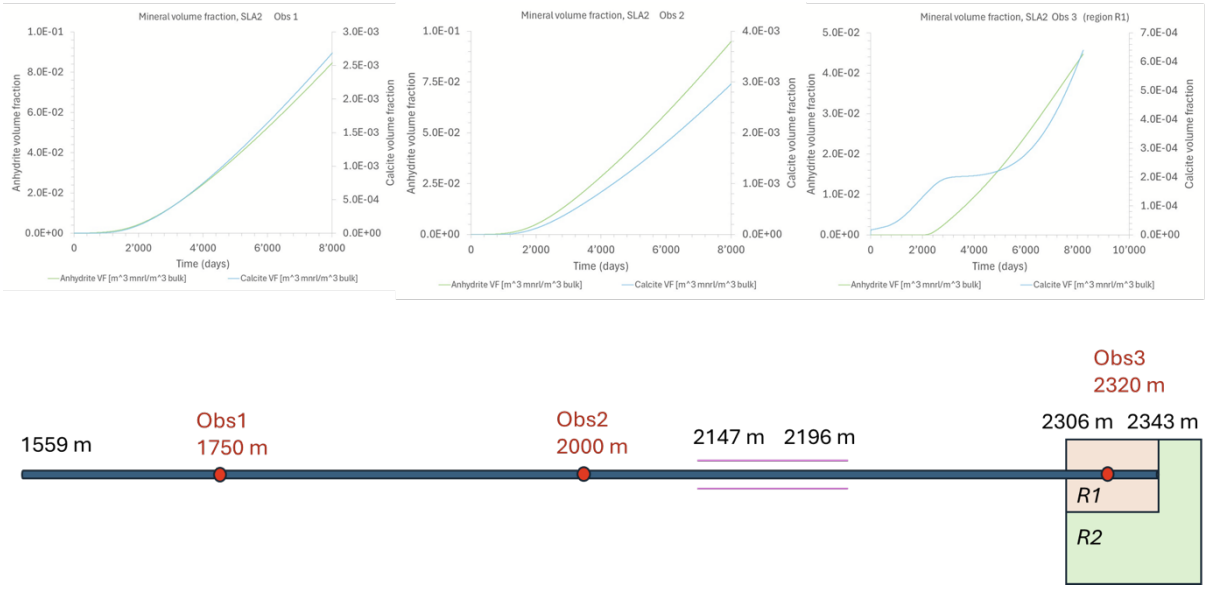


Figure 69: Time series of mineral volumes in the wall of borehole SLA-2 at three observation points, Obs 1-3.

Distances in the lower panel are relative to the western end of the model domain. The time series confirm that anhydrite is the dominant mineral in the scales. All volume fractions increase steadily as there is not yet an inhibition mechanism such as complete clogging of porosity in the model. In region R1, mineral scales are first dominated by calcite and later by anhydrite. Note the different volume scales for anhydrite and calcite on the left and right vertical axis, respectively.

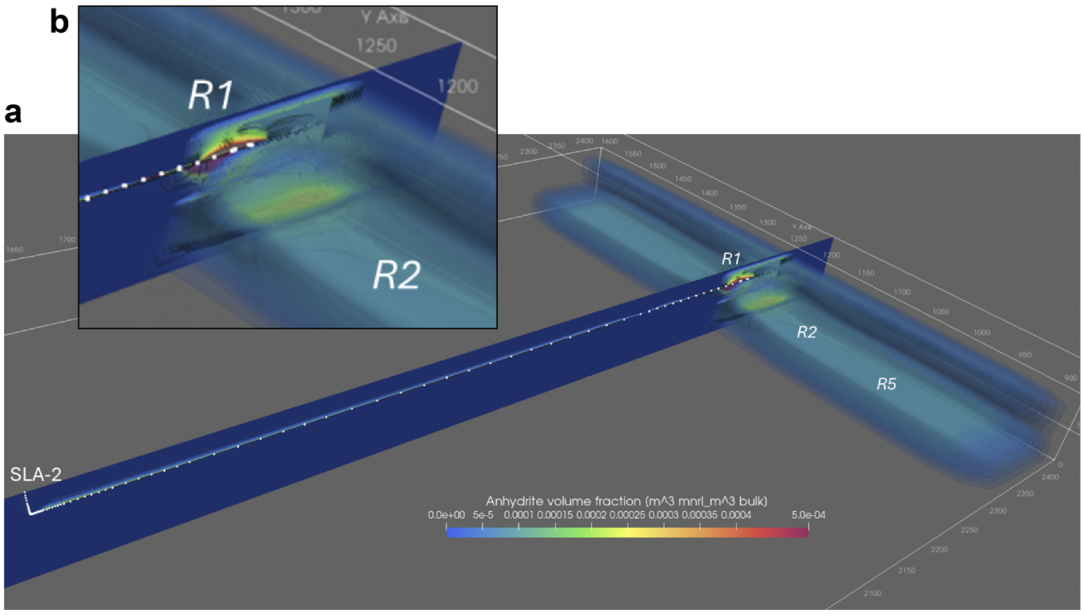


Figure 70: (a) 3D view towards ENE showing the distribution of anhydrite around the horizontal section of the SLA-2 well.

Anhydrite precipitation along the borehole (indicated by white dots) is consistent with Figure 68. (b) Close-up of anhydrite distribution at the eastern end of the well. Important to note is that, in this simulation with instantaneous precipitation rates, large quantities of anhydrite precipitate before the water enters the borehole, notably above the inflow zone and in region R1.

Based on the Uni Bern THC model we consider it worthwhile to follow up on two important issues. The first is related to the hydraulic and chemical properties of the conduit. Specific questions are:

- What are the flow rates and permeability structure in the basement and in the conduit at SLA-2 that reproduce the temperature and salinity at the well head?
- What process has led to the permeability increase in the conduit over the past 10 years?

The second issue is related to the formation of scales in the borehole. Specific questions are:

- What are the implications of mineral scaling due to water mixing along the borehole?
- Can we use observational evidence from the borehole (volume of scales, extent of scale formation beyond the zone of physical mixing) to calibrate precipitation rates?
- Does the permeability structure in the conduit (e.g. anisotropy) affect scaling in the borehole?
- How transferable are these insights to other sites?
- How can scaling be prevented or remedied?

The first issue can be addressed with a larger scale THC model that extends into the crystalline basement. The second issue requires a broader approach, combining experiments and modelling. Specifically, experiments and modelling need to address the implications of scale formation for flow and transport and thus for the mixing process itself. Here it is important to understand whether scale formation is self-limiting and produces a “natural casing” or if it is cumulative and produces clogging of the borehole.

3 Implications for harnessing geothermal energy in the Canton of Thurgau

The 12-year history of successful operation of the Schlattingen geothermal wells has proven the potential of the Muschelkalk aquifer in the Molasse Basin for reliable production of thermal water. This report has revealed new insights into the geological, geochemical and hydrogeological processes within the Muschelkalk aquifer, which determine the success of the Schlattingen site. Based on these insights, the following implications can be drawn for geothermal projects in the wider area of Canton Thurgau.

Implications for exploration for new geothermal sites:

- In the Canton of Thurgau, thermal water can be continuously produced over at least the decade time-scale from two hydraulically different geothermal plays within the Muschelkalk aquifer at rates and temperatures of 5 L/s and 55-60 °C (Figure 71). Both plays are located west of the Randen Fault at a depth of ca. 1100 m below ground, and both are in our opinion promising targets for future exploration.
- The first play ("**regional Muschelkalk**") is accessed by the SLA-1 well. It represents the classical aquifer-geothermal hydrodynamic properties of the Upper Muschelkalk rocks (Schinznach Formation), in the state that they occur over the 37 km region between SLA-1 in the east and the confluence of the Aare and Rhein rivers (near Waldshut) in the west. The aquifer rocks are confined above and below by impermeable evaporite rock units at the regional scale. The Ca-SO_4 type groundwater within the aquifer is slowly moving and is being recharged from the southern margin of the Black Forest Highlands. The temperature of the groundwater is controlled by the regional variations of geothermal gradients and depths of the aquifer. The rock-matrix porosity of the aquifer in the upper part of the Schinznach Fm. (the Stamberg Mb. dolostone, a.k.a *Trigonodus Dolomit*) is elevated and ensures high volumes of stored thermal water. The permeability of the aquifer is controlled by NNW-SSE trending fracture networks that hydraulically connect the vertical sequence of rocks within the Schinznach Fm. and also provide laterally extensive formation-parallel connectivity, as demonstrated by regional-scale flow fields within the confined aquifer. Nevertheless, in some areas flow within the Muschelkalk aquifer is compartmentalized by the occurrence of offsetting faults.
- We expect the rock-matrix porosity of the Muschelkalk aquifer to decrease strongly towards the south, such that in the southern realm of Canton Thurgau relatively little thermal water is stored and available for extraction by pumping. However, it is possible (though not yet confirmed), that the fracture network within the aquifer persists in the south, in which case the potential for geothermal exploitation would remain high.
- The second play ("**faulted Muschelkalk**") is accessed by the SLA-2 well and consists of steeply dipping fault zones that crosscut the Muschelkalk aquifer. Individual faults may have wide apertures and hence high permeabilities. This allows upwelling of highly saline fluids from underlying aquifers, most importantly the fractured crystalline basement. Groundwater in the permeable basement fracture network is under a high and permanent hydraulic-head gradient owing to its hydraulic connection to recharge areas in the crystalline portion of the Black Forest Highlands, and this drives the ascent of basement water into the Muschelkalk aquifer. Similar occurrences are the well-known thermal springs at Baden, Ennetbaden and Schinznach. Although the reservoir temperature of these basement fluids is demonstrated to be on the order of at least 100 °C, the flux of the upwelling deep groundwater may be too small to cause elevated temperatures in the Muschelkalk aquifer. Moreover, the volume of these permeable upflow zones is likely restricted, limiting the production rates. An additional challenge for producing geothermal energy from an SLA-2-type "faulted Muschelkalk" play is that mixing of the upwelling saline fluids with more dilute, Ca-SO_4 type groundwater of the Muschelkalk aquifer may cause significant amounts of scales to precipitate along wells, pumps and surface installations, eventually leading to technical issues. Likewise, the high salinity of the upwelling waters may promote corrosion of all these installations. It follows that scaling

and corrosion processes must be investigated in detail and mitigation measures planned at an early stage of geothermal exploitation of this play type.

- A logical extension of the “faulted Muschelkalk” play is to treat the permeable fault zones that tap hot basement fluids as a third geothermal play in its own right, independent of the Muschelkalk aquifer. This is supported by the high transmissivity measured in the crystalline basement at the bottom of the Schlattingen SLA-1 well (ca. 5E- 6 m^2/s; Frieg et al., 2015). This “**basement fault zone**” play could be accessed by drilling and casing wells down to the top of the basement aquifer (or the top of the Dinkelberg/*Buntsandstein*, which, where present, is hydraulically connected to the basement aquifer). This deep-reaching casing would isolate the wellbore from the complications of fluid mixing and associated scaling that arise when basement water enters the Muschelkalk aquifer. Not only the faults within the Variscan crystalline basement but also the faults that bound and intersect the Permocarboniferous troughs are included in this play. Previous work by Nagra showed that the distributed fracture network in the basement is spatially heterogeneous, such that drilling into the basement specifically with the aim of tapping into this fracture system for geothermal exploitation would have a high risk of failure. In contrast, a more promising approach is to drill into the basement where fault zones at the margins of the Permocarboniferous troughs are well imaged by seismic surveys or where the fault zones have been verified to rise out of the basement into the overlying sedimentary sequence. However, geothermal exploitation of these fault zones would be subject to their susceptibility to seismicity, which may be triggered by altering porewater pressure.
- The demonstrated existence of three distinct geothermal plays within the Muschelkalk in the Canton of Thurgau and adjacent areas implies that future geothermal exploration should consider targeting all three. For the “regional Muschelkalk” play, it is crucial to identify how far to the south the aquifer acts as a well-connected aquifer. This is important because the aquifer lies at ever greater depths towards the south and would therefore contain hotter water of greater interest for geothermal exploitation. Unfortunately, little information is available regarding the hydrodynamic behavior of the aquifer in the southern region of the Canton. Improving this would require drilling new exploration wells. In addition, 3D seismic surveys may provide insights into the location and frequency of steeply dipping fault zones that connect the crystalline basement with the Muschelkalk aquifer. Second- or third-order faults related to the main Randen Fault system may be prospective for this play. Other promising targets are boundary faults of the Permo-Carboniferous troughs.

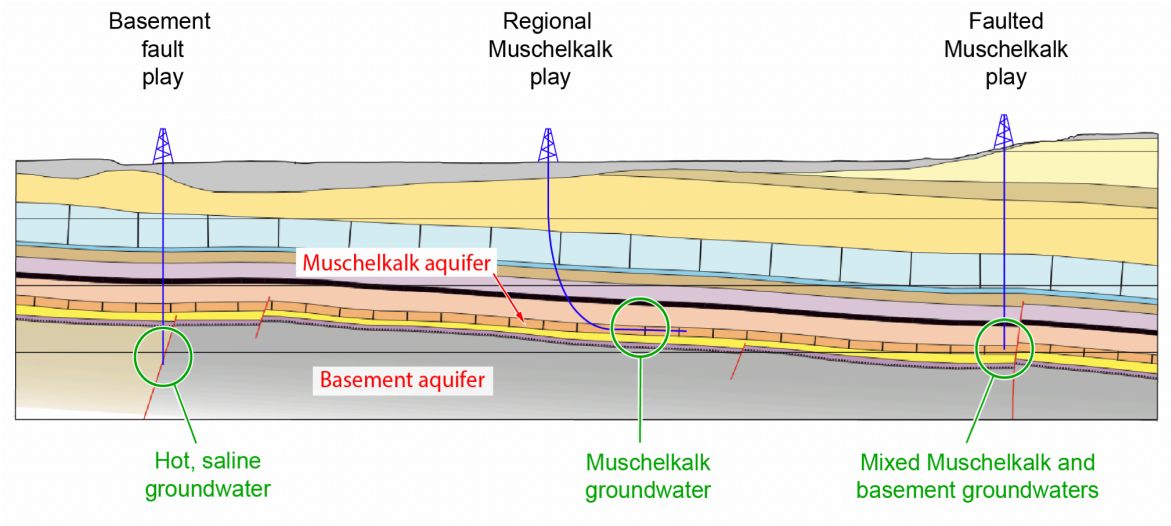


Figure 71: Conceptual illustration of the three exploration plays identified in this study for the Canton of Thurgau.

***Implications for design and operation of new geothermal sites**:*

The long-term production of thermal waters from the two wells in Schlattingen and the accompanying hydrochemical monitoring have provided valuable guidelines for the design and operation of geothermal plants in Canton Thurgau:

- Many geothermal wells in other areas are plagued by problems of corrosion due to high water salinities and high dissolved concentrations of H_2S and other acidic gases. However, such problems have not been encountered in the Schlattingen wells even after 12 years of production Examination of the surface installations and the results of the downhole televiewer survey in SLA-2 have shown that the thermal waters from the Muschelkalk aquifer, including the chemically mixed waters produced from SLA-2, have not significantly corroded the metal components of the surface tubing and well completion. This is notable, because after drilling of the wells and during their initial operational phases, the thermal waters of both boreholes SLA-1 and SLA-2 in fact showed elevated H_2S concentrations. However, these decreased to below detection after several months. The corrosion risk of new wells cannot be predicted reliably, and so this phenomenon, caused by the reaction of the thermal water with newly created surfaces of sulphide minerals, has to be taken into account when planning future drilling activities.
- The dissolved gas concentrations in the two thermal waters are low at 62 Nml/L for SLA-1 and 86 Nml/L for SLA-2. Maintaining high pressure in the installations to avoid gas exsolution and associated scaling is therefore not necessary. Nevertheless, it is possible that higher gas concentrations may be encountered in new wells, especially those tapping into upwelling crystalline waters. In these cases, high operational pressures would be required if groundwater is produced at temperatures > 80 °C.
- Due to the high sulphate concentrations and reduced redox character of the thermal waters, microbiological processes can occur, which can involve sulphate reducing bacteria and hence produce corrosive H_2S. The experience gained from long-term operations at other hydrothermal plants shows that such processes might start only after several years of operation. Hence, the concentration of H_2S needs to be monitored to avoid costly corrosion issues due to the precipitation of metal sulphides.
- The long-term operation of the geothermal plant in Schlattingen shows that there is no serious issue with mineral precipitation in the surface installations. In contrast, the downhole televiewer survey of well SLA-2 revealed mineral scales at depths down to 443 m, which if left untreated can cause clogging of the well. The potential for formation of mineral scales has to be estimated and assessed by advanced THC modelling for subsequent hydrothermal developments. Additionally, the injection of inhibitors in the production well should be planned and designed for all wells.
- The early detection of corrosion, scaling and bacterial processes is mandatory for the sustainable operation of hydrothermal plants. This requires a thorough hydrochemical and operational monitoring as described, for example, in Stopelli et al. (2024).

4 Conclusions and Outlook

The data collected during this project and the complementary numerical simulations have provided novel insights into the thermal, hydraulic and chemical behavior of the Muschelkalk aquifer, allowing a more informed assessment of its suitability for harnessing geothermal energy in the Canton of Thurgau and adjacent areas in Northern Switzerland. As demonstrated by the strongly differing hydrochemical signatures of the two Schlattingen wells (manifested by stable isotopes, concentrations of solutes, ^{81}Kr model ages, and recharge temperatures), the water produced from the Muschelkalk aquifer originates from at least two geological sources. This evidence aligns well with the observation that the SLA-1 and SLA-2 wells are not hydraulically connected via the aquifer, even though they are separated at their closest points by a distance of only 575 m. Together, these points imply that the aquifer is divided into hydraulically disconnected compartments. Moreover, hydraulic data from SLA-2 showed that continuous production of thermal water has increased the permeability of the aquifer by about one order of magnitude. The visual inspection of the SLA-2 casing, however, showed that extensive mineral scaling may occur when producing thermal water from steeply dipping fracture zones such as at SLA-2. The most important conclusions and implications of this project are listed below:

- The groundwater in the Schlattingen SLA-1 well is inherited from the infiltration of meteoric water into the Muschelkalk aquifer during the last glacial cycle (11.5–115 ka ago), most likely through the Muschelkalk outcrops NW of Schlattingen along the Wutach Valley. Its chemical composition is almost exclusively controlled by the interaction with dolomite, anhydrite/gypsum and calcite, which occur within the aquifer. Consequently, with the exception of Ca, Mg and SO_4, the solute concentrations are low.
- The groundwater in the Schlattingen SLA-2 well represents a mixture of (i) a saline, Li-, He-, Si-enriched groundwater of Na-Cl type upwelling from the crystalline basement and (ii) a less saline water of Ca-SO_4 type exclusively flowing within the Muschelkalk aquifer and hence similar to the groundwater produced by the SLA-1 well. The ratio of the two components in the mixture is currently on the order of 1:3. Upwelling of the basement component likely occurs locally via a permeable fault zone, which cuts through several intervening formations including the anhydrite-rich Zeglingen Fm. This leads to dissolution of anhydrite and hence to a chemical modification of the basement component, resulting in a distinct [Ca/Na]-[SO_4/Cl] signature of the thermal water produced at SLA-2. Both groundwater components are of meteoric origin and they both recharged the aquifer during similar climatic conditions as those of today. While the recharge location of the Ca-SO_4 component is presumably the same as that of the groundwater sampled at the SLA-1 well, the upwelling basement component likely infiltrated at higher altitude in the Black Forest Highlands, where the fractured crystalline basement outcrops. Flow of both groundwater components to Schlattingen is driven by the hydraulic head gradient with respect to the Black Forest recharge area. Based on the high ^{81}Kr model age (490 ka) and the $\delta^{18}O$ value above -10‰, recharge of both water components in the SLA-2 groundwater must have occurred in a previous interglacial period and hence more than 115 ka ago.
- It is interesting to note that there are practically no temperature differences between SLA-1 and SLA-2 despite the strong hydrochemical differences and the strong crystalline basement component at SLA-2. Based on coupled thermal–hydraulic–chemical (THC) simulations, the current absence of a temperature anomaly in SLA-2 is due to the limited flux of the upwelling basement component. However, THC modeling results suggest that that the temperature and salinity of the water produced from SLA-2 may increase over the next 1–2 years if water is continuously produced at the current rate of about 6 L/s. If such a chemical and thermal breakthrough were to occur in reality, its characteristics could allow the upflow rate and temperature of the ascending basement fluid to be estimated by advanced THC simulations, with a much better accuracy that was achievable in the present project.
- The most plausible process leading to the observed permeability increase of the reservoir tapped at SLA-2 over the past 10 years is the increase in connected porosity of the fault zone where it passes through the anhydrite-rich Zeglingen Fm. (*Anhydritgruppe*). The ascending

anhydrite-undersaturated basement water has dissolved anhydrite in the wall rocks of the conductive faults and hence created more permeable pore space.

- The possibility that the mineral scales observed along the SLA-2 well are caused by mixing of the two water components present in the SLA-2 water has been investigated by THC simulations. These confirm that, within days of beginning the pumping operation, a layer of mineral scales could precipitate along the entire length of the horizontal part of the SLA-2 borehole due to mixing of these water components. The model predicts anhydrite and calcite precipitation, with anhydrite being dominant. The simulations are simplified, in that they do not fully couple the precipitation of minerals with fluid flow dynamics and kinetic phenomena. Thus, a definitive statement on the hydraulic implications of scale formation is not possible at present. In the hydraulically most favorable case, scaling may have occurred, and may be still occurring, within the pores of the dolostone formation surrounding the open SLA-2 borehole. Clogging of this connected porosity may thus form a natural casing, leaving the interior of the borehole unhindered for fluid flow. In the worst case, kinetic effects may have allowed oversaturated water to enter the borehole, such that precipitation has occurred along the inside walls of the borehole. If left untreated, the accumulation of the scales would eventually clog the borehole and halt production of thermal water. Recent footage from a camera inserted into the borehole revealed partial clogging (filling approximately 50 volume % of the borehole), but only as deep as 443 m in the well. Deeper observations have yet to be made. Moreover, it remains unclear whether the scales consist of anhydrite or calcite, as so far no sample from the scales has been retrieved from the SLA-2 well and analyzed. It follows that the relationship between the mixing of waters in the aquifer and the precipitation of scales in the well remains hypothetical at this stage and must be further evaluated. This requires sampling and analysis of the scales along as much of the length of SLA-2 as possible, and the creation of a more sophisticated THC model with which more realistic predictions can be made of the rate and distribution of scaling in the future at SLA-2. A determination of the presence or absence of scaling in SLA-1 would be a valuable means to confirm or modify our understanding of the scaling process at Schlattingen.
- The scales identified along SLA-2 likely contribute to the lack of hydraulic communication between SLA-1 and SLA-2. Their precipitation along the margin of the SLA-2 borehole during the early operation stage could perhaps have formed a hydraulic barrier between the dolostones of the Muschelkalk aquifer and the well. This process provides an explanation for the very low inferred permeability along most parts of the open hole section of the SLA-2 well (2E-16 m^2). This is important, as there are no obvious geological reasons for such low permeability in the immediate vicinity of the well. Alternatively, or in addition, the presence of a groundwater divide, or a possible hidden fault zone or a gap in the fracture network between SLA-1 and SLA-2 may have contributed to causing the hydraulic compartmentalization observed at Schlattingen. Distinguishing between these various possible causes will require new observations, as outlined in the preceding paragraph.
- The numerical simulations have provided valuable insight into the dynamics of the SLA-2 system, but they have also highlighted the need for more observational constraints. The hydraulic simulations by TK Consult show that there is no unique combination of permeabilities around SLA2 that reproduces the recent pumping data. By using hydro-chemical constraints in the THC model, it is possible to narrow down the plausible parameter space, but not to derive a unique set of parameters that would accurately and reliably describe the system. Major mutually independent unknowns remain with respect to (i) the physical dimensions and hence volume of the high-permeability fault zone, (ii) the along-fault flow pattern, notably the location of zones of upwelling basement fluid, (iii) the rate of upflow of the basement fluid, and (iv) the temperature of that fluid where it enters the sequence of Mesozoic rocks. At the current state of knowledge, in which the system is strongly underdetermined, the numerical simulations mainly serve to confirm the plausibility of the conceptual models developed in this study. For this reason, sensitivity analyses have been only performed for selected parameters such as the

permeability and the upflow rate. Extensive sensitivity analyses would become meaningful in future modelling work once a few of the listed unknowns are quantitatively defined.

- Besides the scales observed in SLA-2, no major operational issues have occurred during the production of thermal waters from the two wells. The metallic down- and uphole installations are not severely influenced by corrosion. Moreover, the gas concentrations in both thermal waters are low, rendering maintenance of high water pressures unnecessary.
- For future hydrothermal projects in the Canton of Thurgau, however, the following hydrochemical challenges have to be considered: higher gas concentrations may occur in association with upwelling of water from the crystalline basement, which may require pressure maintenance, especially if water with temperatures > 80 °C is produced. Moreover, due to the high sulphate concentrations and reducing redox character of the thermal waters, microbiological processes can occur, which can involve sulphate reducing bacteria and lead to production of corrosive H_2S. The experience gained from long-term operations at other hydrothermal plants shows that such processes might start only after several years of operation. Hence, the concentration of H_2S needs to be monitored to avoid costly corrosion issues due to the precipitation of metal sulphides.
- Corrosion leads to increased cleaning and maintenance efforts and costs. To cope with these potential problems, the early detection of processes is mandatory for the sustainable operation of hydrothermal plants. This requires a thorough hydrochemical and operational monitoring as described, for example, in Stopelli et al. (2024). Moreover, injection of inhibitors in the production well should be planned and designed.
- The two wells at Schlattingen represent two distinct geothermal plays, from which thermal water can be produced from the Muschelkalk aquifer in the Canton of Thurgau. The first play ("*regional Muschelkalk*") is accessed and exemplified by the SLA-1 well. It represents the classical aquifer-geothermal hydrodynamic properties of the Upper Muschelkalk rocks. The second play ("*faulted Muschelkalk*") is accessed by the SLA-2 well and consists of steeply dipping fault zones that crosscut the Muschelkalk aquifer. Based on the crystalline basement component in the SLA-2 water and the high transmissivity measured in the basement at the bottom of the Schlattingen SLA-1 well (ca. 5E- 6 m^2/s), fault zones in the crystalline basement represent a third promising play in their own right ("*basement fault zone*").
- For the *faulted Muschelkalk* play, mixing of upwelling saline fluids with more dilute, Ca-SO_4 type groundwater of the Muschelkalk aquifer may cause significant amounts of scales to precipitate along wells, pumps and surface installations, eventually leading to clogging and other technical issues. Likewise, the high salinity of the upwelling basement waters may promote corrosion of all these installations, which is also highly relevant for the "*basement fault zone"* play.
- It follows that the risk of scaling and corrosion processes must be considered in the early planning stage of geothermal exploitation of these play types. This entails understanding the causes of the processes through predictive geochemical modelling, monitoring by means of regular hydrochemical analyses, and designing mitigation measures such as injection of inhibitors.
- It is recommended that future geothermal exploration activities in the Canton of Thurgau and adjacent areas should target all three exploration plays identified in the present study. For the "*regional Muschelkalk"* play, it is crucial to identify how far to the south the Muschelkalk aquifer acts as a regional, well-connected aquifer. This is important because the aquifer lies at ever greater depths towards the south and would therefore contain hotter water of greater interest for geothermal exploitation. Evidence published elsewhere suggests a strong drop in aquifer porosity and permeability at greater depths. Unfortunately, little information is available regarding the hydrodynamic behavior of the aquifer in the southern region of the Canton. Obtaining the necessary information would require drilling new exploration wells. In contrast, 3D seismic surveys may provide better insights into the "*Faulted Muschelkalk"* and "*Basement fault zone"* exploration plays, especially where the faults of interest can be tracked by their offsets of

the stratigraphy. Second- or third-order faults related to the main Randen Fault may be particularly prospective for this play. Other promising exploration targets are the boundary faults of the Permo-Carboniferous troughs.

- This project showcases the high value of a thorough scientific site investigation, including novel analytical and numerical methods. The combination of an extensive hydrochemical characterization of thermal waters (including chemical components, isotopes and noble gases), regional-scale groundwater simulations and local-scale THC simulations has elucidated the governing coupled thermal-hydraulic-chemical processes controlling the temperature, composition, and production rate of thermal waters produced from the Muschelkalk aquifer at Schlattingen. The project particularly showed that coupled THC simulations, constrained by hydrochemical analyses and results from regional groundwater simulations, provide a unique opportunity to quantify key parameters such as upflow rate of thermal waters, the future temperature evolution of the produced thermal waters, and the location and amount of scaling in these complex geothermal systems.

5 Acknowledgments

We would like to express our sincere thanks to the Grob family, in particular Stefan Grob, and the employees of Grob Gemüse AG in Schlattingen (TG). Without their active support and access to the two wells during ongoing operations, this project would not have been possible in this form. In particular, we would like to thank Andrea Brack for her permanent support and assistance with sampling. This should not be taken for granted. In addition, we acknowledge funding by Nagra for the analysis of noble gas concentrations, noble gas isotope ratios, and the determination of the ^{81}Kr model age for one sample collected from the SLA-2 borehole.

6 Reference List

Adams, A. & Diamond, L. W. (2019): Facies and depositional environments of the Upper Muschelkalk (Schinznach Formation, Middle Triassic) in northern Switzerland. - Swiss Journal of Geosciences, 112(2), 357-381.

Albert, W., Bläsi, H.R., Madritsch, H., Vogt, T. & Weber, H.P. (2012): Geologie, Stratigraphie, Strukturgeologie, bohrlochgeophysikalisches Logging und Wasserproben der Geothermiebohrung Schlattingen SLA-1 (Rohdaten). - Nagra Project Report, NPB, 133 pp; Wettingen, Switzerland (unpublished).

Aschwanden, L., Diamond, L. W., Mazurek, M. & Davis, D. W. (2019): Creation of Secondary Porosity in Dolostones by Upwelling Basement Water in the Foreland of the Alpine Orogen. - Geofluids 2019, 5210404.

Bernard, B.B. (1978): Methane in marine sediments. - Deep Sea Research Vol 26A: 429-443. https://doi.org/10.1016/0198-0149(79)90056-6

Birkhäuser, Ph., Roth, Ph., Meier, B.P. & Naef, H. (2001): 3D-Seismik - Räumliche Erkundung der mesozoischen Sedimentschichten im Zürcher Weinland. - Nagra Technical Report, NTB 00-03; Wettingen, Switzerland.

Bläsi, H.R., Hertrich, M., Madritsch, H., Weber, H.P. & Kuhn, P. (2014): Geologie und bohrtechnisches Logging der Geothermiebohrung Schlattingen SLA-2 (Rohdaten). - Nagra Project Report, NPB; Wettingen, Switzerland; https://www.aramis.admin.ch/Default?DocumentID=61203&Load=true.

Blanc, P., Lassin, A., Piantone, P., Azaroual, M., Jacquemet, N., Fabbri, A. & Gaucher, E.C. (2012): Thermoddem: A geochemical database focused on low temperature water/rock interactions and waste materials. - Appl. Geochem. 27(10), 2107-2116. doi.org/http://dx.doi.org/10.1016/j.apgeochem.2012.06.002.

Chevalier, G., Diamond, L. W., & Leu, W. (2010): Potential for deep geological sequestration of CO2 in Switzerland: a first appraisal. - Swiss Journal of Geosciences, 103(3), 427-455.

Diamond, L.W., Aschwanden, L., Mazurek, M., Wersin, P., Caldas, R., Adams, A., Ramseyer, K., Fabbri, S. & Madonna, C. (2013): Reservoir properties of the Upper Muschelkalk drill core at Schlattingen, NE Swiss Molasse Basin. - Rock-Water Interaction Group, University of Bern, 128 pp. DOI: 10.5281/zenodo.15034508. https://zenodo.org/records/15034508

Diamond L.W., Aschwanden, L., Adams, A. & Egli, D. (2019): Revised potential of the Upper Muschelkalk Formation (Central Swiss Plateau) for CO_2 storage and geothermal electricity. - Slides from SCCER-SoE Annual Conference at EPFL-Lausanne, Sept. 2019. 13 pp. *http://static.seismo.ethz.ch/sccer-soe/Annual_Conference_2019/AC19_S3a_08_Diamond.pdf*

Diamond, L. W., Alt-Epping, P., Brett, A. C., Aschwanden, L. & Wanner, C. (2025): Geochemical–hydrogeological study of a proposed CO2 injection pilot at Trüllikon, Switzerland. Contributions to the feasibility study für Project CITru. – Rep. Swiss Geol. Surv. 19, 107 pp. https://shop.swisstopo.admin.ch/en/books-and-publications/swiss-geological-survey/reports-swiss-geological-survey-pdf.

Diehl, T., Madritsch, H., Schnellmann, M., Spillmann, T., Brockmann, E. & Wiemer, S. (2023): Seismotectonic evidence for present-day transtensional reactivation of the slowly deforming Hegau-Bodensee Graben in the northern foreland of the Central Alps. - Tectonophysics, 846, 229659.

Enachescu, C., Frieg, B. & Wozniewicz, J. (2004): A new visual synthesis tool for transient test data. - Paper presented at the 2004 NGWA Conference, Portland Maine, September 13 to 15th, 2004.

Enachescu, C., Dmour, H. & Acs, V. (2016): Integrated well test interpretation of a naturally fractured carbonate reservoir – A case study. - Workshop, Molgroup, Budapest (Hungary),

https://www.researchgate.net/publication/290391450_Integrated_well_test_interpretation_of_a_naturally_fractured_carbonate_reservoir_-_A_case_study

Faber, E. (1987): Zur Isotopengeochemie gasförmiger Kohlenwasserstoffe. - Erdoel, Erdgas, Kohle 103: 210-218. https://doi.org/10.1016/B978-0-08-037236-5.50039-7

Frieg, B. (2015): Geochem – Anwendungsorientierte Produktionsoptimierung der Geothermiebohrung Schlattingen 2. - BFE, Schlussbericht, Dezember 2015, BFE-Vertragsnummer SI/501079-01; https://www.aramis.admin.ch/Default?DocumentID=61117&Load=true.

Frieg, B., Grob, H., Hertrich, M., Madritsch, H. Müller, H., Vietor, T. Vogt, T. & Weber, H. (2015): Novel Approach for the Exploration of the Muschelkalk Aquifer in Switzerland for the CO2-free Production of Vegetables. - Proceedings World Geothermal Congress 2015 Melbourne, Australia, 19-25 April 2015.

Gmünder, C., Malaguerra, F., Nusch, S. & Traber, D. (2014): Regional Hydrogeological Model of Northern Switzerland. - Nagra Working Report, NAB 13-23; Wettingen, Switzerland.

Hammond, G., Noel, M., Leone, R., Park, H. & Frederick, J.(2020): PFLOTRAN. Computer Software. USDOE. 17 Jun. 2020. Web. doi:10.11578/dc.20201103.3. *https://www.pflotran.org/documentation/user_guide/user_guide.html*.

Kastrup, U., Zoback, M.-L., Deichmann, N., Evans, K., Giardini, D. & Michael, A.J. (2004): Stress field variations in the Swiss Alps and the northern Alpine foreland derived from inversion of fault plane solutions. - J. Geophys. Res., 109, B01402, doi: 10.1029/2003JB002550.

Kietäväinen, R., Ahonen, L., Niinikoski, P., Nykänen, H. & Kukkonen, I.T. (2017): Abiotic and biotic controls of methane formation down to 2.5 km depth within the Precambrian Fennoscandian Shield. Geochimica et Cosmochemica Acta 202: 124-145. https://doi.org/10.1016/j.gca.2016.12.020.

Kuhlmann, U. & Balmer, M. (2012): Geothermie-Projekt Schlattingen: Hydrothermisches Modell des Muschelkalk-Aquifers – Nagra Project Report, NPB; Wettingen, Switzerland (unpublished).

König, C.M., Becker, M., Brömme, K., Diehl, A., König, T., Seidel, T., Rosen, B., Rüber, O., Schröder, S. & Zimmermann, C. (2024): Spring Benutzerhandbuch - SPRING Version 6; Witten (Deutschland).

Künze, R. & Kuhlmann, U. (2020): Hydraulische Modellierungen Schlattingen 1 und 2. – Nagra Project Report, NPB; Wettingen, Switzerland (unpublished).

Milkov, A.V. & Etiope, G. (2018): Revised genetic diagrams for natural gases based on a global dataset of > 20,000 samples. - Organic Geochemistry 125: 109-120. https://doi.org/10.1016/j.orggeochem.2018.09.002.

Nagra (2001): 3D Seismik - Räumliche Erkundung der mesozoischen Sedimentschichten im Zürcher Weinland. - Nagra Technical Report, NTB 00-03; Wettingen, Switzerland.

Nagra (2002) Projekt Opalinuston: Synthese der geowissenschaftlichen Untersuchungsergebnisse. - Nagra Technical Report, NTB 02-03, 714 pp; Wettingen, Switzerland.

Nagra (2008): Vorschlag geologischer Standortgebiete für das SMA- und das HAA-Lager - Geologische Grundlagen. - Nagra Technical Report, NTB 08-04; Wettingen, Switzerland.

Nagra (2024): Geosynthesis of Northern Switzerland. - Nagra Technischer Bericht, NTB 24-17; Wettingen, Switzerland.

Parkhurst, D.L. & Appelo, C.A.J. (2013): Description of input and examples for PHREEQC version 3 - A computer program for speciation, batch-reaction, one-dimensional transport, and inverse geochemical calculations. - U.S. Geological Survey Techniques and Methods, book 6, chap. A43, 497 p., available only at https://pubs.usgs.gov/tm/06/a43/.

Pietsch, J. S., Wetzel, A. & Jordan, P. (2016): A new lithostratigraphic scheme for the Schinz- nach Formation (upper part of the Muschelkalk Group of northern Switzerland). *Swiss Journal of Geosciences* 109/2, 285–307 https://doi.org/10.1007/s00015-016-0214-7.

Reinhard, S. & Rösli, U. (2013): Schlattingen Borehole SLA-1 Pumping Tests Muschelkalk – MK5 (MK4). – Nagra Project Report, NPB; Wettingen, Switzerland (unpublished).

Reinhard, S. & Rösli, U. (2015): Schlattingen Borehole SLA-2 Pumping Tests Trigonodus-Dolomite (Muschelkalk) – TD2. – Nagra Project Report, NPB; Wettingen, Switzerland (unpublished).

Sanjuan, B., Millot, R., Innocent, C., Dezayes, C., Scheiber, J. & Brach, M. (2016): Major geochemical characteristics of geothermal brines from the Upper Rhine Graben granitic basement with constraints on temperature and circulation. - Chem. Geol. 428, 27-47.

Schlüchter, C., Akçar, N. & Ivy-Ochs, S. (2021): The Quaternary Period in Switzerland. - In: Reynard, E. (Ed.)(2012): Landscapes and Landforms of Switzerland. - Springer International Publishing, Cham, pp. 47-69.

Stober, I., Grimmer, J. & Kraml, M. (2023): The Muschelkalk aquifer of the Molasse basin in SW-Germany: implications on the origin and development of highly saline lithium-rich brines in calcareous hydrothermal reservoirs. - Geothermal Energy 11, 27.

Stopelli, E., Lupi, N. & Galfetti, T. (2024). Hydrochemical Characterisation of Geothermal Fluids. Guideline for Sampling and Analysis. Rep. swiss geol. Surv. 24 (only as PDF). https://prod-swishop-s3.s3.eu-central-1.amazonaws.com/2025-01/BLGD-24.pdf

Sue, C., Delacou, B., Champagnac, J.-D., Allanic, C. & Burkhard, M. (2007): A seismic deformation in the Alps: GPS vs. seismic strain quantification. - Terra Nova, 19(3), 182-188.

Swisstopo (2024): Tectonic Map of Switzerland 1:500000. – Federal Office of Topography swiss-topo, Wabern.

Ufrecht,W. & Hölzl, S. (2006): Strontium ($^{87}Sr/^{86}Sr$)-Isotopie salinarer Mineral- und Thermalwässer im Oberen Muschelkalk – Entwicklung eines Genesemodells. – Schriftenreihe des Amtes für Umweltschutz, 3/2006: 49-68; Stuttgart

Vuataz, F.-D. (1982) : Hydrogéologie, géochmie et géothermie des eaux thermales de Suisse et des régiones alpines limitrophes. Commission d'Hydrologie. - Organe de la Societe Helvetique des Sciences Naturelles. Vol. 20. 174 pp.

Waber, H. N. & Traber, D. (2022): Die Tiefengrundwässer in der Nordschweiz und im angrenzenden Süddeutschland: Beschaffenheit, Herkunft und unterirdische Verweilzeit. - Nagra Technical Report, NTB 19-02; Wettingen, Switzerland.

Wanner, C., Bucher, K., Pogge, von Strandmann, P. A. E., Waber, H. N. & Pettke, T. (2017): On the use of Li isotopes as a proxy for water–rock interaction in fractured crystalline rocks: A case study from the Gotthard rail base tunnel. - Geochim. Cosmochim. Acta 198, 396-418.

Whiticar, M.J. (1999): Carbon and hydrogen isotope systematics of bacterial formation and oxidation of methane. - Chemical Geology 161: 291-314. https://doi.org/10.1016/S0009-2541(99)00092-3

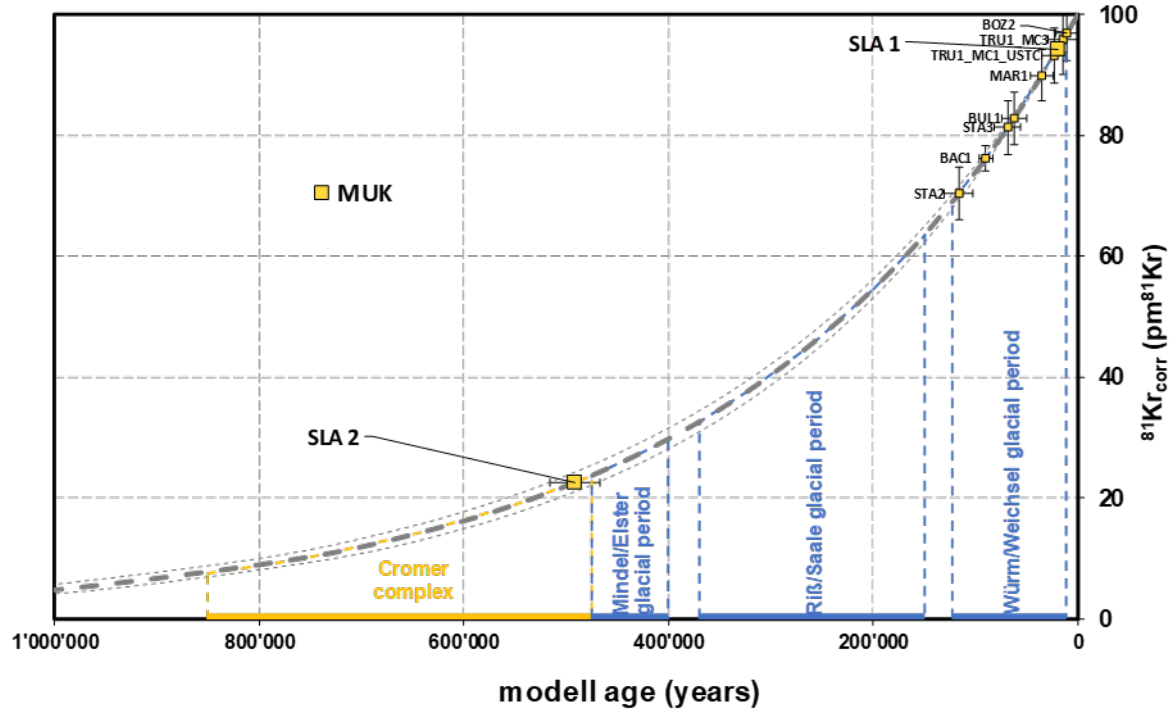
Whiticar, M.J. (1994): Correlation of natural gases with their source. - In: Magoon, L.B. & Dow, W.G. (Eds.)(1994): The Petroleum System – From Source to Trap. - AAPG Mem. 60: 261–283. https://doi.org/10.1306/M60585C16

Whiticar, M.J. (2020): The Biogeochemical Methane Cycle. - In: Wilkes, H. (Ed.)(2020): Hydrocarbons, Oils and Lipids: Diversity, Origin, Chemistry and Fate. - Handbook of Hydrocarbon and Lipid Microbiology. Springer, Cham. https://doi.org/10.1007/978-3-319-54529-5_5-1

Appendix 1:

Extraction and analysis of gases, noble gases and isotopes including $^{85}Kr/^{81}Kr$ and $^{37}Ar/^{39}Ar$ from the thermal water extracted from the Schlattingen wells (SLA-1 and SLA-2)

Extraction and analysis of gases, noble gases and isotopes including $^{85}Kr/^{81}Kr$ and $^{37}Ar/^{39}Kr$ from the thermal water extracted from the Schlattingen wells (SLA 1 and SLA 2)



M. Heidinger

Schweitenkirchen, den 10.11.2025 **Dr. Eichinger**

Index of contents

Seite

1 Introduction 4
2 Gas sampling and preparation for Kr isotope investigations 4
3 Methods and Background of Interpretation 5
3.1 Noble gases concentrations and stable noble gas isotopes (He, Ne, Ar, Kr, Xe) 5
3.2 Krypton-81 and Krypton-85 5
3.3 Argon-39 and Argon-37 6
3.4 Air correction 7
4 Results 9
4.1 Sulphate and Strontium stable isotopes 9
4.2 Normal gases, gaseous hydrocarbons and stable isotopes 10
4.3 Dissolved inorganic carbon and carbon isotopes 13
4.4 Noble gases and stable isotopes 13
4.5 Krypton-85 and Krypton-81 data and corrections 17
4.6 Argon-39 and Argon-37 data and corrections 19
4.7 Helium-4 and Argon-40 accumulation 22
References 26

Index of tables

Table. 1: Composition of extracted gas for ATTA preparation (Argonne, USA)

Table 2: Kr and Ar concentration and Kr/Ar ratios in AIR and equilibration saturation in water (ASW) for 0 and 20 °C temperature

Table 3: Compilation of dissolved gas and stable gas isotopes

Table 4: DIC result and carbon isotopes

Table 5: Recharge temperatures obtained by the application of different models (PR, UA and CE) for the sample including the applied input parameters.

Table 6: Analytical results of radioactive Kr and Ar isotopes via ATTA and decay correction for $^{85}Kr_m$

Table 7: Air-correction for $^{81}Kr_{corr}$ acccording to equation (1) and maximum atmospheric $^{85}Kr_{atm}$ activity.

Table 8: Analytical results of radioactive Kr and Ar isotopes via ATTA and decay correction for $^{85}Kr_m$

Index of figures

Figure 1: Stable carbon versus stable hydrogen isotope signatures of dissolved methane compared to endmembers and influencing processes according to Whiticar (2020) and Milkov & Ethiope (2018).

Figure 2: Isotope ratios of methane and carbon dioxide in the $\delta^{13}C\text{-}CH_4$ versus $\delta^{13}C\text{ -}CO_2$ diagram; the fields and arrows mark different origin and genesis processes of methane according to Whiticar (2020) and Milkov & Ethiope (2018); the numerical values, εc, indicate the degree of oxidation; the high εc indicate high, original, methane concentrations, the low εc strongly oxidized methane concentrations.

Figure 3: Deviation of analysed noble gas isotope ratios of the Schlattingen samples (SLA 1 and SLA 2) to laboratory standard water in equilibrium with air.

Figure 4: Measured concentrations of atmosphere-derived noble gas isotopes (^{84}Kr) versus the in-situ groundwater Cl^- concentrations. Dashed black lines show the range of concentrations expected for mixing of the postulated meteoric and marine (Cl = 19 g/L) endmembers. Arrows show possible effects of secondary gas uptake and degassing.

Figure 5: Corrected value for $^{81}Kr_{corr}$ of the in-situ groundwater samples from Schlattingen (SLA 1 and SLA 2) and calculated ^{81}Kr model age for the half-life 229'000 ± 11'000 years.

Figure 6: $^{37}Ar_{corr}$ versus $^{39}Ar_{corr}$ of the Muschelkalk groundwater samples in Northern Switzerland.

Figure 7: Values for $^{39}Ar_{corr}$ of the Muschelkalk groundwater samples and calculated ^{81}Kr model age for the half-life 229'000 ± 11'000 years.

Figure 8: $^{39}Ar_{corr}$ results of selected Muschelkalk groundwater samples and calculated ^{81}Kr model age with matching of different UEP-values for SLA 1 and SLA 2.

Figure 9: He-isotope data of the Muschelkalk groundwater samples from Northern Switzerland and Southern Germany.

Figure 10: ^4He-isotope data of selected Muschelkalk groundwater samples and calculated ^{81}Kr model age with matching of ^4He-accumulation for SLA 1 and SLA 2 via constant UP-rate.

Index of annexes

Report No. 415039, 415040

1 Introduction

Besides the hydrochemical characterisation of the in-situ groundwater in the Muschelkalk aquifer of SLA 1 and SLA 2 additional analyses were performed, to obtain information about the groundwater age characteristics. Hydroisotop GmbH was assigned to analyse gas/noble gas isotope parameter systematic on separately taken groundwater samples.

2 Gas sampling and preparation for Kr isotope investigations

All on site measured parameters remained quasi-constant during pumping of SLA 1 and SLA 2 and sampling for gas/noble gas isotope analysis was performed by Hydroisotop on the 16th and 17th of July 2024.

The sampled groundwaters were filled in stainless steel cylinder and copper tubes for quantitative gas/noble gas and carbon/hydrogen isotope analysis under onsite pressure and temperature. For the analysis of radioactive Kr-Isotopes outflowing water of SLA1 and SLA2 was degassed on-site separately.

The extraction of dissolved gases was done by a gas separator on-site (Purtschert et al. 2013), with a constant flowrate of 0.15 (SLA 2) and 0,18 (SLA 1) L/s into the vacuum extraction chamber (efficiency of degassing ≥ 70%). The extracted bulk gas was transferred to a 10 L steel containers (SC) and one 1 L aluminium container (MC).

After a sufficient decay time for ^{222}Rn, the first purification steps were carried out at the university of Bern applying chromatographic separation and cryo-separation to obtain a pure Kr- gas phase following the procedure given in Purtschert et al. (2013) and Lu et al. (2014). This involves a stepwise concentration of the Kr with a final purification to separate a pure Kr fraction and was carried out in the laboratory of the University of Bern, Switzerland (Institute of Physics – working group of Dr. R. Purtschert). The aluminium container were analysed for composition of the extracted gas (see Table 1).

Table. 1: Composition of extracted gas for ATTA preparation (Argonne, USA)

Lab.No.		**415039**	**415040**
sample		**SLA 1**	**SLA 2**
date		**16.04.2024**	**15.04.2024**
Hydrogen (H_2)	vol-%	**0.03**	**0.03**
Helium (He)	vol-%	**0.09**	**0.6**
Argon (Ar)	vol-%	**2**	**1**
Oxygen (O_2)	vol-%	**0.3**	**0.16**
Nitrogen (N_2)	vol-%	**81.7**	**50.2**
Carbon dioxide (CO_2)	vol-%	**14.3**	**45**
Methane (CH_4)	vpm	**2407**	**-**
Ethane (C_2H_6)	vpm	**34**	**115**
Propane (C_3H_8)	vpm	**10**	**12**
i-Butane (C_4H_{10})	vpm	**5**	**1**
n-Butane (C_4H_{10})	vpm	**8**	**3**

3 Methods and Background of Interpretation

The analytical methods applied for the reported analyses are compiled in the attached analysis report.

3.1 Noble gases concentrations and stable noble gas isotopes (He, Ne, Ar, Kr, Xe)

During recharge meteoric water exchanges with the atmosphere, leading to an equilibration of gases with the atmospheric air. Therefore, noble gases dissolved in groundwater give information about the characteristics of the reservoir and valuable insights such as palaeotemperatures during recharge and timescales (dating with respect to relative ^{4}He or ^{40}Ar accumulation). If groundwater is formed from freshwater, such as meteoric water, the noble gas equilibriums primarily depend on the temperature, air pressure in the recharge area following Henry's law. For the determination of an excess air component, induced by the recharge processes, a number of models are commonly used, which include:

- Unfractionated excess air (UA) model (Andrews & Lee 1979)
- Partial re-equilibration (PR) model (Stute et al. 1995)
- Closed-system equilibration (CE) model (Aeschbach-Hertig et al. 2008).

Up to now the interpretation of noble gas data from groundwater analysis in the study area is performed based on these models. In this report we use these models to evaluate alteration processes of the noble gas equilibrium or relative components (Kr) by degassing or external gas fluxes and diffusive or retardation processes (aquitard or deep zones), as they are able to influence the interpretation of the ^{81}Kr activity measured in the samples (Sturchio et al. 2014, Gerber et al. 2017). In contrast, no sophisticated fits in the different model approaches for the excess air as ΔNe or A (air) or mixing with non-meteoric components were performed. So far, the recharge conditions for the studied groundwater are not evaluated in detail. Therefore, these model results were used to evaluate sample quality and to consider these effects for the lower and upper limit of the ^{81}Kr model age.

The noble gas isotope analyses (^{3}He, ^{4}He, ^{20}Ne, ^{21}Ne, ^{22}Ne, ^{36}Ar, ^{40}Ar, ^{78}Kr, ^{80}Kr, ^{82}Kr,^{83}Kr, ^{84}Kr, ^{86}Kr, ^{124}Xe, ^{126}Xe, ^{128}Xe, ^{129}Xe, ^{130}Xe, ^{131}Xe, ^{132}Xe, ^{134}Xe, ^{136}Xe) were performed at Woods Hole Coastal and Marine Science Center, USA using a Nu Instrument multi-collector Noblesse HR mass spectrometer interfaced to a noble gas processing and purification inlet system, which allows a full cryogenic separation and purification of the noble gases prior to inlet into the mass spectrometer, with a precision of 0.1 to 2.8% (reproduction of calibration and sample).

Due to the detailed noble gas isotope analyses the calculation of the Ne, Ar, Kr and Xe concentrations is based on the total analysed isotope record of each noble gas element. Only the provided Ar isotope data set was corrected for underground production and accumulation of ^{40}Ar (Ar_{corr} = ^{36}Ar * 298.56) according to Lee et al. (2006).

3.2 Krypton-81 and Krypton-85

Krypton-81 is a radioactive noble gas isotope (^{81}Kr, half-life 229'000 ± 11'000 years), which is constantly subject to atmospheric formation (cosmic rays and proton-, neutron-induced spallation or nuclear reactions of Kr isotopes). In the atmosphere this leads to an equilibrium

between production and decay of ^{81}Kr (^{81}Kr/Kr frequency approx. 9.3×10^{-13} or ^{81}Kr/Kr activity = 100 pm ^{81}Kr). The atmospheric ^{81}Kr isotopic abundance over the past 1.5 Myr was calculated according to Zappalla et al (2020). The very small variation of the equilibrium (^{81}Kr/Kr activity ranging from 100 to max. 105.3 pm ^{81}Kr) provides a well-defined, stable input function for radiokrypton dating.

The stable atmospheric ^{81}Kr input is transferred to the dissolved noble gas inventory (absolute noble gas concentration depending on pressure, temperature and salinity) during groundwater recharge. After isolation from the atmosphere by deeper groundwater circulation, the ^{81}Kr activity in groundwater decreases in accordance with radioactive decay as a function of residence time. The difference of the measured ^{81}Kr activity concentration of a groundwater sample to the stable ^{81}Kr input and the specific ^{81}Kr half-life provides a piston flow model age.

Calculations given by Purtschert et al. (2021) showed that in rock formations with low to moderate U and Th concentrations (i.e. U ≈ < 10 ppm), underground production of ^{81}Kr does not affect ^{81}Kr dating. Production in the water phase itself is also negligible as shown in Warr et al. (2023).

In the absence of significant sinks, ^{81}Kr is an almost ideal dating tracer, supported further by its chemical inertness. The utilisation of Atom Trap Trace Analysis (ATTA) techniques (Chen et al. 1999, Jiang et al. 2012) has increased the prevalence of determining ^{81}Kr activity concentrations in environmental samples for dating old groundwaters.

In contrast to ^{81}Kr, the radioactive noble gas isotope ^{85}Kr (half-life 10.76 years) originates almost exclusively from nuclear fuel treatment and operation of nuclear power plants (nuclear fission of uranium and plutonium) operated worldwide since the mid-1950s. Accordingly, the ^{85}Kr content of atmospheric air is increasing almost steadily since that time. Currently, the specific ^{85}Kr activity (weekly samples) in Southwest Germany (BfS station Schauinsland, Germany: Bollhöfer et al. 2019; including new data of 2020 to 2025) varies between 70 and 160 dpm/cc$_{Kr}$. Between 15 April 2024 and 22 April 2024, the concentration of ^{85}Kr in the atmospheric air at the measuring station Schauinsland, Baden-Württemberg, Germany, was 73.7 ± 0,7 dpm/mlKr.

The determination of the ^{85}Kr activity has been applied for several decades via LLC (Low Level Counting, University of Bern, Institute of Physics), more recently by ATTA (Argonne National Laboratory Chicago, USA or USTC Hefei, China) for the dating of young groundwaters. Additionally, it is used as tracer to quantify the contamination of gas samples obtained from groundwaters by recent atmospheric air introduced by drilling fluids, or by leaks during sampling, gas preparation and shipping. This approach is applied for this study.

3.3 Argon-39 and Argon-37

Argon-39 is a radioactive Ar isotope (39Ar, half-life 269 years) which is generated in the atmosphere primarily by the interaction of cosmic ray neutrons with ^{40}Ar. The input of ^{39}Ar to the groundwater flow system is determined by a rather constant equilibrium concentration in the atmosphere. The ^{39}Ar activity concentration in the present atmosphere is 0.107 ± 0.004 dpm/LAr and is set to 100 pm^{39}Ar (Loosli 1983, Gu et al. 2021). The determination of the ^{39}Ar activity has been successfully applied for several decades via LLC (Low Level Counting, University of Bern, Institute of Physics) and recently also via ATTA (University of Heidelberg,

Germany or USTC Hefei, China). If subsurface production of ^{39}Ar can be neglected, this method has been successfully used in combination with other tracers, in particular with ^{85}Kr and ^{14}C-DIC, to estimate groundwater ages (^{39}Ar model age). However, the ^{39}Ar activities can be influenced by subsurface production of ^{39}Ar, occurring in environments with high U and Th contents (Lehmann et al. 1993, Šrámek et al. 2017) or cosmogenic production via muons in shallow depths (Musy & Purtschert 2023, Musy et al. 2023), which complicates the dating of groundwater.

Argon-37 is a radioactive Ar isotope (^{37}Ar, half-life 34.9 days) naturally produced in the atmosphere via spallation of ^{40}Ar induced by high-energy neutrons from cosmic ray. Due to releases from nuclear reactors the atmospheric background may slightly vary locally (Fritz et al. 2021). Taking into account the location of the study area (relative to nuclear facilities), the atmospheric background can be estimated to be about 1 mBq/m3 of air or 0.00642 dpm/LAr (Fritz et al. 2021, Musy et al. 2023).

In soils and shallow rocks ^{37}Ar derives mainly from ^{40}Ca activation by cosmic ray neutrons or muons (Riedmann & Purtschert 2011, Guillon et al. 2016, Musy & Purtschert 2023). In depths > 50 m neutrons originating from the U-Th decay chain determine the ^{37}Ar (and ^{39}Ar) production rates. Due to the shorter half-live ^{37}Ar is a useful indicator for the subsurface production of ^{39}Ar.

The ^{37}Ar activities determined by LLC (Low Level Counting) have been successfully applied for several decades by the University of Bern, Institute of Physics and were also measured in this study.

3.4 Air correction

In most case studies the measured activity values for ^{81}Kr, ^{39}Ar and ^{37}Ar from extracted gas samples have to be corrected for air contamination before it is used for groundwater age evaluation and further interpretation.

Mechanisms for air contamination are:

- intake of air during sampling and vacuum extraction

  and

- potential contamination by air-equilibrated drilling fluid or alien waters
- potential leakage during cleaning and preparation processes before ATTA (^{85}Kr, ^{81}Kr).

The forced degassing leads to a different gas composition compared to the dissolved gas analysis in the water sample (see attached analysis report). This is due to the different solubility of the dissolved gas species, the efficiency of the extraction and the partial re-dissolution of extracted gas species (e.g. CO_2, CH_4) into the water phase before pumping out of the extraction device. Due these effects a correction for air contamination cannot be reliably based on the analysed gas composition of the sample.

To quantify the contamination of gas samples obtained from groundwaters by recent atmospheric air brought in preferentially during sampling, the specific atmospheric ^{85}Kr activity (weekly samples) has to be applied.

Deep uncontaminated groundwaters, as sampled in the Schlattingen wells (SLA 1 and SLA 2) are assumed to be ^{85}Kr free, based on their expected residence time in the underground of >> 60 years (half-life of ^{85}Kr = 10.76 years).

Based on the current ^{85}Kr input of regional atmospheric air ($^{85}Kr_{atm}$ measurement of continuous 'weekly samples', Federal Office for Radiation Protection, Freiburg i.Br., Germany) and the stable atmospheric $^{81}Kr_{atm}$ activity, the air contamination in the extracted and purified gas samples are quantified ($\alpha = {}^{85}Kr_{m\ (decay\ cor.)}/{}^{85}Kr_{atm}$) and the measured $^{81}Kr_m$ activity is corrected according to:

$$^{81}\mathrm{Kr}_{\mathrm{corr}} = \frac{(\,^{81}\mathrm{Kr}_{\mathrm{m}} - \alpha \times {}^{81}\mathrm{Kr}_{\mathrm{atm}})}{1 - \alpha} \qquad (1)$$

where:

$^{81}Kr_m = {}^{81}Kr_{sample\ gas}$ [pm ^{81}Kr]
$^{81}Kr_{atm}$ = 100 pm^{81}Kr
$\alpha = {}^{85}Kr_{m\ (decay\ corr.)} / {}^{85}Kr_{atm}$

The dissolution of Kr and Ar in water depends on the temperature-dependent Henry coefficients. So, the resulting Kr / Ar ratios differ significantly from air (see Table 2).

Table 2: Kr and Ar concentration and Kr/Ar ratios in AIR and equilibration saturation in water (ASW) for 0 and 20 °C temperature

	Unit	Kr	Ar	Kr / Ar
AIR	[ppm]	1.1	9'340	1.18×10^{-4}
Concentration in ASW at 0 °C	[mol L^{-1}(STP)]	5.50×10^{-9}	2.20×10^{-5}	2.50×10^{-4}
Concentration in ASW at 20 °C	[mol L^{-1}(STP)]	3.10×10^{-9}	1.40×10^{-5}	2.21×10^{-4}

This difference in the Kr / Ar ratios allows an air correction for the measured 39Ar activity in the sampled and purified gas according to:

$$^{39}\mathrm{Ar}_{\mathrm{corr}} = \frac{\left({}^{39}\mathrm{Ar}_{\mathrm{m}} - (\alpha \times (\frac{\frac{\mathrm{Kr}}{\mathrm{Ar}}\mathrm{m}}{1.18E-04}) \times {}^{39}\mathrm{Ar}_{\mathrm{atm}}) \right)}{1 - \alpha \times (\frac{\frac{\mathrm{Kr}}{\mathrm{Ar}}\mathrm{m}}{1.18E-04})} \qquad (2)$$

where:

$^{39}Ar_m = {}^{39}Ar_{sample\ gas}$ [pm Ar]
$^{39}Ar_{atm}$ = 100 [pm Ar]
$\alpha = {}^{85}Kr_{m\ (decay\ corr.)} / {}^{85}Kr_{atm}$
$Kr/Ar_m = Kr/Ar_{NG\ sample}$

$Kr/Ar_{AIR} = 1.18 \times 10^{-4}$

A similar approach can be applied for the air correction of the ^{37}Ar activity, just inserting the different atmospheric activity according to:

$$^{37}\mathrm{Ar}_{\mathrm{corr}} = \frac{\left({}^{37}\mathrm{Ar}_{\mathrm{m}} - \alpha \times \left(\frac{\frac{\mathrm{Kr}}{\mathrm{Ar}}\mathrm{m}}{1.18\mathrm{E}-04}\right) \times {}^{37}\mathrm{Ar}_{\mathrm{atm}} \right)}{1 - \alpha \times \left(\frac{\frac{\mathrm{Kr}}{\mathrm{Ar}}\mathrm{m}}{1.18\mathrm{E}-04}\right)} \quad (3)$$

where:

$^{37}Ar_m = {}^{37}Ar_{sample\ gas}$ [dpm/LAr]
$^{37}Ar_{atm} = 0.00642$ [dpm/LAr]
$\alpha = {}^{85}Kr_{m\ (decay\ corr.)} / {}^{85}Kr_{atm}$
$Kr/Ar_m = Kr/Ar_{NG\ sample}$
$Kr/Ar_{AIR} = 1.18 \times 10^{-4}$

4 Results

Krypton and other noble gas concentrations in water can be influenced by different in-situ processes like mixing or diffusion of noble gases (flux) from/into adjacent rocks. To get knowledge about such processes, noble gas samples (copper tubes) were taken in a way to minimise the influence by pumping and sampling procedures.

These noble gas and noble gas isotope data are further evaluated to obtain information about potential processes, which have influence on the Kr/^{81}Kr inventory of the single samples.

Within the evaluation workflow such processes should be quantified and potentially applied for the interpretation of the affected sample.

In order to achieve consistent interpretation, the results of further isotope analyses will be taken into account.

4.1 Sulphate and Strontium stable isotopes

As part of the sampling of SLA 1 and SLA 2 in April 2024, separate sample bottles were filled in accordance with the order for the determination of the isotope signature of the dissolved sulphate and strontium content

In the samples examined, the signature of the stable isotopes of sulphate ($\delta^{34}S/\delta^{18}O$) was analysed with δ-values of 18.1 or 18.9 ‰-VCDT for sulphur-34 and 14 to 14.4 ‰-VSMOW for oxygen-18, while the $^{87}Sr/^{86}Sr$ signatures were determined to 0.708437 and 0.708996.

The analysed signatures show complete agreement with the expected geochemical type range for regional groundwater in contact with evaporites and marine limestone of the Muschelkalk (Nagra NTB 19-02, Ufrecht & Hölzl 2006).

4.2 Normal gases, gaseous hydrocarbons and stable isotopes

Dissolved gas composition and gas isotope signatures were determined in the groundwater sample taken in stainless steel cells (3 cells) in flow-through directly at the well.

During the pumping and sampling, the oxygen concentration was determined at < 0.1 mg/l and the original groundwater of SLA 1 and SLA 2 is oxygen free in both wells.

The total content of dissolved gases amounted to 62 (SLA 1) and 86 (SLA 2) ccSTP/kg. The main components are N_2 (38.6 ccSTP/kg) in SLA 1 and CO_2 (52.9 ccSTP/kg) in SLA 2 (Table 3).

Ar was detected in relatively low proportions of 0.852 (SLA 1) and 0.508 (SLA 2) ccSTP/kg. The N_2/Ar volume ratios of 45 (SLA 1) or 62 (SLA 2) and hence higher than air saturated water (40) but below air (78), indicating only low portions of additional nitrogen source, e.g. from biogenic material. The detected He content of 0.255 ccSTP/kg in the steel container SLA 2 indicates significant He-production by U- and Th-bearing minerals attributed to a prolonged residence time in the underground.

The dissolved concentration of methane is only ≈ 0.05 (SLA 1) and 0.79 (SLA 2) ccSTP/kg with higher hydrocarbons up to butane present in very low concentrations ranging between 0.00035 and 0.0046 ccSTP/kg (see Table 3). The low C_1/C_2+C_3 ratio of 35 and 153 indicates no clear provenance of the low amounts of dissolved methane.

Table 3: Compilation of dissolved gas and stable gas isotopes

Labor-Nr.		**415039**	**415040**
		SLA 1	**SLA 2**
		16.04.2024	**15.04.2024**
Physico-chemical onsite parameter			
Temperature at sampling	°C	29.6	39.2
Spec. electr. conductivity (25 °C) at sampling	µS/cm	2730	12700
pH value at sampling		6.8	6.7
Dissolved oxygen content	mg/l	0.13	0.13
Redox potential (related to NHE)	mV	-20	154
Alkalinity (pH 4,3) onsite	mmol/l	3.0	6.45
Dissolved gas contents			
Hydrogensulfide	ccSTP/kg	< 0,09	< 0,12
Hydrogen	ccSTP/kg	0.029	0.048
Oxygen	ccSTP/kg	< 0.1	< 0.1
Nitrogen	ccSTP/kg	38.6	31.5
Carbon dioxide	ccSTP/kg	22.3	52.9
Helium	ccSTP/kg	< 0,02	0.255
Argon	ccSTP/kg	0.852	0.508
Methane	ccSTP/kg	0.0498	0.7927
Ethane	ccSTP/kg	0.00106	0.00461
Propane	ccSTP /kg	0.00035	0.00056
Butane	ccSTP /kg	0.00035	< 0,00001
Pentane	ccSTP /kg	< 0,00012	< 0,00016
Sum Gases	ccSTP /kg	62	86
Gas ratios			
$C_1/(C_2+C_3)$		35	153
N_2/Ar		45	62
Stable Isotopes of dissloved gases			
Carbon-13 ($\delta^{13}C$-CO_2)	‰-VPDB	-13.5	-16.3
Carbon-13 ($\delta^{13}C$-CH_4)	‰-VPDB	-41	-21.8
Deuterium ($\delta^{2}H$-CH_4)	‰-VSMOW	-197	-116
Carbon-13 ($\delta^{13}C$-C_2H_6)	‰-VPDB	-33.5	-29.4
Carbon-13 ($\delta^{13}C$-C_3H_8)	‰-VPDB	-31.2	-

The analysed isotope signatures of CH_4 in SLA 1 and SLA 2 ($\delta^{13}C$-CH_4; $\delta^{2}H$-CH_4 and $\delta^{13}C$-CO_2 in table 1) refer to a significant oxidation of CH_4, probably via sulphate reduction (see Figure 1 and 2).

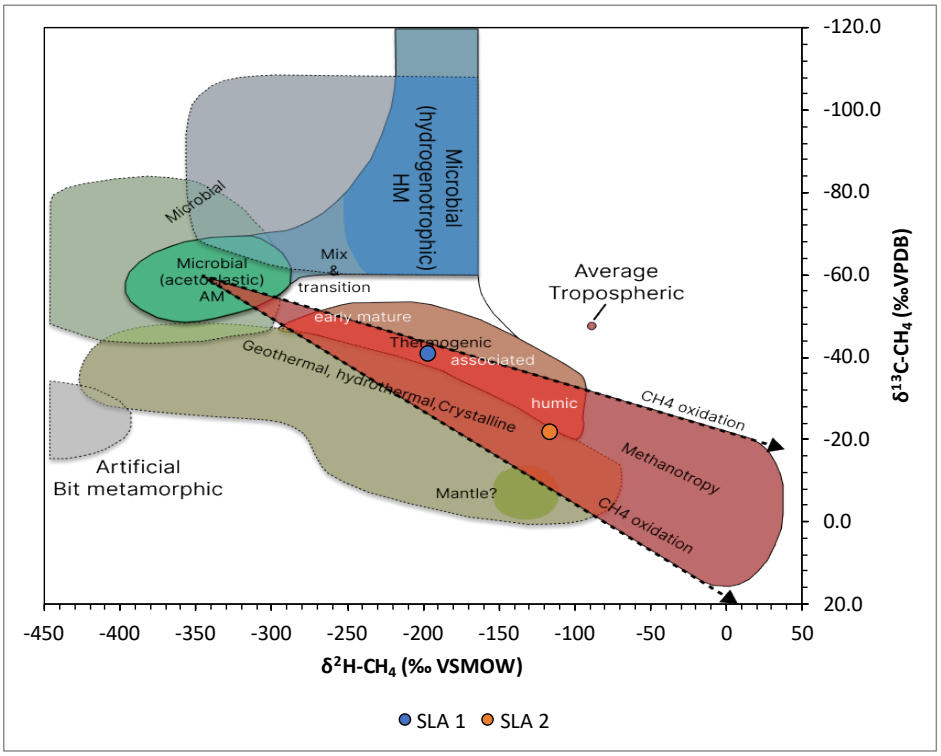


Figure 1: Stable carbon versus stable hydrogen isotope signatures of dissolved methane compared to endmembers and influencing processes according to Whiticar (2020) and Milkov & Ethiope (2018).

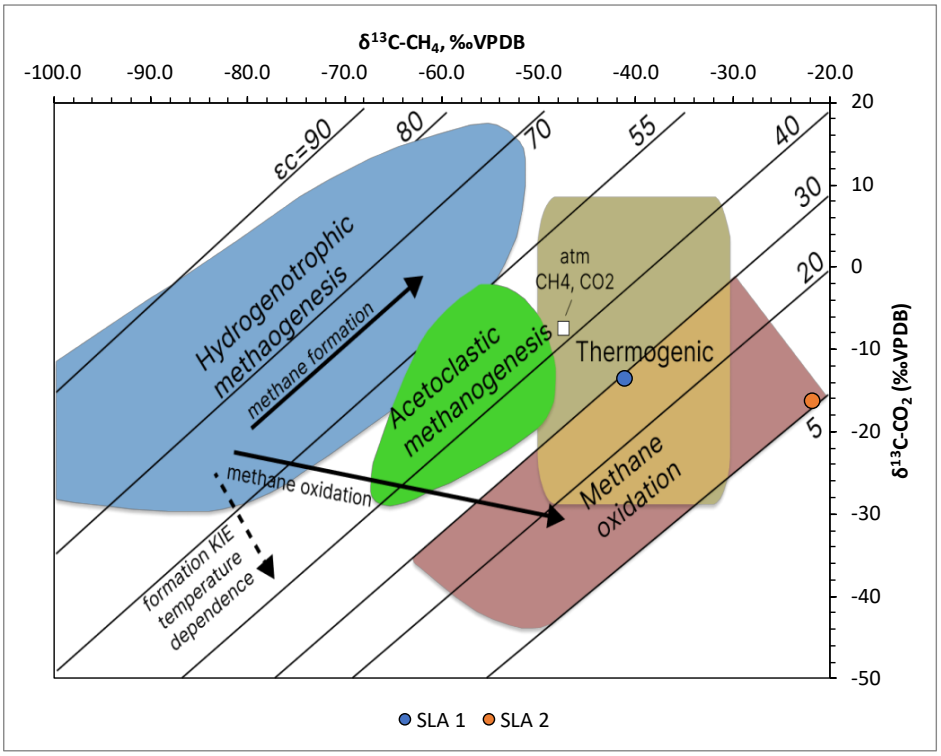


Figure 2: Isotope ratios of methane and carbon dioxide in the $\delta^{13}C$-CH_4 versus $\delta^{13}C$ -CO_2 diagram; the fields and arrows mark different origin and genesis processes of methane according to Whiticar (2020) and Milkov & Ethiope (2018); the numerical values, εc, indicate the degree of oxidation; the high εc indicate high, original, methane concentrations, the low εc strongly oxidized methane concentrations.

4.3 Dissolved inorganic carbon and carbon isotopes

The total content of dissolved inorganic carbon amounted to 95 (SLA 1) and 200 (SLA 2) ccSTP/kg in the stainless steel cells.

The DIC and carbon isotope results for SLA 1 are well within the known range of regional groundwater, showing only moderate isotope exchange with the Muschelkalk aquifer and still a detectable ^{14}C-DIC activity concentration.

In contrast, the DIC level in SLA 2 is significantly elevated. At the same time, the results of the isotope analyses show a depleted stable isotope signature parallel to a ^{14}C-DIC activity below detection (< 2 pmC).

Table 4: DIC result and carbon isotopes

Labor-Nr.		**415039**	**415040**
		SLA 1	**SLA 2**
		16.04.2024	**15.04.2024**
Total DIC (steel container)	ccSTP/kg	94.9	199.8
	mmol/l	4.24	8.92
Isotopes of DIC (steel container)			
Carbon-13 ($\delta^{13}C$-DIC)	‰-VPDB	-7.5	-9.3
Carbon-14 (^{14}C-DIC)	pmC	2.9 ± 0.2	<2

4.4 Noble gases and stable isotopes

The noble gas spectrum of the in-situ groundwater (Ne, Ar, Kr, Xe) was originally equilibrated with the atmospheric air pressure, and concentrations in groundwater are inversely proportional to the palaeotemperature in the recharge area. In this context the derivation of a uniform Kr isotope spectrum and a plausible recharge temperature for Kr within the noble gas pattern (Ne – Xe) is a proof that the analysed fractions are preferentially related to atmospheric air and the prevailing recharge conditions. If the noble gas patterns show a similar uniform recharge temperature, main effects of noble gas flux for Kr can be excluded.

The noble gas isotope datasets of the groundwater samples from the Schlattingen wells were performed at University of Heidelberg, germany (standard noble gas isotope analysis; abundance measurement) and with a extended isotope parameter set analysed at Woods Hole Oceanographic Institution, USA. The complete datasets are given in the attached lab report and show good agreement of the laboratory results. To derive the recharge palaeotemperature the total sum of the isotope values for Ne, Kr and Xe at Woods Hole Oceanographic Institution, USA was used and Ar was corrected for ^{40}Ar-accumulation according to LEE ET AL. (2006).

For the evaluation of potential alterations of the noble gas equilibrium pattern or single components (e.g. Kr), multiple calculations with fit parameter variations (A, p, s, T, and F_Pr, F_CE) were performed simulating plausible scenarios using the PR model programme (Stute et al. 1995) and the Panga platform for UA and CE models (Jung et al. 2018). In accordance with

previous regional studies (Waber & Traber 2022), the model scenarios for the PR, UA and CE models were defined (recharge elevation 500 m asl / 0.96 atm, salinity ≤ 0.01 mol/L).

Table 5: Recharge temperatures obtained by the application of different models (PR, UA and CE) for the sample including the applied input parameters.

	EQ-model	s	P	Δ Ne [%]	Ne	Ar	Kr	Xe	Tav	±	TKr-Xe	±
		[g/kg]	[atm]	[%]	[° C]	[° C]	[° C]	[° C]	[° C]	[° C]	[° C]	[° C]
SLA 1	PR (M.Stute)	0.01	0.96	94	2.5	4.7	1.9	0.9	2.5	1.6	1.4	0.7
	UA	0.01	0.96	99	-	-	-	-	0.9	1.1		
	CE	0.01	0.96	104	-	-	-	-	*-0.6*	*1.4*		
SLA 2	PR (M.Stute)	0.01	0.96	-	-	21.7	19.7	22.6	21.3	1.5	21.2	2.1
	UA	0.01	0.96	-	-	-	-	-	21.2	2.1		
	CE	0.01	0.96	-	-	-	-	-	-	-		

The overall model results (PR; UA, CE) for SLA 1 suggest a very low recharge temperature compared to climatic conditions in the Holocene period, but the determined range of the palaeotemperature for the sample coincides with the signature of stable water isotopes.

In contrast the noble gas pattern for sample of SLA 2 indicates an alteration due to preferential degassing of Ne during pumping and sampling. In these cases the CE model cannot be applied without sophisticated modelling, but the PR and UA model results for SLA 2 show good plausibility for an elevated recharge temperature (≈ 21 °C) for the heavier noble gases Ar-Xe which correspond with the stable water isotopes.

The model recharge temperature results for the samples indicate a complex and different noble gas pattern with clear equilibrium (Ar, Kr, Xe) for each sample. As the results for Tav and TKr-Xe agree (see table 2) within the measured noble gas pattern no clear indication of possible gain or loss of Kr within the noble gas spectrum is evident.

A robust evaluation within the analysed noble gas spectra can be performed based on the noble gas isotope ratios for each noble gas element compared to air equilibrated water (20 °C; 1.0 atm) used as standard for the noble gas isotope analyses (^{3}He, ^{4}He, ^{20}Ne, ^{21}Ne, ^{22}Ne, ^{36}Ar, ^{40}Ar, ^{78}Kr, ^{80}Kr, ^{82}Kr,^{83}Kr, ^{84}Kr, ^{86}Kr, ^{124}Xe, ^{126}Xe, ^{128}Xe, ^{129}Xe, ^{130}Xe, ^{131}Xe, ^{132}Xe, ^{134}Xe, ^{136}Xe).

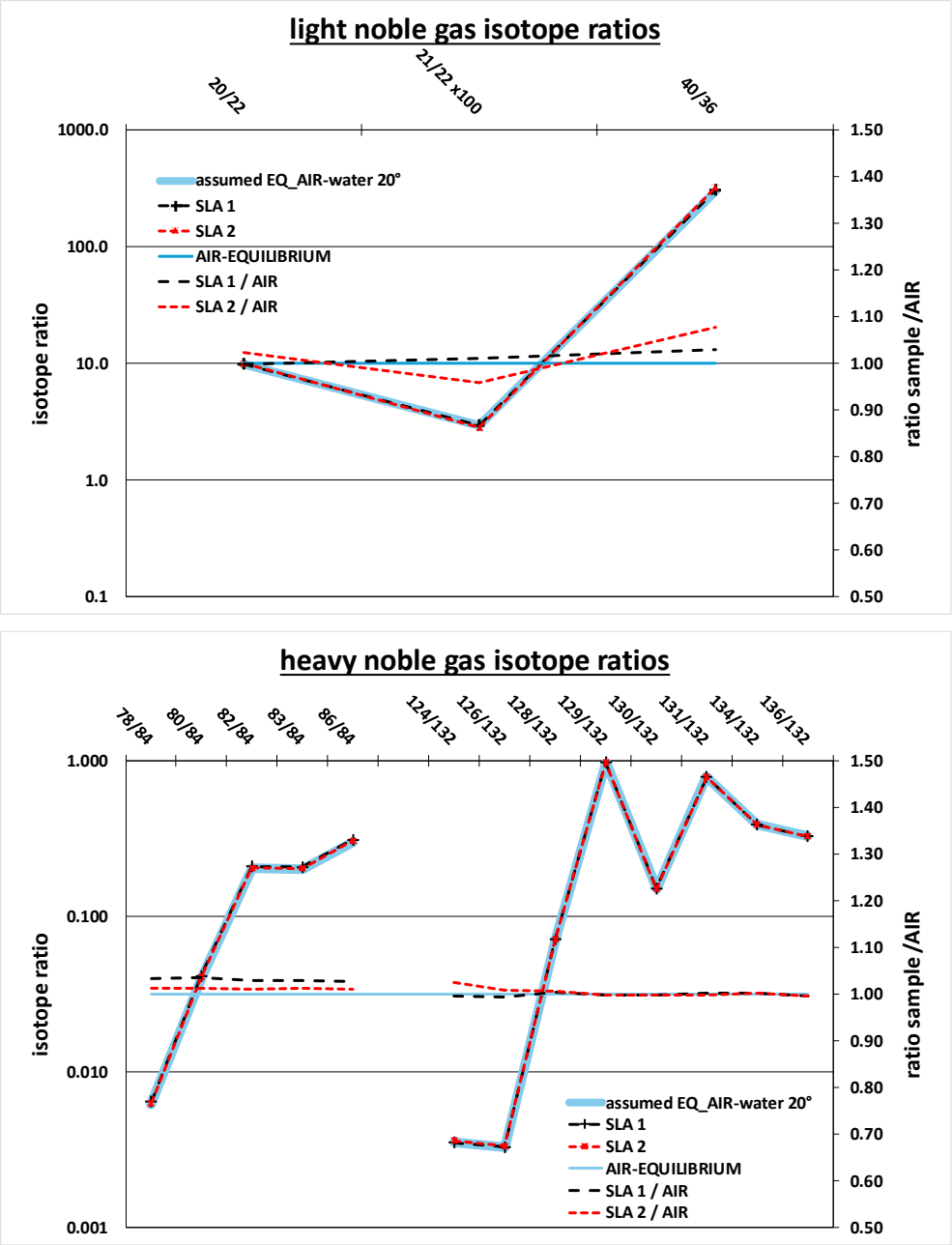


Figure 3: Deviation of analysed noble gas isotope ratios of the Schlattingen samples (SLA 1 and SLA 2) to laboratory standard water in equilibrium with air.

With the exception of the results for the radiogenic components ^{3}He, ^{4}He, ^{21}Ne produced by neutrons from uranium fission on oxygen or magnesium and ^{40}Ar by ^{40}K decay, it can be summarised that no indicators for significant alterations of the noble gas isotope spectrum above the analytical precision can be derived from the analysed data set (see Figure 3).

Based on the strictly atmospheric Kr isotope ratios, a significant diffusive Kr flux (loss or gain) can be excluded for both Schlattingen samples (SLA 1 and SLA 2). This is of importance for the ^{81}Kr dating method.

With regard to the hydrochemical of SLA 2 (e.g. marin Br / Cl ratio) a mixture of genetically different components (very old marine water with meteoric water of negligible salinity and possibly ^{81}Kr bearing) is likely.

The effects of mixing of very old marine water (brines) and low noble gas inventory with meteoric water with negligible salinity and possibly elevated noble gas inventory (including Kr) on ^{81}Kr dating can be quantified using simplified estimations based on the approach of Gerber et al. (2017).

The noble gas characteristics of the postulated endmembers (meteoric water ASW + excess air and seawater AS-MOW) can be calculated on the Panga platform (Jung et al. 2018) for ^{84}Kr, using the plausible range for pressure (p), temperature (T), salinity (s) and excess air (maximum A in scenarios).

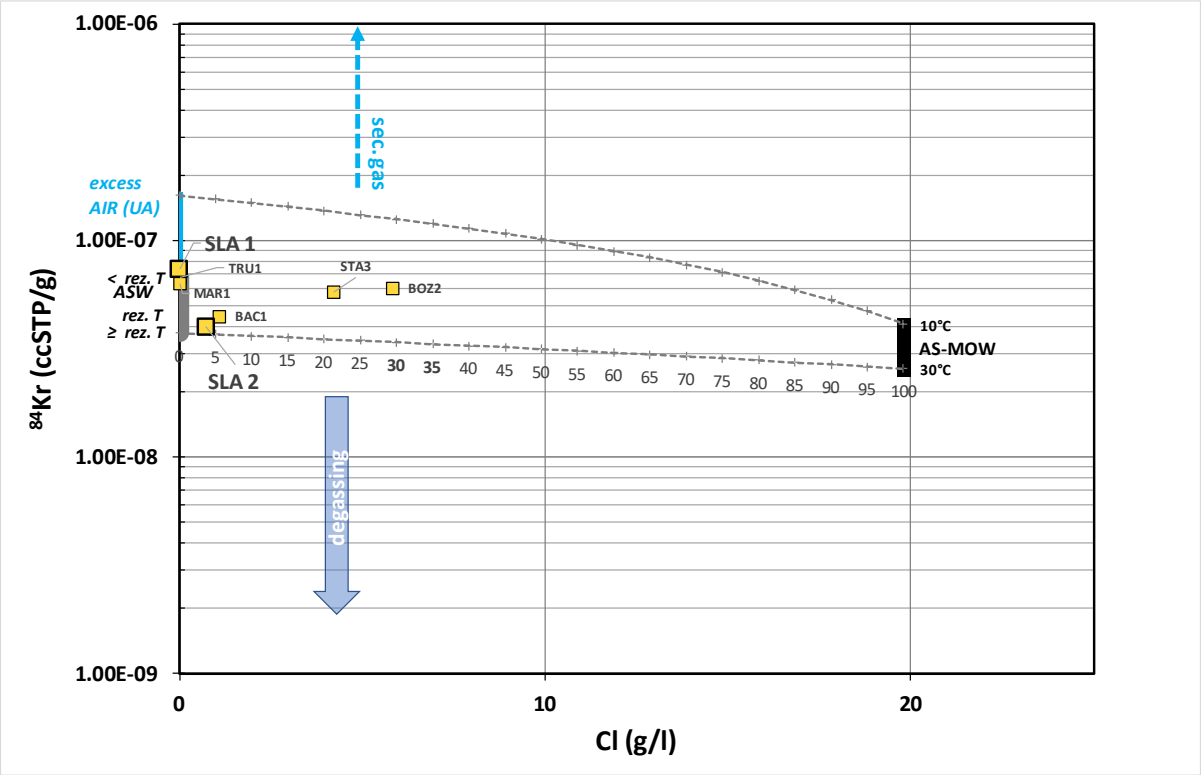


Figure 4: Measured concentrations of atmosphere-derived noble gas isotopes (^{84}Kr) versus the in-situ groundwater Cl^- concentrations. Dashed black lines show the range of concentrations expected for mixing of the postulated meteoric and marine (Cl = 19 g/L) endmembers. Arrows show possible effects of secondary gas uptake and degassing.

As shown in Figure 4, the slightly elevated Cl- concentration of the groundwater sample from SLA 2 well may contain a plausible proportion of a marine component of < 5 % with an assumed Cl concentration of 19 g/L. At the same time, the comparison shows only small differences of the Krypton noble gas inventory for the genetically different components (very old marine water with meteoric water of negligible salinity and possibly ^{81}Kr bearing).

In consequence for the dating with ^{81}Kr a dilution effect for ^{81}Kr by the low Kr gas inventory of a very old, unaltered marine endmember component may not exceed a portion in the range of 5 % of the analysed Kr content of the SLA 2 sample.

4.5 Krypton-85 and Krypton-81 data and corrections

The results of the ^{85}Kr and ^{81}Kr analyses of the samples SLA 1 and SLA 2 and basic data for the atmospheric ^{85}Kr activity are given and summarised in Table 3. Due to the time between sampling and analysis the analytical results for ^{85}Kr (ATTA) are corrected for decay to $^{85}Kr_{m\ (decay\text{-}corr)}$ before they are used for model age interpretation and for correction of $^{81}Kr_m$. The atmospheric ^{85}Kr activity is important for the correction of contamination with air.

Table 6: Analytical results of radioactive Kr and Ar isotopes via ATTA and decay correction for $^{85}Kr_m$

		415039	**415040**
		SLA 1	**SLA 2**
PN-Datum		**MUK**	**MUK**
$^{81}Kr_{ATTA}$	**pm^{81}Kr**	94.5	22.9
±	**pm^{81}Kr**	0.13	0.06
$^{85}Kr_{corr}$	**dpm/mLKr**	**2.36**	**0.28**
±	**dpm/mLKr**	**0.19**	**0.07**
max$^{85}Kr_{atm}$	dpm/mLKr	**73.7**	**73.7**
±	dpm/mLKr	**0.7**	**0.7**
α Kr		0.0320	0.0038
±		0.0026	0.0010
$^{81}Kr_{corr}$	**pm^{81}Kr**	**94.3**	**22.6**
±	**pm^{81}Kr**	**0.1**	**0.1**

The correction of the analytical results gained by ATTA for contamination with air (see Section 3.3) is a standard procedure using the α attempt for $^{81}Kr_m$ (see Eqs. 1; Chapter 3). The correction for $^{81}Kr_{corr}$ is summarised in Table 5 and follows a conservative scenario to determine a lower limit of the ^{81}Kr model age. Consequently, the maximum atmospheric $^{85}Kr_{atm}$ activity (including an uncertainty of 0.7 dpm/cc$_{Kr}$) during the sampling and preparation procedure (see Table 4 and Table 5) is used.

Table 7: Air-correction for $^{81}Kr_{corr}$ acccording to equation (1) and maximum atmospheric $^{85}Kr_{atm}$ activity.

Lab.No.		**415039**	**415040**
Sample		**SLA 1**	**SLA 2**
AQ		**MUK**	**MUK**
sampling date		17.04.2024	16.04.2024
analysis date		20.11.2024	20.11.2024
$^{85}Kr_m$	dpm/mLKr	2.27	0.27
±	dpm/mLKr	0.18	0.07
$^{81}Kr_m$	**pm^{81}Kr**	94.5	22.9
±	**pm^{81}Kr**	0.13	0.06
$^{85}Kr_{corr}$	**dpm/mLKr**	**2.36**	**0.28**
±	**dpm/mLKr**	**0.19**	**0.07**
$^{85}Kr_{atm}$	dpm/mLKr	**73.7**	**73.7**
±	dpm/mLKr	**0.7**	**0.7**
α Kr		0.0320	0.0038
±		0.0026	0.0010
α_{Kr} x 100	%	3.2	0.4
±	%	0.3	0.1
$^{81}Kr_{corr}$	**pm^{81}Kr**	**94.3**	**22.6**
±	**pm^{81}Kr**	**0.1**	**0.1**
^{81}Kr-model age	**a**	**19'000**	**491'000**
lower		18'000	467'000
upper		21'000	516'000
mean	a	19'326	491'266
minus	a	1'376	24'435
plus	a	1'422	24'522
min. age	a	17'950	466'832
max. age	a	20'748	515'788

The corrected result ($^{81}Kr_{corr}$) of the low mineralised groundwater sample from SLA 1, with an ^{81}Kr model age of approximately 19’000 years, show very good agreement with the ^{81}Kr age information obtained to date from the Muschelkalk of northern Switzerland (see Figure 5).

In conclusion the higher mineralised groundwater sample from SLA 2 - corrected for contamination with air - is characterised by a low ^{81}Kr activity content (22.6 ± 0.1 pm^{81}Kr) and a resulting high ^{81}Kr model age. As the sample is a plausible mixture between only low amounts (< 5 %) of very old marine / brackish water and dominant meteoric water with only minor differences in absolute Kr contents (see Figure 6). The corrected result ($^{81}Kr_{corr}$) for SLA 2 is based on a mixture of both components involved, but is almost identical to the circulation age of the dynamic non-marine/brackish components.

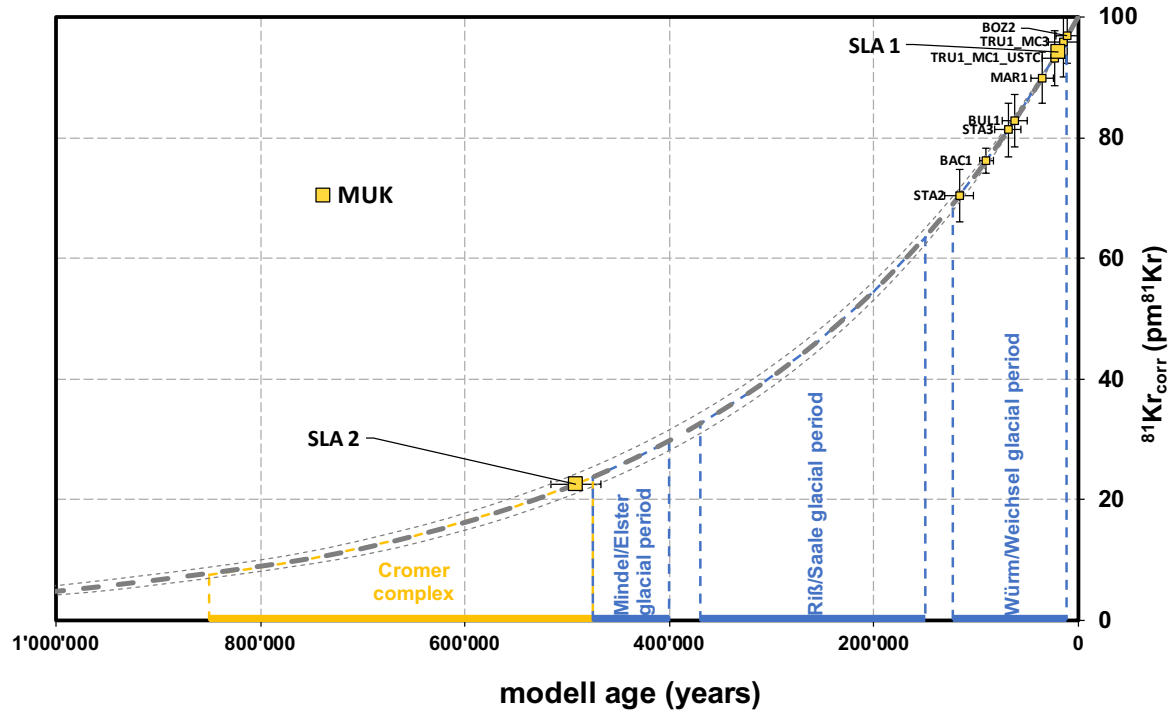


Figure 5: Corrected value for $^{81}Kr_{corr}$ of the in-situ groundwater samples from Schlattingen (SLA 1 and SLA 2) and calculated ^{81}Kr model age for the half-life 229'000 ± 11'000 years.

4.6 Argon-39 and Argon-37 data and corrections

The results of the ^{39}Ar and ^{37}Ar analyses of the samples SLA 1 and SLA 2 summarised in Table 6 and basic data for the atmospheric ^{37}Ar activity (0.00642 [dpm/LAr]) are used for corrections according to Eqs. (2) and (3) in Section 3.4. Due to the time between sampling and analysis the analytical results are corrected for decay before they are used for correction.

Table 8: Analytical results of radioactive Kr and Ar isotopes via ATTA and decay correction for $^{85}Kr_m$

Lab.No.		415039	415040
Sample		**SLA 1**	**SLA 2**
AQ		**MUK**	**MUK**
sampling date		16.04.2024	15.04.2024
$^{85}Kr_{ATTA}$	dpm/ccKr	2.27	0.27
±	dpm/ccKr	0.18	0.07
$^{39}Ar_m$	pm^{39}Ar	41	55
±	pm^{39}Ar	7	8
$^{37}Ar_m$	dpm/LAr	0.096	0.045
±	dpm/LAr	0.012	0.012
$^{85}Kr_{corr}$	dpm/ccKr	2.36	0.28
±	dpm/ccKr	0.19	0.07
$^{85}Kr_{atm}$	dpm/ccKr	73.7	73.7
±	dpm/ccKr	0.7	0.7
α_{Kr}		0.0320	0.0038
±		0.0026	0.0010
Kr/Ar	sample	2.36E-04	2.33E-04
Kr/Ar	AIR	1.18E-04	1.18E-04
F		2.00	1.97
α_{Ar} x 100	%	6.4	0.8
±		0.5	0.2
$^{39}Ar_{corr}$	pm^{39}Ar	**37**	**55**
±	pm^{39}Ar	**7**	**8**
$^{37}Ar_{corr}$	dpm/LAr	**0.1025**	**0.0453**
±	dpm/LAr	**0.0128**	**0.0121**

According to a low contribution to underground production by muons at greater depth (Musy et al. 2023, Musy & Purtschert 2023), the elevated values of $^{39}Ar_{corr}$ and $^{37}Ar_{corr}$ in this study are caused by the U-Th decay chain (Lehmann et al. 1993, Šrámek et al. 2017).

In comparison, the $^{39}Ar_{corr}$ values in the Schlattingen wells show only a moderate range for underground production. However the missing correlation to $^{37}Ar_{corr}$ (see Figure 6) indicates a complex underground equilibrium production (UEP) of ^{39}Ar and ^{37}Ar in the Muschelkalk aquifer of the Schlattingen region and a comparison of the ^{81}Kr model ages with the $^{39}Ar_{corr}$ results (see Figure 7 and 8) shows a UEP variation between SLA 1 and SLA 2 of more than +30 %.

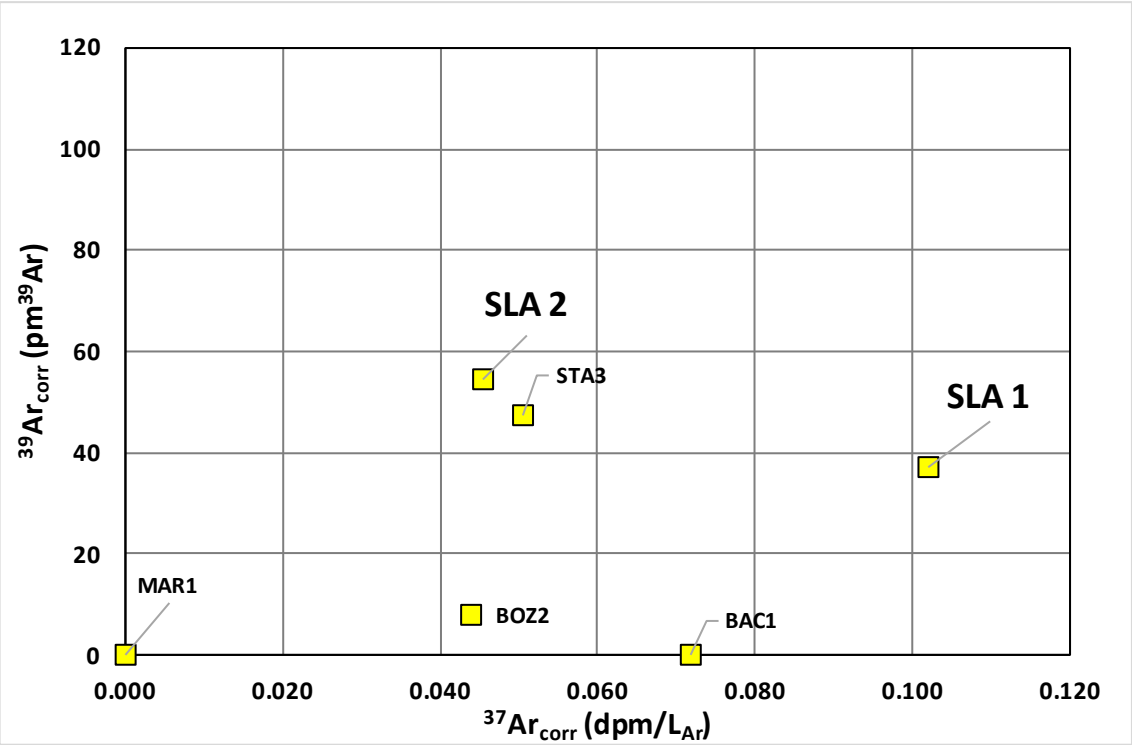


Figure 6: $^{37}Ar_{corr}$ versus $^{39}Ar_{corr}$ of the Muschelkalk groundwater samples in Northern Switzerland.

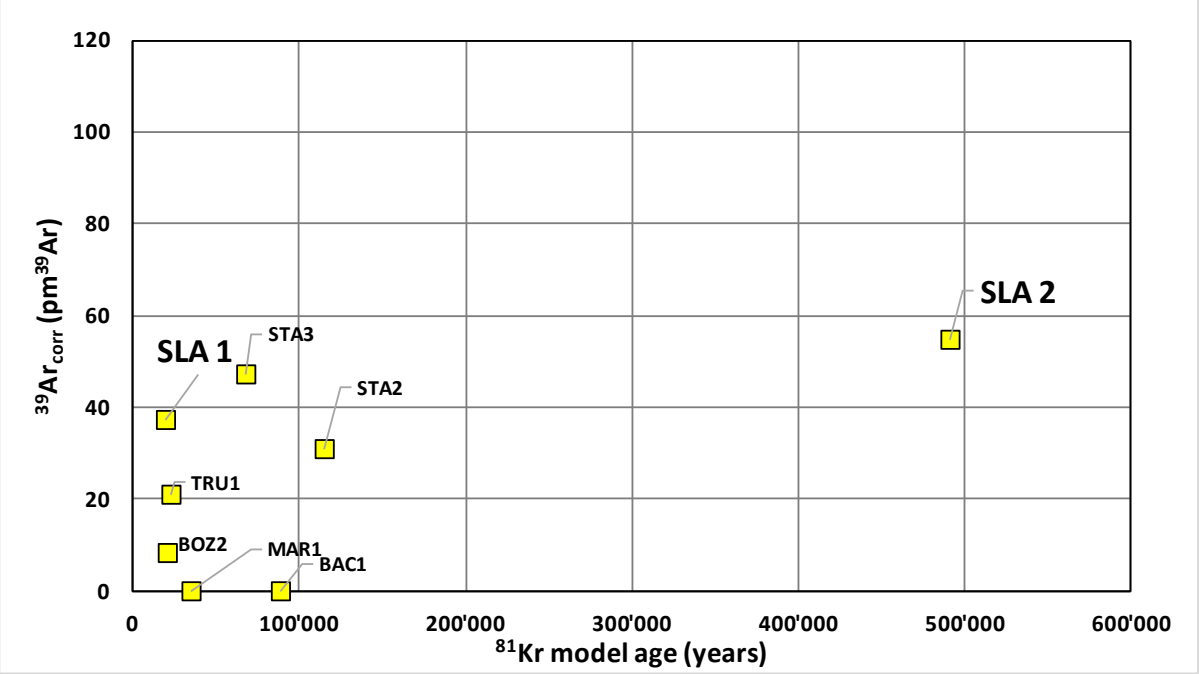


Figure 7: Values for $^{39}Ar_{corr}$ of the Muschelkalk groundwater samples and calculated ^{81}Kr model age for the half-life 229'000 ± 11'000 years.

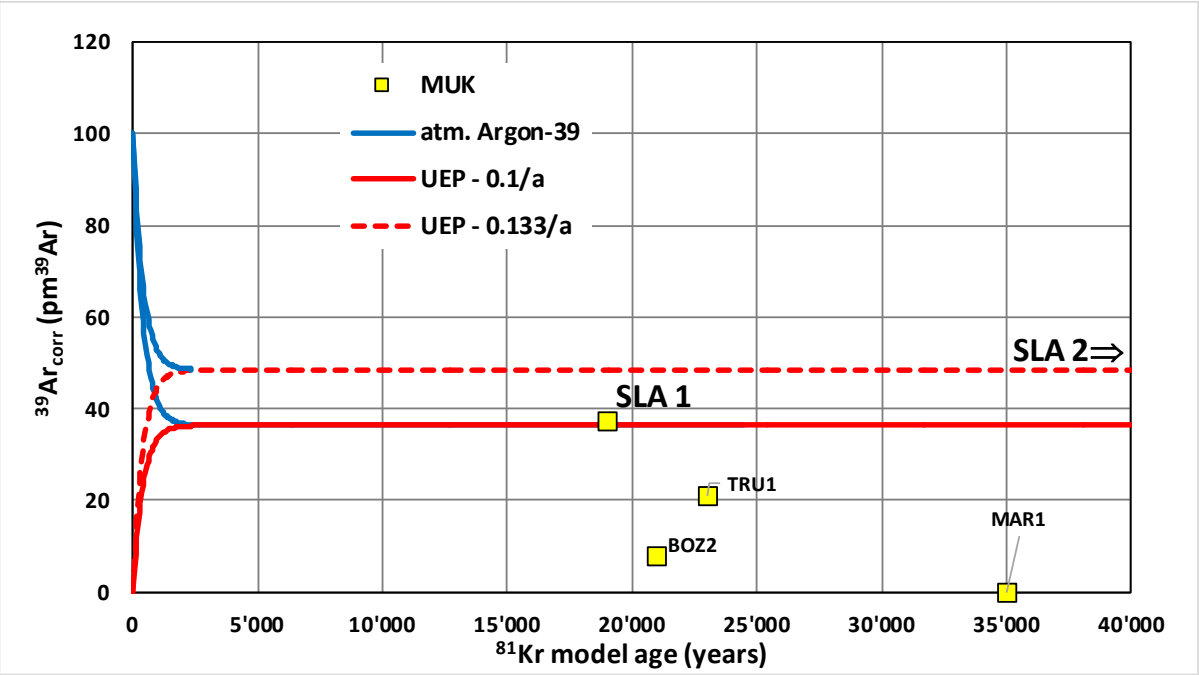


Figure 8: $^{39}Ar_{corr}$ results of selected Muschelkalk groundwater samples and calculated ^{81}Kr model age with matching of different UEP-values for SLA 1 and SLA 2.

4.7 Helium-4 and Argon-40 accumulation

The evaluation of the He-isotope data (see Figure 9) from Northern Switzerland and Southern Germany shows that in the Schlattingen region an ^{3}He/^{4}He isotope ratio in the range of ≈ 3.0E-07 is a plausible approximation for helium accumulation. This might include some minor regional influence of the mantle helium (< 5 %) or significantly elevated Li- versus U/Th-contents in the Muschelkalk primarily responsible for the differentiation in ^{3}He/^{4}He accumulation compared with the more westerly areas of Northern Switzerland.

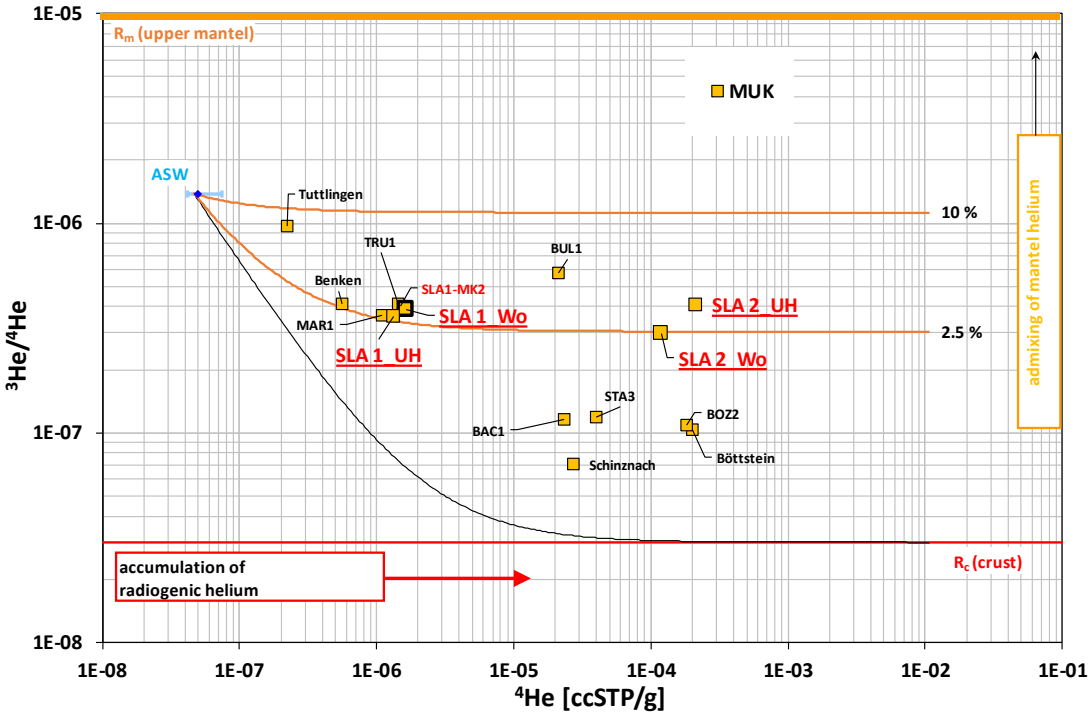


Figure 9: He-isotope data of the Muschelkalk groundwater samples from Northern Switzerland and Southern Germany.

For the regional selection the correlation ^{4}He to the ^{81}Kr model ages is very good ($R^2 > 0.9$) indicating a mixing system of Pleistocene groundwater with a very old end member.

Alternatively, however, a relative constant transfer of underground ^{4}He-production to the Muschelkalk groundwater in the range of ≈ 2.5E-7 ccSTP/g in 1'000 years could also be seen as a plausible approximation for the region (see Figure 10).

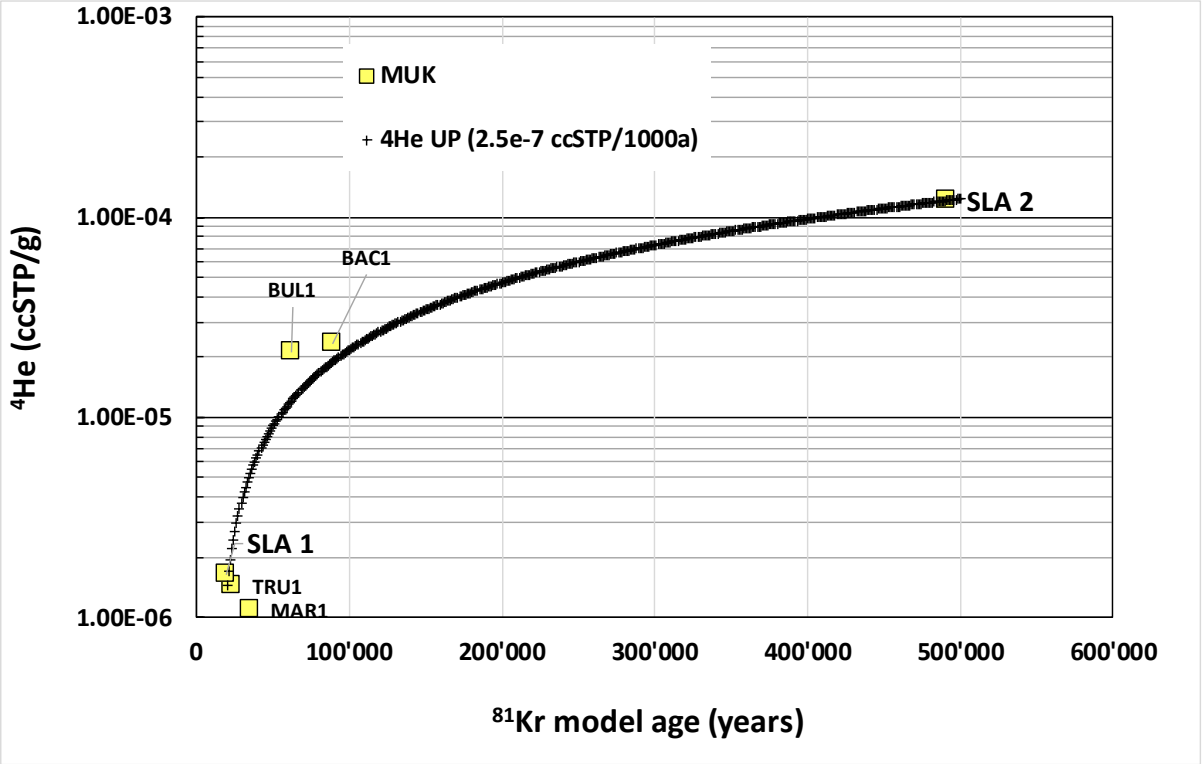


Figure 10: ^{4}He-isotope data of selected Muschelkalk groundwater samples and calculated ^{81}Kr model age with matching of ^{4}He-accumulation for SLA 1 and SLA 2 via constant UP-rate.

Both samples (SLA 1 and SLA 2) show a significantly elevated ^{40}Ar/^{36}Ar isotope ratio compared to the atmosphere and the groundwater in the Muschelkalk aquifer system of northern Switzerland (see Figure 11). The results indicate significant ^{40}Ar production from ^{40}K decay in the underground.

To estimate the relative ^{40}Ar production, the ^{36}Ar contents, which differ by a factor of 1.8 (SLA 1 > SLA 2), must be taken into account. However the comparison of ^{40}Ar/^{36}Ar to the ^{81}Kr model ages already indicates a much higher ratio of ^{40}Ar production for SLA 1 as for regional Pleistocene groundwater in the Muschelkalk.

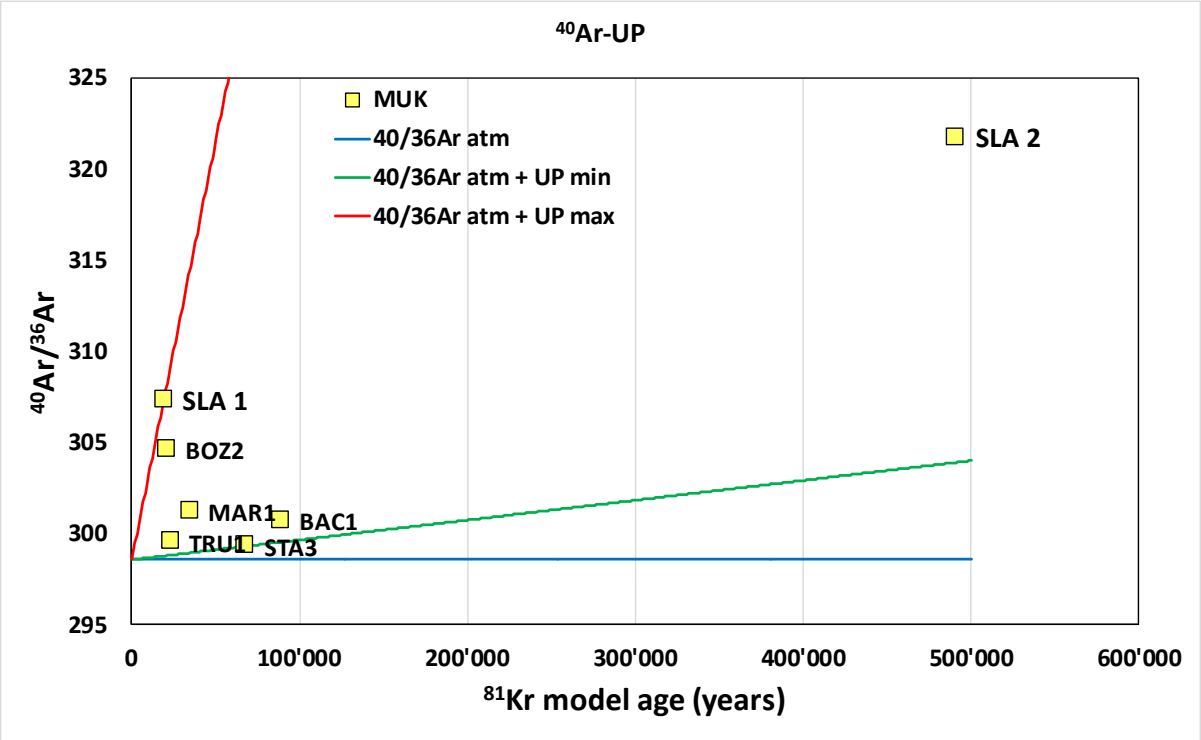


Figure 11: ^{40}Ar/^{36}Ar-isotope ratios of selected Muschelkalk groundwater samples and calculated ^{81}Kr model age and matching of ^{40}Ar accumulation via constant UP-rate.

References

Andrews J.N. and Lee D.J. (1979) Inert gases in groundwater from the Bunter Sandstone of England as indicators of age and palaeoclimatic trends, Journal of Hydrology, Volume 41, Issues 3–4, 1979, Pages 233-252, ISSN 0022-1694, https://doi.org/10.1016/0022-1694(79)90064-7.

Aeschbach-Hertig W., El-Gamal H., Wieser M. and Palscu L. (2008) Modeling excess air and degassing in groundwater by equilibrium partitioning with a gas phase: modeling gas partitioning. Water Resources Research, 44, W08449, https://doi.org/10.1029/2007WR006454

Bollhöfer A., Schlosser C., Schmid S., Konrad M., Purtschert R. and Krais R. (2019) Half a century of Krypton-85 activity concentration measured in air over Central Europe: Trends and relevance for dating young groundwater, Journal of Environmental Radioactivity, Volumes 205–206, 2019, Pages 7-16, ISSN 0265-931X, https://doi.org/10.1016/j.jenvrad.2019.04.014.

Gerber C., Vaikmäe R., Aeschbach W., Babre A., Jiang W., Leuenberger M., Lu Z.-T., Mokrik R., Müller P., Raidla V., Saks T., Waber H.N., Weissbach T., Zappala J.C. and Purtschert R. (2017) Using 81Kr and noble gases to characterize and date groundwater and brines in the Baltic Artesian Basin on the one-million-year timescale, Geochim Cosmochim Acta. 205:187-210.

Jung M. and Aeschbach W., (2018) A new software tool for the analysis of noble gas data sets from (ground)water, Environmental Modelling & Software, Volume 103, 2018, Pages 120-130, ISSN 1364-8152, https://doi.org/10.1016/j.envsoft.2018.02.004

Lee J.-Y., Marti K., Severinghaus J., Kawamura K., Yoo H.-S., Lee J. and Kim J. S. (2006). A redetermination of the isotopic abundance of atmospheric Ar. Geochimica Et Cosmochimica Acta - GEOCHIM COSMOCHIM ACTA. 70. 10.1016/j.gca.2006.06.1563.

Lu Z.-T., Schlosser P., Smethie W.M., Sturchio N.C., Fischer T.P., Kennedy B.M., Purtschert R., Severingshaus J.P., Solomon D.K., Tanhua T. and Yocochi P. (2014) Tracer applications of noble gas radionuclides in the geosciences, Earth Sci Rev. 138:196-214.

Milkov, A. and Etiope, G. (2018). Revised genetic diagrams for natural gases based on a global dataset of >20,000 samples. Organic Geochemistry. 125, 2018, Pages 109-120, ISSN 0146-6380, https://doi.org/10.1016/j.orggeochem.2018.09.002.

Nagra NTB 19-02 (2023) Die Tiefengrundwässer in der Nordschweiz und imangrenzenden Süddeutschland: Beschaffenheit, Herkunft und unterirdische Verweilzeit

Purtschert R., Yokochi R. and Sturchio N. C. (2013) 81Kr dating of old groundwater. In Isotope Methods for Dating old Groundwater (eds. A. Suckow, P. Aggarwal and L. Araguas-Araguas). IAEA, Vienna, pp. 91–124. Available at: http://www-pub.iaea. org/books/IAEABooks/8880/Isotope-Methods-for-Dating-Old-Groundwater.

Purtschert R., Yokochi R., Jiang W., Lu Z.-T., Mueller P., Zappala J., Van Heerden E., Cason E., Lau M., Kieft T.L., Gerber C., Brennwald M.S. and Onstott T.C. (2021) Underground production of 81Kr detected in subsurface fluids, Geochimica et Cosmochimica Acta, Volume 295, 2021, Pages 65-79, ISSN 0016-7037, https://doi.org/10.1016/j.gca.2020.11.024.

Sturchio N.C., Kuhlman K. L., Yokochi R., Probst P. C., Jiang W., Lu Z.-T., Mueller P. and Yang G.-M. (2014) Krypton-81 in groundwater of the Culebra Dolomite near the Waste Isolation Pilot Plant, New Mexico, Journal of Contaminant Hydrology, Volume 160, 2014, Pages 12-20, ISSN 0169-7722, https://doi.org/10.1016/j.jconhyd.2014.02.002.

Stute M., Forster M., Frischkorn H., Serejo A., Clarke J.F., Schlosser P., Broecker W.S. and Bonani G. (1995) Cooling of tropical Brazil (5C) during the last glacial maximum. Science 269: 379-383.

Waber H.N. & Traber D. (2022): Die Tiefengrundwässer der Nordschweiz und im angrenzenden Süddeutschland: Beschaffenheit, Herkunft und interirdische Verweilzeit. Nagra Technischer Bericht NTB 19-02.

Whiticar, M. (2020). The Biogeochemical Methane Cycle. 10.1007/978-3-319-54529-5_5-1.

Zappala J. C., Baggenstos D., Gerber C., Jiang W., Kennedy B. M., Lu Z.-T., Masarik J., Mueller P., Purtschert R., and Visser A. (2020) Atmospheric 81Kr as an integrator of cosmic-ray flux on the hundred-thousand-year time scale. Geophysical Research Letters, 47, e2019GL086381. https://doi.org/10.1029/2019GL086381

Ufrecht,W. & Hlözl, S. (2006): Strontium (87Sr/86Sr)-Isotopie salinarer Mineral- und Thermalwässer im Oberen Muschelkalk – Entwicklung eines Genesemodells. – Schriuftenreihe des Amtes für Umweltschutz, 3/2006: 49-68; Stuttgart.

Appendix 2: The modified TK consult numerical groundwater model

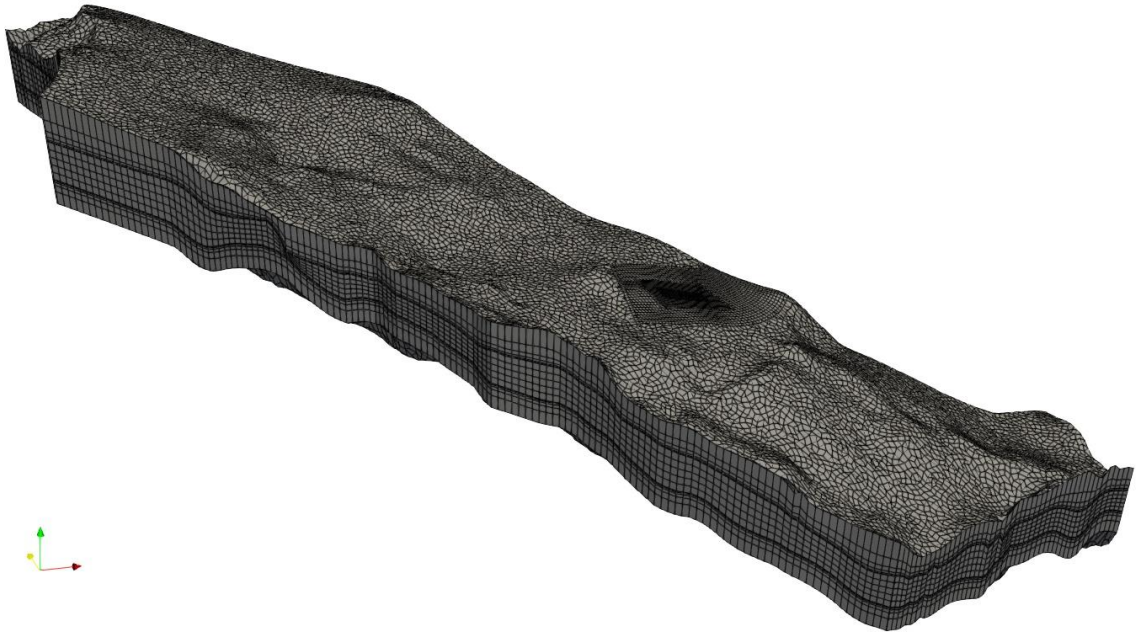
TK CONSULT AG
NUMERISCHE MODELLIERUNGEN

Hydrothermal Simulations for the Deep Geothermal Well Schlattingen

Model Update 2025

Technical Report – English Version

19. November 2025



Kanton Thurgau
Amt für Energie
Thomas Volken
Promenadenstrasse 8
8510 Frauenfeld

TK CONSULT AG
Neugasse 136
CH-8005 Zürich
Phone: +41 (0) 44 288 81 81
tkc@tkconsult.ch
www.tkconsult.ch

TKC 10077.01

Version	Date	Editor	QM	Revision Marks	Mailing List
v1.0	19.11.2025	BAM	KUR	-	Kanton Thurgau Enevista Energy AG University of Bern

Table of Contents

1 Background and Goals 1

1.1 Current Situation 1

1.2 Project Goal 3

2 Geological Concept and Model Update 4

2.1 Modelling Concept 2020 4

2.2 Transport Concept Research Project 4

2.3 Mesh Update 5

3 Data and Approach 7

4 Calibration and Simulation Results 10

4.1 Initial Conditions 10

4.2 Case 1 and 2 10

4.3 Performance pumping test 2015 14

5 Conclusion 15

Bibliography 17

1 Background and Goals

1.1 Current Situation

At the beginning of the last decade, the company Grob Gemüse AG decided to cover its long-term heat demand by the use of deep geothermal energy. To this end, two boreholes, SLA-1 and SLA-2, were drilled in 2011 and 2013. From the early beginnings, the project is numerically supported by TK CONSULT AG [1]. The 3D hydrothermal model spans from the outcrop zones of the Muschelkalk in the Wutachtal, about 35 km in the direction southeast (see Figure 1). Around the boreholes SLA-1 and SLA-2 (Figure 2), it includes the geological formations Trigonodus-Dolomit, Hauptmuschelkalk, Anhydritgruppe as well as Wellengebirge (Figure 3). The model ends in the southeast at Herdern (Frauenfeld), where measurements at the borehole Herdern-1 can be used for the formulation of a first type boundary condition (fixed pressure head). The latest model update dates to the year 2020. It was performed in the context of the licence application [2]. The included calibration was based on the pumping test 2015 (Figure 4). For the correct reproduction of the measured pressure dops, a special concept for the geological layering around SLA-2 had to be developed.

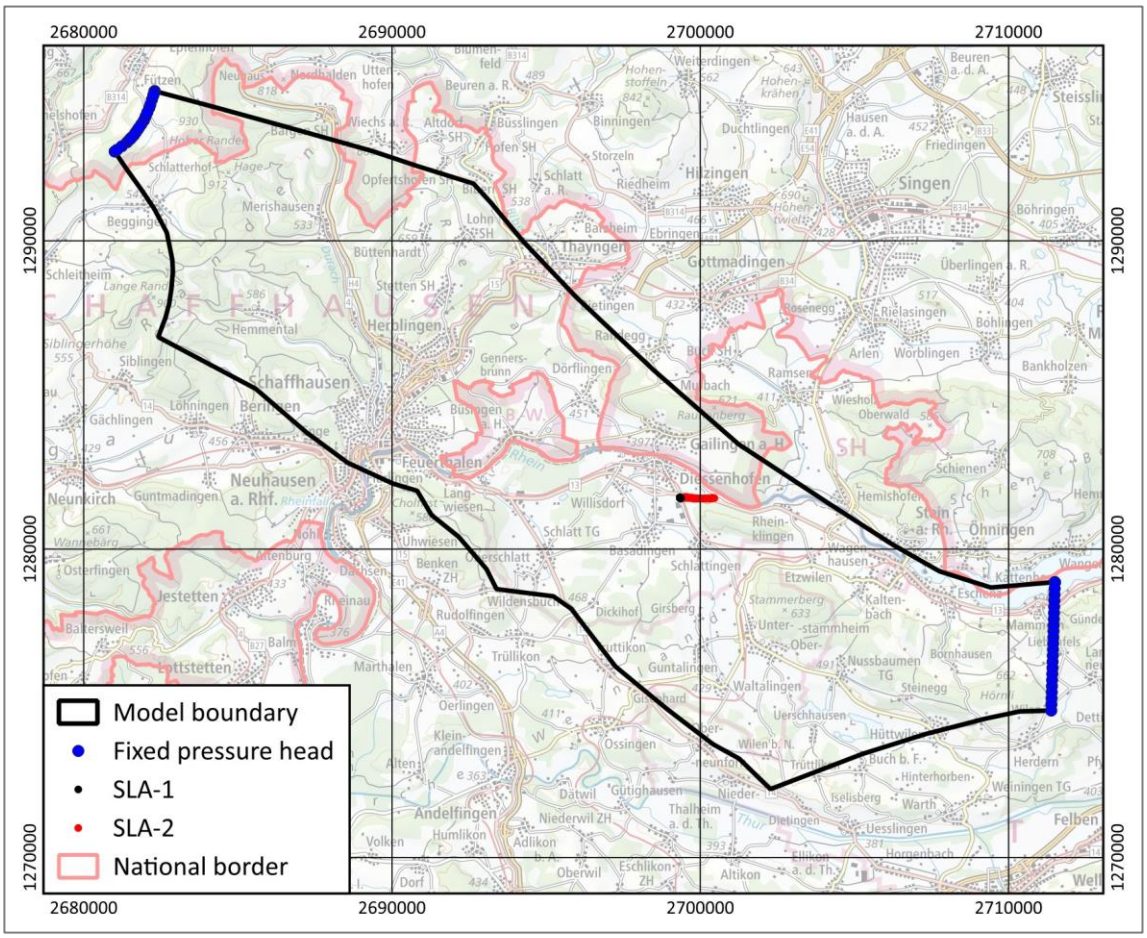


Figure 1: Perimeter of the 3D hydrothermal model.

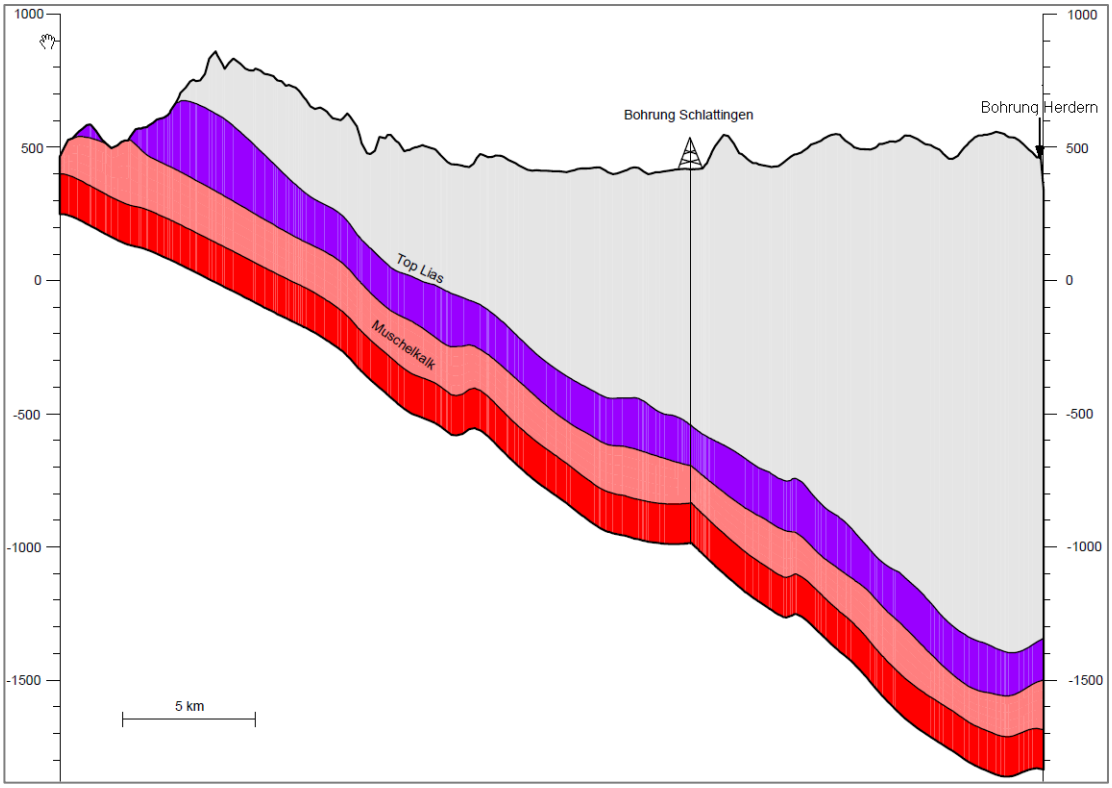


Figure 2: Cross section (NW-SO) along the numerical model, see [1].

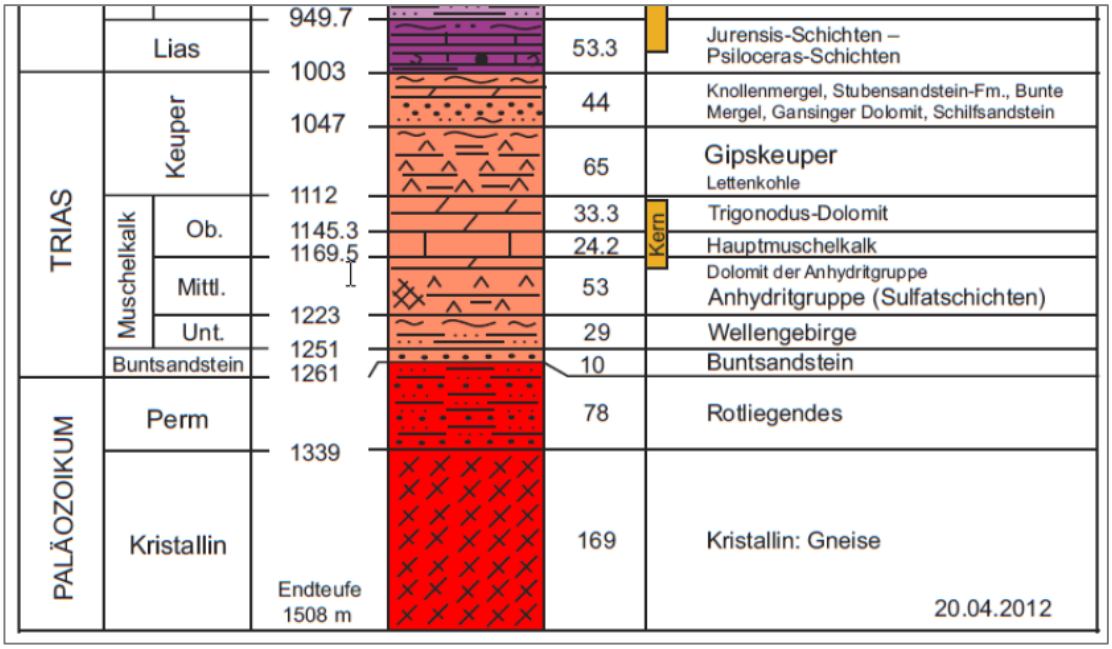


Figure 3: Extract drilling profile SLA-1 (Albert et al., 2012), see [1].

1.2 Project Goal

The 2020 calibration showed, that the SLA-2 borehole is located in a complex geological structure, which was conceptually mapped by numerically implementing a low-permeability shell. With this concept, the measured pressure drops could be reproduced very well. After the concession had been granted, the boreholes were used permanently for the heat production for the greenhouses. This production phase could be evaluated as long-term pumping tests. Additionally hydro-chemical and isotope analyses have been conducted on the produced fluids. The evaluation of the hydro-chemical data of the fluids from the two geothermal wells showed that there are hydro-chemically separated compartments of the Muschelkalk aquifer in the Schlattingen region. This conceptual modeling approach was confirmed by the accompanying numerical reactive transport modeling [3].

In the framework of a research project [3], the hydrogeological concept of 2020 was conceptually extended based on the mentioned findings. The aim of this project has been to integrate the new findings into the existing regional hydrothermal model, evaluate the effects on the modeled pressure heads, recalibrate the model, and make the resulting fluxes in the area of the SLA-1 and SLA-2 boreholes available for the University of Bern for detailed transport simulations.

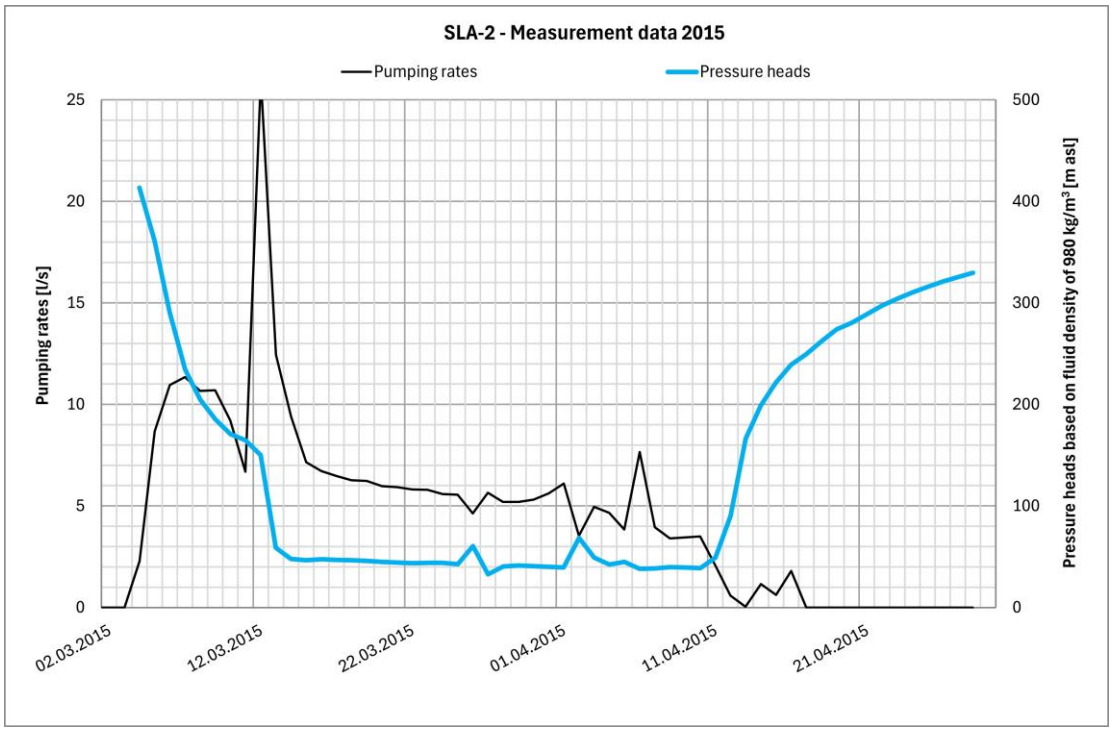


Figure 4: Measured pumping rates and pressure heads in SLA-2 from March to May 2015.

2 Geological Concept and Model Update

2.1 Modelling Concept 2020

Figure 5 shows the original hydrogeological concept around SLA-2, which was used for the licence application [2]. Three rectangular kf-value (permeability) zones, R1, R2, and R3, were defined around the horizontal filter well. The overlying Keuper layer (1.0E-12 m/s, 5.0E-20 m²) limits all other formations. The calibration yielded to a value of 3.0E-7 m/s (1.5E-14 m^2) for R1, 2.0E-7 m/s (1.0E-14 m^2) for R2, and 3.5E-9 m/s (2.0E-16 m^2) for R3. The high contrast between R3 and R1 and R2, respectively, enables a short-term rapid use of a limited but quickly available volume of water. R3 prevents rapid refilling and thus rapid pressure recovery, as observed in the 2015 pumping test.

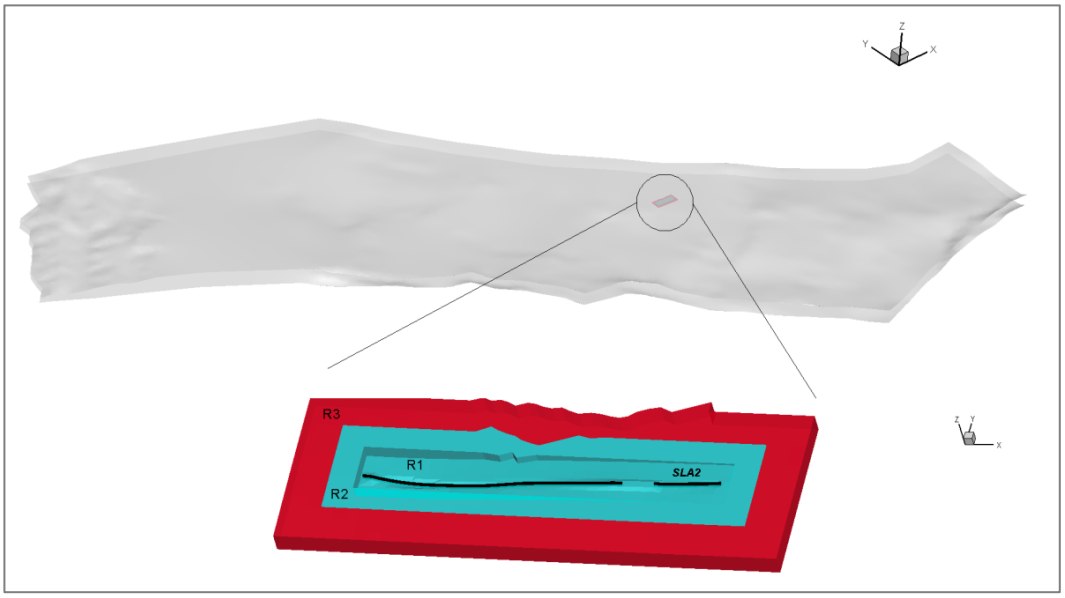


Figure 5: Hydrogeological concept SLA-2 2020 [2].

2.2 Transport Concept Research Project

The extended new concept of the research project is shown in horizontal and vertical direction in Figure 6. The Zones 4 and 5 were further added. The spatial location and connectivity of the zones were also adjusted based on the new findings. The more conductive zones R1 and R2 (in the Trigonodus Dolomite and Hauptmuschelkalk / Upper Muschelkalk) are again horizontally enclosed by the poorly conductive zone R3 (in the Trigonodus Dolomite). However, they do not cover the entire filter area of SLA-2, but only the last 34 m. R3 is bounded downward by the Hauptmuschelkalk. The thickness of R3 corresponds to the thickness of the Trigonodus dolomite according to borehole SLA-1 and is 35 m. Zone R5 lies below zones R1 and R2 at the level of the anhydrite group (middle Muschelkalk) and Wellengebirge. It acts as a subvertical connectivity zone, thus enabling the rise of crystalline deep water to the well SLA-2, as suggested by chemical analyses. Due to the small extent of the well-permeable fissures and fault zones along SLA-2 and the contrasting regional model character, their geometric mapping is

omitted. The related flow effects are mapped by adjusting the corresponding bulk parameters (porosity and permeability).

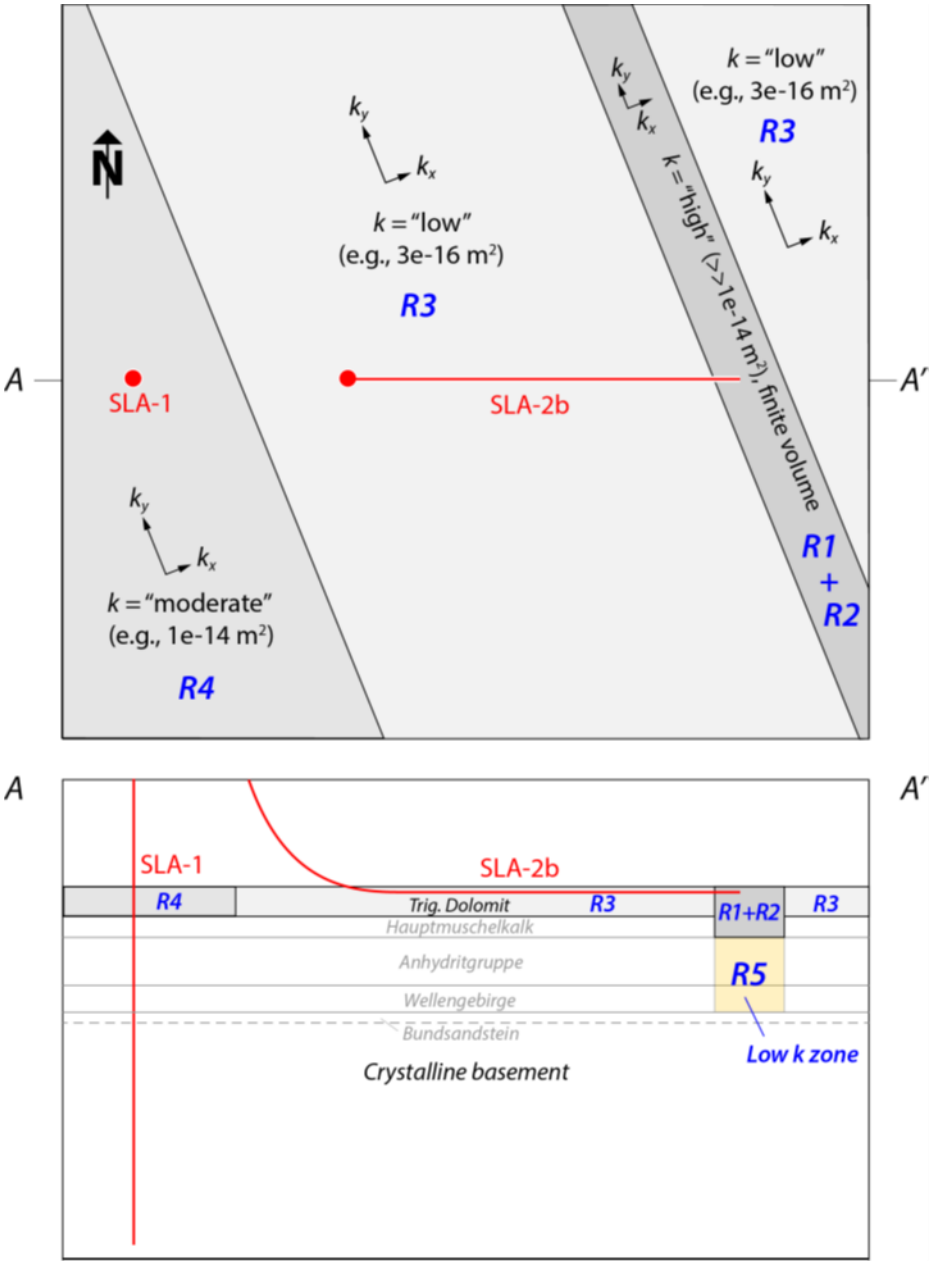


Figure 6: Concept Research Project for SLA-1 and SLA-2 [4].

2.3 Mesh Update

To map the updated concept, the existing model mesh in the area of SLA-1 and SLA-2 had to be completely renewed (see Figure 7). Beside the construction of the zones R1 to R5, the mesh was aligned in a way that the element edges are congruent with the local transport model of the research project. This enables an easy extraction of volume flows and pressure heads as well as simple extensions and adjustments of the zones R1 to R5. The vertical discretization is

visualized in Figure 8. The geometries of the zones R1 and R2 have been adjusted during calibration in a way that R2 limits zone R1 to the east and downwards. This enables a smooth transition from conductive to less conductive between R1, R2, R5, and the adjacent aquifer.

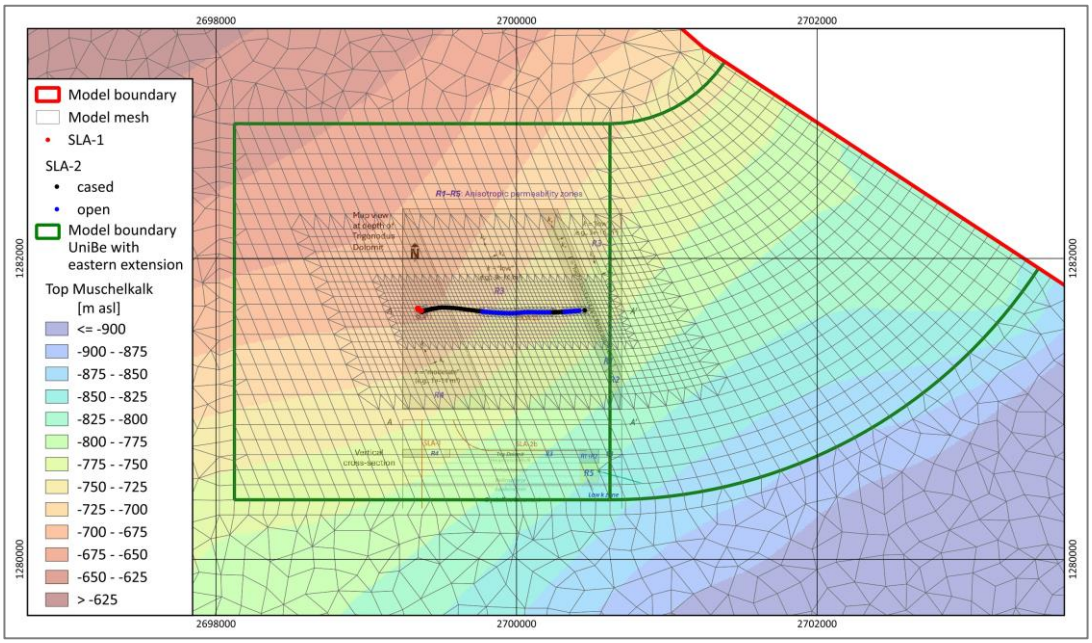


Figure 7: Updated horizontal mesh.

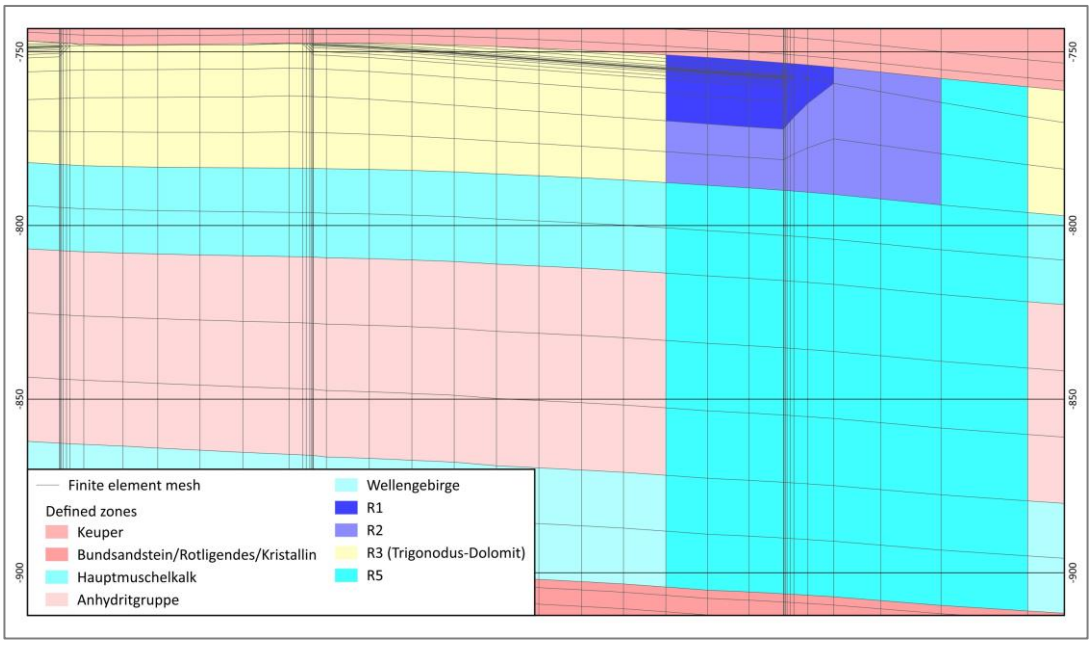


Figure 8: Updated vertical mesh.

3 Data and Approach

Figure 9 shows the latest measurement data (production rates and pressure heads) at well SLA-2. Compared to the measurements taken between 2013 and 2015 (see Figure 4), which served as basis for the calibration 2020 [2], two things are worth noting: On the one hand, the average pressure head at SLA-2, at approximately 250 m asl (based on a density of 980 kg/m^3), exceeds average levels measured during early pumping tests. On the other hand, the pressure fluctuations during pumping are significantly lower, with a maximum of approximately 50 m.

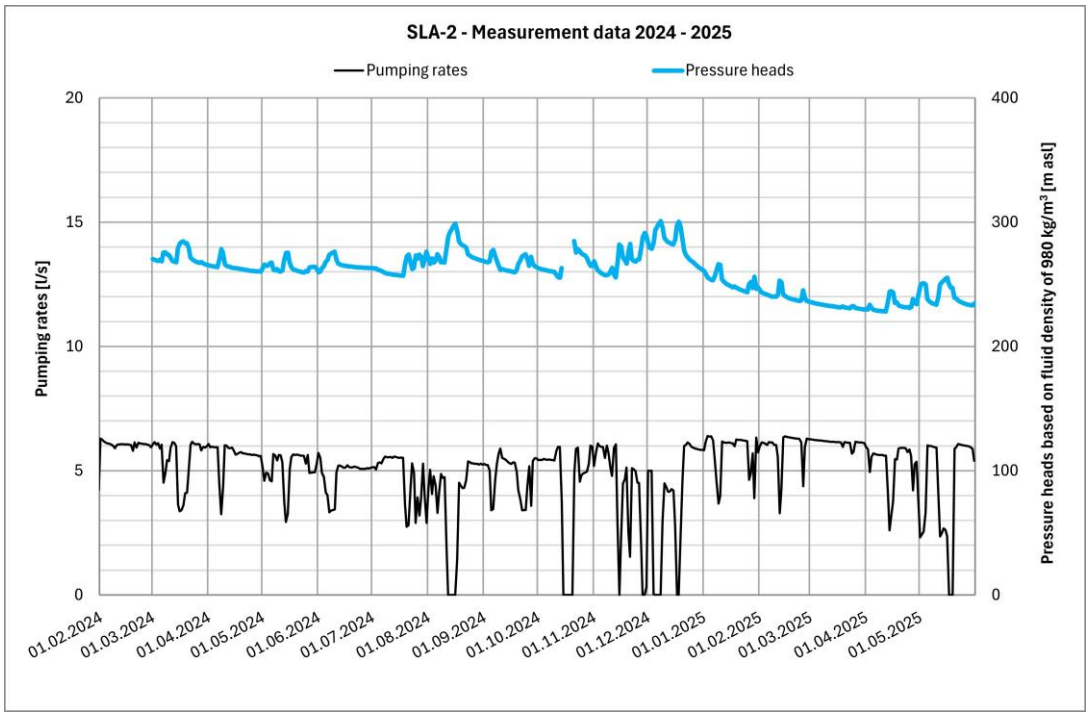


Figure 9: Measured pumping rates and pressure heads SLA-2 from February 2024 to June 2025.

The latter indicates an increase in permeability in the zones R1, R2, and R5. The increase in permeability is likely to have been caused by the dissolution of sulfates (anhydrite) and lime. However, currently there is a lack of data to fully confirm such a process. For validation purposes and to investigate the hypothesis numerically, the current measurement period was also simulated using the model of 2020. To capture correct initial conditions, the entire simulation period from 2015 was taken into account. Figure 10 shows the measured and simulated pressure curve at SLA-2 from 2024 to 2025. The production rates from 2019 to 2024 were extrapolated according to [5] (see section 4.1) as pressure data for well SLA-2 is not available or deficient for this period.

The simulations show, that with the calibrated permeabilities the pressure level at well SLA-2 drops strongly to approx. 100 m. Simultaneously, large pressure fluctuations occur at only moderate changes in the production rate. In contrast the reproduction of the 2015 measurements has been very good with the same model [2]. This supports the thesis of a change in permeability over the latest years. As an outcome of a project team meeting (TKC, UniBe, Enevista Energy AG), it was agreed on not to reproduce the measurement data prior to 2024 with

the new concept. The calibration of permeability values in zones R1 to R5 is therefore solely performed for the period from 2024.

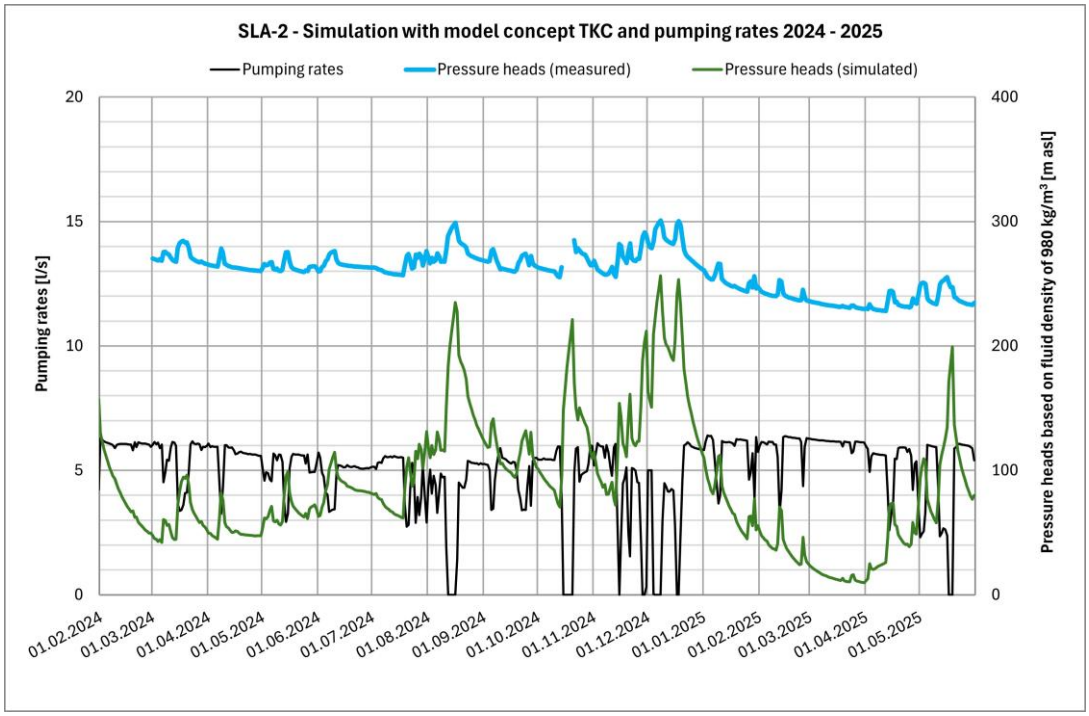


Figure 10: Measured and simulated pressure heads at SLA-2 (model 2020) from 2024 to 2025.

Table 1: Permeabilities of the different geological zones and formations.

Zones / Layers	K [m²]	kf [m/s]	δ [kg/m³]	η [kg/(ms)]	Calibration Status
Keuper	5E-20	1.0E-12	980	0.45	Assumption Model 2012 [1]
Muschelkalk (outside local transport model UniBe) – model boundary (northwest)	3E-14	2.0E-07	1000	1.30	Calibration 2012
Muschelkalk (outside local transport model UniBe) – central area (SLA-1/2)	4E-15	8.5E-08	980	0.45	Calibration 2012
Muschelkalk (outside local transport model UniBe) – model boundary (southeast)	5E-16	1.5E-08	965	0.30	Calibration 2012
Bundsandstein/Rotligendes/Kristallin			980	0.45	Calibration parameter
Hauptmuschelkalk			980	0.45	Calibration parameter
Anhydritgruppe	5E-20	1.0E-12	980	0.45	Assumption (UniBe)
Wellengebirge			980	0.45	Calibration parameter
R1			980	0.45	Calibration parameter
R2			980	0.45	Calibration parameter
R3 (Trigonodus-Dolomit)			980	0.45	Calibration parameter
R4 (Trigonodus-Dolomit)			980	0.45	Calibration parameter
R5			980	0.45	Calibration parameter

Table 1 shows a summary of the used geological layers and zones for the adapted hydrogeological concept, as well as the corresponding permeabilities and the calibration status. The kf-value of the zones R1 to R5, as well as those of the main shell limestone, the Wellengebirge and the crystalline rock, are free parameters of the calibration. The calibration is performed

manually. The simulations are executed using the software SPRING [7]. Due to the relatively constant temperatures [5], a coupling wit a thermal model is not required. The corresponding parameters for the flow simulations can therefore be considered constant at an ambient temperature of 60 °C. The determination of the zone volumes of R1, R2, and R5 is part of the calibration. The porosity in the Muschelkalk is set at 20 % according to the model setup of 2012. Due to the extremely confined conditions, the porosity has only influence on the transport velocities, which are not considered in the current project phase. A sensitivity analysis regarding the proposed anisotropy in R3 shows, that rotating kf_x and kf_y by 20° results in only minor changes in the simulation results. Therefore, implementation was not pursued, and all zones inherit isotropic conditions ($kf_x = kf_y = kf_z$).

Based on the chemical composition of the water, the UniBe estimates that around 25 % of the extracted water origins from crystalline rock. The remaining 75 % mainly come from Muschelkalk limestone and Trigonodus dolomite. Only a negligible proportion is supplied by the Wellengebirge. This information is taken into account during the calibrating.

4 Calibration and Simulation Results

4.1 Initial Conditions

As mentioned above, the measured pressure head has significantly lowered over the last years due to the continuous pumping at SLA-1 and SLA-2. For a correct reproduction of the measured heads from 2024 to 2025, it crucial to map this process correctly. Based on [6] and after consultation with the project team, the estimated pumping rates shown in Figure 11 were used for the simulations from 2015 to 2023, respectively for the construction of the initial conditions.

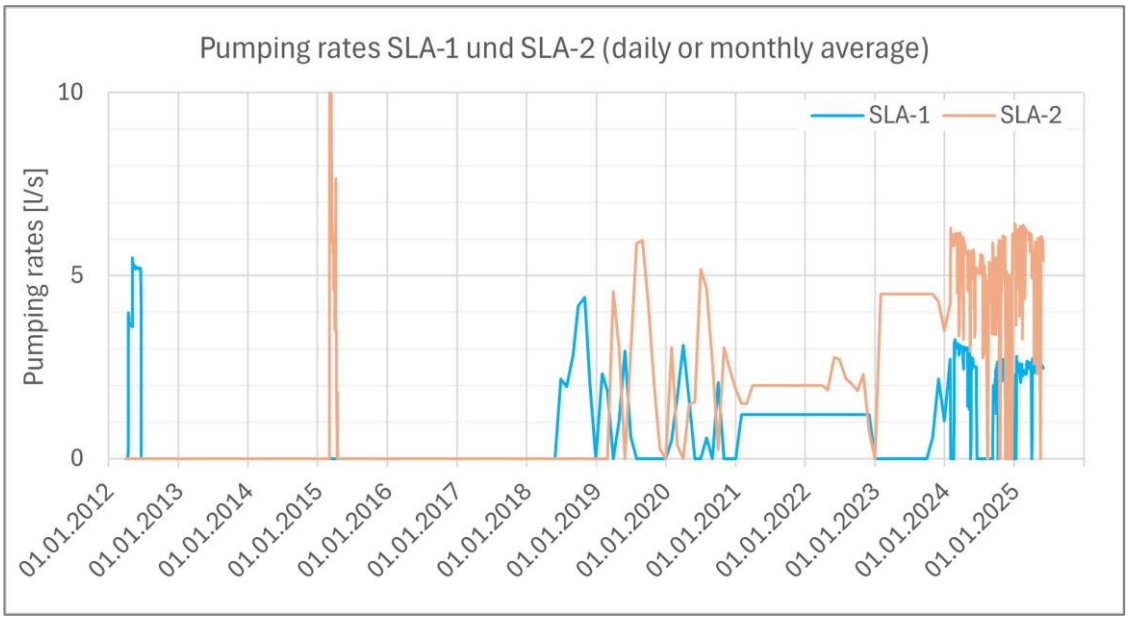


Figure 11: Used pumping rates at SLA-1 and SLA-2.

4.2 Case 1 and 2

Due to the large number of degrees of freedom (kf-values Hauptmuschelkalk, Wellengebirge, and crystalline rock, zones R1 to R5, volumes R1, R2, and R5 as well as extrapolated production rates 2016–2023) that are in contrast to the limited number of flow-relevant measurement data (pressure measurements at the wells SLA-1 and SLA-2), two cases could be determined that lead to a comparably good reproduction of the measured pressure heads. These cases 1 and 2 are discussed below. We restrict ourselves here to the results at well SLA-2 (the modeled pressure heads at SLA-1 match the observations consistently good). The boundary conditions for both cases are supplied to the UniBe. Reactive transport modeling, that leads to an additional reduction of degrees of freedom, will then be used to determine the more probable case.

Table 2 shows the calibrated kf-values and volumes for the cases 1 and 2. The volumes of the zones R1, R2, and R5 are identical for both cases. The modeled pressure heads are shown in Figure 12. Both cases reproduce the average pressure heads as well as their amplitudes and

dynamics very well. The cases differ only marginally in the modeled pressure heads. However, they show large differences in the kf-values of the zones R1, R2, and R5. The kf-values of case 2 are 5e-6 m/s for R1, R2, and R5. They are almost two orders of magnitude lower than in case 1 for R1 and R2, and five times higher for R5. From a hydraulic point of view, it is not required to split the vertical connectivity region into three zones. This is due to the fact that the largest pressure drop occurs between the aquifer and R1/R2/R5 and not within these zones. In both cases, 95 % of the extracted water volume is taken from zone R1 in the last 35 m of the filter. The pressure drops at a distance of about 2000 m from SLA-2 is still 10 m for both cases.

Table 2: Calibrated volumes and kf-values for the cases 1 and 2.

	Case 1			Case 2		
Zones / Formations	**V [m³]**	**K [m²]**	**kf [m/s]**	**V [m³]**	**K [m²]**	**kf [m/s]**
Hauptmuschelkalk		5E-15	1.0E-07		5E-15	1.0E-07
Wellengebirge		5E-18	1.0E-10		5E-18	1.0E-10
Bundsandstein/Rotligendes/Kristallin		3E-16	7.0E-09		3E-16	7.0E-09
R1	2E+04	9E-12	2.0E-04	2E+04	2E-13	5.0E-06
R2	2E+05	5E-12	1.0E-04	2E+05	2E-13	5.0E-06
R3 (Trigonodus-Dolomit)		2E-16	5.0E-09		2E-16	5.0E-09
R4 (Trigonodus-Dolomit)		9E-15	2.0E-07		9E-15	2.0E-07
R5	6E+06	5E-14	1.0E-06	6E+06	2E-13	5.0E-06

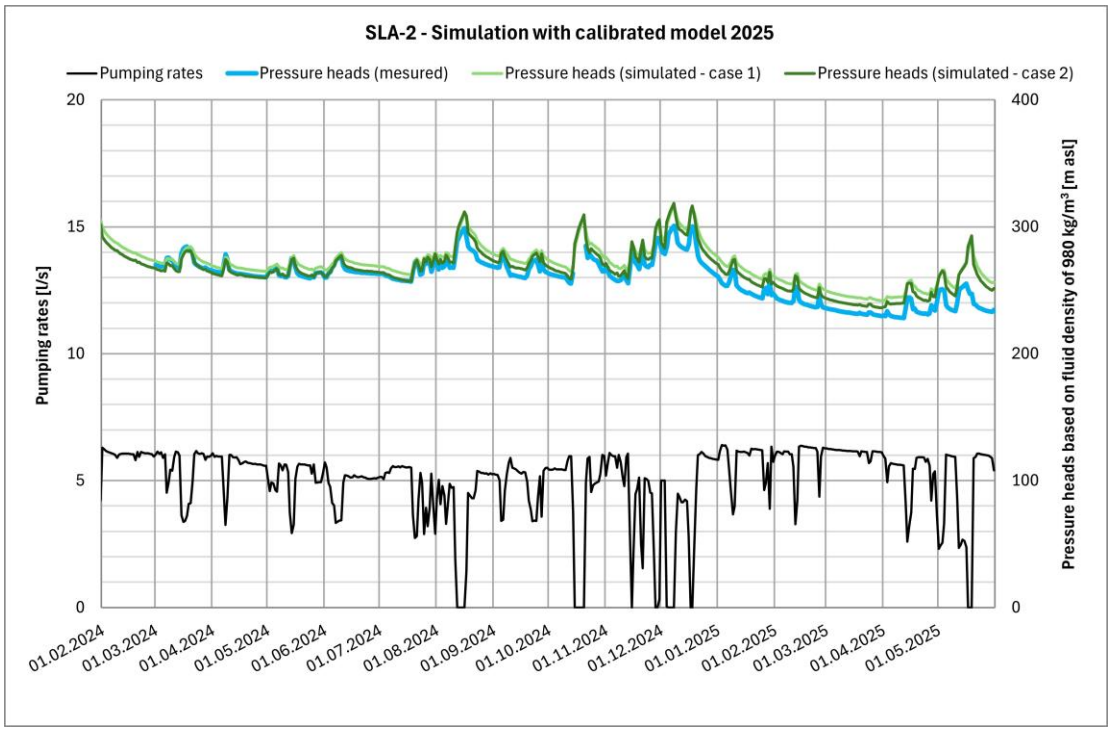


Figure 12: Calibrated pressure heads SLA-2 for the cases 1 and 2.

Figure 13 shows for the case 2, the quasi-stationary volume flows in steady state conditions and at a constant pumping rate of 6 l/s in SLA-2 and 2.5 l/s in SLA-1 across the model boundaries of the local transport model of the research project. The arrow directions indicate the significant change in the pressure gradient during pumping.

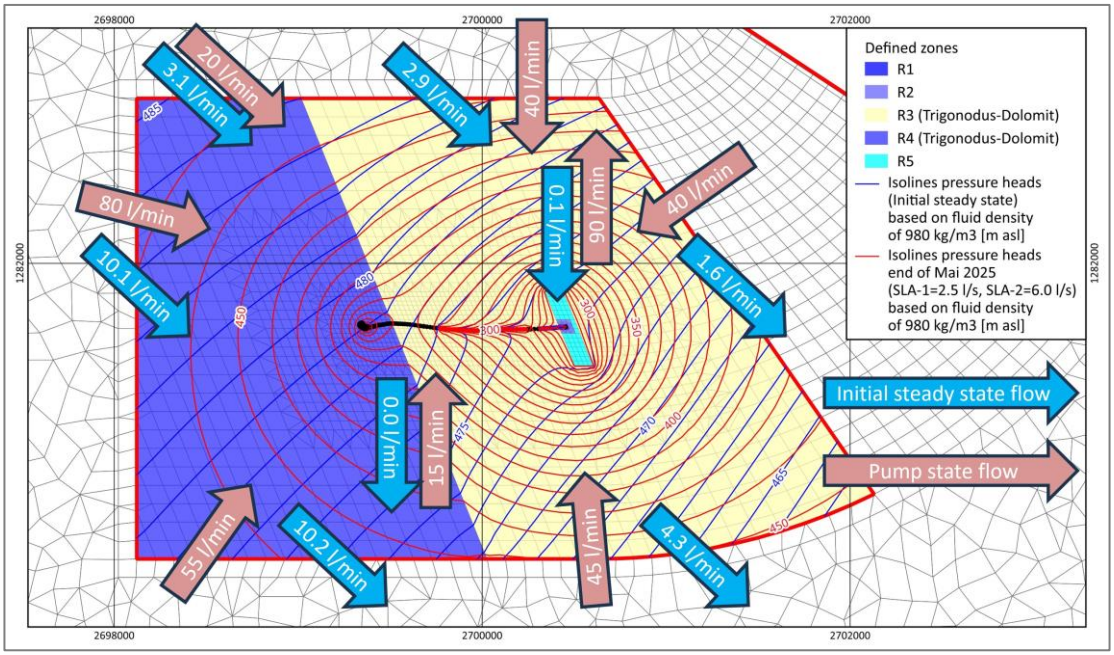


Figure 13: Quasi-stationary volume flows at model boundaries of the local transport model for case 2.

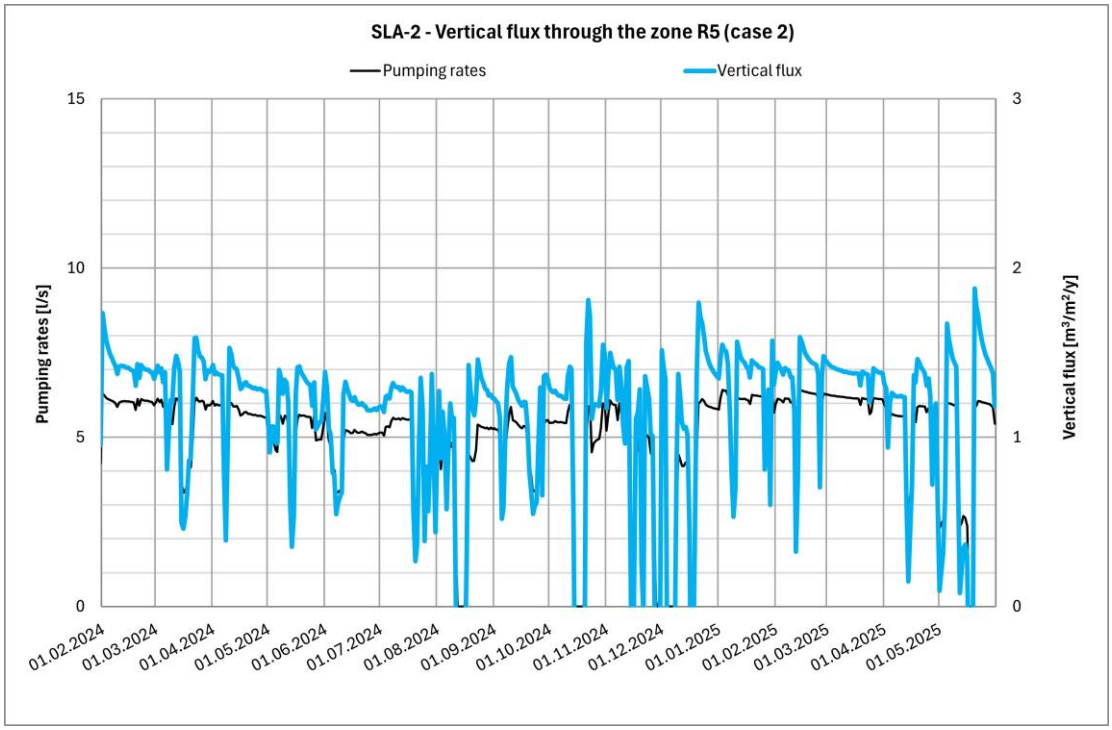


Figure 14: Vertical flux through the zone R5.

The corresponding transient vertical flux through the zone R5 is shown in Figure 14. As it is again identical for both cases, we limit ourselves to case 2. The maximum value is 1.9 $m^3/m^2/y$. As expected, it correlates completely with the pumping rates and partially ceases.

Table 3 shows the composition of the water extracted in SLA-2 for case 1. The quantities expected based on the chemistry can be well reproduced with the model. The quantities from the Keuper, the anhydrite group, and the Wellengebirge are negligible. Muschelkalk accounts for the largest part of about 60 %, followed by crystalline rock (27 %) and Trigonodus-Dolomit (13 %).

Table 3: Composition of the produced water in SLA-2 (case 1)

Zone / Layers	Composition
Keuper	0.0 %
R3 (Trigonodus-Dolomit)	13.0 %
Hauptmuschelkalk	58.9 %
Anhydritgruppe	0.3 %
Wellengebirge	0.5 %
Bundsandstein/Rotliegendes/Kristallin	27.3 %

Figure 15 shows the transient fluxes for case 1 at the boundaries of the local transport model for the different zones in logarithmic scale. The shell limestone was examined separately according to the cardinal directions. The steadily increasing flux at the boundaries of the local transport model clearly show that a steady state condition has not yet been reached.

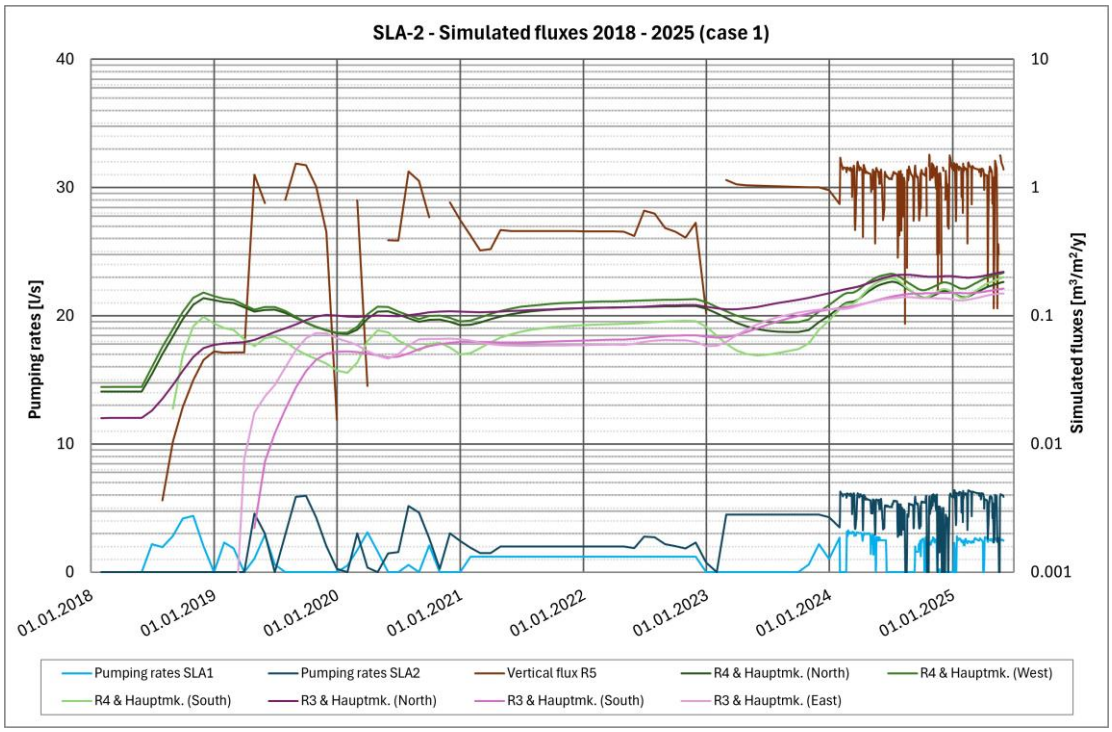


Figure 15: Transient flux across the boundaries of the local transport model for case 1.

4.3 Performance pumping test 2015

For an additional validation of the assumed increase in permeability that was discussed in chapter 3, the pumping test of 2015 was remodeled with case 1. Figure 16 shows the simulated pressure heads in light green. It can be seen that neither the average level nor the dynamics can be reproduced. The kf-values of zones R1, R2, and R5 as well as the adjacent aquifer (main shell limestone and crystalline) were adjusted iteratively until the quality of the calibration 2015 [2] was met. The resulting kf-values are 10 to 25 times lower than in case 1, which numerically supports the assumption of an increase in permeability with simulation time (see Table 4). It is important to note that without a reduction in permeability in the adjacent aquifer, no satisfactory results can be achieved.

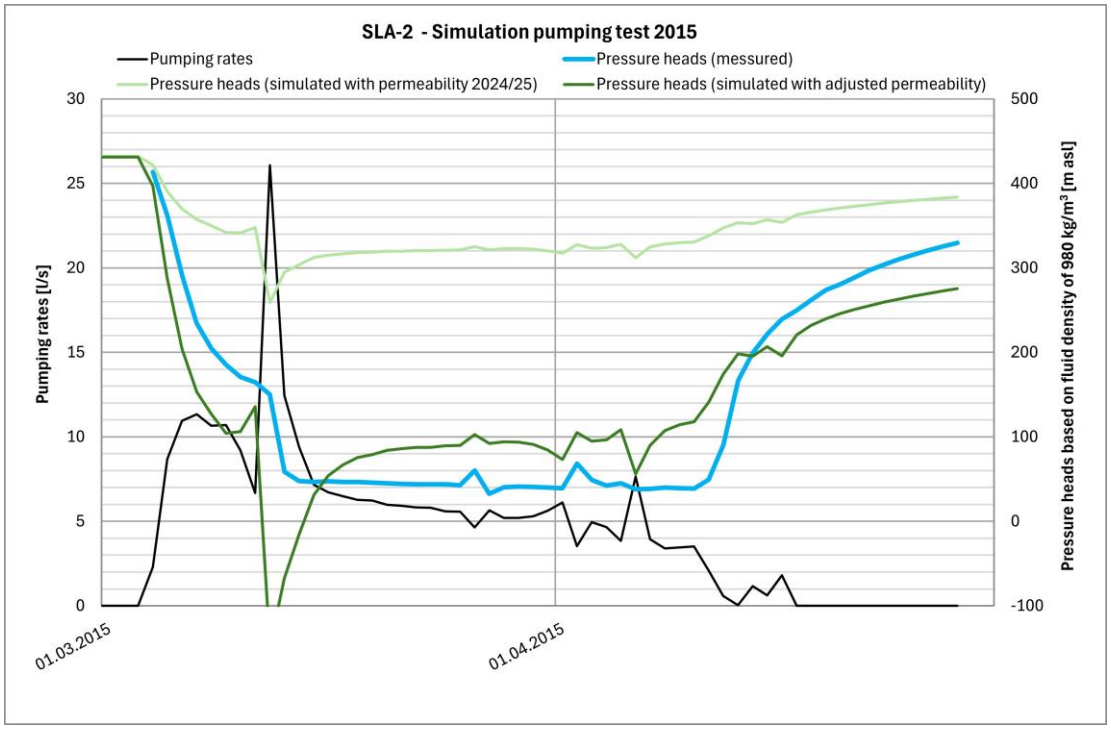


Figure 16: Simulated pressure heads 2015 for case 1 as well as with adjusted permeabilities.

Table 4: Adjusted kf-values case 1 for the simulation of 2015.

Zones / Layers	2025 kf [m/s]	2015 kf [m/s]	factor [-]
Hauptmuschelkalk	1.0E-07	1.0E-08	10
Wellengebirge	1.0E-10	1.0E-10	1
Bundsandstein/Rotligendes/Kristallin	7.0E-09	7.0E-10	10
R1	2.0E-04	8.0E-6	25
R2	1.0E-04	8.0E-6	25
R3 (Trigonodus-Dolomit)	5.0E-09	5.0E-09	1
R4 (Trigonodus-Dolomit)	2.0E-07	2.0E-07	1
R5	1.0E-06	4.0E-8	25

5 Conclusion

Within the scope of model uncertainties and limited availability of flow-relevant spatial data, two simulation cases were identified that accurately reproduce the pressure drops of the most recent measurement period with the adapted concept of the research project. The corresponding volume flows for the boundaries of the reactive, local transport model of the UniBe were extracted and supplied for both cases. Extended modeling can now be used to reduce uncertainties and determine the best case. The increase in permeability derived from the measurement data over the last few years of production can be very well justified with both model approaches (2020 and 2025). Without permeability adjustments, the 2020 model significantly overestimates the pressure drop in the 2024/25 period, and the 2025 model significantly underestimates the 2015 pumping test pressure drop.

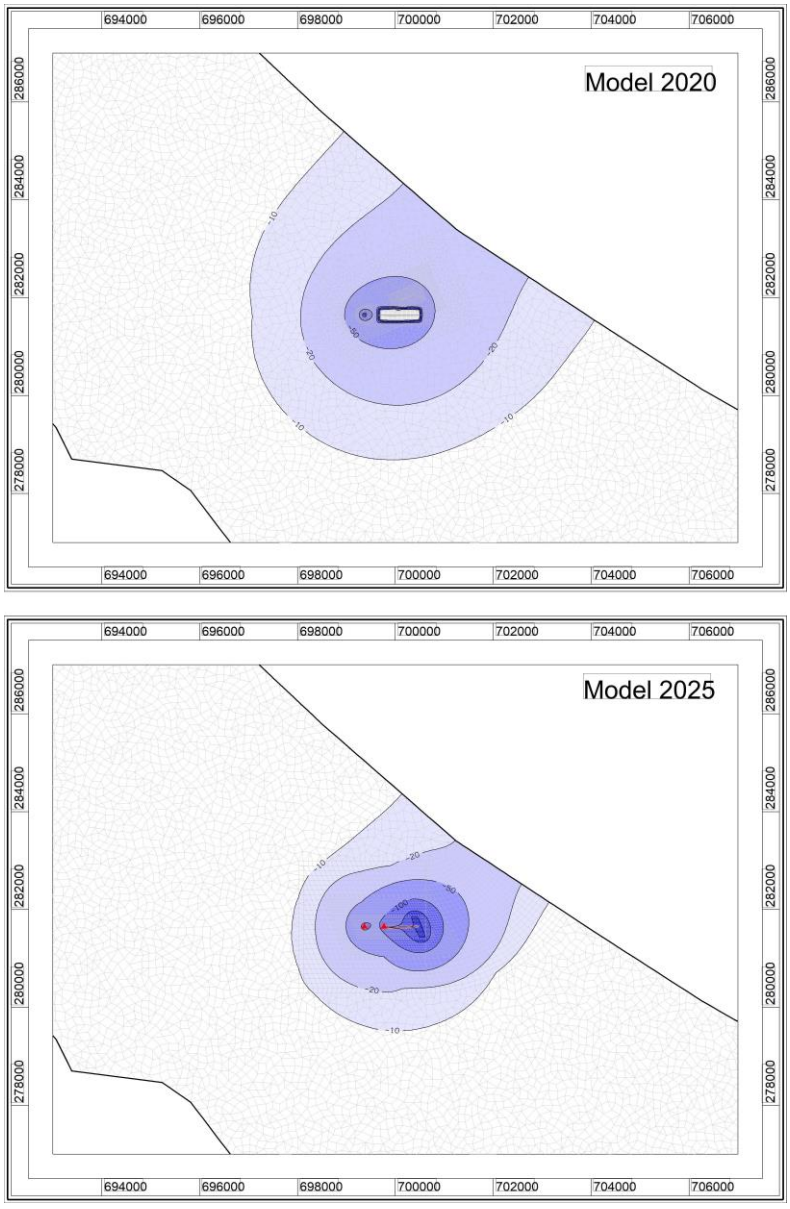


Figure 17: Long-term pressure drop comparison for the models 2020 and 2025.

The model updates during this project enabled a combination of the two existing conceptual model approaches of 2020 [2] and 2025 [4]. The new model concept thus allows a reproduction of the measured flow data and the lates hydro-chemical measurements. Since the adjustments are limited to the nearby region of the well SLA-2 and involve an increase in local permeability, the long-term pressure drops calculated in [2] for the licence application are still valid or should be considered as worst-case scenario (see Figure 17).

Zurich, 19. November 2025

Editors: M. Ballmer / R. Künze

TK CONSULT AG

Dr. Rouven Künze
Project Manager
rouven.kuenze@tkconsult.ch
044 288 81 88

Michael Ballmer
Project Manager
michael.ballmer@tkconsult.ch
044 288 81 82

Bibliography

[1] Kuhlmann, U. & Ballmer, M.: Geothermie Projekt Schlattingen: Hydrothermisches Modell des Muschelkalk-Aquifers, Project-Report NPB 12, 19.10.2012.

[2] Künze, R. & Kuhlmann, U.: NPB 20-01. Hydraulische Modellierungen Schlattingen 1 und 2. - Nagra Project Report, NPB 20-01, TK CONSULT AG report from 13.05.2020.

[3] Frieg, B., Wanner, C., Eichinger, F., Alt-Epping, P. & Diamond, L. (2024): Reservoir characterization of the Upper Muschelkalk aquifer in the canton of Thurgau for the optimization of geothermal utilization, Zwischenbericht Forschungsprojekt Kanton Thurgau z.Hd. Bundesamt für Energie (BFE), Section Energy Research and Cleantech from 20.12.2024.

[4] Wanner, C., Alt-Epping, P. &, Diamond, L. (2024): Conceptual Model SLA-2. – University of Bern, 2 pages power point presentation from the working group online meeting, 24.06.2025.

[5] Enevista Energy AG (2025a): Measurement data SLA-1/SLA-2, 2024 – 2025. – Measured data Grob Gemüse AG (processed), 10.06.2025.

[6] Enevista Energy AG (2025b): Monthly and annual reports with measurement data SLA-1/SLA-2 2018 – 2023. – Reports and measured data from Grob Gemüse AG (processed), 01.10.2025.

[7] König, C.M., Becker, M., Brömme, K., Diehl, A., König, T., Seidel, T., Rosen, B., Rüber, O. Schröder, S. & Zimmermann, C. (2024): Spring Benutzerhandbuch - SPRING Version 6; Witten (Deutschland).